

MICROPHYSICAL PROPERTIES AND
INTERPLAY OF NATURAL CIRRUS,
CONTRAIL CIRRUS AND AEROSOL
AT DIFFERENT LATITUDES



Elena De La Torre Castro



**MICROPHYSICAL PROPERTIES AND INTERPLAY OF
NATURAL CIRRUS, CONTRAIL CIRRUS AND AEROSOL
AT DIFFERENT LATITUDES**

MICROPHYSICAL PROPERTIES AND INTERPLAY OF NATURAL CIRRUS, CONTRAIL CIRRUS AND AEROSOL AT DIFFERENT LATITUDES

Dissertation

for the purpose of obtaining the degree of doctor
at Delft University of Technology
by the authority of the Rector Magnificus, Prof. dr. ir. T. H. J. J. van der Hagen,
chair of the Board for Doctorates
to be defended publicly on
Tuesday 21 January 2025 at 15 o'clock

by

Elena DE LA TORRE CASTRO

Master of Science in Aerospace Engineering,
Technical University of Munich, Germany
born in Madrid, Spain.

This dissertation has been approved by the promotor.

Composition of the doctoral committee:

Rector Magnificus,	chairperson
Prof. Dr. V. Grewe	Delft University of Technology, <i>promotor</i>
Prof. Dr. C. Voigt	Johannes Gutenberg Universität Mainz, <i>promotor</i>

Independent members:

Prof. Dr. A. Gangoli Rao	Delft University of Technology
Prof. Dr. A. P. Siebesma	Delft University of Technology
Prof. Dr. M. Rapp	Ludwig-Maximilians-Universität, Germany
Prof. Dr. J. Curtius	Goethe-Universität Frankfurt, Germany
Dr. F. Yin	Delft University of Technology, <i>reserve member</i>

Other members:

Dr. T. Jurkat-Witschas	German Aerospace Center, <i>supervisor</i>
------------------------	--



This research was part of the project "Microphysics and climate impact of ice clouds in high latitudes" (MICRO-ICE), contributing to the High Altitude and Long Range Research Aircraft (HALO) mission CIRRUS-HL. It has been funded by the German Research Foundation (Deutsche Forschungsgemeinschaft in German, DFG) under the Priority Program SPP 1294 and grant agreements Nos. VO1504/6-1, VO1504/7-1, and VO1504/9-1; TRR 301, project ID 428312742.

Keywords: Cirrus clouds, contrail cirrus, aerosol, in situ measurements, microphysical properties, HALO research aircraft, CIRRUS-HL, ice crystal number concentration, effective diameter, relative humidity, mid-latitude, high latitude, backward trajectories, Cloud Droplet Probe, Cloud Imaging Probe, Precipitation Imaging Probe

Front & Back: Morning sky over the Westpark (Munich) showing evolving contrails, contrail cirrus and natural cirrus. Photo and design by Elena De La Torre Castro.

Copyright © 2024 by E. De La Torre Castro

An electronic version of this dissertation is available at <http://repository.tudelft.nl/>.

CONTENTS

Summary	ix
Samenvatting	xi
1 Introduction	1
1.1 Motivation	1
1.2 Research questions	5
1.3 Outline	6
2 Ice clouds: nature and human influence	9
2.1 Introduction	9
2.2 Ice crystal formation	10
2.2.1 Cloud droplet formation	12
2.2.2 Ice nucleation mechanisms	14
2.3 Cirrus	17
2.3.1 Cirrus origin and life-cycle	17
2.3.2 Microphysical properties	19
2.3.3 Atmospheric aerosol and their role in cirrus formation	21
2.4 Aviation-induced cloudiness	23
2.4.1 Contrail formation	25
2.4.2 Contrail cirrus: evolution of contrails	26
2.4.3 Microphysical properties of contrails and contrail cirrus	28
3 Measurement techniques	29
3.1 Forward scattering probes	30
3.1.1 Working principle	31
3.1.2 Particle size determination	32
3.1.3 Measurement limitations and uncertainties	34
3.1.4 Cloud and Aerosol Spectrometer with Depolarization (CAS-DPOL)	35
3.2 The Optical Array Probes	37
3.2.1 Working principle	37
3.2.2 Particle size determination	41
3.2.3 Measurement limitations and uncertainties	43
3.3 Definitions of microphysical properties	44
4 Methods	49
4.1 CDP methods	49
4.1.1 Sizing calibration	50
4.1.2 Investigating time resolution	52
4.1.3 CDP and CAS-DPOL intercomparison	55

4.2	OAPs methods	65
4.2.1	Image data processing: Filters and corrections.	65
4.2.2	Calibration.	76
4.3	Combined size distribution	79
4.3.1	CIPgs-PIP Overlap region characterization.	79
4.3.2	Calculation of the combined size distribution	82
4.3.3	Remarks on uncertainties and implications	83
5	Differences in the microphysical properties of high and mid-latitude cirrus	87
5.1	The CIRRUS-HL campaign	88
5.2	Methods	92
5.2.1	Cloud particle, relative humidity, and aircraft reference measurements	92
5.2.2	Air mass trajectories	93
5.3	Overview of the microphysical properties.	94
5.4	Cirrus origins at mid- and high latitudes	100
5.5	Influence of cloud formation on cirrus properties.	105
5.6	Aerosol-cloud interactions	108
5.6.1	Aerosol model data	108
5.6.2	Results.	111
5.7	Discussion of limitations	117
5.7.1	Influence of the method	117
5.7.2	Representativeness	118
5.8	Summary and conclusions	119
6	Contrail cirrus and natural cirrus interaction	123
6.1	Introduction	123
6.2	Methodology	124
6.3	Influence of contrail cirrus on natural cirrus	126
6.4	Summary	130
7	Background aerosol concentrations from observations and model	133
7.1	Introduction to contrail particles activation in the low-particle regime and contrail formation from hydrogen aircraft	134
7.2	Comparison of measured and modelled background aerosol concentration during CIRRUS-HL.	136
7.2.1	Overview of measurement techniques and model setup	136
7.3	Analysis and results	138
7.4	Summary	141
8	Conclusion	145
8.1	Overview	145
8.2	Answers to research questions	147
9	Outlook	151
9.1	Prospects of cloud measurement techniques	151
9.2	Further research on cirrus and contrail cirrus.	154

Acronyms	157
Symbols	159
A Appendix: Additional Figures	187
A.1 CDP and CAS-DPOL intercomparison	187
A.2 Extinction coefficient of high and mid-latitude cirrus	192
A.3 In situ and liquid origin measurements per day	193
A.4 Sensitivity study of latitude threshold 60°N	193
A.5 Additional analyses for aerosol-cloud interaction	195
A.5.1 Extra analyses with climatological data	195
A.5.2 Sensitivity study of simulations including ammonium sulfate and glassy organics	195
A.5.3 Sensitivity study for years 2020 and 2019.	196
B Appendix: Image data decompression	199
Acknowledgements	207
Curriculum Vitae	209
List of Publications	211

SUMMARY

Cirrus clouds play a crucial role in the Earth's energy budget. They reflect incoming sunlight and absorb and re-emit terrestrial infrared radiation. The magnitude of these components depends on the cirrus microphysical properties (e.g., ice crystal number and effective diameter), which can result in either net warming or cooling effects. This thesis investigates the differences in those properties of high- and mid-latitude cirrus, as well as their interactions with atmospheric aerosol and aviation-induced contrail cirrus.

To explore these differences, cirrus clouds were measured with the German research aircraft HALO (High Altitude and LOng Range) during the CIRRUS-HL (CIRRUS at High Latitudes) campaign in June and July 2021. A total of 24 flights and 35 hours of in situ measurements of cirrus particle data were collected with the Cloud Droplet Probe (CDP), the Cloud Imaging Probe Grayscale (CIPG) and the Precipitation Imaging Probe (PIP). A comprehensive intercomparison among the instruments, along with a detailed uncertainty analysis, was performed, resulting in an accurate and quality-controlled data set.

The results of these measurements show that high-latitude cirrus, compared to mid-latitude cirrus, have lower median ice number concentration (0.001 and 0.0086 cm^{-3}), higher median effective diameter (210 and $165 \text{ }\mu\text{m}$), and lower median extinction coefficient (0.042 and 0.072 m^{-1} , respectively). In addition, high relative humidity over ice is observed, particularly at high latitudes, with median values around 125%. The influence of the formation region on cirrus properties was assessed by combining measurements with weather model data and backward trajectories starting at the flight tracks. The results show that a large part of the high-latitude cirrus were formed at mid-latitudes, leading to different properties compared to cirrus formed directly at high latitudes. Simulations from an aerosol-chemistry-climate model were combined with the backward trajectories and a strong contribution of heterogeneous nucleation was identified in the measured cirrus. Thus, the low concentrations of ice nucleating particles at high latitudes (from the model) combined with high ice supersaturation levels might explain the lower ice number concentration and larger effective diameter of cirrus measurements at high latitudes compared to mid-latitudes.

Aviation emissions have a large local impact on the cirrus microphysical properties through contrail formation and their evolution to contrail cirrus. The CIRRUS-HL data set shows a higher occurrence of contrail cirrus at mid-latitudes, and a potential impact on natural cloudiness by reducing supersaturation levels at cirrus altitudes. The effect of contrails from future propulsion technologies may depend on background aerosol concentrations. Comparisons of measurements and model data for total aerosol number concentrations show good agreement for the larger particle size mode ($> 250 \text{ nm}$), but likely an underestimation above 300 hPa in the Aitken mode ($> 12 \text{ nm}$).

By combining observations with model data, this study contributes to enhancing the understanding of the variability in cirrus properties due to different formation mechanisms and aerosol influences, as well as the interaction of natural and contrail cirrus.

SAMENVATTING

Cirruswolken spelen een cruciale rol in de energiebalans van de aarde. Ze reflecteren inkomend zonlicht en absorberen en heruitzenden terrestrische infrarode straling. De omvang van deze componenten hangt af van de microfysische eigenschappen van cirrus (bijv. het aantal ijskristallen en de effectieve diameter), wat kan resulteren in netto opwarmende of afkoelende effecten. Deze scriptie onderzoekt de verschillen in deze eigenschappen van cirruswolken op hoge en middelhoge breedtegraden, evenals hun interacties met atmosferische aerosolen en door de luchtvaart veroorzaakte contrail-cirrus.

Om deze verschillen te onderzoeken, werden cirruswolken gemeten met het Duitse onderzoeks vliegtuig HALO (High Altitude and Long Range) tijdens de CIRRUS-HL (CIRRUS at High Latitudes) campagne in juni en juli 2021. In totaal werden 24 vluchten uitgevoerd en 35 uur aan in situ metingen van cirrusdeeltjes verzameld met de Cloud Droplet Probe (CDP), de Cloud Imaging Probe Grayscale (CIPG) en de Precipitation Imaging Probe (PIP). Een uitgebreide vergelijking tussen de instrumenten, samen met een gedetailleerde onzekerheidsanalyse, werd uitgevoerd, wat resulteerde in een nauwkeurige en gecontroleerde dataset.

De resultaten van deze metingen tonen aan dat cirrus op hoge breedtegraden, vergeleken met cirrus op middelhoge breedtegraden, een lagere mediane ijskristalconcentratie hebben (0.001 en 0.0086 cm^{-3}), een grotere mediane effectieve diameter (210 en $165 \text{ }\mu\text{m}$), en een lagere mediane extinctiecoëfficiënt (0.042 en 0.072 m^{-1}). Bovendien wordt een hoge relatieve luchtvochtigheid over ijs waargenomen, vooral op hoge breedtegraden, met mediane waarden rond 125% . De invloed van het vormingsgebied op de eigenschappen van cirrus werd beoordeeld door metingen te combineren met weermodelgegevens en terugtrajecten beginnend bij de vluchttrajecten. De resultaten tonen aan dat een groot deel van de cirrus op hoge breedtegraden werd gevormd op middelhoge breedtegraden, wat leidt tot andere eigenschappen vergeleken met cirrus die direct op hoge breedtegraden zijn gevormd. Simulaties van een aerosol-chemie-klimaatmodel werden gecombineerd met de terugtrajecten en een sterke bijdrage van heterogene nucleatie werd geïdentificeerd in de gemeten cirrus. Zo kunnen de lage concentraties ijssnucleërende deeltjes op hoge breedtegraden (volgens het model) in combinatie met hoge ijssupersaturatieniveaus de lagere ijskristalconcentratie en grotere effectieve diameter van cirrusmetingen op hoge breedtegraden vergeleken met middelhoge breedtegraden verklaren.

Luchtvaartemissies hebben een grote lokale impact op de microfysische eigenschappen van cirrus door contrailvorming en hun evolutie tot contrail-cirrus. De CIRRUS-HL dataset toont een hogere frequentie van contrail-cirrus op middelhoge breedtegraden, en een potentiële impact op natuurlijke bewolking door de reductie van supersaturatieniveaus op cirrushoogten. Het effect van contrails van toekomstige voortstuwingsstechnologieën kan afhankelijk zijn van de achtergrondconcentraties van aerosolen. Vergelijkingen van metingen en modelgegevens voor totale aerosolconcentraties tonen een

goede overeenkomst voor de grotere deeltjesgrootte modus (> 250 nm), maar waarschijnlijk een onderschatting boven 300 hPa in de Aitken modus (> 12 nm).

Door observaties te combineren met modelgegevens draagt deze studie bij aan een beter begrip van de variabiliteit in cirrus-eigenschappen als gevolg van verschillende vormingsmechanismen en aerosolinvloeden, evenals de interactie tussen natuurlijke en contrail-cirrus.

1

INTRODUCTION

1.1. MOTIVATION

Climate refers to long-term patterns of atmospheric conditions observed in a specific region, while weather fluctuates on shorter timescales. Cloudiness plays a significant role in regulating the Earth's climate (Liou, 1986). Large-scale circulation patterns determine cloud occurrence, while clouds, in turn, influence these processes through their radiative effects (Stephens, 2005). Additionally, clouds play a crucial role in regulating the Earth's water cycle and in processing and transporting chemical tracers and aerosol particles within the atmosphere (Stephens, 2005). Understanding cloud processes and feedbacks is essential for improving climate predictions in a changing environment.

Clouds impact the energy budget of the atmosphere based on their macro- and microphysical properties. Compared to clear skies, clouds absorb and re-emit thermal-infrared (longwave) radiation from the Earth's surface. This contribution typically being positive and more significant for clouds with colder cloud top temperatures (Hartmann et al., 1992; Liou, 1986; Stephens, 2005; Cotton et al., 2011; Gasparini & Lohmann, 2016). Clouds also reflect incoming solar (shortwave) radiation, contributing to the planetary albedo, which is the fraction of sunlight reflected back into space by the earth (Twomey, 1974). Clouds generally have a higher albedo than the surface, except for ice or sand surfaces, which are brighter. As a result, they reduce the portion of solar radiation reaching the ground, with the extent of this effect mainly dependent on cloud optical thickness (Hartmann et al., 1992; Liou, 1986; Stephens, 2005; Cotton et al., 2011; Gasparini & Lohmann, 2016). Cloud optical thickness, a crucial cloud property, depends on cloud microphysical properties (e.g., cloud phase, size, shape, and concentration of cloud particles) and vertical extent (Cotton et al., 2011).

Whether a cloud exerts a net positive or negative radiative effect depends on the difference between shortwave and longwave radiative effect, which varies based on cloud type, the horizontal and vertical cloud location, season, solar angle, and ground surface conditions (Stephens, 2005). Low clouds typically have a strong net cooling effect during the day due to their high concentrations of small droplets, leading to a high albedo and

a significant negative shortwave radiative effect. Additionally, their temperature does not differ much from the surface temperature, resulting in a minimal positive longwave radiative effect (Cotton et al., 2011). Conversely, high clouds, known as cirrus clouds, can have either have a net positive or negative radiative effect. Located at higher altitudes where cloud top temperature is lower, they exhibit stronger longwave radiative effect. Whether the shortwave cooling compensates for the positive longwave radiative effect depends largely on the cirrus microphysical properties, such as size or crystal habit (Zhang et al., 1999; Wendisch et al., 2005; Wendisch et al., 2007). Optically thin cirrus can significantly contribute to a warming effect due to their low reflectivity and small shortwave cooling effect. Additionally, the radiative effect of cirrus clouds exhibits strong day-night and seasonal variability due to the changing solar radiation (Gasparini & Lohmann, 2016; Gasparini et al., 2017). On average, as illustrated in Fig. 1.1 from Gasparini et al. (2017), cirrus clouds exert a net positive radiative effect. However, uncertainties persist regarding the radiative effects of cirrus clouds, particularly concerning the size, mass, and shape of ice crystals and the representation of thin cirrus, which are often not detectable by satellites (Boucher et al., 2013; Spang et al., 2023). This emphasizes the importance of observing cirrus microphysical properties to enhance their representation in global climate models.

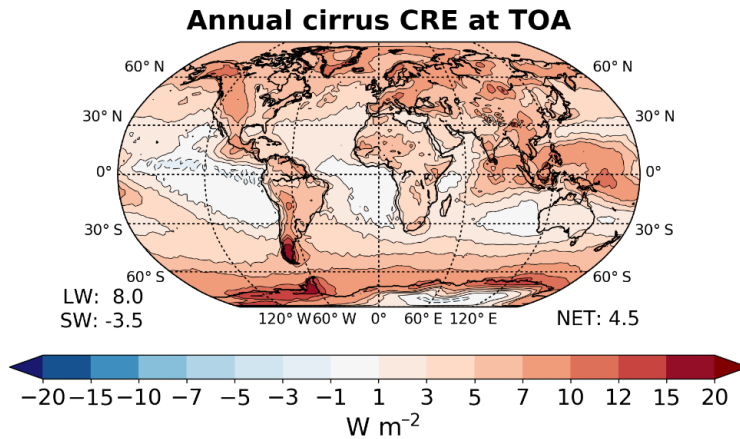


Figure 1.1: Anomalies of the annual average over five years cirrus cloud radiative effects (CRE) at the top of the atmosphere (TOA). Overall averages of the longwave (LW) and shortwave (SW) radiative effects are indicated in the bottom left, while the net radiative effect is indicated in the bottom right. (Adapted from Gasparini et al. (2017), used under CC BY 3.0).

The properties of cirrus display considerable variability and are influenced by multiple factors, including thermodynamic conditions (such as temperature and relative humidity), dynamic conditions (like updraft velocity), aerosol loading and chemical composition (Hendricks et al., 2011; Patnaude & Diao, 2020; Maciel et al., 2022). The interplay of these factors governs the cloud particle nucleation process and determines the number, size, and shapes of ice crystals within the cirrus cloud. Consequently, cirrus properties can vary substantially among different synoptic regimes (Muhlbauer et

al., 2014). For instance, gravity waves can induce the nucleation of a large amount of small ice crystals (Kärcher & Lohmann, 2002b; Hendricks et al., 2011; Jensen et al., 2013). However, cirrus forming in high-pressure systems typically do not reach high supersaturations, resulting in lower ice particle concentrations (Krämer et al., 2016). Essentially, the formation of ice particles in cirrus is characterized by a very dynamic interplay of ice supersaturation and aerosol concentration and composition, leading to either heterogeneous or homogeneous ice particle nucleation. Heterogeneous freezing on solid aerosol particles with the ability to nucleate ice, known as ice nucleating particle (INP), requires lower supersaturations than homogeneous nucleation. Therefore, heterogeneous nucleation can initiate earlier and prevent the occurrence of homogeneous nucleation. However, the number of ice crystals produced is lower compared to homogeneous nucleation on abundant solution aerosol particles (e.g., sulfuric acids) (Möhler et al., 2003; Kärcher et al., 2006; Kärcher et al., 2022).

Heterogeneous nucleation processes are not yet well understood, with INP concentrations varying across different regions of the globe (DeMott et al., 2010). Additionally, the freezing properties of different INP types are still not well characterized (Hoose & Möhler, 2012), primarily due to the challenges posed by direct atmospheric measurement at colder temperatures (Hoose & Möhler, 2012; Kanji et al., 2017). Among the natural sources of INPs emitted into the atmosphere, mineral dust particles play a dominant role (Möhler et al., 2006; Froyd et al., 2022). However, other natural sources such as volcanic eruptions or oceans, as well as anthropogenic sources like agriculture, industries, biomass burning, or transport contribute to the presence of INPs but their activation properties are not fully understood (Kanji et al., 2017; Froyd et al., 2022). According to Forster et al. (2021), anthropogenic INPs influence ice crystal numbers in cirrus and thereby their radiative properties. Particularly, soot particles from aviation are directly emitted at cirrus altitudes, reaching the highest concentrations in the mid-latitudes in the Northern Hemisphere, and can act as INPs, potentially affecting the cirrus microphysical properties indirectly (Kanji et al., 2017; Urbanek et al., 2018; Groß et al., 2022). However, the nucleation efficiency of this type of INPs is not well known, leading to significant uncertainty regarding their impact (Righi et al., 2021).

While many unknowns remain regarding the effects of INPs in cirrus, the microphysical properties of cirrus have been extensively studied over the last decades using various approaches, including global modelling (Mitchell et al., 2008; Spichtinger & Gierens, 2009b, 2009a; Gasparini et al., 2018), active and passive remote sensing techniques (Sassen & Campbell, 2001; Gryspeerdt et al., 2018; Sourdeval et al., 2018), and in situ measurements, primarily conducted in mid-latitudes and tropical regions (Heymsfield et al., 2013; Jensen et al., 2013; Muhlbauer et al., 2014; Krämer et al., 2016; Luebke et al., 2016; Voigt et al., 2017; Krämer et al., 2020). Although there is considerable research on cirrus properties in these regions, few studies have focused on high-latitude cirrus (V. Wolf et al., 2018; Marsing et al., 2023). Despite the urgency to understand the drivers and feedbacks of accelerated warming of the Arctic (Serreze & Barry, 2011), understanding the processes contributing and modulating the so-called Arctic Amplification, including the role of clouds and their modifications through these mechanisms, is critical for addressing questions regarding current and future climate (Wendisch et al., 2017; Schmale et al., 2021; Shupe et al., 2022; Wendisch et al., 2023).

The natural cloudiness in the upper troposphere can be altered by anthropogenic activities, particularly aviation. Aviation accounts for approximately 4% of the total effective radiative forcing from human activities (Kärcher, 2018; Lee et al., 2021). Beyond the impact of CO₂ emissions, non-CO₂ effects such as NO_x emissions, contrails and contrail cirrus can contribute to nearly two-thirds of aviation's effective radiative forcing, though these effects are associated with large uncertainties (Kärcher, 2018; Lee et al., 2021). Understanding their direct influence on the climate is crucial, but it is also essential to examine how they interact with atmospheric water vapor and natural cloud cover, particularly, cirrus clouds. The atmospheric conditions conducive to contrail formation and persistence are often similar to those required for cirrus clouds, leading to their co-existence in the same regions and potential impacts on the formation and life-cycle of natural cloudiness (Schumann, 1996; K. Gierens, 2012; Schumann et al., 2015).

While newly formed contrails, within the initial minutes of emission, typically exhibit ice particles concentrations exceeding 100 cm⁻³ and sizes of a few micrometers (Petzold et al., 1997; Voigt et al., 2010; Voigt et al., 2011; Jeßberger et al., 2013; Schumann et al., 2017; Kleine et al., 2018), their properties undergo significant transformations upon mixing with the surrounding ambient air. Processes such as sublimation, growth, and sedimentation, controlled by ambient conditions, drive these changes (Schumann et al., 1998; Kärcher et al., 2015; Kärcher, 2018; Kärcher et al., 2018). Depending on the atmospheric conditions, contrails may disperse and lose their linear shape, evolving into contrail cirrus, which can extend over vast areas, particularly in regions with heavy air traffic areas where they merge with one another. In addition, contrails can interact with and alter natural cirrus by increasing their number concentration and optical thickness (Tesche et al., 2016; Marjani et al., 2022; Verma & Burkhardt, 2022), and by reducing their effective diameter (Kristensson et al., 2000; Li et al., 2022; Wang et al., 2023). Although the microstructure of contrail cirrus closely resembles that of natural cirrus, it still differs by the higher concentrations of smaller ice crystals (Voigt et al., 2017). However, when contrails form within existing cirrus, their microphysics can be influenced depending on the ambient conditions, making it challenging to distinguish between them (Unterstrasser et al., 2017a; Unterstrasser et al., 2017b).

In short, advancing the understanding of the microphysical properties of cirrus clouds is crucial for comprehending their role in the Earth's climate system. These properties exhibit significant variability and are influenced by numerous factors, including atmospheric dynamics and radiation, aerosol concentrations, and temperature. Therefore, a closer look at the mechanisms driving the life cycle of cirrus clouds will not only enhance our understanding of local and regional variations but also shed light on broader climate processes. In situ observations play a pivotal role in gaining insight into cloud dynamics, particularly when accompanying cloud microphysical properties by measurements of aerosols, relative humidity, and updraft speeds. High-latitude regions, such as the Arctic, are of particular interest due to the phenomenon of Arctic Amplification and their relatively pristine atmospheric conditions. A comparative analysis of observations from high-latitude regions with those from more anthropogenically influenced mid-latitudes, where aviation plays a significant role, can provide valuable insights into how human activities impact cirrus properties. In addition, observations of high-latitude cirrus are scarce, but necessary to validate and improve climate models

and satellite retrievals.

1.2. RESEARCH QUESTIONS

The primary hypothesis addressed in this study concerns potential differences in the microphysical properties of cirrus clouds between high-latitude and mid-latitude regions. Building upon this central premise, additional questions are formulated to deepen the comprehension of cirrus microphysical characteristics, including an examination of the factors influencing their formation and evolution. The research questions (RQs) guiding this work are as follows:

- Do measurable differences exist in the microphysical properties of cirrus clouds between high latitudes and mid-latitudes? If so, what are they?
- How do air masses from mid-latitudes influence cirrus at high latitudes? How do their properties change compared to cirrus purely developed at high latitudes?
- What role do aerosols and atmospheric dynamics play in influencing the properties of high-latitude cirrus in comparison to those at mid-latitudes? How does simulated aerosol concentrations compare to measurement data in air traffic relevant regions?
- How does aviation influence the microphysical properties of natural cirrus?

To address these research questions, I performed in situ measurements and evaluated the data during the airborne experiment CIRRUS in High Latitudes (CIRRUS-HL), conducted in June and July 2021. The primary data set that I have analysed comprises cirrus cloud particle samples from two state-of-the-art cloud probes that I operated during the campaign: the Cloud Combination Probe (CCP) and the Precipitation Imaging Probe (PIP). These instruments measure the number, size, and form of the ice crystals within the cirrus clouds. An essential aspect of my work involved processing and integrating the instruments data to provide a unified data set, serving as the foundation for the analyses. This data set contains key microphysical properties of the observed cirrus, including number concentration (N), effective diameter (ED), and ice water content (IWC).

The diagram presented in Fig. 1.2 provides an overview of the research questions and objectives addressed in this study. Particularly, it shows the atmospheric processes that impact cirrus formation and life-cycle, which will be thoroughly explained and investigated along this thesis.

To answer RQ1, I examined the microphysical properties in relation to the latitude of the measurements, requiring aircraft positional data for precise analysis. Additionally, to gain deeper insights into the diverse influences acting over the lifespan of cirrus clouds, I identified their formation points using backward trajectories starting at the measurement positions. This approach enabled me to analyse cirrus properties not only based on measurement locations but also on their formation, leading to answers for RQ2 and RQ3. To further address the third question, I integrated modelling data on ice nucleating particles (INPs) with the backwards trajectories to discern the aerosol loadings influencing the cirrus formation and evolution. Furthermore, I evaluated the model data

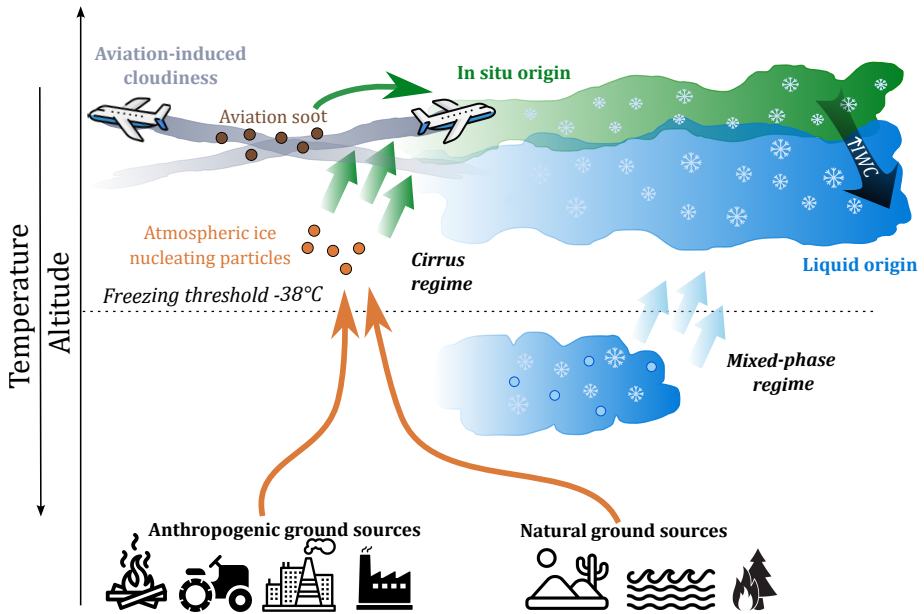


Figure 1.2: Schematic overview of the research topics investigated in this thesis.

against in situ observations of total aerosol concentrations. Finally, I included information on relative humidity and nitrogen oxides to assess the aviation influence during the CIRRUS-HL campaign and address the fourth question, RQ4.

This research is part of the project "Microphysics and climate impact of ice clouds in high latitudes" (MICRO-ICE), contributing to the High Altitude and Long Range Research Aircraft (HALO) mission CIRRUS-HL, funded by the Deutsche Forschungsgemeinschaft under the Priority Program SPP 1294.

1.3. OUTLINE

Outlined below is a structured overview of the chapters and contents comprising this thesis, offering a comprehensive journey through the experimental investigation and analysis of natural ice clouds and their modification by the effect of aviation.

In Chapter 2, insights into the fundamental processes governing ice formation are provided, along with an exploration of the diverse types of cirrus clouds, focusing on the main factors influencing their microphysical properties. Additionally, the role of aerosol particles in cirrus formation and evolution processes is briefly discussed, and an introduction to contrails, the human-made ice cloud type, is provided.

Subsequently, Chapter 3 delves into the theoretical concepts of the measurement techniques employed in this study. The working principles and limitations of the Cloud Droplet Probe (CDP) and Cloud Imaging Probe Grayscale (CIPG), components of the Cloud Combination Probe (CCP), as well as, the Precipitation Imaging Probe (PIP), used

for the measurements of cloud particles within this work, are described. These instruments are further characterized in Chapter 4, which elaborates on the methods and developments conducted for data analysis. In particular, the software I implemented to decompress and interpret binary data from the the CIPG and PIP instruments, generating two-dimensional images for further post-processing, is explained in detail. Finally, this chapter addresses the combination of the cloud probe measurements to obtain a unified data set.

In Chapter 5 I introduce the CIRRUS-HL campaign, which sets the frame and location of the experimental setup and provides the primary data source of this thesis. I present the scientific findings regarding properties and formation processes of cirrus measured during the campaign, including a differentiation of cirrus according to the latitude of the measurement. Furthermore, I conduct additional analyses considering cloud history and formation point. Additionally, I propose a novel classification based on latitude at formation and measurement to enhance our understanding of the measured cirrus properties. Finally, in this chapter, I investigate aerosol-cloud interactions with support from modelling data. Chapter 6 examines the effects of aviation on the CIRRUS-HL data set, while Chapter 7 investigates background aerosol concentrations from both observations and model simulations for the CIRRUS-HL flights. This chapter also provides an outlook on the relevance of background aerosol for contrail formation from future propulsion technologies, such as hydrogen-powered aircraft. Lastly, Chapter 8 provides a summary of the main findings and discusses their implications for society, and Chapter 9 offers an outlook on future research directions and suggestions for further improving and continuing this work.

2

ICE CLOUDS: NATURE AND HUMAN INFLUENCE

2.1. INTRODUCTION

Cirrus clouds, together with contrails and contrail cirrus are clouds composed purely of ice crystals and occur at a wide range of temperatures. Cirrus are located at high altitudes, above 8 km in the mid-latitudes and 12 km in the tropics, and have a translucent threadlike appearance (Heymsfield et al., 2017a). Contrary to natural cirrus clouds, contrails and contrail cirrus are not natural clouds, as the ice crystals form from the cooling and mixing with the ambient air of hot and humid aircraft exhaust plumes. Therefore, they are also found at high altitudes, where air traffic is present (at cruise levels between 32000-43000 ft, corresponding to 9.8-13 km) and the ambient temperature is below -38°C , the temperature at which droplets freeze at those altitudes. Contrails are line-shaped in the early stage, and can be visually easily distinguished from cirrus clouds. However, as they evolve over time, their coverage expands and they lose their linear shape, transitioning to contrail cirrus. They may also cluster together covering large areas, becoming similar to natural cirrus clouds. The picture in Fig. 2.1 shows probably cirrus clouds with some crossings from contrails of different extension and age.

This chapter provides the reader with the basic knowledge from the literature to place the scientific questions of this work within the atmospheric physics frame and to introduce some concepts necessary to better understand subsequent discussions. Since this work deals with ice clouds properties and their interaction with the atmosphere, we start with the formation of ice crystals from the non-equilibrium states of water in Section 2.2, the formation of liquid droplets (Section 2.2.1) and the ice nucleation mechanisms (Section 2.2.2). Later, the origin and life-cycle of cirrus clouds, as well as their microphysical properties are introduced in Sections 2.3.1 and 2.3.2. The relevant role of aerosols in cirrus formation is also exposed in Section 2.3.3. Finally, Section 2.4 will provide a concise overview of aviation-induced cloudiness, including contrail formation in Section 2.4.1, their transition into contrail cirrus in Section 2.4.2, and relevant information regarding

their microphysical properties in Section 2.4.3.



Figure 2.1: Picture of likely cirrus clouds and contrails over the German Alps but with no clear distinction between them.

2.2. ICE CRYSTAL FORMATION

The presence of water vapor in the atmosphere is fundamental for the formation of clouds and precipitation. Clouds consist of a group of liquid (droplets) or solid water (ice crystals) particles which can be held in suspension due to the vertical movement of air masses. They are seen with a white color from the sun light scattering on the cloud particles. These particles result from nucleation processes in air parcels containing water vapor. The amount of water vapor contained in the air can be quantified by the water vapor partial pressure, e , and can be written in the following form, assuming water vapor behaves as an ideal gas (Pruppacher & Klett, 2010).

$$e = \rho_v R_v T, \quad (2.1)$$

where ρ_v represents the specific density of water vapor, R_v is the specific gas constant for water vapor and T is the ambient temperature. Saturation with respect to a surface (liquid or ice) is defined when the flux of water molecules across the surface is equal in both directions. The air becomes supersaturated when the available water vapor at a given temperature and pressure exceeds the equilibrium saturation state, resulting in an enhanced flux of water molecules from the surrounding environment across the surface. The relative humidity (RH) is a useful definition in order to quantify the onset to saturation conditions and it is calculated as the ratio of ambient partial vapor pressure (e_{amb}) to the water vapor saturation pressure over ice or liquid water ($e_{\text{sat}_{\text{ice,w}}}$) (Pruppacher & Klett, 2010):

$$\text{RH}_{\text{ice,w}} = \frac{e_{\text{amb}}}{e_{\text{sat}_{\text{ice,w}}}} \quad (2.2)$$

The pressure and temperature conditions for the existence of the liquid, solid or vapor phase and the phase transitions are described theoretically by the Clausius-Clapeyron relationship, whose detailed derivation can be found in Pruppacher and Klett (2010), and takes the following expression:

$$\frac{d \ln e_{\text{sat}_{\text{ice,w}}}}{dT} = \frac{\mathcal{L}_{s,e}}{\mathcal{R}T^2}, \quad (2.3)$$

where \mathcal{R} is the universal gas constant and $\mathcal{L}_{s,e}$ is the latent heat of sublimation or evaporation, depending if the supersaturation is with respect to ice or liquid water ($e_{\text{sat}_{\text{ice,w}}}$). The phase diagram in Fig. 2.2(a) shows the partial pressure of equilibrium between phases as a function of temperature. The three phases can only coexist in equilibrium at the triple point. Saturation is achieved when the ambient vapor partial pressure equals the equilibrium partial pressure, which is provided by the solutions of the Clausius-Clapeyron equation (along the lines). Saturation of air parcels in the atmosphere is typically attained as warm, lighter air ascends and cools during its ascent.

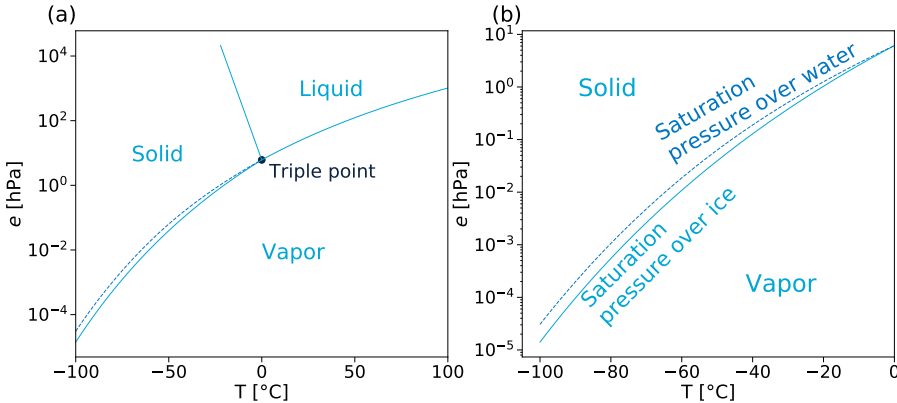


Figure 2.2: (a) Water phase diagram. (b) Zoom-in of water phase diagram for temperatures below 0 °C. The saturation pressure over ice and liquid water curves are given by Murphy and Koop (2005).

Since supersaturation is not an equilibrium state, the system will move back to equilibrium (saturation) nucleating particles by condensation (phase change from water vapor to liquid) or by deposition (water vapor to ice). Similarly, subsaturation is also not stable and the way back to saturation is by evaporation (liquid to water vapor) or sublimation (ice to water vapor). Therefore, nucleation involves a phase change that spontaneously occurs from a non-equilibrium state, typically characterized by supersaturation. In this state, the prevailing conditions, including temperature, relative humidity, and the presence of a suitable surface for nucleation, are energetically favorable for the nucleation process.

It is important to notice that the saturation vapor pressure over liquid water is higher than over ice, as represented in Fig. 2.2(b). However, it is misleading to suggest from this that ice formation might precede the formation of water droplets. The formation of the

crystalline structure of the ice crystals requires additional conditions to be met, as we will see in the following sections.

2.2.1. CLOUD DROPLET FORMATION

In the atmosphere, the condition of supersaturation is not sufficient to nucleate a water droplet. The Clausius-Clapeyron equation (Eq. (2.3)) and thus, the phase diagrams of Fig. 2.2 do not describe the equilibrium conditions of curved water surfaces. In addition, a surface is necessary for water vapor to condense and form a cloud droplet. The surface for nucleation is provided by an aerosol particle with the ability to nucleate droplets, known as cloud condensation nuclei (CCN). The need for aerosol particles to be present in order to form cloud droplets is understood by the non-equilibrium of pure water droplets. The derivation of the equilibrium states of pure water droplets and solution droplets is explained in detail in Seinfeld and Pandis (1998) and Pruppacher and Klett (2010), but the main theses are exposed briefly in the following.

The ratio between the vapor pressure of a pure water droplet, $e(D_p)$, with diameter D_p and that of flat surface, e° , is given by the Kelvin equation:

$$\frac{e(D_p)}{e^\circ} = \exp\left(\frac{4M_w\sigma_w}{\mathcal{R}T\rho_w D_p}\right), \quad (2.4)$$

where M_w is the molar mass of water, σ_w is the surface tension in the water interface, ρ_w is the water density and D_p is the droplet diameter.

The Kelvin equation is graphically represented in Fig. 2.3 by a navy dashed line, and it illustrates several noteworthy implications. Firstly, it indicates that the vapor pressure of equilibrium over a curved surface is always higher than over a flat one, and that the partial pressure increases drastically for small diameters. This means that water molecules find it easier to escape from a small droplet (larger curvature) than from a bigger one. And secondly, it describes the non-equilibrium of the pure water droplet. This is exemplified when considering the effects of a small perturbation in size in a water droplet of a certain size, which is assumed to be in equilibrium with its surroundings. The perturbation causes the increase of its critical diameter with no variation of the ambient conditions, leading to a decrease of the vapor pressure of equilibrium in the interface. Since the ambient pressure did not vary and now it is higher than that at the water droplet interface, a further increase in the droplet size is produced. In turn, a perturbation on the other direction would originate the evaporation of the droplet.

As we see here, water droplets can not exist in equilibrium and therefore, in reality, they contain dissolved solutes. They help to lower the high partial pressure of the small droplets, which prevents these small droplets from quickly evaporating. To account for this effect, the Kelvin equation needs to be extended.

The water vapor partial pressure of a solution of a flat surface is described by Eq. (2.5) with the help of the mole fraction of water in the solution, x_w , and an activity coefficient, γ_w , that accounts for non-ideal solutions (goes towards to 1 for the ideal case) (Seinfeld & Pandis, 1998).

$$e_s^\circ = \gamma_w x_w e^\circ \quad (2.5)$$

Exchanging e° in Eq. (2.4) by e_s° of Eq. (2.5) to take into account the general case of a solution droplet, and simplifying for dilute solutions, one obtains an expression of the Köhler equations:

$$\ln \frac{e(D_p)}{e^\circ} = \frac{4M_w\sigma_w}{\mathcal{R}T\rho_w D_p} - \frac{6n_s M_w}{\pi\rho_w D_p^3}, \quad (2.6)$$

where n_s is the number of solute moles.

The partial pressure is then determined by two contributions: the Kelvin effect (curvature) and the Raoult effect (solute), illustrated in Fig. 2.3. The Kelvin effect describes the increase of vapor partial pressure over curved surfaces compared to flat surfaces. The solute effect, in turn, contributes to a reduction of the partial pressure compared to pure water. Similarly, the derivation can be extended to a solution containing insoluble particles. The inclusion of these particles reduces the volume fraction of the solution, leading to a consequent further decrease in partial pressure, thereby promoting the nucleation of water droplets.

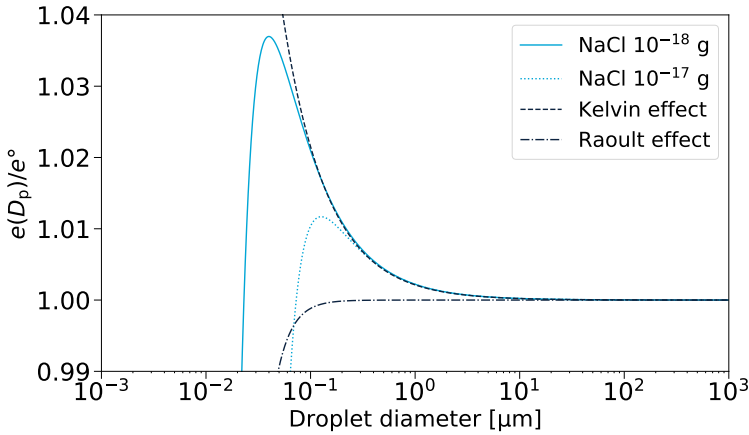


Figure 2.3: Equilibrium vapor pressure over an aqueous solution droplet with NaCl particles of two different masses (blue lines) as function of droplet diameter for $T = 293K$. Navy lines indicate the Kelvin effect (vapor pressure over a pure water droplet) and the Raoult or solute effect. Adapted from Seinfeld and Pandis (1998).

Fig. 2.3 also shows the equilibrium partial pressure for two solution droplets of distinct size. Now, the curves have also an unstable branch (the descending branch) as for the pure water droplet, but the ascending branch is stable. In this context, when a droplet experiences a slight increase in size, it tends to lose some of its mass through evaporation. This occurs because the ambient pressure is not conducive to maintaining the larger size of the droplet.

The critical supersaturation and critical radius are given by the maximum of the Köhler curve. When the critical supersaturation is overcome, the particle is considered to be activated, entering the unstable region of the Köhler curve, and subsequently growing into a large cloud droplet. Below this threshold, the aerosol particles are thermodynamically stable and no cloud particles are formed. In this way, the ability of an aerosol particle to serve as nuclei for the formation of a cloud droplet depends on its size and type,

and the amount of water vapor in the ambient. All existing particles of the same sort and size become activated simultaneously when the required supersaturation is achieved.

2.2.2. ICE NUCLEATION MECHANISMS

Once we have understood the essential role that aerosols play in forming cloud droplets, we can easily extrapolate their significant contribution to the formation of ice crystals, enabling us to finally explore the matter of ice nucleation mechanisms. The energy barrier to form a new phase (ice) from a water droplet at atmospheric conditions is quite high, making it rare under typical atmospheric conditions. To lower the energy barrier and favour the formation of the ice phase, the surface of an aerosol with the ability to nucleate ice can help the process (a solid ice nucleating particle, INP) (Kanji et al., 2017). Therefore, two distinct types of ice crystal nucleation are recognized: homogeneous or heterogeneous (Heymsfield et al., 2017a; Kanji et al., 2017).

Homogeneous nucleation refers to the direct ice nucleation of small liquid solution particles or supercooled water droplets without the intervention of an INP (Kärcher & Lohmann, 2002b, 2002a). It occurs below $-38\text{ }^{\circ}\text{C}$ and requires high RH_i values above 140–150% (Kärcher & Lohmann, 2002b, 2002a).

Heterogeneous nucleation, involving various physical processes, implies the participation of an INP in initiating the freezing process (Kärcher & Lohmann, 2003). These processes include *deposition nucleation*, *immersion freezing*, *contact freezing*, and *condensation freezing*. The schema in Fig. 2.4 shows an overview of all the different nucleation mechanisms taking place in the atmosphere, depending on the temperature regime.

Starting from the liquid phase, cloud droplets form after the activation of CCN, as briefly explained in the previous section. Cloud droplets at temperatures below $0\text{ }^{\circ}\text{C}$ are considered supercooled droplets. Immersion freezing happens when an INP gets immersed in the supercooled cloud droplet and the temperature gets sufficiently low to activate it and trigger the freezing process. The condensation freezing mode refers to the formation of a droplet from a CCN below $0\text{ }^{\circ}\text{C}$ and the subsequent freezing, however, it has not been fully observed in the laboratory at microscopic scale (Vali et al., 2015). Contact freezing is also initiated from a supercooled droplet and the freezing takes place when it collides with an INP. The last mode, deposition nucleation, is different from the others because it is believed to occur directly from supersaturated water vapor on the surface of an INP without prior formation of a liquid phase. However, the non-existence of liquid has not been proven and it could involve a transitory stage in which liquid is present. In addition, freezing of condensed water on surface cavities, for example, might be wrongly observed as deposition nucleation (Vali et al., 2015).

The ambient conditions where homogeneous or heterogeneous nucleation take place are illustrated in the diagram of Fig. 2.5. Starting from the warmer temperatures above $-38\text{ }^{\circ}\text{C}$, the presence of INPs is a prerequisite to form ice. Liquid droplets can survive in cold temperatures down to $-38\text{ }^{\circ}\text{C}$ in the form of supercooled water droplets. They do not freeze unless they get in contact with an insoluble aerosol particle (an INP) with certain characteristics, since a solid surface is necessary to trigger the crystallization. Therefore, between -38 and $0\text{ }^{\circ}\text{C}$ ice crystals and droplets can coexist in the clouds, leading to so-called mixed-phase clouds.

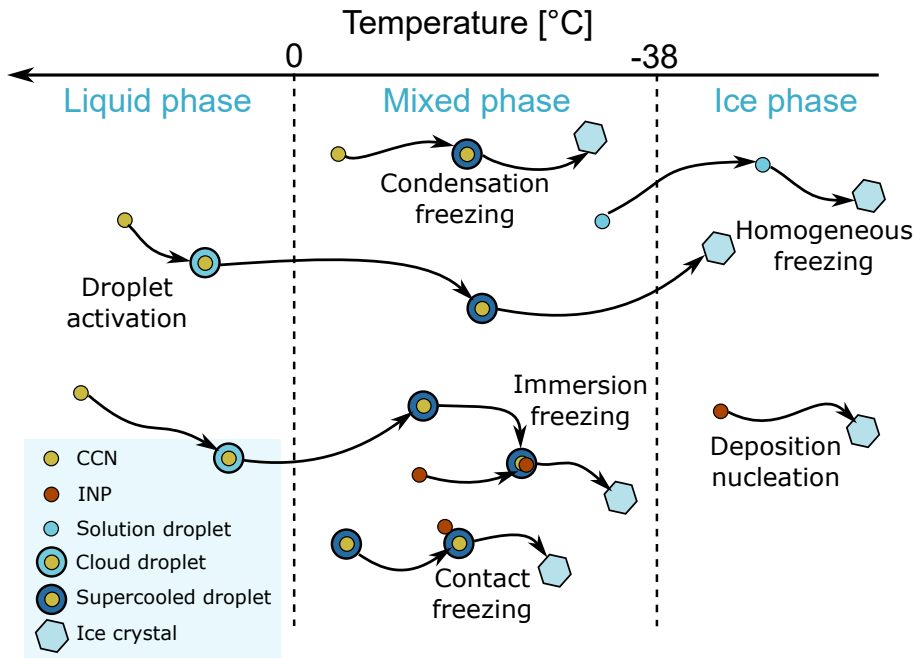


Figure 2.4: Schema of ice crystals nucleation mechanisms based on Kanji et al. (2017). Heterogeneous nucleation includes deposition nucleation, immersion freezing, contact freezing, and condensation freezing.

When the temperature falls below -38°C , the ice crystals can nucleate either by heterogeneous or homogeneous nucleation, depending on the relative humidity (or cooling rate), the concentration and the nucleation ability of the available INPs. Since the homogeneous freezing threshold is achieved at a lower RH_i than the necessary to reach saturation over liquid water, the liquid phase can no longer exist, as shown in Fig. 2.5. This means that, if any liquid droplets remain, which have not frozen upon contact with INPs, they will freeze homogeneously below -38°C . However, if there are INPs available in the air, ice is preferably formed with the aid of INPs instead of by homogeneous nucleation. This occurs because INPs lower the supersaturation necessary to start the process. Already at slight supersaturations with respect to ice, the excess of water vapor can be depleted directly by deposition nucleation on the aerosol surface forming an ice crystal.

In the upper troposphere we find a competition of homogeneous and heterogeneous nucleation, characterized by non-equilibrium processes, which lead to constant dynamics and changes. The key aspect here is to understand under what circumstances one or the other mechanism dominates and in which regions of the planet each one usually occurs. Numerous modeling studies have focused on these aspects, simulating various scenarios involving different combinations of updrafts, INP concentrations, and nucleation efficiencies (Kärcher & Lohmann, 2002b, 2002a, 2003; Kärcher et al., 2006; Hoose & Möhler, 2012; Jensen et al., 2013; Gasparini & Lohmann, 2016; Kärcher et al., 2022).

Assuming the simple example of an ascending air parcel, the updraft generates cool-

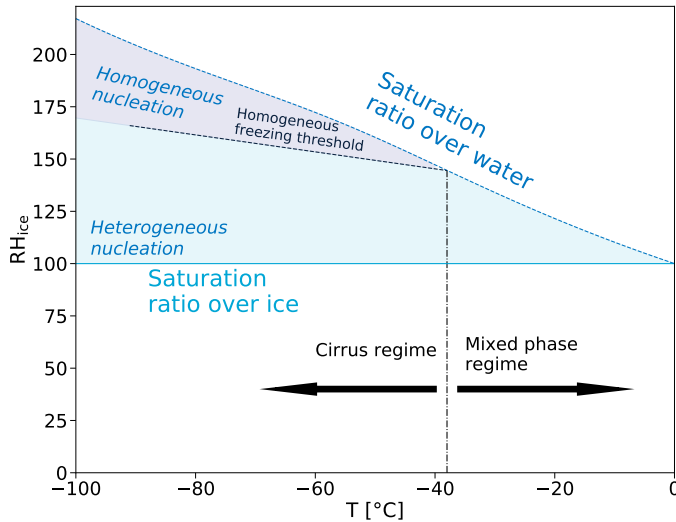


Figure 2.5: Boundaries for ice crystal nucleation processes in terms of relative humidity over ice (RH_i) as a function of temperature. The saturation pressure over ice and liquid water curves are given by Murphy and Koop (2005). The homogeneous freezing threshold is calculated as Koop et al. (2000) for 500 [nm] aerosol particles and a nucleation rate of 10^8 [$\text{cm}^{-3} \text{s}^{-1}$]. The blue (navy) shaded region highlights the area where the conditions allow the forming of ice crystals through heterogeneous (homogeneous) nucleation.

ing of the air mass and without the presence of INPs, the supersaturation increases steadily. At a certain relative humidity ($RH_i \approx 150\%$), the solution droplets, which are abundant in the upper troposphere, become activated and produce a large amount of homogeneously nucleated ice crystals. The strength of a homogeneous nucleation event is mainly determined by the evolution of the relative humidity. The higher the achieved maximum relative humidity, the greater the amount of ice crystals that can form (Spichtinger & Cziczo, 2010). The addition of INPs causes ice crystals to be nucleated heterogeneously at an earlier stage. Depending on the amount of ice crystals produced and the cooling rate, the supersaturation can either continue increasing again until overcoming the threshold for homogeneous freezing or it can be lowered through water vapor diffusion growth of the ice crystals. How it actually occurs in the atmosphere can become more complex, taking into account other processes such as sedimentation or sublimation, leading to a number of stages in the cirrus evolution.

Two decades ago, the community suggested a major role of homogeneous nucleation as the mechanism of cirrus formation (e.g. Lin et al. (1998) and Jensen et al. (1998)). This was partially due to a lack of understanding of heterogeneous nucleation (Kärcher & Lohmann, 2003). However, nowadays the more we know about heterogeneous nucleation, the more we understand that it plays an important role in cirrus formation (Cziczo et al., 2013). While heterogeneous nucleation dominates in many regions of the globe and across different altitudes in the upper troposphere, homogeneous nucleation is believed to occur mainly in the uppermost part of the troposphere and lower stratosphere, preferentially in high updraft regions over mountains, associated with jet streams, or in

winter at high latitudes with less availability of INPs (Gasparini & Lohmann, 2016).

The dominance of one or the other mechanism becomes particularly relevant when considering climate geoengineering approaches such as cloud seeding. However recent studies discourage this method for reducing the cirrus feedback on climate (Storelvmo et al., 2014; Muri et al., 2014; Gasparini & Lohmann, 2016). Given the numerous open questions and uncertainties, there is the potential for unintended consequences to arise.

2.3. CIRRUS

The clustering of ice crystals at high altitudes form cirrus clouds. Clouds are usually classified as cirrus at ambient temperatures below -38°C , so that the cloud is only composed of ice crystals. The various pathways of ice formation are linked to the origin of cirrus clouds and play a significant role in defining their properties, which can also change over time in response to varying atmospheric conditions. Accurate understanding and representation of the microphysical properties of cirrus are fundamental for modeling their radiative impact and assessing their influence on both local and global climate systems.

Cirrus clouds have a dual effect on the Earth's radiation balance: they scatter incoming shortwave solar radiation (resulting in a cooling effect) and absorb and re-emit outgoing infrared (longwave) radiation from the Earth surface (resulting in a warming effect). The net effect, whether cooling or warming, depends on the interplay between these two contributions (Liou, 1986; Stephens, 2005; Cotton et al., 2011). This interplay is determined by the optical properties of the cirrus, which are directly related to their microphysical properties, mainly the total area cross-section and mass of the ice crystals within the cloud (Wendisch et al., 2005; Wendisch et al., 2007). The scattering and absorption properties of a cirrus cloud are determined by the combined contribution of all ice crystals within the cloud, which, in turn, depend on factors such as ice crystal size and shape, refractive index, and scattering phase function (Yang et al., 2005).

The following sections provide an overview on cirrus clouds from a macroscopic and microscopic perspective.

2.3.1. CIRRUS ORIGIN AND LIFE-CYCLE

Various attempts have been made to classify cirrus clouds over the years. Cirrus occur under a wide diversity of weather systems (Sassen & Campbell, 2001). A very careful and extended analysis was performed by Muhlbauer et al. (2014) based on the synoptic conditions of atmospheric states that lead to different cirrus types: ridge-crest cirrus (from upper level ridges or high pressure systems), frontal cirrus (from cyclones with an embedded cold front), subtropical jet stream cirrus (moist subtropical flows) and anvil cirrus (from convection). Each atmospheric state is characterized by a combination of different temperature gradients, updrafts, available moist and pressure conditions and determine the microphysical processes involved in the formation of cirrus.

Recently, another cirrus classification regarding the formation pathway has been introduced by Krämer et al. (2016), Luebke et al. (2016), and Wernli et al. (2016) and appears to be more convenient for relating cirrus properties with the dynamic and thermodynamic states, which are directly connected to the cloud particle nucleation and

growth. This classification is based on the origin of the ice crystals that constitute the cirrus clouds: in situ and liquid origin cirrus. A simple sketch of the main characteristics of these two types is depicted in Fig. 2.6.

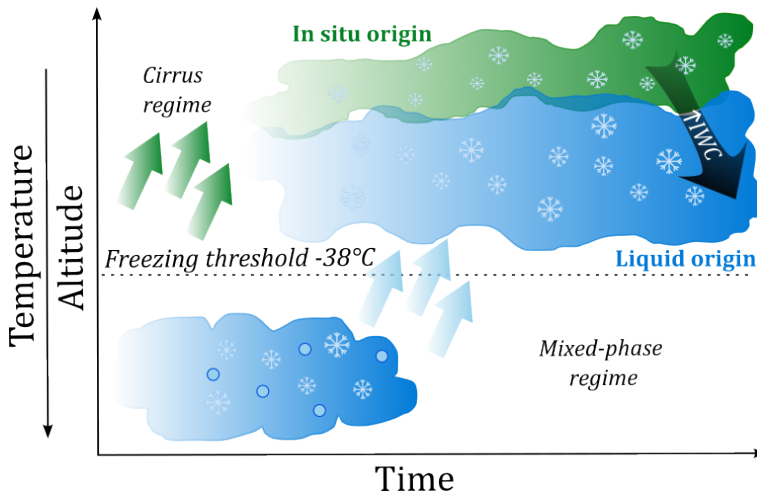


Figure 2.6: Sketch of the in situ (green) and liquid (blue) origin of cirrus clouds in the atmosphere and the formation mechanisms involved. The schema represents the dynamics of the air parcels ascending from their origins to form one or the other cirrus type. The freezing threshold line at -38°C divides the cirrus from the mixed-phase regime and indicates the limit where liquid droplets can no longer exist. The black arrow indicates the higher *IWC* contained in liquid origin cirrus with decreasing altitude (increasing temperature) compared to lower *IWC* in the in situ origin cirrus. Inspired by Fig. 13 of Krämer et al. (2016) and Fig. 1 of Luebke et al. (2016).

A cirrus is considered of in situ origin if the ice crystals are directly formed in the cirrus regime below the freezing threshold of -38°C . Among the nucleation mechanisms described in Section 2.2.2, the in situ cirrus particles can be formed either by homogeneous nucleation of solution aerosol particles or by heterogeneous nucleation (deposition nucleation) from the water vapour phase, since supersaturation with respect to liquid water can no longer be reached (region below -38°C in Fig. 2.5).

Liquid origin cirrus originate at lower altitudes where temperatures are above -38°C from liquid or mixed-phase clouds. These clouds are then lifted to cirrus altitudes, typically above 8 km, where the liquid droplets freeze at some point during their ascent. If the updraft speeds are sufficient, liquid droplets can survive until reaching -38°C where they freeze homogeneously. Otherwise, the liquid droplets freeze heterogeneously at warmer temperatures via immersion or contact freezing (see Section 2.2.2). These possibilities are a result of the intricate processes occurring within mixed-phase clouds.

The evolution of a mixed-phase cloud is closely related to the thermodynamic characteristics of the cloud. It depends on the in-cloud vapor pressure (e) relative to the saturation pressure over liquid ($e_{\text{sat,w}}$) and ice ($e_{\text{sat,ice}}$) (Korolev & Mazin, 2003; Korolev, 2007a, 2008). This results in three possible scenarios:

- a) $e_{\text{sat,ice}} < e_{\text{sat,w}} < e \rightarrow$ ice and liquid particles grow

- b) $e_{\text{sat,ice}} < e < e_{\text{sat,w}} \rightarrow$ ice particles grow and liquid droplets evaporate
- c) $e < e_{\text{sat,ice}} < e_{\text{sat,w}} \rightarrow$ ice and liquid particles evaporate

For case (a), the ambient air is supersaturated with respect to ice and liquid water which allows both ice and liquid droplets to grow competing for the available water vapor. The situation is sustained as long as the condition is satisfied through strong updrafts or isobaric mixing (Korolev, 2007a). As for case (b), the ambient air is subsaturated with respect to liquid water but supersaturated with respect to ice. This process implies that the liquid droplets evaporate while the ice crystals grow and is called the Wegener-Bergeron-Findeisen (WBF) process. It is important to recognize that the evaporation of the liquid droplets increases the ambient water vapor and, therefore, feeds the growth process of the ice crystals. Lastly, scenario (c) describes the situation when the ambient air is subsaturated with respect to ice and liquid water and causes the evaporation of the ice and liquid particles. This situation may occur in downdrafts or mixing with dryer air outside the cloud and could result in the complete evaporation of the cloud. If both processes (a) and (b) are maintained long enough and reach cirrus altitudes, they originate cirrus of liquid origin, as shown in the schema of Fig. 2.6.

2.3.2. MICROPHYSICAL PROPERTIES

The last section described the different pathways for the cirrus formation. Among others, the availability of INPs or CCNs and their ability to become activated, the updraft speed, or the relative humidity are factors influencing the formation of ice crystals. Each different combination of factors determine the amount of ice crystals that nucleate, as well as their size and shape. The definition of standard cloud microphysical properties, that comprise measurable quantities, is essential to allow a comparison between cirrus. The most important ones are the ice crystal number concentration (N in cm^{-3}), the ice water content (IWC in g m^{-3}), the effective diameter (ED in μm), mean mass or volume diameter (MMD or MVD in μm), the particle size distribution (PSD in cm^{-3} or $\text{cm}^{-3} \mu\text{m}^{-1}$) and ice crystal shapes.

Insights on the cirrus microphysical properties can be derived from in situ observations or remote sensing retrievals, which require at the same time validation from the in situ measurements (Heymsfield et al., 2017a). Although some of the most relevant knowledge is briefly summarized below, compilations of extensive cirrus clouds data sets can be found in the literature studies of (Schiller et al., 2008; Heymsfield et al., 2013; Luebke et al., 2013; Muhlbauer et al., 2014; Krämer et al., 2016; Heymsfield et al., 2017b; Voigt et al., 2017; Krämer et al., 2020). In particular, the work from Krämer et al. (2016), Heymsfield et al. (2017b), and Krämer et al. (2020) compiled measurements from numerous field campaigns. In general, the medians of IWC in cirrus clouds range between 0.001 and 0.01 g m^{-3} and the number concentrations are usually in the order of 0.0001 and 0.1 cm^{-3} .

Given the different formation pathways of the two cirrus origins described above (Section 2.3.1), their microphysical properties are expected to differ. The source of liquid origin cirrus is the nucleation of droplets at lower altitudes with abundant water vapor. Droplet nucleation is triggered by CCNs, which are more abundant than INPs. In addition, the formation of water droplets is subject to different mechanisms than the pro-

cesses governing ice crystal formation, as seen previously in Section 2.3.3 (Pruppacher & Klett, 2010). In these conditions, a large number of droplets are formed in both the liquid and mixed-phase regimes, resulting in a higher ice crystal number concentration of cirrus with liquid origin compared to those of in situ origin. In addition, the larger amount of water vapor at lower altitudes enables an increased growth of the ice crystals, which are usually larger than in situ-formed. In particular, cirrus associated with convection are also formed from the liquid phase, where the strong updrafts produce a high amount of particles and bring the air masses to higher altitudes (Heymsfield et al., 2017a). All together, liquid origin cirrus are frequently characterized by higher *IWC* and are optically thicker than in situ cirrus. As observed, the microphysical properties of cirrus can exhibit significant variations depending on their origin (Luebke et al., 2016; Krämer et al., 2016; Krämer et al., 2020).

Krämer et al. (2016) extensively describe two different types of in situ cirrus, which display varying properties depending on the intensity of the updraft involved in their formation. The first type of in situ cirrus is driven by slow updrafts. In general, the relative humidity in these cases does not reach the homogeneous nucleation threshold and the main ice crystal nucleation process is the heterogeneous freezing. Homogeneous nucleation might happen if the updraft is sustained long enough, allowing heterogeneously generated crystals to settle due to a slow updraft, or as a result of temperature fluctuations. Since the availability of INPs is limited, the number of ice crystals formed in this cirrus type is not particularly high and the ice crystals tend to be large, which results in low or moderate *IWC*. The second type of in situ cirrus is characterized by high updrafts, where homogeneous nucleation dominates and produces a high amount of ice crystals and high *IWC*, but reduced ice crystal sizes. This is explained because a homogeneous nucleation event suddenly triggers the freezing of as many solution droplets as the cooling rate allows, and quickly depletes the water vapor reducing the RH_i very efficiently. The high number of nucleated particles and the subsequently reduced RH_i limit the growth of the ice crystals.

An important characteristic of cirrus clouds is the Particle Size Distribution (PSD). The particle size distributions represent the size spectrum of cloud particles within a cloud and the amount of particles present for each size. Usually, PSDs from cirrus clouds vary depending not only on the formation mechanism but also on the temperature, aerosol concentration, updraft speeds and further parameters. Therefore, a certain PSD profile cannot be directly associated with a cirrus origin type. What it generally applies is the extension to larger sizes in the case of liquid origin cirrus, which can also be associated with convection and an enhanced ice crystals growth. In addition, the size distributions are also broader with increasing temperature. This is due to liquid origin cirrus being usually found at lower altitudes (warmer temperatures) where large crystals sedimented from higher levels also appear (Krämer et al., 2016; Heymsfield et al., 2017a). While the size distributions of in situ cirrus are typically unimodal and can be better approximated by gamma functions (McFarquhar et al., 2015), particle size distributions of liquid origin clouds are rather multimodal (Luebke et al., 2016; Krämer et al., 2016). The reason lies in the different nucleation mechanisms, which can take place at different stages in the cloud lifetime. The smaller particle mode is likely associated to an outburst of homogeneously nucleated particles, where the larger particles modes are

a result of aggregation and growth. Therefore, an in situ cirrus freshly formed in a fast updraft, where many particles are spontaneously formed after a homogeneously nucleation event, is likely to be unimodal. In this case, there has not been enough time for the particles to grow and precipitate out of the cloud.

Throughout the lifetime of a cirrus cloud, its microphysical properties are not permanent. The clouds experience changes as they travel along with the air masses and are exposed to different atmospheric conditions. In general, the ice crystals grow after nucleation, if supersaturation is sustained. Once ice crystals reach a certain size, the upward motion cannot counterbalance the sedimentation caused by their increased mass and inertia. As a result, they fall out of the cloud. This process, in turn, diminishes the *IWC* of the cloud. An increment in the supersaturation might trigger a new nucleation event, increasing the *IWC*.

Not only the size and number of the ice crystals change under different atmospheric conditions, but also the shape. Although current scattering and optical array probes struggle to accurately resolve the complex crystals shapes in airborne measurements, previous research relied on the cloud particle imager CPI, which offers high-resolution images, to study ice crystal habits (Lawson et al., 2001; Lawson et al., 2006). However, a substantial portion of our knowledge regarding ice crystal complexity comes from satellite retrievals and laboratory experiments (Järvinen et al., 2018).

Current knowledge indicates that ice crystals habits mainly depend on the ambient temperature and relative humidity (Heymsfield et al., 2017a). A laboratory study by Bailey and Hallett (2004) found out that within the temperature range of -20 to -40 °C and with supersaturations of about 2%, the predominant crystal morphology observed was plate-like, with complexity increasing as supersaturation levels grew. Higher supersaturations of about 25% favor the growth of bullet rosettes and columns. At temperatures colder than -60 °C needles and columnar shapes dominate. However, field measurements did not find any dependence of the ice crystal complexity on the cirrus origin type (Järvinen et al., 2018). In short, this topic needs further development in the future in order to estimate better the radiative effect of cirrus, which depends to a large extent on the single-scattering properties of the ice crystals, determined by their size and shape (Baran, 2004; Yang et al., 2015; Järvinen et al., 2018).

2.3.3. ATMOSPHERIC AEROSOL AND THEIR ROLE IN CIRRUS FORMATION

In the previous sections, the crucial role played by specific aerosol particles in the process of ice formation was addressed, revealing their relevance in the formation and evolution of cirrus clouds. Here, the nature and characteristics of the aerosol particles are detailed, as well as their influence on the cirrus properties.

The concept of *aerosol* refers to a suspension of solid or liquid particles in the air (Seinfeld & Pandis, 1998) and it plays an important role in the atmosphere. On the one hand, aerosols absorb or scatter solar shortwave radiation and longwave radiation emitted by the Earth, and thus affect the energy budget of the atmosphere. On the other hand, they are crucial for the formation of clouds (Bellouin et al., 2020). Aerosol particles can be either directly emitted into the atmosphere (primary aerosol) or formed by the conversion of gas into particles (secondary aerosol). The aerosol present in the troposphere has diverse origins and a significant part is generated by anthropogenic activities such as con-

struction, agriculture, biomass or fossil fuel combustion (Bellouin et al., 2020). However, they can also be introduced into the atmosphere by natural processes like sand storms, volcanic eruptions, wildfires, sea spray and biogenic emissions (Bellouin et al., 2020). The major aerosol particles present in the atmosphere are soil dust, sea salt, volcanic dust, biological debris, sulfates from biogenic gases and volcanic SO_2 , organic matter and nitrate from NO_x among the natural sources. Among the anthropogenic contributions, industrial dust, soot, sulfates from SO_2 , biomass burning, nitrates from NO_x , and organics are found.

Aerosol particles are considered to range in sizes from a few nanometers to several micrometers (Seinfeld & Pandis, 1998). A schema of the aerosol size spectrum is illustrated in Fig. 2.7. Here, the distinction between *fine particles* for sizes $< 2.5 \mu\text{m}$ and *coarse particles* for sizes $> 2.5 \mu\text{m}$ is relevant, since the mechanisms taking place in the formation and life-cycle are different, as well as their microphysical and optical properties (Seinfeld & Pandis, 1998). The size distribution spectrum of the fine particles is characterized by two modes: the *Nuclei* or *Aitken Nuclei* and the *Accumulation* mode. The Aitken mode extends from about 5 nm to 0.1 μm in size and tends to have a relatively short lifespan due to particles coagulating with larger counterparts. The accumulation mode covers the remaining range from 0.1 μm to 2.5 μm (Seinfeld & Pandis, 1998). The removal processes for these particles are less efficient than in the other two groups, and therefore remain longer in the atmosphere. The sizes, and thereby the masses, of the coarse mode particles ($> 2.5 \mu\text{m}$) are sufficiently large to sediment, which limits their residence time in the atmosphere. Typically, tropospheric aerosol survives in the atmosphere between days and weeks (Bellouin et al., 2020).

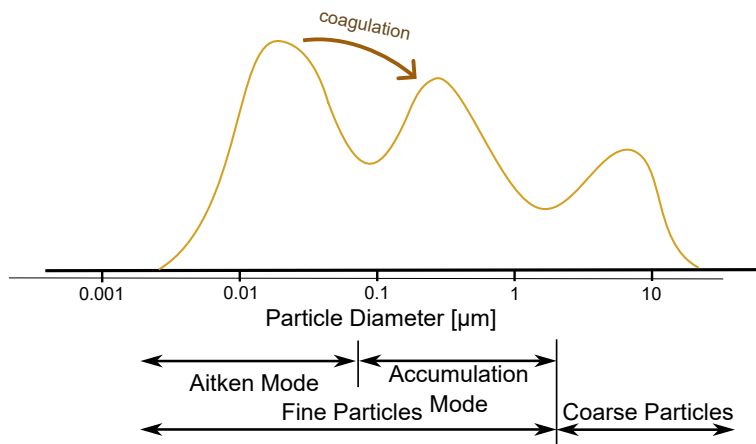


Figure 2.7: Schema of the modes in the atmospheric aerosol particle size distribution.

In general, the availability of such particles depends on many factors. The concentration is observed to decrease with height and also varies among the seasons. Usually, higher concentrations are found over continents than over marine backgrounds. In addition, it depends on the existence of emitting sources; for example, the concentration of aerosol particles over industrial areas or crowded cities is higher than in pristine air

masses. Moreover, meteorological conditions such as wind speed and direction, as well as the presence of cloudiness and precipitation, also play a role.

Typical aerosol types that act as INPs are mineral dust, soot, solid ammonium sulfate and certain organic acids in a glassy state (Kanji et al., 2017). The concentration of INPs in the upper troposphere is relatively low compared to CCN concentrations and usually takes values around 0.01 cm^{-3} , but with a large variability depending on various factors such as temperature or region (DeMott et al., 2003). The ice nucleation efficiency depends to a large extent on the aerosol particle composition. Current knowledge points to the dominant role of mineral dust as main ice initiator (Cziczo et al., 2013; Froyd et al., 2022). The main sources of dust particles are deserts, volcanic eruptions and agriculture soils (Kanji et al., 2017). However, the ice nucleating properties of the different aerosol types are still not well understood, in part due to a lack of measurements in the lower temperature range below $-38 \text{ }^\circ\text{C}$. For example, laboratory studies indicate the potential effect of coatings in reducing the ice nucleating abilities of INPs, however, it is unclear whether these experiments can be extrapolated to atmospheric conditions (Storelvmo, 2017).

The direct impact of aerosol as clouds precursors is evident. With the same atmospheric conditions in an air mass with few CCNs and another with many CCNs, a cloud with few but larger droplets will result from the environment with less CCNs (Storelvmo, 2017). In the second case, many small droplets would form the cloud and it would be optically thicker (increased cloud albedo), which is an effect known as the *Twomey effect*. At the same time, high amount of droplets with reduced size increase the lifetime of the cloud, since collision and coalescence are less efficient and the formation of rain is prevented and so the cloud persists longer. This effect is referred to as the *Albrecht effect*.

Similar to the aerosol effects on liquid clouds, varying the INP concentration also can alter the properties of cirrus clouds (Storelvmo, 2017). Assuming that homogeneous nucleation takes place, increasing the concentration of INPs would reduce or even suppress the homogeneous freezing, and therefore, reduce the number and increase the size of nucleated ice crystals. This implies an optically thinner cloud and thus a reduction of the cloud radiative forcing. If heterogeneous nucleation dominates, increasing the number of INPs would produce the opposite effect (similar to the Twomey effect on liquid clouds). A particular case here is the result of increasing sulfur emissions. They contribute to a larger amount of solution droplets that nucleate homogeneously given sufficient supersaturation, increasing the number of ice crystals and producing an effect similar to the Twomey effect (Storelvmo, 2017).

2.4. AVIATION-INDUCED CLOUDINESS

In this section, we will look at another type of ice clouds that are human-made, known as aviation-induced clouds (AIC): condensation trails (contrails) and their subsequent evolution into contrail cirrus. Contrails are line-shaped ice clouds produced by the exhaust gases of aircraft cruising in the upper troposphere, typically at altitudes ranging from 8 to 13 kilometers. They can extend considerable distances across the sky and vary in persistence, living for a few minutes or even hours (Kärcher et al., 2015; Bock & Burkhardt, 2016). During their evolution, contrails undergo a transformation as an effect of wind shear, losing their initial linear shape and transitioning into contrail cirrus clouds. This

makes them progressively more difficult to distinguish from natural cirrus formations.

The existence of these clouds means a change in the cloud coverage that translates into an AIC effective radiative forcing (ERF) component. Radiative forcing RF and ERF are metrics used to quantify the impact of various factors on the Earth's climate (IPCC, 2013). RF is usually defined as the change in the net radiation flux (incoming minus outgoing) at the top of the atmosphere (TOA) caused by a perturbation. ERF, on the other hand, measures the change in net irradiance due to a perturbation, while also accounting for rapid adjustments in the atmosphere and surface. These adjustments include changes in factors such as clouds, water vapor, and temperature profiles that occur over short timescales (IPCC, 2013). The effects of aviation on the climate are not negligible and accounted for almost 4% of the total anthropogenic RF in 2018 (Kärcher, 2018; Lee et al., 2021). While the cumulative CO₂ emissions contribute by one-third of the global aviation ERF, it is actually the contrail cirrus that can make the largest contribution ($\approx 60\%$ of the total 100.9 mW m^{-2} , according to Lee et al. (2021)), as shown in Fig. 2.8. However, there are large uncertainties associated with this term and recent studies such as Bier and Burkhardt (2022) and Teoh et al. (2024) suggest a smaller contribution than reported by Lee et al. (2021). Given the larger extent and longer lifetime of contrail cirrus compared to linear contrails, they accounted for 80% of the AIC RF in 2011 (Kärcher, 2018).

Global Aviation Effective Radiative Forcing (1940-2018)

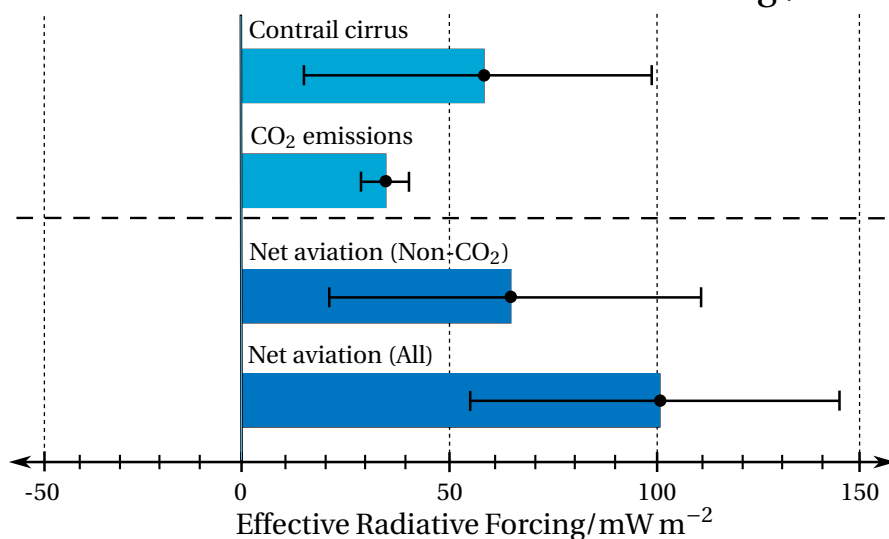


Figure 2.8: Summary of the terms contributing to the global aviation effective radiative forcing (ERF) (Based on estimations from Lee et al. (2021))

What sets properties of AIC apart from natural cirrus, and consequently their radiative effects, is the formation process primarily driven by the emissions from aircraft engines. Unlike natural cirrus, where ice nucleation occurs on atmospheric background aerosols, the precursors of ice in contrails originate from particulates emitted in the exhaust gases. Under suitable ambient conditions, as explained in the following section,

this process ultimately results in the formation of a high concentration of small ice crystals trailing behind the aircraft.

2.4.1. CONTRAIL FORMATION

The processes taking place in the formation of a contrail are schematically represented in the Fig. 2.9 from Kärcher (2018), where a more detailed description can be found. The exhaust gases leave the engine at high temperature and high water vapor mixing ratio containing soot particles and aqueous aerosol particles. As the hot plume mixes with the ambient air, it expands and cools as well as incorporates ambient aerosol particles. The cooling of the plume through turbulent mixing leads to supersaturation with respect to liquid water, which enables the activation of the abundant soot particles into many small droplets. These processes occur within the first second of the formation phase, which is known as *jet regime*. During the next 10 seconds approximately, the water droplets freeze homogeneously below $-38\text{ }^{\circ}\text{C}$ (see Section 2.2.2) and grow in size (up to $\approx 1\text{ }\mu\text{m}$) by water vapor uptake, if the air is supersaturated with respect to ice. This threshold temperature is determined by the Schmidt-Appleman theory, extensively described in Schumann (1996) and briefly explained below. The plumes of the engines get embedded in the wing tip vortices and form two wakes evolving in a downward motion. At this stage, the vortices get separated into an upper wake (secondary wake) that remains at flight level, and a lower part of the wake (primary wake), where the ice crystals may sublimate if the saturation over ice is no longer sustained, as the wake descends and mixes with warmer and drier air. Meanwhile, the ice crystals in the upper part continue growing. These processes occur during the *vortex regime*, which takes place from the first seconds until a few minutes after emission. After that, the organised flow mixes with the ambient air and the *dissipation regime* starts.

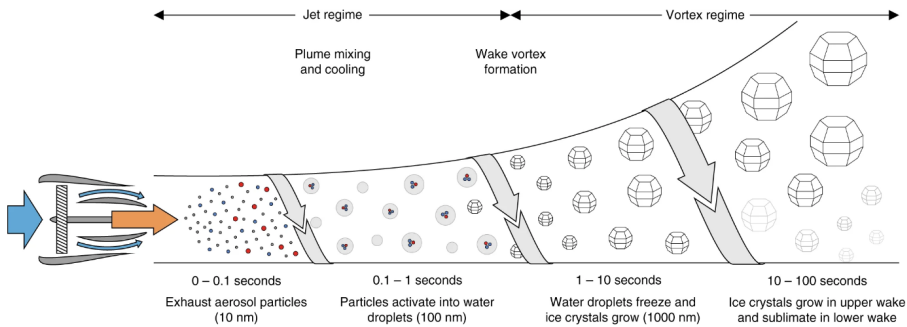


Figure 2.9: Schematic of the mechanisms and phases of the contrail formation from an aircraft exhaust (Source: Kärcher (2018), used under CC BY 4.0).

The thermodynamic theory and the empirical observations establish that the plume must be liquid water-saturated to allow the condensation of supercooled water droplets on aerosols particles from the engine and the environment acting as CCNs. In the cold temperatures, where contrails form, liquid water can not survive (ice supersaturated conditions but water subsaturation, as in case (b) of Section 2.3.1), and the many small droplets undergo homogeneous freezing at temperatures below $-38\text{ }^{\circ}\text{C}$ (Kärcher et al.,

2015). The residence time of a contrail in the atmosphere is controlled by the thermodynamic equilibrium of the ice phase. Even though there is some evidence of contrails subsisting in slightly subsaturated environments (Li et al., 2022), in general, the persistence of contrails requires supersaturated conditions that prevent the ice crystals from sublimating.

In the thermodynamic Schmidt-Appleman theory, the cooling of the exhaust gases is described by an isobaric mixing with the ambient air, represented by a linear relation in an e - T chart. In the real atmosphere, emitted and ambient aerosol particles facilitate the nucleation process and have to be considered together with the thermodynamic contrail formation theory. The ambient conditions (temperature, T and relative humidity over liquid water, RH) and the overall propulsion efficiency of the aircraft determine the cooling and moist reduction process of a plume through its mixing line (Schumann, 1996). One requirement for contrail formation is the crossing of the liquid water saturation curve, and this implies that not every cooling process leads to a contrail. In addition, the tangent mixing line to the liquid water saturation curve defines the warmest possible temperature (T_c in Fig. 2.10) to form a contrail, and ambient temperatures above this threshold do not lead to a contrail. Below the threshold or SA temperature, ice supersaturation conditions are required for the contrail to persist. This temperature threshold only depends on the mixing line slope (G):

$$G = \frac{EI_{\text{H}_2\text{O}}C_p p}{\varepsilon Q(1 - \eta)}, \quad (2.7)$$

where $EI_{\text{H}_2\text{O}}$ is the emission index of water vapor of the engine, C_p is the specific heat of air at constant pressure, p is the ambient air pressure, ε is the ratio of gas constants of air and water vapor, Q is the specific heat of combustion and η is the overall propulsion efficiency.

Different mixing lines representing diverse ambient conditions for the same aircraft, fuel, and flight pressure altitude (same slope) are shown in Fig. 2.10. The critical mixing line (red) contains the threshold temperatures for contrail formation as a function of partial pressure (or relative humidity). For a given RH (ambient relative humidity over liquid water), T_c is the threshold temperature for contrail formation (Schmidt-Appleman temperature). Colder temperatures than the threshold satisfy the criterion for contrail formation (e.g. point P_1 at temperature T_1), while the mixing line for warmer temperatures (gray) does not cross the liquid water saturation curve and the environment reaches only supersaturation over ice. In theory, contrail formation could occur in this case by heterogeneous freezing of activated INPs (from the aircraft emissions and ambient) but the number of ice crystals would be few, with no visible contrail. The area enclosed by the liquid water and ice saturation curves and the critical mixing line defines the possible ambient conditions conducive to persistent contrail formation. If the mixing line crosses the ice saturation curve again (as for P_3), the contrail particles begin to sublimate until they disappear (water and ice subsaturation, as in case (c) of Section 2.3.1).

2.4.2. CONTRAIL CIRRUS: EVOLUTION OF CONTRAILS

In regions with heavy air traffic, contrails from various aircraft can cluster, creating a thin layer of ice clouds that blankets vast areas. In such cases, the individual contrail shapes

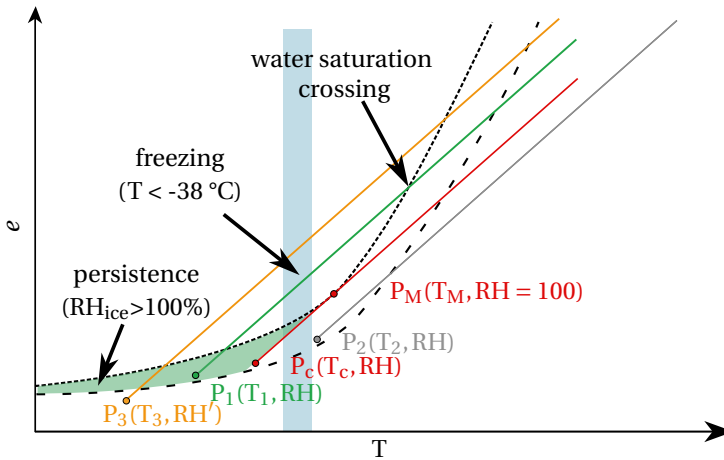


Figure 2.10: Sketch of four examples with different ambient conditions for contrail formation. The short (large) spaced dashed line represents the curve of saturation pressure over liquid water (ice). The red line indicates the critical mixing line and P_M is the tangent point to the liquid water saturation curve, with T_M as the warmest possible temperature for contrail formation. The point P_C marks the limit for persistent contrail formation at an ambient relative humidity with respect to water RH . For P_1 , the cooling process (green line) produces a contrail and the gray line ending in P_2 does not. P_3 and the orange line represents a cooling process for subsaturated ambient conditions, where a contrail forms but sublimates. The light blue shaded area represents the temperature range in which the freezing process of the plume particles occurs. The green shaded area highlights the ambient conditions where contrails can form and persist.

are usually not clearly distinguishable. From their formation until several hours later, contrails undergo several transformations and their properties change with time (Bock & Burkhardt, 2016). There are several factors that play a role in these processes. Wind shear contributes to the spread of contrail particles and increases the coverage. Apart from that, turbulent mixing is the main influencing factor for dilution, which causes the decrease of the ice crystal concentration over time (Kärcher, 2018). At the same time, the remaining ice crystals can grow further through water vapor deposition, which also changes the particles shapes. Since the ice crystals fall speed is dependent on size, when they reach a certain size ($> 30 \mu\text{m}$), they sediment out of the contrail and sublimate when encountering subsaturated conditions below. These mechanisms also imply that the vertical extent of the contrail increases and that contrail ice crystals can be found in lower altitudes if the conditions do not force them to sublimate (Unterstrasser et al., 2017a; Unterstrasser et al., 2017b).

These processes can take from a couple of seconds or minutes up to hours, depending on the contrail (number, size, and shape of the ice crystals) and meteorological situation (temperature and ice supersaturation). Areas with contrail clusters (contrail out-breaks) can cover extensions of a couple tens of thousands km^2 (Kärcher, 2018). Contrails and contrail cirrus can also appear many kilometers away from where they were formed due to the transport of air masses. Recently, satellite observations have revealed that the formation of contrails within pre-existing cirrus clouds affects their properties by increasing the number concentration in that area and making it optically thicker

(Tesche et al., 2016; Marjani et al., 2022). However, there are still many unknowns and this topic is still under investigation (Verma & Burkhardt, 2022). While contrails can be observed in situ with the help of aircraft emissions dilution tracers such as CO, CO₂ or NO_x and trajectory analyses, they can also be detected remotely through satellite retrievals (Wang et al., 2023; Dekoutsidis et al., 2023). However, differentiating contrail cirrus from natural cirrus and identifying natural cirrus perturbed by aircraft emissions sometimes presents a challenge. This is especially true because, after several hours, contrail cirrus can exhibit similar properties to some types of natural cirrus (Bock & Burkhardt, 2016).

2.4.3. MICROPHYSICAL PROPERTIES OF CONTRAILS AND CONTRAIL CIRRUS

The processes governing ice formation in contrails display some differences from those responsible for ice crystal formation in natural cirrus clouds. Consequently, variations in the microphysical properties of contrails and contrail cirrus are anticipated. The key parameters determining the formation and persistence of a contrail are the ambient temperature and relative humidity (apart from pressure altitude, fuel, and overall propulsion efficiency) (Dischl et al., 2022). Together with the number of soot particles emitted, these parameters determine to a significant extent the initial number of ice crystals in the contrail which, in turn, control the evolution of the microphysical and radiative properties (Voigt et al., 2021). As dilution occurs over time, these properties are typically calculated with respect to the contrail's age.

Initially, a high number of ice crystals are homogeneously nucleated, typically $> 10^4 \text{ cm}^{-3}$ (Schumann et al., 2017). Considering the large number of particles into which the water vapor must be divided, the contrail's effective ice crystal diameter barely exceeds $2 \mu\text{m}$ in its early stages (Voigt et al., 2010; Voigt et al., 2011). However, the strong dilution and ice crystal loss taking place subsequently lead to a significant reduction in ice number. For example, Bräuer et al. (2021a) observed maximum ice crystal numbers between 10^2 and 10^3 cm^{-3} for ages ranging from 30 to 150 s. As contrail age and transition to contrail cirrus, the ice number concentrations can fall below 1 cm^{-3} , yet they still exhibit distinct microphysical properties compared to natural cirrus, characterized by a higher number of smaller ice crystals (Voigt et al., 2017). With the growth of ice crystals over time, the properties of contrail cirrus gradually converge towards those of natural cirrus.

3

MEASUREMENT TECHNIQUES

In the preceding chapter, we gained insight into the intricate nature of clouds, where a complex interplay of microphysical processes dictates their properties and life-cycle. Given their relevance for climate modelling and weather forecasting, significant efforts have been dedicated to advance our understanding of these phenomena. Initially, clouds were studied on a large scale through ground-based remote sensing instruments and satellite imagery. However, the emergence of airborne measurement systems in the last decades of the past century has revolutionized our capabilities, enabling direct sampling and characterization of cloud particles within their natural environment. In situ measurements provide real-time data of cloud properties at a smaller scale, capturing changes in the clouds, which is crucial for studying dynamical processes. Furthermore, they facilitate the validation of remote sensing instruments and climate models, thereby enabling their improvement.

There exist various techniques and a diverse set of instruments available for the measurement of specific cloud properties, as comprehensively detailed in Baumgardner et al. (2011). The determination of cloud number concentration commonly involves counting and sizing individual particles. Instruments designed for measuring concentrations often rely on optical detection, achieved either by recording light scattering from the particles or by capturing their diffraction pattern. Microphysical properties can be inferred through single-particle counting, or they can be directly obtained using instruments that provide bulk measurements of liquid or ice water content, for instance. Similarly, specialized instruments enable the direct measurement of cloud optical properties such as the scattering phase function or extinction coefficient.

In this work, I employed instruments of single-particle counting. Their primary specifications are outlined in Table 3.1. They are usually installed under the wings of the aircraft intended as research platform, as in Fig. 3.1. The Cloud Droplet Probe (CDP) and Cloud and Aerosol Spectrometer with Depolarization (CAS-DPOL) are scattering probes and the Cloud Imaging Probe Grayscale (CIPG) and Precipitation Imaging Probe (PIP) are imaging probes (also called Optical Array Probes (OAPs)).

This chapter provides the reader with technical details and working principles about

Table 3.1: Summary of the main characteristics of the instruments used in this work.

Instrument	Acronym	Type	Range [μm]	Product
Cloud and Aerosol Spectrometer with Depolarization	CAS	For- and Backward Scattering Probe	0.5 – 50	Particle concentration and sizes
Cloud Droplet Probe	CDP	Forward Scattering Probe	2 – 50	Particle concentration and sizes
Cloud Imaging Probe	CIPG	Optical Array Probe	15 – 960	Particle shadow images
Precipitation Imaging Probe	PIP	Optical Array Probe	100 – 6400	Particle shadow images

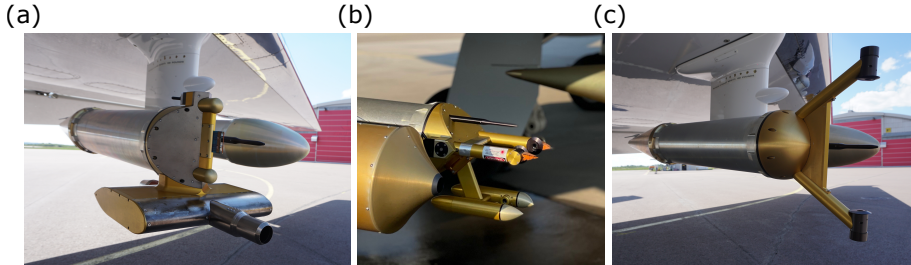


Figure 3.1: Pictures of the cloud probes used in this work and mounted under the HALO aircraft wings. (a) Cloud and Aerosol Spectrometer (CAS) on the outer position on the left wing. (b) Cloud Droplet Probe (CDP) and (c) Cloud Imaging Probe Grayscale (CIPG) parts of the Cloud Combination Probe (CCP) mounted on the outer position of the right wing. (d) Precipitation Imaging Probe (PIP) mounted on the inner part of the left wing. Photographed by T. Jurkat-Witschas.

the instruments primarily used in this work. The scattering probes are described in Section 3.1 and the OAPs in Section 3.2. The definitions and formulations employed for the calculation of cloud microphysical properties are outlined in Section 3.3. The methods developed to process and analyse the collected data will be subsequently introduced in Chapter 4.

3.1. FORWARD SCATTERING PROBES

The here employed scattering probes are applied to measure particles with sizes $< 50 \mu\text{m}$. All scattering probes are based on the same concept and share similar working principles. In this section, the primary focus for describing these types of instruments will be on the Cloud Droplet Probe (CDP), which is the main forward scattering probe used in this work. Additionally, some information about the Cloud and Aerosol Spectrometer (CAS) is included, since it has also been used for comparative purposes

alongside the CDP. Both instruments have been manufactured by DMT LLC.

3.1.1. WORKING PRINCIPLE

The forward scattering probes are instruments conceived for using the forward scattering of light to measure the size and number of particles in a sample volume (Baumgardner et al., 2011). Establishing a proportional relationship between the intensity of the scattered light received by the instrument and the size of the scattering object, cloud particle sizes can be derived with this measurement technique. The instruments consist of a light source that scatters light when particles pass through the beam. For particles larger than the laser wavelength, the majority of the light is scattered in the forward direction, therefore it is used for sizing and counting. Other probes, such as the CAS also use the back-scattered light for particle shape discrimination.

The CDP employs a laser with a wavelength of 658 nm as light source and is capable of measuring particles within a size range between 2 and 50 μm . The optical configuration of this probe is illustrated in Fig. 3.2. The instrument is an open-path probe with two arms positioned facing each other. The laser beam is located in one of the arms and is aligned in the sample area. The forward-scattered light is captured within the angles between 4 and 12° and subsequently split into a sizer and a qualifier signal. When a particle deviates from the center of the depth of field (DoF), its image gets blurrier and larger, and it is denominated as *out-of-focus* and classified as disqualified. Qualified particles are identified when comparing the signals in the qualifier and sizer photodetectors. The photon pulses are converted into electrical signals, and the qualifier voltage is multiplied by two. For a qualified particle, the qualifier voltage is greater than the sizer voltage. Subsequently, the amplitude of the sizer voltage is digitized, allowing for the determination of the corresponding particle's diameter.

The area where particles fall within the DoF and are in-focus is referred to as the qualified sample area, covering 0.24 mm^2 , as indicated by the manufacturer. A precise determination is important to calculate the density of the particle's flux through the sample area. Klingebiel et al. (2015) calibrated the same probe, now owned by DLR, and reported $0.27 \pm 0.025 \text{ mm}^2$. This updated value is the one used in this work for the microphysical properties calculation, which are introduced in Section 3.3.

The manufacturer DMT LLC provides a Windows-based LabVIEW software package called the Particle Analysis and Display System (PADS) as the standard pre-processing and control interface system for the CDP. This program enables real-time monitoring of measurements and stores data in files for subsequent post-processing. It performs calculations of various properties, such as the number concentration or effective diameter, for the specified sample intervals (typically set at 1 Hz). This information is stored in a so-called bulk-file or 1-Hz file. In theory, the sampling rate can be selected between 0.1, 1 or 10 Hz, however, the manufacturer does not recommend higher frequencies than 2 Hz (according to DOC-0029 Rev M-1). The file contains among others, the number of particle counts in every channel, and the measured probe air speed (PAS) derived from the static pressure and ambient temperature measured by the pitot tube attached to the probe's housing. Housekeeping data (laser temperature, current, voltages...) is also included and is helpful to determine a failure in the normal functioning of the instrument.

Newer versions of the CDP, including our own, incorporate the option to record what

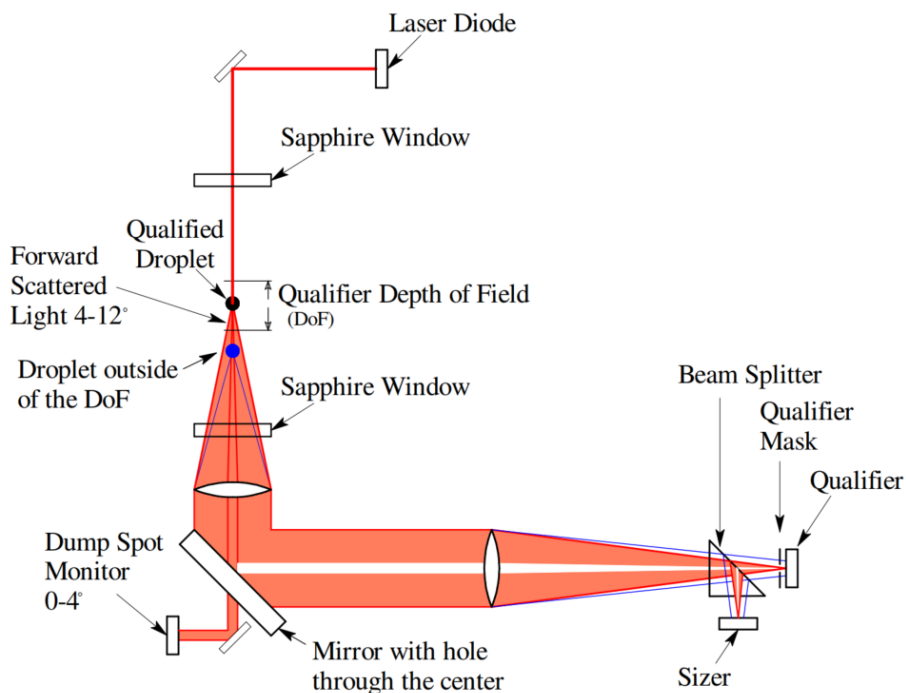


Figure 3.2: Schema of the CDP working principle. (Source: Lance et al. (2010), used under CC BY 3.0)

is known as particle-by-particle (PbP) data. This feature allows for the recording of up to 256 particles during each sample interval, including their respective interarrival times (elapsed time between two consecutive particles) and digital peak amplitudes.

3.1.2. PARTICLE SIZE DETERMINATION

Mie theory establishes a relationship between the light scattered by spherical particles and their diameter (Mie, 1908). Therefore, it becomes possible to calculate the size of a particle composed of a known material (refractive index) when exposed to an incident light of known wavelength and range of scattering angles over which the light is collected. This principle allows us to determine the size of water droplets employing the forward scattering technique. Along with Mie theory, there exist alternatives to provide the scattering cross sections of particles others than spheres, such as the T-matrix calculations (Borrmann et al., 2000), or the discrete dipole approximation (DDA) (Yurkin & Hoekstra, 2007; Yurkin & Hoekstra, 2011; Jang et al., 2022). These methods are further discussed in the outlook (Chapter 9) regarding their prospects for future studies but they have not been studied in this work. Since the variety of complex ice crystal shapes of cirrus are not addressed by these methods, I follow the standard assumption of the applicability of Mie theory and discuss the uncertainties of this assumption in Section 3.1.3.

The CDP collects scattered light from particles within an angular range between 4 and 12°. The scattering cross-sections as a function of water droplet diameter are de-

picted in Fig. 3.3 for the CDP's collection angles. However, several challenges must be taken into account in deriving particle sizes. Firstly, the size determination in the probe is not continuous, so the size range needs to be discretized in 30 bins. Secondly, the scattering cross-section curve is not a monotonous function of diameter, making it challenging to define the bin thresholds. As Fig. 3.3 shows, there are oscillations in the curve, particularly pronounced below 20 μm . This characteristic is known as Mie ambiguity or resonance and introduces uncertainties in measurements with scattering probes.

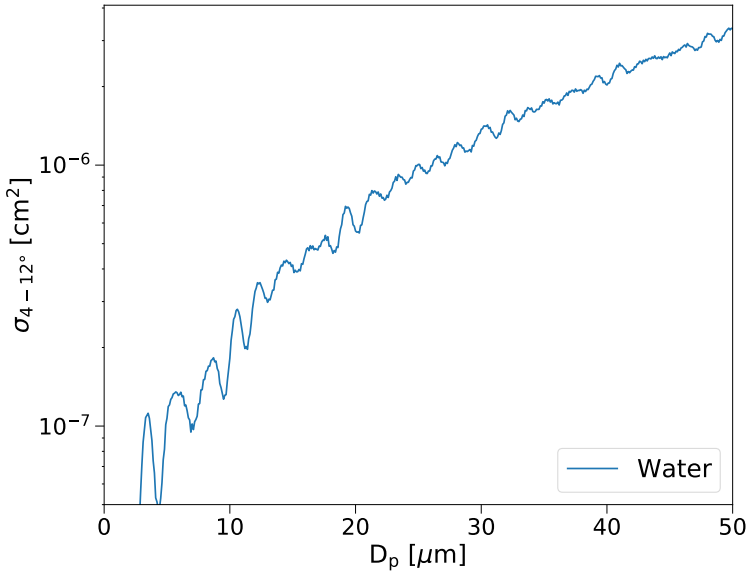


Figure 3.3: Scattering cross sections as function of spherical water droplet diameters for the annular area between 4 and 12° and $\lambda = 658 \text{ nm}$, assuming Mie theory. Calculation of the Mie curve performed with the software MieConScat 1.1.8. provided by Rosenberg et al. (2012).

The instrument does not directly provide the scattering cross-sections. An Analog-to-Digital Converter (ADC) transforms the sizer signal voltage into a 12-bit digital signal, resulting in AD-Counts ranging from 0 to 4095. By calibrating the instrument with particles of known sizes, a linear relationship can be established between the theoretical scattering cross-sections and the recorded AD Counts, enabling a direct link between AD Counts and particle diameter. In this way, by knowing the instrument response and accounting for Mie oscillations, it becomes possible to define appropriate AD-thresholds (Pinnick et al., 1981; Dye & Baumgardner, 1984). Calibrations are typically carried out using glass beads with known sizes and refractive indexes or with a water droplet generator. Comprehensive descriptions of these methods can be found in Nagel et al. (2007), Lance et al. (2010), and Rosenberg et al. (2012). Regular calibrations are recommended to identify potential changes in the instrument optics, which can result in under- or oversizing errors.

Importantly, the AD Counts conversion into the corresponding sizes depends on the scattering cross-section function, which is applicable under the assumption of spherical

water droplets and the specified collection angles of the CDP. Ice crystals can have multiple shapes and orientations, and Mie theory is in principle no longer valid. Borrmann et al. (2000) and Febvre et al. (2012) applied T-matrix calculations to derive the sizes of ice crystals spheroids of several aspect ratios for the geometry of a Forward Scattering Spectrometer Probe (FSSP).

3.1.3. MEASUREMENT LIMITATIONS AND UNCERTAINTIES

Limitations and uncertainties in the measurements of scattering probes have been deeply investigated in the last decades. Brenguier et al. (1998) presented a detailed overview for a Forward Scattering Spectrometer Probe (FSSP) and Lance et al. (2010) focused on the CDP.

Since the bin definition of the probe is restricted to 30 bins, the size resolution of the probe is limited. The manufacturer specifies a $1 - \mu\text{m}$ and $2 - \mu\text{m}$ bins. These bins can also be modified in a proper way to minimize the effect of the Mie resonance structure and avoid sizing ambiguities, which is particularly pronounced for the CDP that utilizes a single-mode laser. However, the assumption of spherical water droplets when measuring ice crystals does not facilitate the bin definition, since different particle shapes and orientations result in diverse scattering functions, which are usually difficult to compute with the actual methods (Borrmann et al., 2000; Yurkin & Hoekstra, 2007). In addition, the collecting angles of the probes can deviate from their nominal values, resulting also in a different scattering cross-section function. These deviations might occur during the manufacturing and assembly of the optical and mechanical components of the CDP (Baumgardner, 2012).

Another issue is related to the utilization of Gaussian mode lasers. The light intensity is reduced towards the borders, and particles not crossing the laser at its maximum intensity get undersized, leading to a broadening of the size distribution. On the other hand, the utilization of a single-mode laser in the CDP reduces uncertainties more present in probes using multi-mode lasers, which have greater inhomogeneities (Lance et al., 2010).

Early scattering probes experienced undercounting due to a delay in the electronic response known as *dead-time losses*. Newer probes, including the CDP, have improved electronics and the effect has become negligible.

The most important issue affecting not only scattering probes but also OAPs is *shattering*. Until the late 2000's, past measurements of ice clouds with scattering probes were characterized by high concentrations of small particles ($< 20 \mu\text{m}$) frequently observed in subsaturated and supersaturated environments. These findings could not be explained by model simulations, which showed that small ice particles grow rapidly in a supersaturated ambient or disappear in subsaturated conditions, and pointed to a contamination of the measurements in the lower size range of the ice particle spectrum (Korolev et al., 2013a).

After different studies and discussions, the generally accepted explanation was an instrument-induced particle shattering (Field et al., 2003; Field et al., 2006; McFarquhar et al., 2007; Heymsfield, 2007; Jensen et al., 2009; Korolev et al., 2011; Korolev et al., 2013a; Korolev et al., 2013b). This refers to the impact of larger ice particles on instrument surfaces breaking into small fragments before entering the sampling volume, re-

sulting in an artificial increase in the count rates of the smaller size bins. Shattering can occur from two different processes: the direct impact of ice particles with instrument surfaces upstream of the sample area, which generates a high amount of small fragments; or by aerodynamic forces caused by the flow leading to particle breakup in larger and fewer fragments than in the first case.

Several efforts have been done in order to minimize and correct the effects of these artifacts. Korolev et al. (2013b) developed a modification of the probe tips to prevent shattered particles entering the sample volume. The CDP obtained a modification of the two aerodynamic arms with pointed asymmetric tips upstream of the laser beam. As a further measure, shattering can be detected and corrected applying algorithms using the interarrival times (Field et al., 2003; Field et al., 2006). I discuss this problematic in Chapter 4 in more detail.

Another problem that experience scattering probes in general is *coincidence*. This effect is caused when more than one particle cross the sample area at the same time and appears in two different ways: standard coincidence and extended coincidence (Lance et al., 2010; Lance, 2012). The standard coincidence occurs when several particles transit the qualified sample area so close that the event is counted as only one particle with a larger size (undercounting and oversizing). Its probability of occurrence can be significant for high particle concentrations ($> 100 \text{ cm}^{-3}$) but an influence in low concentrations of ice clouds is not expected (Lance et al., 2010). The extended coincidence is much more common and occurs when only one particle passes through the qualified sample area, while others traverse a surrounding region known as the extended sample area. In this case, particles in the extended area, although unqualified, can still affect the measurement. Either the qualified particle is detected as larger than it actually is, or it gets rejected if the signal collected by the sizer exceeds the qualifier signal. Lance (2012) proposed a modification to reduce the size of the extended sample area but our probe does not include this modification. However, these studies were performed for liquid cloud conditions with substantially higher concentrations than expected in cirrus. Additionally, the concentration in aged contrail measurements is also expected to be lower due to dilution effects (Schumann et al., 1998). Therefore, this type of coincidence is also not considered in this study.

3.1.4. CLOUD AND AEROSOL SPECTROMETER WITH DEPOLARIZATION (CAS-DPOL)

The Cloud and Aerosol Spectrometer with Depolarization (CAS-DPOL) is the third generation of the instrument with the newer feature of depolarization detection to improve the differentiation between ice and water in clouds or between aerosol particles. The second generation of the instrument was the Cloud and Aerosol Spectrometer (CAS), part of the Cloud and Aerosol and Precipitation Spectrometer (CAPS), which also has a CIPG instrument Baumgardner et al., 2001. The Forward Scattering Spectrometer Probe (FSSP) was the forerunner of the CAS-DPOL, and was developed by Particle Measurement Systems (Boulder, Colorado) (e.g., Brenguier et al. (1998)). The CAS instrument has found extensive use, particularly for studying contrails. Originally designed for measuring also aerosol particles, it has the capability to measure sizes as small as $0.5 \mu\text{m}$, what makes it suitable for the small particles in young contrails.

Although this instrument was not the primary focus of this thesis and was mainly used for comparison purposes, I will outline its key characteristics that distinguish it from the CDP. For further details, please refer to Kleine (2019), where this probe has been extensively characterized.

Contrary to the CDP, CAS-DPOL is not an open-path instrument, the laser beam is covered by a tubular housing attached to the instrument where the particles pass through, as seen in Fig. 3.1. The optical configuration for the particle size determination is based on the same principle as the CDP but has some differences, as we will see in the following. Similar to the CDP, the forward scattered light of a 658nm laser beam is also collected between 4 and 12°. As in the CDP the signals at the detectors need to be amplified. The only gain stage in the CDP is optimized for its lower size range. The CAS-DPOL, however, is conceived for a wider particle size range including aerosol and therefore, it needs to effectively amplify all signals in the broader range. For that purpose, it divides the size range and uses three gain stages instead of one, what in turn introduces other problems, such as the gain stages overlaps (Kleine, 2019).

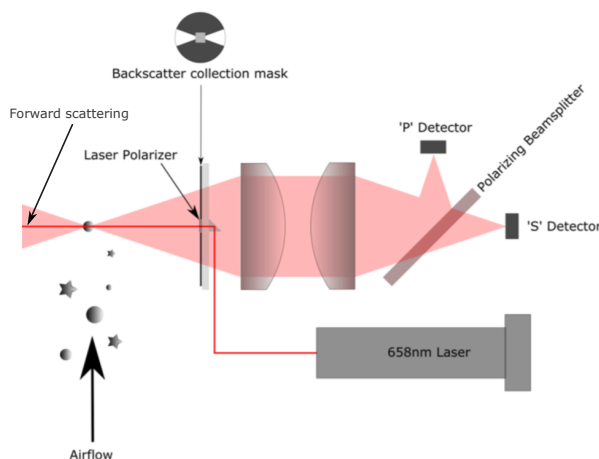


Figure 3.4: Components of the optical system of the back scattering part of the CAS-DPOL, modified from DMT, 2018, p. 6. Schema of the forward scattering part is similar to Fig. 3.2.

The CAS-DPOL incorporates additional optics to measure backward scattered light in a collection angle range of 168 and 176° and a schema of the configuration is shown in Fig. 3.4. This functionality is useful to distinguish aspherical from spherical particles and the aspect ratio of ice particles, delivering information on the particle shape (Baumgardner et al., 2005; Costa et al., 2017). To improve this functionality, a detector and a beam splitter are added to the backscattering optical path, as well as a 90° rotated polarization filter is located before the second backscattering detector. This principle of measuring polarized light to differentiate between spherical and aspherical particles was based on its application in the lidar community (e.g., Urbanek et al. (2018) and Groß et al. (2022)).

The general uncertainties and limitations of the scattering probes discussed in Section 3.1.3 also apply to the CAS-DPOL but the level of severity of the affections depends

on the specific particularities of each instrument. For example, CAS-DPOL is more prone to suffer from shattering due to the housing surrounding the sample volume. This difference is analysed and discussed in detail in Section 4.1.3.

3.2. THE OPTICAL ARRAY PROBES

Scattering probes are designed to measure particles up to 50 μm due to limitations related to the diffraction limit of light, which affects the accuracy of measurements for larger particles. Beyond this range, the scattering efficiency and optical clarity of the probe become compromised, hindering precise characterization of larger particles. The OAPs cover a wider size range, extending beyond 50 μm . What sets them apart is their capability not only to count and size particles but also to retrieve information about their shape.

The OAPs described in the following are the ones employed and used in this work: the Cloud Imaging Probe Grayscale (CIPG), part of the CCP, and the Precipitation Imaging Probe (PIP), both manufactured by DMT LLC. The data acquisition of both instruments is controlled by the PADS software (as for the CDP).

3.2.1. WORKING PRINCIPLE

The measurement principle of these instruments is the arrangement of a photodiode array illuminated by a collimated laser beam. When a particle passes through the laser beam, it projects a shadow onto the diode array resulting from refraction, absorption, diffraction and reflection (Knollenberg, 1970). The resulting image of the particle is formed by appending consecutive slices, each corresponding to the state of the diode array as the particle crosses the beam. The appending of slices occurs at a rate proportional to the particle's velocity, and the width of the slices depends on the probe's resolution¹.

The light intensity falling at each photodetector is converted into a logical digital signal which considers that the element is active if the intensity level falls below a certain threshold. Since only sequences with particle shadows are of interest, the array state is recorded if at least one element in the array is activated. Monoscale probes differentiate only between shadow (more than 50% obscured) or illuminated state, like the PIP, and most of the current available probes, do. The CIPG, however, is a grayscale probe, which includes two more shadow intensity levels, that define four pixel states: no shadow, at least 25, 50, and 75% obscured (nominal thresholds). This functionality allows to record images already at 25% dimming, which helps to constrain the DoF in the OAPs, as we will see in the following, and adds details for the particle shape analysis (Baumgardner et al., 2011).

The data transmission occurs in two different forms (DMT, 2017b). One-dimensional (1D) sizing data is obtained from a digital signal processor, which monitors and keeps track of the diode array state. It determines the size of each particle according to the maximum shadow length detected in the diode array (i.e. sized based on the particle extension perpendicular to the flow direction). It also counts the number of particles of

¹Here and in the following sections, the term "resolution" will be used to refer to the pixel size (in micrometers) of the probe's photodiode array.

each size per sampling interval. This information can be displayed in PADS and stored into a file. For grayscale probes, the grayscale threshold for 1D data storing can be adjusted through the variable "1D Sizing Threshold" in PADS or the initialization file (.ini file), which contains the initialization settings for the probe. Only images containing pixels above the grayscale threshold are sized and accounted in the 1D data.

In addition to the 1D sizing data, the two-dimensional (2D) image data can also be stored and live monitored through the PADS software. Together with the image data, the particle measurement time, particle counter, and other information are compressed using run-length encoding to ensure that the images can be exactly reconstructed. Every time a 4096-byte buffer is filled, the buffer is stored and a new one starts. As well as for the 1D data, the image data storing can also be limited by the grayscale threshold changing the setting of the "Imaging Threshold" in PADS or the .ini file. For both thresholds are applicable the following rules: a 0 enable the storing of only particles with at least 75% shadow intensity pixels, a 1 means storing particles with at least 50%, with the setting = 2 all detected particles are stored (at least 25% shadow intensity).

The optical layout and working principle of an OAP is illustrated in Fig. 3.5. The object plane is the location of true focus, and at any distance from it, the particle appears larger and less obscured, as an effect of diffraction (Knollenberg, 1970). The distance between the particle and the object plane is denominated as Z_d . The range of distances from the object plane, where the shadow image of the particle has at least one pixel at the selected shadow intensity level, is comprised by the DoF. The sample area (SA) is constrained by the DoF and the effective array width. The determination of both quantities is not trivial and different options are available for different evaluation criteria.

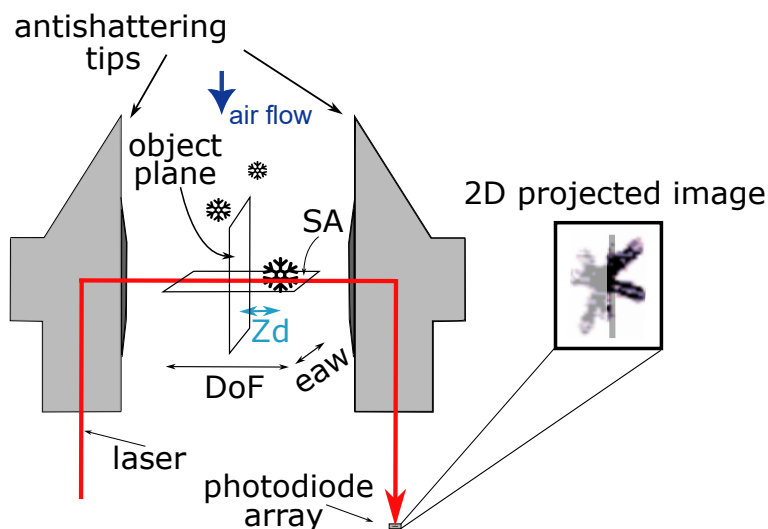


Figure 3.5: Schematic of the optical design of an OAP. The shadow image is a real image from the CIPG.

The shadow images of spherical particles can be represented by the Fresnel diffraction pattern of an opaque disc (Korolev et al., 1991; Korolev et al., 1998; Vaillant de Guélis et al., 2019), as in Fig. 3.6(a). As shown in the picture, the representation of the particle

perfectly in focus corresponds to a dark image with its real diameter. When moving away from the object plane, several rings of different shadow intensity become visible, along with a bright region in the center known as the Poisson spot (Korolev et al., 1991). As a result of the diffraction phenomenon, the size of the particle becomes overestimated by more than 10% (Vaillant de Guélis et al., 2019). Increasing distances from the object plane enlarge the overestimation. However, the size of spherical out-of-focus particles can be corrected by determining the relationship between the spot diameter and the ring (Korolev et al., 1998; Korolev, 2007b). This correction is not explained in detail here because only ice particles processing is of interest in this work, where this correction cannot be applied.

The dimensions of the image can vary depending on the chosen shadow intensity threshold. Furthermore, as the shadow intensity threshold is raised, the particle can move a shorter distance away from the object plane before completely losing all the pixels at the selected shadow threshold. In addition to the shadow threshold value, the DoF also depends on the particle's size. While bigger particles can move larger distances from the object plane before being out-of-DoF, the image of smaller particles quickly disappear at already short distances. In this way, the DoF is proportional to D^2/λ and is calculated in the following form (Knollenberg, 1970; Korolev et al., 1998):

$$\text{DoF} = \frac{cD^2}{2\lambda} \quad (3.1)$$

where λ is the wavelength of the light beam, D is the particle diameter, and c is a constant that depends on the shadow threshold level (Korolev et al., 1998; Gurganus & Lawson, 2018). The DoF as a function of particle diameter for the standard shadow intensity thresholds is illustrated in Fig. 3.6(b). The DoF is physically limited at some point by the distance between the probe arms, and therefore constant for the large particle size range. The advantage of choosing a lower shadow threshold (also called grayscale threshold) is the increase of the sample area (through the increase in the DoF) and the improvement of the counting statistics. However, the loss of quality of the images and the artificial increase of the size shown in Fig. 3.6(a) leads to higher uncertainties in the particle size determination. This issue becomes less problematic for spherical particles, since the Korolev correction can be applied (Korolev et al., 1998; Korolev, 2007b), but it is not applicable to ice crystals of diverse forms. Some studies advocate for more restrictive shadow thresholds (e.g. 67% or 75%) to improve the quality of the images and obtain a higher accuracy in the size determination (S. O'Shea et al., 2019; S. O'Shea et al., 2021). However, this also implies that more particles get sorted out, reducing the statistics.

Besides the DoF, the SA is also constrained by the effective array width, L_{eff} , which can be determined by the different methods shown in Fig. 3.7 (Knollenberg, 1970). The *all-in* method shown in Fig. 3.7(a) only considers fully imaged particles and reject those which touch one of the end diodes. For the accepted particles, the effective array width can be calculated as:

$$L_{\text{eff}} = (n - 2) \cdot \text{res} - D \quad (3.2)$$

Here, n indicates the number of diodes in the array, res the pixel resolution, and D represents the particle diameter. For bigger particles, L_{eff} becomes smaller and the prob-

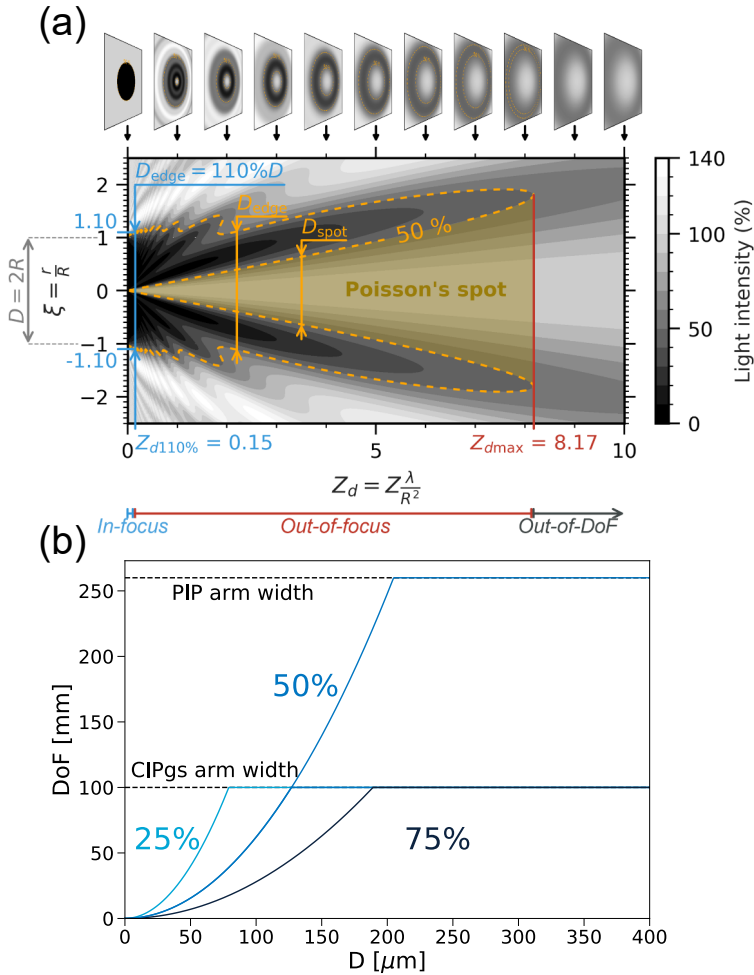


Figure 3.6: (a) Diffraction pattern of an opaque disc as a function of the disc diameter D and the distance to the object plane Z_d . (b) Depth of field (DoF) dependence on the shadow intensity level and particle diameter. The horizontal lines indicate the limitation by the probe arms and correspond to 10 cm for the CIPG and 26 cm for the PIP. The c values correspond to 21, 8.18 and 3.68, for the shadow intensities 25, 50, and 75%, respectively (Korolev et al., 1998). (Source of (a): Vaillant de Guélis et al. (2019), used under CC BY 4.0)

ability for large particles to touch the end diodes is relatively high. The lower counting in the larger particle size is compensated with the smaller sample area that results, but the poor statistics in this range have a high uncertainty associated. Further methods were developed applicable to spherical particles, since their geometry is known. The *center-in* method in Fig. 3.7(b) considers particles whose center lies within the diode array and its expression is simply $L_{eff} = n \cdot res$. The array width do not vary with particle size using this method. Fig. 3.7(c) shows a further option for spherical particles, where the L_{eff} gets elongated thanks to a reconstruction of particles at the diode edges (Heymsfield & Par-

rish, 1978). Finally, Fig. 3.7(d) exemplifies the difficulty of inferring the dimensions of the aspherical forms of ice crystals when they are not fully captured within the array. Therefore, the only trustworthy method for ice crystals is the all-in method, which is applied in this thesis.

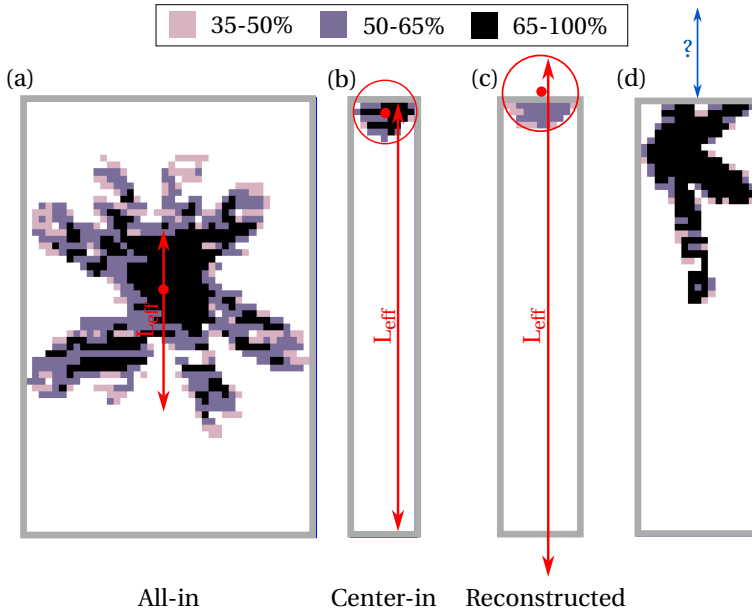


Figure 3.7: Schema of the methods for the calculation of the effective array width for CIPG images. (a) Ice crystal and array width using the all-in method. (b) Spherical particle and array width using the center-in method. (c) Spherical particle and array width using the reconstruct method. (d) Ice crystal outside the array with no possibility of applying the reconstruct method. Note that the grayscale levels are not the nominal for these images.

By applying the various methods to calculate L_{eff} for the CIPG and PIP specifications and multiplying them with the DoF contribution, the SA for each particle diameter can be determined, as illustrated in Fig. 3.8. For these cases, the CIPG DoFs are calculated for a 50% shadow threshold, as applied in this work. As seen before, reducing (increasing) the shadow threshold increases (reduces) the DoF and thus, a shift to the left (right) would be obtained in the SA curves. As anticipated, the SA gets dramatically reduced for particle sizes approaching the photodiode array width applying the all-in method. This has an impact on the concentration uncertainties (see Section 3.2.3) but it can be mitigated, as we will see in Chapter 4.

3.2.2. PARTICLE SIZE DETERMINATION

The 2D image of the particles is obtained by the concatenation of slices formed by pixels representing the photodetectors. Both CIPG and PIP feature a diode array with 64 photodiodes, and 15 and 100 μm pixel resolution, respectively. Therefore, the pixel units of an image can be translated into a physical dimension in micrometers.

Fig. 3.9 displays various sizing methods for defining the diameter of a particle. Some

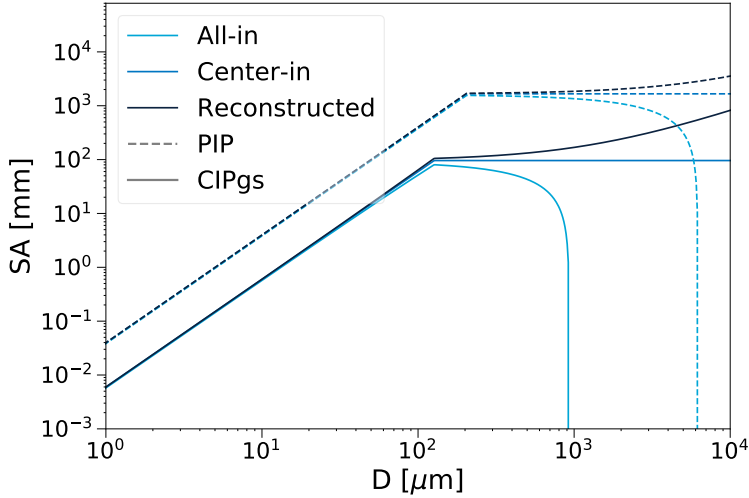


Figure 3.8: Sample area (SA) variation with diameter for the PIP and CIPG at 50% grayscale threshold. The SA is shown for the different methods of the effective array width calculation (all-in, center-in and reconstructed).

studies have explored impact of diameter definitions on cloud microphysical properties and have found substantial differences (Wu & McFarquhar, 2016; Leroy et al., 2016). Since the sample volume depends on the particle diameter, the chosen definition not only affects the particle's dimension itself but also the sample volume. However, there is no consensus on the optimal size determination method. The fastest and simplest options are D_x , which corresponds to the number of pixels parallel to the diode array, and D_y , the dimension parallel to the flow. These definitions may misrepresent the particle's dimension because they are heavily influenced by the particle's shape and orientation (Wu & McFarquhar, 2016). Additionally, D_y is particularly sensitive to the sampling rate, and errors in airspeed or an incorrect fixed PAS value can result in artificially elongated or shrunken particles, leading to an inaccurate diameter determination. However, D_x is independent of the sampling rate and is useful for calibration purposes because the shadow images' forms are spherical.

Other common methods usually involve the definition of an auxiliary circle. The maximum dimension is typically determined as the diameter of the minimum enclosing circle (in Fig. 3.9 denoted as D_{\max}) (Heymsfield et al., 2013; Wu & McFarquhar, 2016). The area equivalent diameter, $D_{\text{eq}} = \sqrt{\frac{n \cdot \text{res}^2}{4\pi}}$, is determined as the diameter of a circle of equivalent area to the particle's projected surface (total number of obscured pixels). The advantage here is that this definition is unambiguous compared to D_{\max} , which depends on the method for the circle computation (Leroy et al., 2016). While for spherical particles, both definitions are quite similar, for ice crystals can be quite different, as illustrated in Fig. 3.9. D_{eq} tends to underestimate the spatial extension of an ice particle but represents better its volume. The maximum dimension definition, in turn, overestimates the volume of the particle but it is a better measure of the space that the particle occupies, which influences the minimum distance between particles.

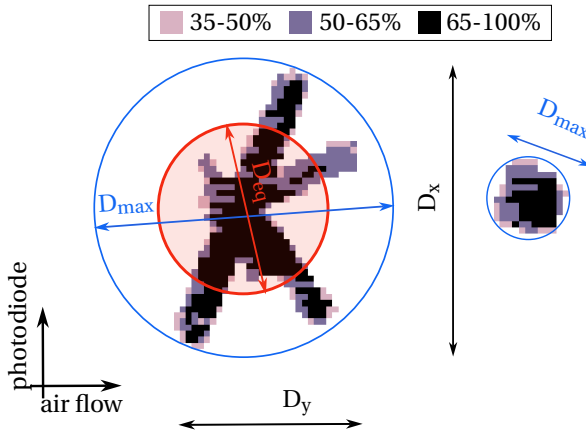


Figure 3.9: Schema of particle diameter determination for an ice crystal and spherical particle. The diameters depicted in the schema are for illustrative purposes and provide a general sense of scale. Note that the grayscale levels are not the nominal for these images.

3.2.3. MEASUREMENT LIMITATIONS AND UNCERTAINTIES

Numerous studies have focused on addressing some of the uncertainties and limitations associated with the OAPs (Knollenberg, 1970; Korolev et al., 1991; Korolev, 2007b; Connolly et al., 2007; McFarquhar et al., 2017; Baumgardner et al., 2017). One significant limitation is related to the discretization in pixels of the images, which is subjected to the pixel resolution. The result is that a particle size can be assigned to ± 1 size dimension depending on its position within the photodiode array. For instance, particles between 37.5 and 52.5 μm may be classified as 45 μm particles in the CIPG. This error diminishes as particle size increases, but becomes more pronounced with coarser pixel resolutions (Baumgardner et al., 2017).

The definition of particle diameter already introduces a significant source of uncertainty, particularly for ice crystals. McFarquhar et al. (2017) observed variations in particle size distributions when employing six different diameter definitions. Furthermore, in the case of ice crystals, 2D images do not provide sufficient information to accurately determine their 3D dimensions. For example, the same shadow image might correspond to a column or a plate traversing laterally to the laser beam. Utilizing the minimum enclosing circle for ice particles typically leads to an overestimation of their mass and volume, as an aspherical particle never completely fills the enclosing sphere. This is intrinsic to the maximum diameter as size definition for ice crystals. As commented in Section 3.2.2, alternative definitions also disregard other factors, and even though the community has not reached a consensus on the optimal definition, the maximum dimension is frequently used in other studies (e.g., Heymsfield et al. (2013), Wu and McFarquhar (2016), and Kirschler et al. (2023)).

A major source of uncertainty in sizing is attributed to the diffraction effect of particles. As previously explained, when particles move away from the object plane, their shadows lose intensity and extend, resulting in a blurred image and a systematic overes-

timination of particle size. For spherical water droplets, this effect can be corrected using the relationship between the Poisson spot and the shadow ring, known as Korolev correction (Korolev et al., 1998; Korolev, 2007b). However, it becomes exceptionally challenging for ice crystals because each unique habit, orientation, and dimensions generate a distinct diffraction pattern (Vaillant de Guélis et al., 2019). Consequently, the Korolev correction method is not applicable to ice crystals. Apart from that, false Poisson spots can be created in ice crystal images due to very thin parts of ice crystals (e.g. plate-like forms), which could be semitransparent. Even though there are some attempts to better constrain the DoF and improve the size determination using the grayscale levels (S. O’Shea et al., 2019; S. O’Shea et al., 2021), currently, there exist no algorithm that can correct the size of the ice crystals.

In terms of limitations and uncertainties in the concentration, the calculation of the effective array width for ice crystals has a non-negligible effect. Since their form cannot be reconstructed, the only possibility is the use of the all-in calculation with the subsequent reduction of the sample area in the larger sizes and a high rejection of large particles. This leads to an increased uncertainty in the concentration of the last bins of the particle size distribution. However, this problem can be mitigated for the CIPG in combination with the PIP by cutting off the CIPG size distribution at an early stage and concatenating the PIP size distribution (see Section 4.3).

As mentioned in Section 3.1.3, shattering also affects measurements of the OAPs. The CIPG has modified triangular tips that deflect the artifacts generated by the shattering of large ice crystals to avoid entering the sample volume (Korolev et al., 2013b). This modification is very efficient at reducing shattering effects (Korolev et al., 2013a), however, an interarrival time analysis is also necessary to identify and remove the remaining shattering events (Field et al., 2006). Although the PIP does not include antishattering tips, little influence of shattering in the PIP is expected, since the PIP can only detect particles from 100 μm and shattered fragments are usually smaller. Splashing is another event of particle fragmentation occurring usually to rain drops that collapse due to the change of pressure in the flow between the arm probes. This type of events are usually captured in the OAP images and can be easily filtered out, as well as diverse image artifacts and pixel errors, as we will see in Chapter 4.

3.3. DEFINITIONS OF MICROPHYSICAL PROPERTIES

In this chapter, the working principles and primary outputs of the cloud probes employed in this study have been described. These probes yield measurements of particle size and the number of particles per sample interval. These fundamental quantities form the basis for deriving additional properties essential for describing cloud microphysics.

SAMPLE VOLUME

The sample volume (SV) represents the volume within each sample interval (Δt). The sample area (SA) is perpendicular to the airflow (see Fig. 3.5); it remains constant in the scattering probes and varies with particle size in the OAPs. The distance travelled in the direction of the flow per sample rate is determined by the probe air speed (PAS). The sample volume can be then calculated with the following expression:

$$SV = SA \cdot PAS \cdot \Delta t \quad (3.3)$$

ICE NUMBER CONCENTRATION

The particle number concentration per bin size (N_i) can be calculated by dividing the number of particles n_i sampled in a size bin i by the sample volume within the sample interval Δt .

$$N_i = \frac{n_i(\Delta t)}{SV(\Delta t)} \quad (3.4)$$

This is the general expression, applicable when the sample volume does not depend on the individual particle sizes. In the opposite case, as in the OAPs, the calculation of the particle number concentration in the size bin i would involve summing each particle's sample volume:

$$N_i = \frac{n_i}{\sum_j SV_j} \quad (3.5)$$

For simplicity, the standard sample volume is denoted in the denominator as shown in Eq. (3.4), multiplied by the sum of each particle's weights $\frac{SA_j}{SA}$ (where j represents particles in bin i), as in the following expression:

$$N_i = \frac{n_i}{SV(\Delta t) \sum_j \frac{SA_j}{SA}} \quad (3.6)$$

The concentration is usually represented graphically as a function of particle size for the instrument's size bins (dN/dD) to generate a Particle Size Distribution (PSD). However, when comparing instruments with different size resolutions (i.e., different bin widths), this approach can result in a misleading interpretation of the graph. Therefore, it is preferable to use a normalized concentration ($dN/d\log D$), where the concentration per bin is divided by the ratio of the logarithm of the bin edges, and the resulting normalized concentration is independent of the bin width:

$$dN/d\log D = \frac{dN}{d\log D} = \frac{N_i}{\log D_{i,u} - \log D_{i,l}} = \frac{N_i}{\log\left(\frac{D_{i,u}}{D_{i,l}}\right)} \quad (3.7)$$

The total number concentration per sample interval, N , is calculated summing the concentration in each size bin, N_i .

$$N = \sum_i N_i \quad (3.8)$$

EFFECTIVE DIAMETER

The effective diameter (ED) serves as a valuable measure of the relationship between the scattering properties of a cloud and its microphysical properties (Fu & Liou, 1993). Defining an effective diameter for liquid clouds is relatively straightforward. However,

for ice clouds, numerous definitions exist, depending on the choice of directly measured variables and derived quantities (McFarquhar & Heymsfield, 1998). In this study, a general definition is adopted, based on the ratio of the third to the second moment of the cloud spectrum (Parol et al., 1991; Schumann et al., 2011). In the following expression, D_i represents particle size, and it is important to note that the ED then depends on the specific particle diameter definition used (Wu & McFarquhar, 2016). For the combined distribution from several instruments, D_i is substituted by the center of each size bin (in the linear scale).

$$ED = \frac{\sum_i D_i^3 N_i}{\sum_i D_i^2 N_i} \quad (3.9)$$

ICE WATER CONTENT

The ice water content (IWC) is another relevant property of ice clouds. For the liquid clouds, since the volume of the spheres is determined by knowing the particle' diameter, the liquid water content (LWC) can be derived from a sphere volume and the liquid water density. This calculation becomes more complicated for ice masses, since the volume of each particle is not known, and just 1D or 2D dimensions are available. Therefore, parameterisations of the ice mass and particle diameter need to be obtained experimentally and several expressions are available in the literature (Brown & Francis, 1995; Baker & Lawson, 2006; Heymsfield et al., 2010). IWC calculations slightly differ depending on the chosen relationship (Afchine et al., 2018). In this work, the ice mass-dimension relationship for cirrus clouds is utilized, as provided by Heymsfield et al. (2010) in CGS system of units:

$$m_{ice,i} = 0.0058D^{2.1}, \quad (3.10)$$

where $m_{ice,i}$ represents the ice mass per size bin or per particle, since D can assume either the values corresponding to the center of the size bins (general approach, applicable to scattering probes or a combined size distribution) or, in the case of the particle-by-particle (PbP) approach used in the OAPs, it represents the diameter of each individual particle. In the former case, the resulting ice mass is calculated assuming that all particles within a size bin have the same diameter of the size bin's center. The IWC per sample interval is obtained by multiplying the ice mass by the number concentration per size bin, $m_{ice,i}$, and summing across all bins:

$$IWC = \sum_i m_{ice,i} N_i \quad (3.11)$$

In the particle-by-particle calculation, the mass of each particle is divided by its respective weight, and by the sample volume per time interval:

$$IWC = \frac{\sum_j m_{ice,j}}{SV(\Delta t) \sum_j \frac{SA_j}{SA}} \quad (3.12)$$

EXTINCTION

The extinction coefficient β_{ext} is another useful parameter for quantifying the radiation impact of a cloud and can be calculated based on the particle projected area (Schumann et al., 2011; Mitchell et al., 2011; Thornberry et al., 2017).

$$\beta_{\text{ext}} = \int Q_{\text{ext}} A_p(D) N(D) dD = Q_{\text{ext}} A, \quad (3.13)$$

where Q_{ext} represents the extinction efficiency, A_p corresponds to the mean projected area of particles within the interval D to $D + dD$, and N is the number concentration of particles in that interval. The value of Q_{ext} depends on the particle size and the wavelength but can be approximated to 2 for large particle sizes relative to the wavelength λ ($\pi ED/\lambda \gg 1$). Assuming a constant Q_{ext} , the extinction coefficient can be directly related to the density of projected area A . Another way to calculate the extinction through the relation between IWC and ED :

$$\beta_{\text{ext}} = \frac{3IWC}{\rho_{\text{ice}} ED}, \quad (3.14)$$

where ρ_{ice} is the ice density.

Using the definition of Eq. (3.13) with the combined particle size distribution data from the CDP, CIPG and PIP, we can calculate the extinction coefficient as:

$$\beta_{\text{ext}} = 2 \left[\sum_i N_i \pi \left(\frac{D_i}{2} \right)^2 + \sum_j \frac{A_j}{SV_1 \frac{SA_j}{SA}} + \sum_k \frac{A_k}{SV_2 \frac{SA_k}{SA}} \right] \quad (3.15)$$

The first term refers to the PSD of the CDP, where the projected area density can be calculated from the particle number concentration per bin, N_i , and the corresponding mean projected areas calculated from the center of each bin, D_i , assuming spherical shapes. The second and the third terms correspond to the projected area density calculation from the OAPs. Since imaging probes provide directly information on the surface projection for each particle, it is preferable to use the PbP data here. The total projected area is given by the sum of the individual particle areas, divided by the product of the corresponding sample area weights and the standard CIPG and PIP sample volumes, SV_1 and SV_2 , respectively. The sets of CIP and PIP particles per second are represented by j and k , respectively.

4

METHODS

Following the introduction in the measurement techniques in Chapter 3, the characteristics of the main instruments used in this thesis were described. This chapter provides an extensive report on the main methods and investigations that I conducted in order to improve the instrument processing and data quality, and better understand and mitigate the source of uncertainties and further instrumental issues. Similar to Chapter 3's structure, methods are separated for scattering probes (CDP) in Section 4.1, and optical array probes (CIPG and PIP) in Section 4.2. Among the CDP methods, an intercomparison between CDP and CAS-DPOL is shown in Section 4.1.3. In the Section 4.2 the whole processing method for OAP data is described, while the detailed description of the modules developed for binary data reading into raw particle-by-particle image data can be found in Appendix B. Finally, the combination of the different size distributions of the three instruments is addressed in Section 4.3.

4.1. CDP METHODS

As mentioned in Chapter 3, the CDP served as the scattering probe for the measurements in this work. As introduced in Section 3.1.1, the data acquisition and recording in the cloud probes are carried out using the software PADS provided by the manufacturer DMT LLC. This program allows for the control of measurement parameters and real-time data visualization. The software generates a bulk file or 1Hz-file, where information from the instrument's electronics is recorded at a sampling frequency of 1 Hz. This file includes directly measured information and user-specified settings. It records the number of particles per sample interval in each size channel, implying a pre-definition of channel boundaries (size binning) either set by the manufacturer by default or modified by the user. However, specific information about each individual particle, such as their exact sizes, is not provided in this file.

In addition to the bulk file, PADS generates a particle-by-particle (PbP) file that records information about each individual particle, up to a total of 256 particles. For every entry, the file includes a corresponding timestamp, the equivalent AD Counts

representing the particle's scattering cross-section, and the *interparticle* or *interarrival* time, defined as the elapsed time between two consecutive particles. As this section will elaborate, the choice between using one file or the other depends on the intended purpose.

This section outlines the methods applied to analyse the data produced by this instrument. The size calibration is detailed in Section 4.1.1, an analysis of the time resolution effects of the CDP is presented in Section 4.1.2 and, finally, a comprehensive intercomparison between the CDP and CAS is explained in Section 4.1.3, addressing the differences in shattering effects on both instruments and suggesting a possible detection criterion.

4.1.1. SIZING CALIBRATION

As introduced in Section 3.1.2, the CDP utilizes forward scattering of light on particles to determine their size. The light intensity received at the detectors is directly proportional to the scattering cross section σ_{4-12° and is translated into an analog to digital value (AD Counts) ranging from 0 to 4095. As discussed in Section 3.1.2, the forward scattering cross section of particles can be related to their sizes applying various methods such as Mie theory, T-matrix calculations, discrete dipole approximation, among others (Mie, 1908; Borrmann et al., 2000; Yurkin & Hoekstra, 2007; Yurkin & Hoekstra, 2011). In this study, Mie theory is assumed for the calculation. The relationship between the AD Counts, the scattering cross sections and, thus, particle sizes is established through size calibration (Nagel et al., 2007; Lance et al., 2010; Rosenberg et al., 2012; DMT, 2017a). The calibration ensures equivalence between AD Counts and diameters across the entire size range. Regular performance of calibrations is crucial to verify this relationship over time, as it may change due to factors such as aging or misalignment of the laser. For the CIRRUS-HL campaign, size calibrations were conducted before and after the campaign, and the results were compared to a previous calibration from the MOSAiC campaign (data provided by Manuel Moser and Valerian Hahn, German Aerospace Center (DLR)).

The calibration process followed the standard procedure, employing precision glass beads with known sizes. Glass beads of sizes {1.9, 4.6, 10, 23, 32.5, 49} μm were included in the example calibration of Fig. 4.1. Borosilicate glass beads were used for sizes below 25 μm , and soda-lime glass beads were employed for larger sizes. As already mentioned, PADS provides an additional PbP file, which records the time and AD Counts for each particle. This file is very useful for verifying the AD thresholds defined in the bulk file.

In Fig. 4.1(a), the AD Counts generated by different glass bead sizes are summarized in distinct frequency distributions. Larger sizes correspond to greater AD Counts, mirroring the behavior of the scattering cross section σ_{4-12° shown in Fig. 4.1(b). The figure also illustrates differences in scattering between glass and water. The CDP is calibrated for water, implying that the measured AD Counts in Fig. 4.1(a) correspond to smaller diameters than the specified glass bead sizes. Consequently, determining the size of an equivalent water droplet that scatters the same as the glass bead becomes necessary. However, due to the non-monotonic behavior and ambiguities of the function, multiple equivalent water droplet diameters can produce the same level of scattering. Additionally, deviations from the nominal glass bead sizes exist, ranging from 0.3 to 1.0 μm , depending on the nominal size.

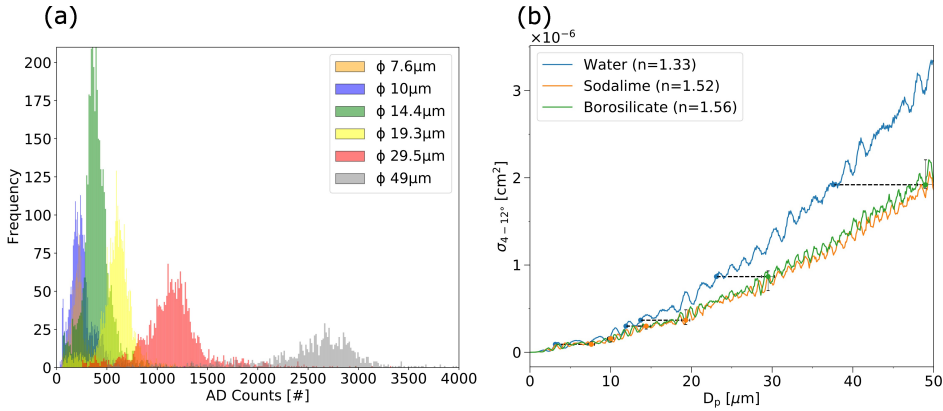


Figure 4.1: Summary of the frequency distribution of the AD Counts from the PbP file corresponding to different glass sizes (a). Scattering cross section σ_{4-12° as function of diameter for the CDP size range and different materials characterized by their refractive index n (b). The glass bead diameters for the two materials are indicated with filled circles, as well as the equivalent water droplet diameter.

For the frequency distribution of each glass bead size, the mean value is calculated. The relationship between the scattering cross section σ_{4-12° and the averaged AD Counts is linear and can be expressed by the following equation:

$$\sigma_{4-12^\circ} = m \cdot \text{ADC} + b, \quad (4.1)$$

Thus, the AD Counts generated by glass beads of a specific size can be associated with their theoretical scattering cross section. The parameters m and b in the expression of Eq. (4.1) are then determined through a linear fit, as illustrated in Fig. 4.2. The calibration data set presented in Fig. 4.1 corresponds to the "December2020" calibration, serving as a reference and compared with subsequent calibrations, namely "June2021", and an earlier calibration, "February2020", conducted for the MOSAiC campaign (provided and calculated by Manuel Moser and Valerian Hahn). The overlaid lines of Fig. 4.2 demonstrate a satisfactory agreement across the different calibration data sets.

Finally, knowing the coefficients of the relationship between AD Counts and σ_{4-12° , a function expressing AD Counts dependent on diameter can be calculated. With this information, a bin definition can be established, determining the equivalences between particle diameter and AD Counts. However, this function, like the scattering cross section function, exhibits ambiguities. Therefore, defining thresholds accordingly is crucial to minimize this issue. Particle diameters associated with the same scattering cross section must be categorized within the same size channel.

For this study, the nominal binning provided by DMT LLC (DMT, 2017a) is adopted for simplicity. As discussed in Sections 3.1.2 and 3.1.3, the instrument samples a variety of ice crystal shapes with different orientations during cirrus clouds measurements, resulting in a wide range of scattering cross-section functions. Consequently, fixing a binning definition based on a single scattering cross-section is just one of several potential binning definitions. Currently, accurately determining the spectrum of scattering

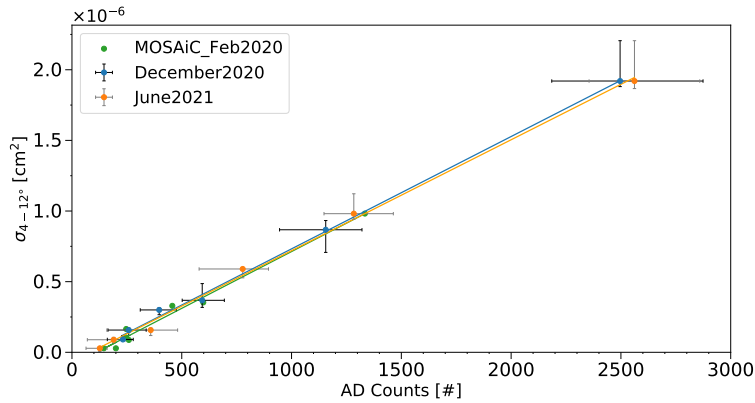


Figure 4.2: Comparison of calibrated relationships between the calculated scattering cross sections for the glass beads employed and the experimentally measured mean AD Counts for the corresponding distribution shown in Fig. 4.1. Calibrations in December 2020 and June 2021 include the error in the y-direction from the standard deviation indicated by the manufacturer for each glass bead size, and the 25 and 75 percentiles in the x-direction from the AD Counts distribution.

cross-sections is not feasible with existing methods (Yurkin & Hoekstra, 2007; Yurkin & Hoekstra, 2011). The operational principles of the instrument for ice crystal measurement inherently introduce uncertainty into the results.

4.1.2. INVESTIGATING TIME RESOLUTION

The calibration process of Section 4.1.1 has shown how the PbP file can be very useful for having a deeper view of each particle that is detected. Unfortunately, the PbP file has a limitation of 256 particles per sample interval. This translates to a maximum number concentration of approximately $\sim 6 \text{ cm}^{-3}$ for a PAS value of 150 m/s. While cirrus clouds typically do not exceed this concentration, freshly formed contrails can achieve N values between larger than 10^3 cm^{-3} within the first 100 s of their lifetime (Bräuer et al., 2021a). Using the PbP file would imply assuming the portion of time of the first 256 particles as representative for one sample interval, typically one second.

On the other hand, the 1Hz-file imposes a lower limit on N , determined by the minimum particle count within the sample interval, which corresponds to the occurrence of a single particle in the 1-second time resolution (Krämer et al., 2020). Assuming a PAS value of 150 m/s as in the earlier case, the minimum N value is $\sim 0.025 \text{ cm}^{-3}$. It is not uncommon to register only one particle within a 1-second time interval in cirrus due to the small sample area of a scattering probe. This leads to an artificially high frequency of observations of the same N value, often the median N in cirrus clouds (Krämer et al., 2016; Heymsfield et al., 2017a; Krämer et al., 2020). Additionally, as shown in this section, the lower the particle concentration within a sample period, the less precise the information from the 1Hz-file becomes, as the inhomogeneities within a cirrus cloud are not well captured.

The standard method explained in Section 3.3 to calculate the number concentration in the 1Hz-file has been widely applied in previous studies using also other instruments

(e.g., Heymsfield et al. (2010) and Krämer et al. (2020)). However, an alternative to the 1-second rate calculation of the number concentration is proposed by (Baumgardner et al., 2014) and the advantages of this method are discussed in the following. The interparticle time (IPT) method is based on the definition of an average particle rate (APR):

$$\text{APR} = \frac{\sum n_{\text{particles}}}{\sum \Delta\tau_i} \quad (4.2)$$

where τ_i represents the interarrival or interparticle time. The concentration is then calculated by dividing by the sample volume per second (SA · PAS). The schematic in Fig. 4.3 provides a visual representation of this method in comparison to the standard one. The diagram depicts four 1-second intervals for which the number concentration N (standard) and N' (IPT) are calculated. The standard method involves taking the number of particles within the sample interval and dividing it by the sample volume within that second. In contrast, the IPT method determines the elapsed time during sampling by summing up the interarrival time of the particles. Consequently, in situations such as particles 5 and 6, it makes a difference whether a single-particle is measured after a long time without particles or in the consecutive time interval. As a result, the number concentration in the third and fourth periods is the same calculated with the standard method, contrary to the IPT method.

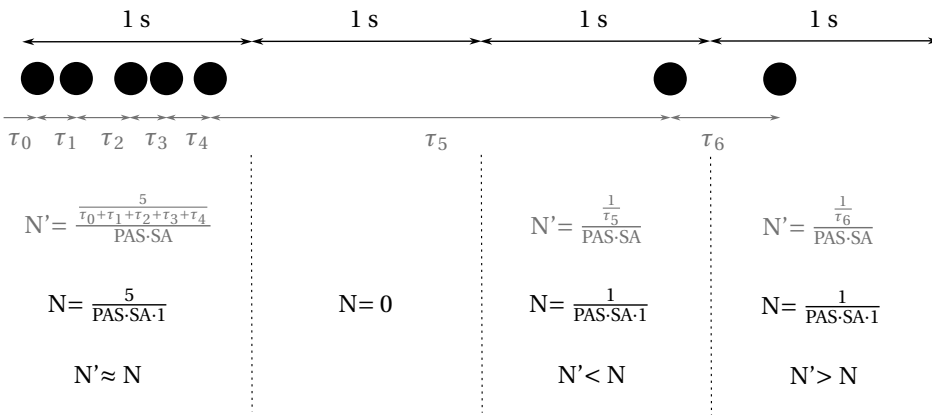


Figure 4.3: Diagram illustrating the contrast between two approaches for calculating particle number concentration, denoted as N and N' , using a simple example. τ_i represents the interparticle times, and a constant PAS is assumed. The notation associated with the interparticle time (IPT) method is depicted in gray, while the standard method is shown in black.

In Fig. 4.4, the outcome obtained using the conventional method from the 1Hz-file is contrasted with that from the IPT method using actual aircraft measurements in the cirrus regime. The histogram in panel (a) illustrates the number concentration per sample interval of 1 second. The remarkable distinction between the two methods lies in the treatment of single-particle events. While the conventional method consistently assigns a value of approximately 0.025 cm^{-3} to these events, the IPT method yields significantly lower values when the events are well-separated. The IPT method proves effective in overcoming the limitation of the 1Hz-file and better reflects the cloud's inhomogeneities,

making it particularly suitable for thin clouds. It weights concentrations based on the surrounding conditions, offering a clearer identification of well-isolated events.

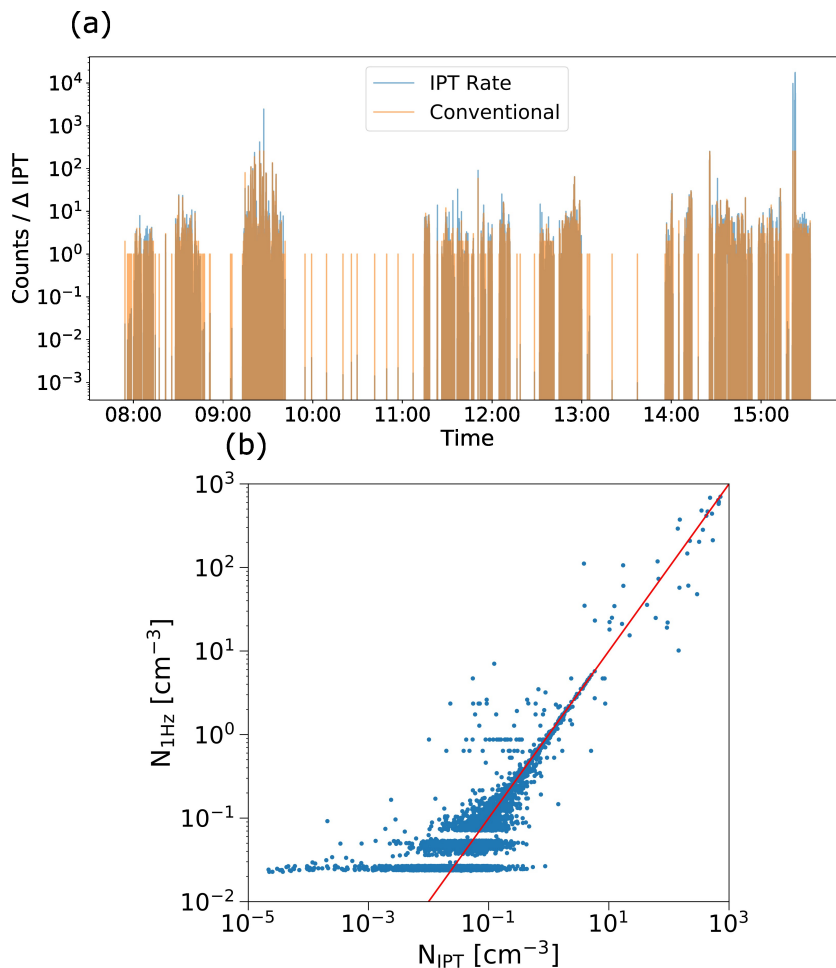


Figure 4.4: Comparison of the number of counts divided by the sample time along the flight between the IPT (in blue) and conventional (in orange) methods (a). Correlation between the number concentration obtained with the IPT method for PbP data and the concentration from the 1Hz-file calculated with the conventional method. The red line indicates the ideal 1:1 correlation.

In reference to Fig. 4.4(b), the concentrations derived from the PbP data set computed the IPT method is represented against the concentrations obtained from the 1Hz-file. As the number concentration decreases, the correlation spreads due to the lower limit in concentration of the 1Hz-file. As previously mentioned, the minimal concentration determined through the conventional method is approximately 0.025 cm^{-3} for the 1Hz-file. However, the application of the IPT method introduces a broader spectrum of concentrations for these scenarios, including not only lower values but also higher ones,

ranging from 0.00001 to 1 cm^{-3} , depending on the temporal separation of the event from the preceding one.

Nevertheless, utilizing the PbP data set reveals a limitation when the particle concentration is high and considerably variable. While the 1Hz-file provides the concentration based on the real number of particles measured during one-second sample period, the PbP file only allows for 256 particles within the sample interval. In principle, using the IPT method with the PbP data circumvents the limitation, allowing for larger concentration values. This is attributed to the higher likelihood of numerous particles being uniformly distributed within a sample interval, making the density of the first 256 particles a reasonable approximation for the entire interval. Depending on the elapsed time during the sampling of the 256 particles, different concentrations can be obtained. However, as indicated by the variability in the correlation with the 1Hz data set in Fig. 4.4(b), heterogeneities within the sample interval may persist. The initial 256 particles may not offer a sufficiently accurate solution, in particular in contrail and contrail cirrus sequences, where the variability is higher than in natural clouds. Additionally, even if the concentration is well estimated, the particle size distribution might not be precisely represented using only the first 256 particles.

In summary, the decision was to continue utilizing the 1Hz-file for calculating cloud properties from the CDP. This choice is based on the presence of contrails and contrail cirrus measurements embedded in the data, rendering the use of the PbP data set impractical for these specific sequences. The reasoning behind this decision is grounded in the necessity for consistency in data analysis across all cloud sequences, instruments, and with respect to prevailing practices in the field. The conventional method, employed for analyzing data from the OAPs, aligns with this consistency. However, I would recommend considering the IPT method on PbP data for future data analysis involving cirrus measurements, especially for thin cirrus.

4.1.3. CDP AND CAS-DPOL INTERCOMPARISON

In this part, I present an analysis conducted subsequent to the data evaluation using the combined CDP-CIPG-PIP setup. This investigation was prompted by questions regarding the comparability between the CDP and CAS, given their shared particle size range. Notably, in some cases, higher concentrations were observed in the CAS, motivating a more in-depth exploration to elucidate the discrepancies between the two instruments.

Particle size distributions such as the one of Fig. 4.5, offer a detailed examination of these differences. In these 10-minute sequences for a cirrus case (a) and a liquid cloud example (b), the PSDs of the CDP and CAS are plotted together, with the CIPG included as a reference. Focusing on Fig. 4.5(a), two distinct regimes emerge from the comparison between the CDP and the CAS. Firstly, in the first three bins of the CAS (ranging between 2 and $4 \mu\text{m}$), there is a declining profile of concentration with increasing diameter, whereas the CDP registers minimal measurements in this range. The second range spans from 4 to approximately $30 \mu\text{m}$, where both PSDs exhibit a similar profile. However, the concentrations recorded by the CAS are consistently elevated by one order of magnitude across all these bins.

It is important to note that the last 2-3 bins of the CDP are typically excluded from the analysis. Previous campaigns have indicated an overestimation of concentration in this

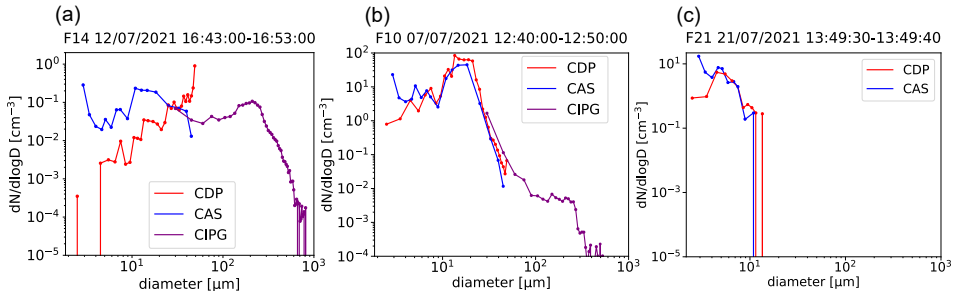


Figure 4.5: Comparison of the particle size distributions (PSDs) between the CDP (in red) and the CAS-DPOL (in blue) for an example cirrus sequence of flight F14 (a), a sequence of liquid clouds of flight F10 (b), and a short sequence of a contrail encounter of flight F21 (c). The PSD of the CIPG (in purple) is also included as a reference.

4

range, and our current data also reflect systematically an artificially high concentration in this segment.

Key insights were derived from a preliminary analysis encompassing numerous sequences from various flights within the campaign. Surprisingly, the discrepancies in concentration were not consistently observed across all sequences, suggesting a lack of systematic over- or underestimation by either instrument. During periods involving low clouds or contrail cirrus measurements, a remarkably high level of agreement was evident between the two instruments, as shown by the PSDs in Fig. 4.5(b) and (c). This concordance implies that both instruments operated effectively throughout the entire campaign and raises the question of why cirrus sequences appear to be problematic. A more systematic approach is provided in Section 4.1.3 and further examples of sequences are presented later in Figs. 4.11, A.3 and A.4.

Cirrus typically exhibit low particle concentrations, notably much lower than liquid clouds or contrails (see Chapter 2). If there is an underlying issue affecting the measurements, the low concentrations in cirrus clouds allow such errors to manifest. Intuitively, it seems that the CAS may be exhibiting an overestimation in the concentration of the lower particle size range. In aged cirrus, small particles often disappear through sublimation or grow to larger sizes, and this phenomenon might not be accurately captured by the CAS, resulting in elevated concentration profiles. One known mechanism for artificially creating an enhancement of small particles is shattering, which will be explored in the following sections.

SHATTERING EFFECTS

The CAS instrument presents a widespread applicability in the cloud measurements community. Its lower size limit of $0.6 \mu\text{m}$ makes it particularly well-suited for contrail measurements. This is attributed to the fact that ice particles smaller than $2 \mu\text{m}$ are present in the early stages of a contrail, specifically during the aircraft wake vortex phase (within the first 1 – 2 minutes) (see Kleine et al. (2018), Bräuer et al. (2021a), and Bräuer et al. (2021b)). Comprehensive insights into the climatology of microphysical properties of cirrus have been obtained based on a CAS-CIPG combination Luebke et al., 2016; Krämer et al., 2016; Krämer et al., 2020. However, as explained in Section 3.1.3, it is es-

sential to note that forward scattering probes, including the CAS, have historically been significantly impacted by contamination from small particles resulting from shattering of larger ones, particularly when high *IWC* was present (Field et al., 2003; Field et al., 2006; McFarquhar et al., 2007; Heymsfield, 2007; Jensen et al., 2009; Korolev et al., 2011; Korolev et al., 2013a; Korolev et al., 2013b). Significant progress has been made over the last decade through modifications to the arm tips and the development of methods for identifying and correcting shattered particles. Despite these advancements, there are occasions where these issues may still persist, as it will be discussed in the following paragraphs.

The study by Field et al. (2003) investigated the overestimation of small particles in mid-latitude cirrus, revealing factors ranging between 2 or 3 and 5 or 6. Larger particles were found to have a higher probability of suffering shattering (Korolev & Isaac, 2005). Field et al. (2003) analysed the interarrival times (IAT, or interparticle times, IPT) of both natural particles and artificial fragments. They identified the shattered pieces by their shorter transit times compared to natural particles. The underlying theory explains that when an ice crystal impacts and breaks into many smaller pieces, these fragments tend to travel together in a cluster. Consequently, they reach the sample volume at a higher frequency, resulting in a higher concentration than naturally distributed cirrus ice particles. In such cases, the IPT frequency distribution would exhibit two distinct modes, typically around 0.01 and 0.0001 s, depending on cloud properties and instrument type. Shattering events can be identified and filtered based on the IPT. Excluding particles with IPT shorter than a specified threshold (commonly between 0.0001 and 0.001 s) has the potential to mitigate the impact of shattering on N (Korolev & Isaac, 2005; Field et al., 2006).

The filtering methods discussed rely on the idealized theory that shattering events are distinctly clustered and separated, making them distinguishable from natural particles. However, as noted by Korolev and Isaac (2005), it is not always feasible to reliably distinguish shattering events through IAT analysis. In some cases, particles shattered into larger pieces may have fragmented due to turbulence or wind shear induced by the probe housing, rather than through mechanical impact with the probe's surfaces.

The schema in Fig. 4.6(b) illustrates the ideal scenario where particles in the cluster are easily identifiable due to their short interarrival times, contrasting with the case in (a) where the natural particles are more separated, resulting in larger interarrival times. However, the actual case may differ. Shattered fragments might not necessarily be clustered and could reach the sample volume within other natural particles. Alternatively, natural particles could be embedded in a cluster of shattered fragments (Korolev et al., 2013a). The schema in Fig. 4.6(c) depicts these cases, demonstrating how fragments and natural particles can be mixed together, exhibiting larger interarrival times than in the shattered particle cluster but smaller than the case of purely natural particles. In such a scenario, detecting shattered fragments within the natural particle population becomes challenging, and they might be erroneously assimilated as additional natural particles.

The primary distinction between the CDP and the CAS lies in the design of their sample area housings. The CDP is an open-path instrument with the sample area well-separated from the probe arms (≈ 2 cm, Lance et al. (2010)). On the other hand, the CAS encloses the sample area within a tube, introducing additional surfaces for particle

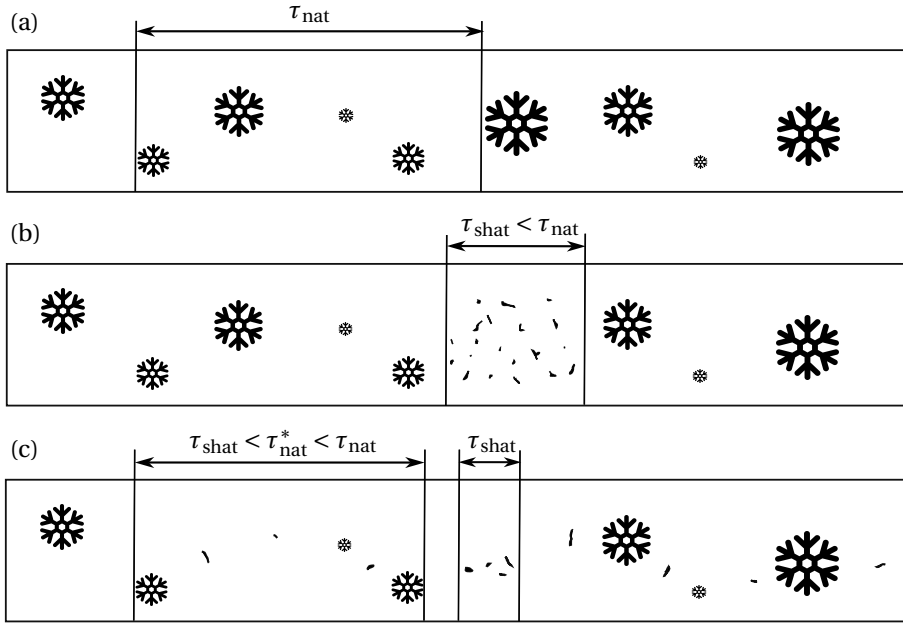


Figure 4.6: Conceptual schema illustrating various scenarios of particle interarrival times. Hypothetical case without shattering with interarrival times τ_{nat} (a). Ideal case of shattering occurring in clusters of multiple small fragments passing together through the sample area with interarrival times $\tau_{\text{shat}} < \tau_{\text{nat}}$ (b). Hypothetical real case in the CAS inlet tube with some small shattered particle clusters and dispersed shattered fragments among natural particles with reduced interarrival times τ_{nat}^* , compared to the original τ_{nat} (c).

impact and potentially causing alterations in the velocity field. To investigate the incidence of shattering detectable with IAT analysis, the IAT histograms of the CAS and CDP from several flights were compared (as illustrated in Figs. A.1 and A.2). The CAS IAT histograms frequently exhibit two modes, while the CDP shows no shattering. This finding is further discussed in Section 4.1.3 along with additional diagnostics.

SENSITIVITY TO AEROSOL PARTICLES

The CAS-DPOL, with a lower size range of $0.6 \mu\text{m}$, is capable of measuring not only contrail ice particles but also the larger size range of aerosol particles (Baumgardner et al., 2001). In general, CAS-DPOL measurements are designated as aerosols within the 0.6 to $3 \mu\text{m}$ range and cloud particles within 3 to $50 \mu\text{m}$, with the exception of contrail measurements, where ice crystals from young contrails can be smaller than $1 \mu\text{m}$ (Bräuer et al., 2021a). As discussed earlier, an interarrival time analysis aids in detecting and removing clusters of shattered particles.

However, since particles smaller and larger than $3 \mu\text{m}$ are measured simultaneously in the CAS, and the IAT is calculated for every particle based on the time shift with respect to the previous one, it is necessary to recalculate the IAT considering only the particles within the desired size range. Consequently, the values of the apparent interarrival times of cloud particles in the CAS appear lower than in the CDP, given that the latter

records only particles with diameters greater than $2\ \mu\text{m}$. This distinction is crucial to note, especially considering that N can also be calculated from the IAT, as shown earlier in Section 4.1.2.

The question that arises is whether the first bins (in the cloud size spectrum) of the CAS-DPOL (ranging between 2 and $4\ \mu\text{m}$) could be contaminated by background aerosol. Unlike the CDP, the CAS-DPOL is designed to measure also aerosol particles. Therefore, the frequently observed higher N in the smallest bins in the CAS range compared to the CDP could potentially be attributed to this effect.

To investigate these suppositions, the encounter of a biomass burning aerosol layer at high altitude, outside of cloud during flight F10 of CIRRUS-HL, provided an excellent opportunity to compare the PSDs of the CAS and CDP measurements at that time. The comparison is illustrated in Fig. 4.7. To enhance the comparability of the mean PSD between the instruments, only time instances where both probes measured at least one particle are considered (M. Krämer, personal communication, February, 1, 2023). Under purely aerosol conditions, the difference in N in the first two size bins between the two probes is almost an order of magnitude. Furthermore, the PSDs exhibit a similar decreasing profile, consistent with the observed trend in the first bins of the CAS PSD in Fig. 4.5.

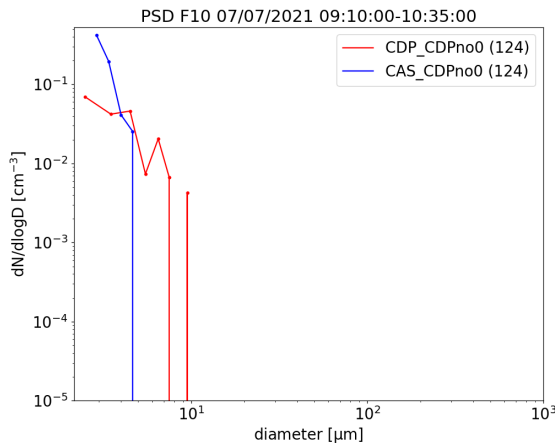


Figure 4.7: Particle size distribution of the CAS (blue) and the CDP (red) for a biomass burning aerosol layer out of cloud at $13 - 14\ \text{km}$. The number of samples in the selected interval is indicated in parenthesis.

This test provides robust evidence for the consistently increased N in the first bins of the CAS-DPOL. Given that only aerosol particles were present in the sampled air masses, it suggests a higher sensitivity to aerosol particles by the CAS-DPOL, aligning with the hypothesis put forth earlier. However, to fully validate this theory, it would be necessary to verify whether such large aerosol particles can also be found in cirrus sequences. Addressing this issue through aerosol measurements poses challenges, as comparisons between wing probes and aerosol inlets on the fuselage must be interpreted with caution. Up to this point, this analysis serves as an indication of potential aerosol particle

contamination in the first bins of the CAS.

DETECTION CRITERION

As mentioned earlier, the disagreement between the CDP and the CAS is not systematic; it emerges under specific atmospheric conditions. This implies that neither instrument consistently underestimates nor overestimates the ice number concentration due to a technical problem. To dive deeper into this phenomenon, combined data of the CIRRUS-HL campaign (comprising 22 flights) were analysed to identify and characterize the correlation between the number concentration in the CDP (N_{CDP}) and the CAS (N_{CAS}) based on the measured cloud properties. The process of combining data from various instruments into a unified data set is described in Section 4.3.

In Fig. 4.8, a correlation between N_{CDP} and N_{CAS} for all campaign data is presented, with a 10-second average to homogenize the cloud sequences. The corresponding ED of the 10-second average sequence from the combined distribution is indicated for three ED ranges. For the smallest ED ($< 200 \mu\text{m}$), there is a notable agreement, with most points aligned along the ideal 1:1 correlation. The highest concentrations ($N > 1 \text{ cm}^{-3}$) exhibit a slight systematic higher N_{CDP} with reduced spread along the ideal fit, regardless of the ED . This aligns with the earlier observations of better agreement in liquid clouds or contrail sequences, characterized by high N and low ED .

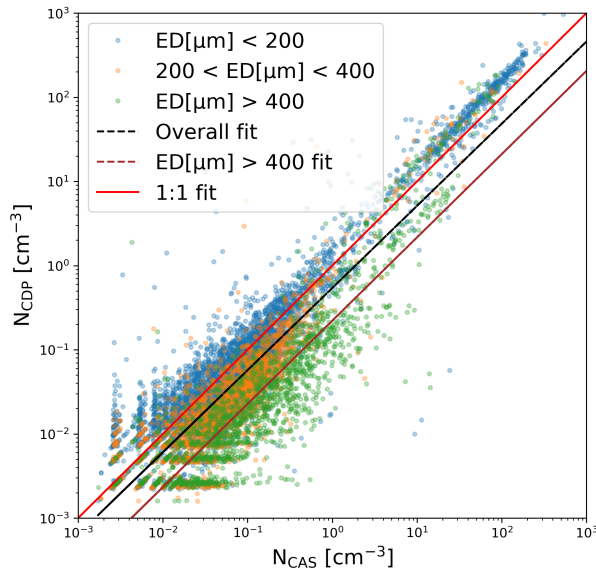


Figure 4.8: Correlation of the number concentration between the CDP and the CAS for different ED using combined distributions from all 22 flights, averaged over 10-second intervals.

Interestingly, in samples with ED larger than $400 \mu\text{m}$, N_{CAS} consistently and predominantly surpasses N_{CDP} . The fit of these samples (brown dashed line) shows a larger deviation from the 1:1 ideal fit compared to the overall fit (black dashed line). This analysis suggests a strong connection between the N retrieved by the scattering probes and

the overall cloud properties.

To investigate further this effect, the ratio N_{CAS}/N_{CDP} is calculated and its correlation with cloud properties N , ED , and IWC is examined in Fig. 4.9. In Fig. 4.9(a), distinct clusters emerge, with higher N corresponding to liquid clouds and contrails, and lower N associated with cirrus. The ratio N_{CAS}/N_{CDP} exhibits a positive correlation with ED , as indicated by the linear fit in Fig. 4.9(b). Notably, for $ED > 300 \mu\text{m}$, the ratio consistently surpasses the 1:1 relation. Analyzing the relationship with IWC in Fig. 4.9(c) reveals a combined effect of N and ED , with the most significant disparity between N_{CAS} and N_{CDP} occurring within the 0.001 to 0.1 g m^{-3} range. These findings are consistent with the studies conducted by Field et al. (2006) and Korolev et al. (2013a), which emphasized the significance of particle size in determining the extent of shattering. According to Field et al. (2006), when a significant proportion of ice crystals are large in size, the likelihood of shattering increases, irrespective of the overall particle concentration.

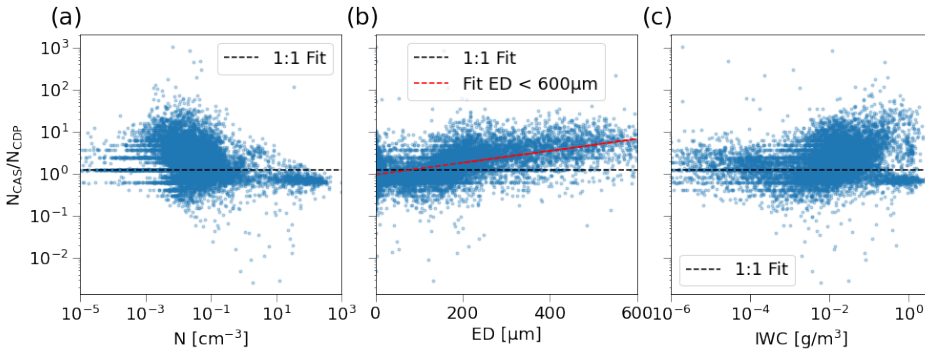


Figure 4.9: Relationship between the N_{CAS} to N_{CDP} ratio and overall cirrus properties during the CIRRUS-HL campaign, shown in 10-second averages: number concentration (a), effective diameter (b), and ice water content (c). The black dashed line represents the ideal 1:1 correlation between the CAS and CDP. Additionally, the red line in (b) denotes the linear fit of ED with the N_{CAS} to N_{CDP} ratio for $ED < 600 \mu\text{m}$.

In addition, Fig. 4.10 shows phase diagrams depicting the relationship between N and ED (a) and between IWC and ED (b) for three ranges of the N_{CAS}/N_{CDP} ratio. Samples are categorized as exhibiting either "good" (green) or "bad" (red) agreement based on a defined threshold value for N_{CAS}/N_{CDP} (3 for (a) and (b), and 5 for (c) and (d)). Values below 1, indicating a slight overestimation by the CDP, are displayed but not considered in the analysis as they are not the focus of this study. Given the qualitative nature of the study, determining a precise threshold for N_{CAS}/N_{CDP} is challenging. Consequently, the threshold of N_{CAS}/N_{CDP} is varied to observe its impact.

Firstly, it is evident that increasing the threshold results in a reduction of samples classified as exhibiting bad agreement, as expected. However, the range of ED where these instances occur remains unchanged, covering ED s from $100 \mu\text{m}$ and above. It is confirmed that the disagreement exacerbates with growing ED , but specifically for ED values exceeding $100 \mu\text{m}$.

Secondly, there a transition or coexistence zone between 100 and $400 \mu\text{m}$ is observed where either good or bad agreement may happen. Within the cirrus cluster ($N < 1 \text{ cm}^{-3}$),

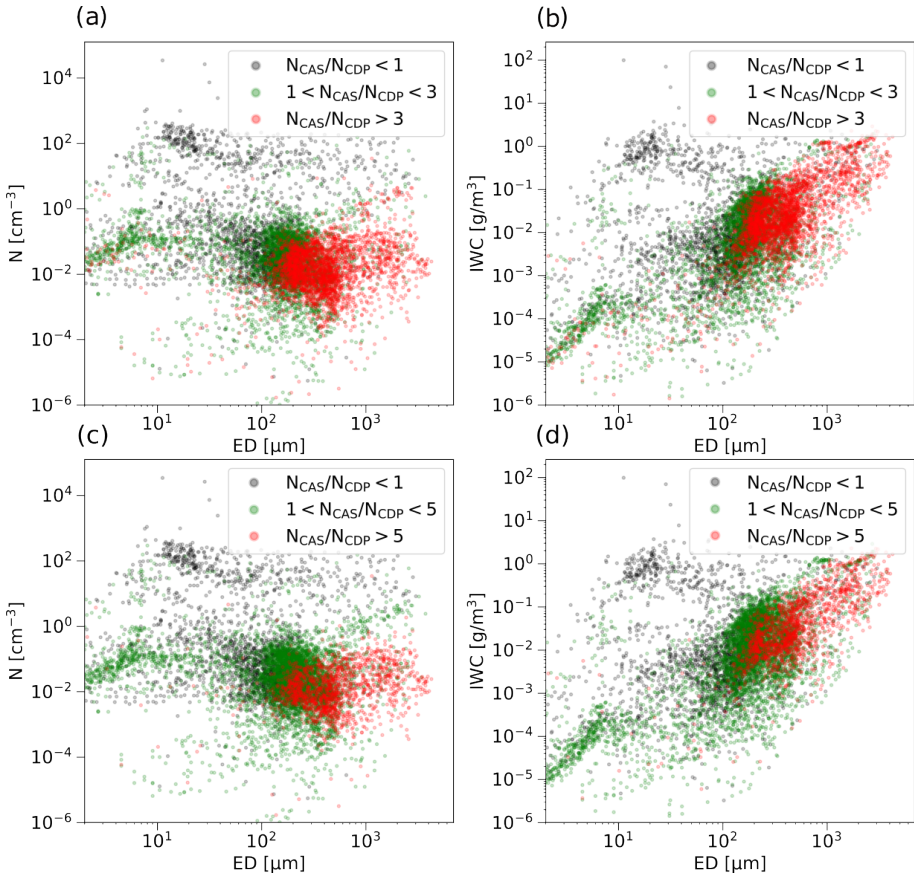


Figure 4.10: Phase plots depicting the relationship between number concentration (a, c) and ice water content (b, d) with the effective diameter of the 22 flights in 10-second averages. A threshold value of $N_{\text{CAS}}/N_{\text{CDP}} = 3$ (a, b) and $N_{\text{CAS}}/N_{\text{CDP}} = 5$ (c, d) is employed to distinguish between good agreement for lower values (green) and bad agreement for higher values (red). Data points with $N_{\text{CAS}}/N_{\text{CDP}} < 1$ are denoted in black, representing the infrequent overestimation of the CDP over the CAS.

the occurrence of bad sequences is independent of N and solely hinges on ED , as indicated by the horizontal displacement from good to bad sequences in Fig. 4.10(a, c). Based on these analyses, a reasonable criterion for identifying sequences with potential disagreement is $ED > 100 \mu\text{m}$ and $0.001 < N[\text{cm}^{-3}] < 0.2$.

SYSTEMATIC ANALYSIS OF CLOUD SEQUENCES

Revisiting the comparison of the PSDs, similar to the initial identification of disagreement between the two instruments, a focus is placed on various cirrus sequences from two distinct flights of the CIRRUS-HL campaign (F03 and F14). These flights were selected randomly as two representatives for mid-latitudes (F03) and high latitudes (F14), containing various sequences with cirrus and low clouds. Additionally, an analysis of the IAT histograms is conducted to exclude the possibility of shattering, and sequences are

classified according to the defined criterion ($ED > 100 \mu\text{m}$ and $0.001 < N[\text{cm}^{-3}] < 0.2$). Further examination involves inspecting the CIPG images to gain insights into particles shape. The inclusion of data from the CIPG in the PSDs allows for observing the whole particle size distribution, including the larger particles, to discern their relationship with the CAS-CDP disagreement. This final analysis combines different diagnostic methods for a comprehensive understanding of the observed phenomena.

In Fig. 4.11, two examples of sequences are presented, one illustrating good agreement (lower row) and the other showing bad agreement (upper row). It is crucial to note that the terms "good" and "bad" agreement are used theoretically, indicating whether they fulfill the criterion or not ("bad" agreement within the red shaded rectangle in (c) and (f)). Furthermore, Fig. 4.12 displays a representative sample of images corresponding to these sequences. The complete sequence analysis for both flights is shown in Figs. A.3 and A.4, and the corresponding images extracted from the sequences are included in Figs. A.5 and A.6. Subplots (c) and (f) from Fig. 4.11 illustrate the locations of the samples from the combined size distribution with respect to the defined criterion limits. This serves as an indication of the potential quality of agreement observed in the PSD for that sequence.

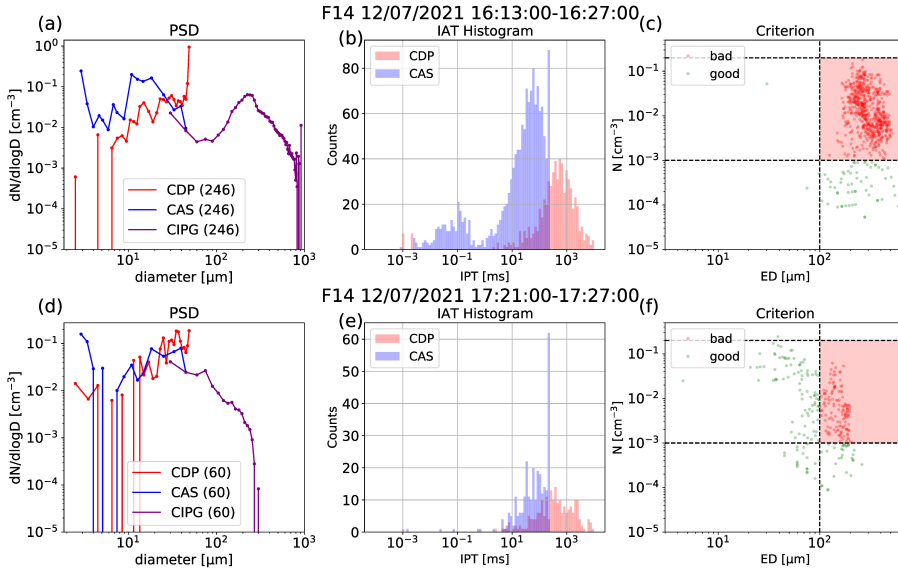


Figure 4.11: Analysis of example cirrus sequences from the flight F14, where the upper row represents a case of "bad agreement" and the lower row a "good agreement". Particle Size Distribution (PSD) of the CDP (red), CAS (blue) and CIPG (purple) with the number of samples in parenthesis (a, d). Interarrival time (IAT) histograms of the CDP (red) and CAS (blue) from the particle-by-particle information (b, e). Phase plots of N as a function of ED of the combined size spectrum (CDP-CIPGs-PIP) (c, f). Dashed lines indicate the limits of the criterion definition ($ED > 100 \mu\text{m}$ and $0.001 < N[\text{cm}^{-3}] < 0.2$), and the critical area is shaded in red. Green dots indicate points outside the critical area (good agreement), and red dots indicate points inside (bad agreement).

Upon examining all examples in Figs. A.3 and A.4, sequences characterized by numerous samples classified as "bad" under the criterion consistently exhibit less similar

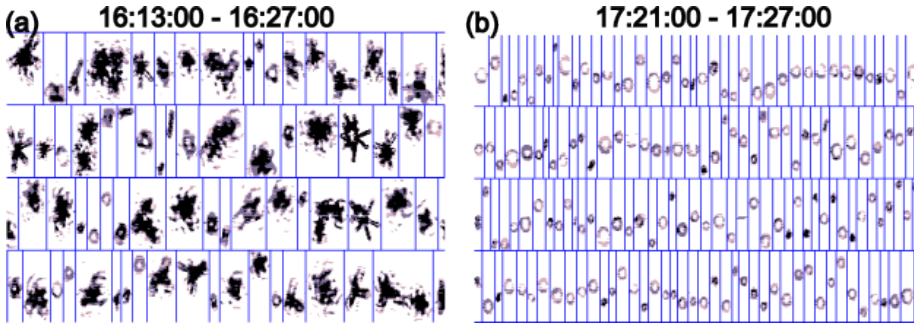


Figure 4.12: Extracts of the set of particle images from the CIPG corresponding to the sequences shown in Fig. 4.11.

4

PSDs, with higher N in the lower bins of the CAS compared to the CDP. Interestingly, these sequences also show a faster mode in the IPT histogram, indicative of shattering events, as seen previously. However, attempting to mitigate the impact of shattered particles by setting a threshold at 0.5 ms showed negligible improvement in the PSD (not shown here). The conclusion drawn is that although the disagreement is not directly caused by the shattered particles mode, the same mode is systematically observed in sequences with "bad agreement", suggesting that additional shattering may occur without being detectable through the IAT analysis approach, possibly resembling the scenario depicted in Fig. 4.6(c).

Regarding the aerosol influence discussed in Section 4.1.3, all the examples of Figs. A.3 and A.4 show the declining profile in the first three bins of the PSD, while the CDP show rather low or no concentration in those bins, and an increasing concentration with size, connected with the general profile of the cloud. Particular examples of this behavior are the PSDs in Fig. A.3(a) and (g).

A further important finding is extracted from particle size distribution and the ice crystal shapes derived from the CIPG images. The sequences with "bad agreement" are usually connected with a more pronounced second mode, which is located between 200 and 300 μm in the CIPG size distribution. Liquid origin cirrus are characterized by particle size distributions with a pronounced second mode, which contains more complex ice crystals than in in situ origin cirrus, where preferentially quasi-spherical or plate-like forms grow (V. Wolf et al., 2018). Bullet-rosettes are usually found between -40 and -60°C (within the liquid origin cirrus temperature range) according to Bailey and Hallett (2004). Complex shapes of ice crystals are observed in the bad sequences, as in Fig. 4.12 (or Figs. A.5 and A.6), while smaller and quasi-spherical forms are rather found in good sequences.

The sequences identified as problematic are strongly correlated with the complex shapes of larger ice crystals that fall outside the measurable range of the scattering probes. It is hypothesized that these crystals are more susceptible to breakage. These breakup processes may occur, particularly at the borders or interior surfaces of the CAS inlet, or due to pressure changes inside the tube. Previous studies have highlighted the significant influence of particle size and shape on the occurrence of shattering events

(e.g., McFarquhar et al. (2007) and Korolev et al. (2013a)). The fast mode observed in the IAT histograms is considered a part of this breakup process.

The drawn hypothesis further suggest that not many fragments result from the breakup, preventing the formation of a cluster of numerous small particles. Instead, fewer and larger pieces are produce, getting embedded in other natural particles, making it challenging to distinguish between them (as illustrated in Fig. 4.6(c)). In-depth investigations by Vidaurre and Hallett (2009) into breakup processes of ice particles indicate that the number of resulting fragments largely depends on the particle size, shape and impact angle. McFarquhar et al. (2007) identified a similar mismatch between CAS and CDP data in ice clouds. They explored whether optics of CAS and CDP had different responses to aspherical particles but found no noticeable differences, suggesting the shattering in the CAS inlet tube could be the cause of the increased number concentrations in the CAS. Schlenczek (2018) conducted an intercomparison for a holographic imaging probe (HALOHolo) using measurements from the RACEPAC field campaign and found better agreement with the CDP than with the CAS.

4.2. OAPS METHODS

The working principle of the OAPs was described in Chapter 3. In Section 4.2.1 all the necessary steps to postprocess the raw image data and corrections made are described and discussed. Finally, the calibration of both instruments is briefly presented in Section 4.2.2. Additionally, the reader can get an overview on how the OAP data are pre-processed and on the details of the decompression algorithm, which I developed for monoscale (e.g. PIP) and grayscale (CIPgs) DMT LLC probes (Appendix B).

4.2.1. IMAGE DATA PROCESSING: FILTERS AND CORRECTIONS

The image data decompression provides the raw PbP data, i.e. mainly the timestamp and particle counter of each recorded image, and the shadow image itself in form of a matrix of ones and zeros for monoscale, and 0 to 3 for grayscale images (3 represents the image background or fully illuminated, and 2 to 0 stands for grayscale level 1 to 3, respectively). In the Appendix B and in the general case, the grayscale levels are specified as 25%, 50%, and 75% of shadow intensity. The images I show in the following were captured using different levels: 35, 50 and 65, in an attempt to minimize noise (the reason will be explained later in this section).

Different operations and calculations need to be performed with the set of raw images in order to generate a data set with values per second of the cloud microphysical properties defined in Section 3.3. Ideally, the imaging probes only record "valid" images, which correspond to ice crystals with a shape fully retrieved. However, electronic noise can interfere with real particle recordings or generate artificial images which are not real particles and need to be filtered. In addition, as described in Section 3.2.1, if the particles are at any distance from the object plane, the shadow image appears larger and less sharp due to diffraction. The images may be so distorted that it is not possible to derive the size correctly or to recognize their shape. As it was shown in Fig. 3.6, the diffraction patterns (diffraction fringes) of spherical particles are known and the size can be accordingly corrected. The way of each ice crystal with a different shape and orientation

diffract is uncertain.

Fig. 4.13 shows a variety of ice crystal images collected in ice clouds at different temperature and humidity regimes. Bullet rosettes and columns (a)-(d) are frequent at high ice supersaturation since many sites become active and the crystalline structure grows in different preferred directions (Bailey & Hallett, 2004). Out-of-focus rosettes have wider bullets and can present some small bright spots. The images of panels (f) and (g) show plate-like crystals where different diffraction patterns with large bright parts are present, and the edges of the crystal are no longer well distinguishable. The orientation of the plates plays a major role in both the diffraction pattern and the size of the projection into a 2D image, where, in the extreme case, they could be considered as columns. Graupel particles, such as (h) or (i) have an irregular form, and present a variety of diffraction patterns as they move away from the focus, e.g. (l)-(n). Ice crystals can also stick together forming aggregates, either of columns, bullet rosettes (e), graupel particles (j) or a mix of particle habits (k).

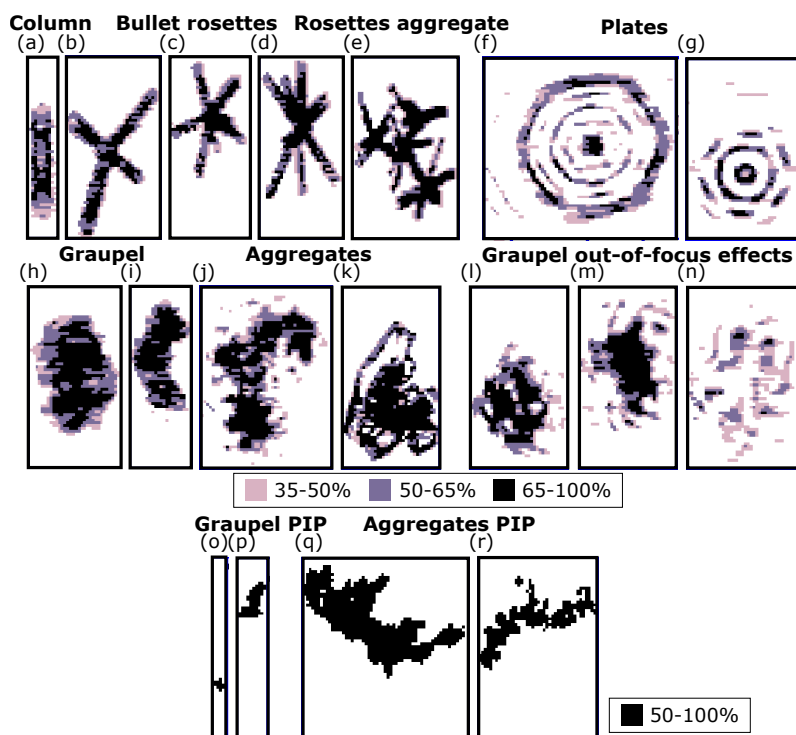


Figure 4.13: Examples of ice crystals images from the CIPG. Bullet rosettes with 4, 6, 8 bullets are shown in (b)-(d), respectively. (e) Aggregated bullet rosettes or coincidence. Ice crystals of similar size are shown in (o) and (p) seen with the PIP, while (q) and (r) include larger aggregates of several millimeters.

The observation of the different shadow projections is easier with the grayscale function of the imaging probes. The PIP images of Fig. 4.13(o)-(r) are in monochrome, where only background or shadow (from 50 to 100% shadow intensity) are visible. This probe, however, is capable of recording images of very large particles, exemplified by the aggre-

gates in (q) and (r), each measuring over 3 millimeters in length.

Fig. 4.14 provides a comprehensive overview of the different steps involved in processing image data, beginning with raw data in the form of a PbP data set. In the following part, detailed explanations of the various filters, corrections, and calculations that have been applied will be provided.

The first filter applied to CIPG image data aims to eliminate "repeated" particles (particle entries, which were written several times by different processors) resulting from a task assignment issue in the cluster, where overlaps occur, and particles may be read and saved multiple times. This issue can be easily identified by comparing the particle counter and timestamp, which should not be the same for non-repeated particles. Since processing image data from the PIP is considerably faster than from the CIPG, it is typically done locally with 8 processors, mitigating the occurrence of this anomaly.

Most of the functions used during the image post-processing were designed and implemented by Kirschler (2023) for the monoscale images of the 2D-S (Stereo) Probe (2D-S). I implemented the grayscale filter and adapted the functions for a grayscale mode, with additional parameters for the different grayscale levels. I also modified the filters to adjust to the CIPG and PIP images characteristics, including the necessary changes and additions to deal with grayscale images.

FILTERS

The images presented in Fig. 4.15 offer a comprehensive summary of the main types of images that are filtered during the image data processing. The different artifacts and filters applied are outlined in the following paragraphs.

The grayscale filter acts by excluding particles that fall below a predefined grayscale level. This filter allows to restrict the DoF, ensuring that only particles with a minimum of one pixel at grayscale level 2 (50% shadow intensity) are considered. Moreover, it provides the flexibility to further refine the selection by exclusively retaining particles with at least one pixel at grayscale level 3 (75% nominal shadow intensity). Increasing the grayscale level threshold ensures a higher accuracy of the particles' sizing but reduces the SA and with it, the number of accepted particles and the counting statistics (S. O'Shea et al., 2019; S. O'Shea et al., 2021) (see also Section 3.2.1). Only particles with at least one pixel at grayscale level 2 are considered and sized in this work.

For filtering grayscale level 1 images, they are excluded if none of the elements in their image matrix are equal to or less than 1 (zeros represent the third grayscale level and ones represent the second grayscale level). Examples of images exclusively at grayscale level 1 are shown in Fig. 4.15(a)-(d). Ideally, only images resampling (d) are intended to be included in this set. These images correspond to particles too distant from the object plane whose shadow intensity is minimal (out-of-DoF particles). However, a systematic issue in the central elements of the diode array, referred to as a "stuck bit", has been identified for the CIPG used in this work. A diode array element is triggered continuously for a brief yet variable time period, as evidenced by the varying lengths of the images in the first panel.

Whenever an element is triggered, image recording initiates, resulting in a substantial number of recorded images that are essentially noise. The problem typically manifests in the form of the images in (a), but it can also appear as (b) or (c), with a shifted

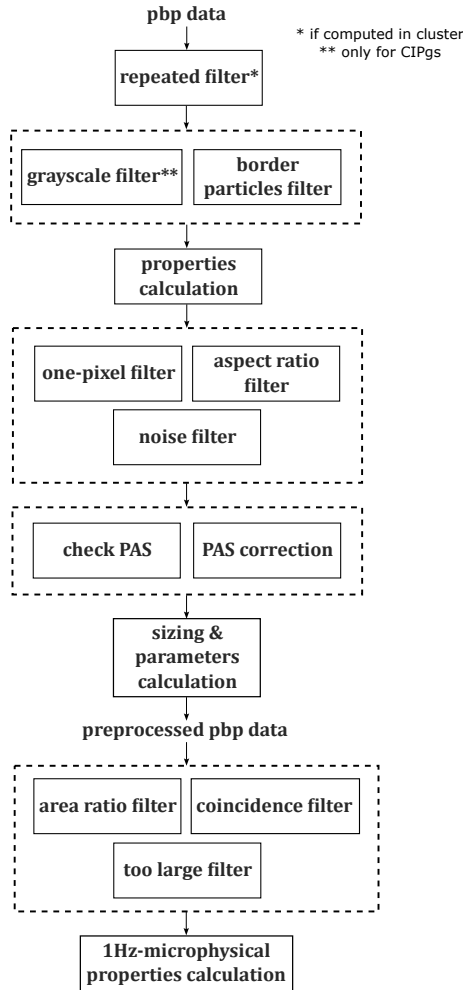


Figure 4.14: Workflow for processing image data to ultimately calculate cloud microphysical properties.

position of the stuck bit or additional triggered elements. This problem has undergone thorough laboratory testing and the observation of this issue mainly in the first grayscale level (between 25% and 50% shadow intensity), motivated the decision to adjust the grayscale levels to the ones used in this work (35%, 50%, and 65%). By raising the shadow intensity level the number of images recorded is also reduced but the problem was still present. It means that the element is triggered with a shadow intensity between 35 and 50%.

As discussed in Section 3.2.1, the all-in method stands as the sole viable option for characterizing the effective array width in ice particle measurements due to the impossibility to determine the ice crystal center or reconstruct its non visible part. Consequently, the utilization of this method necessitates the exclusion of all particles that are

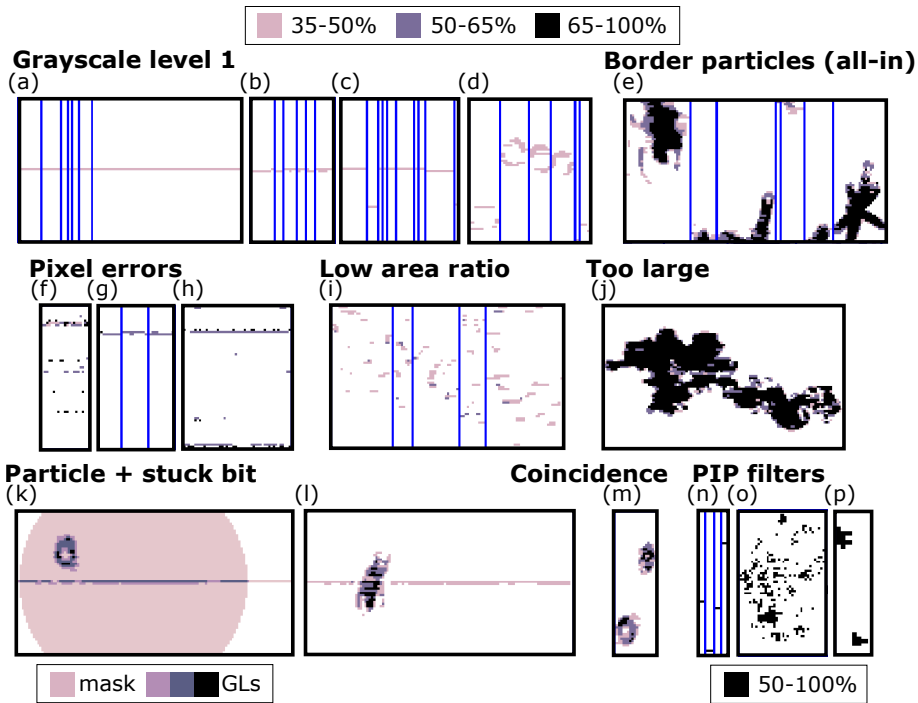


Figure 4.15: Examples of image errors mainly from the CIPG. (a)-(d) Images filtered by grayscale threshold at 50%, only (d) contains real particles. (e) Border particles filtered out for all-in method. (f)-(h) Pixel errors in all grayscale levels. (i) Images with low area ratio (e.g. multiple out-of-focus particles). (j) Particle larger than photodiode array. (k) filtered particle with wrong diameter due to a stuck bit in grayscale level 2 (50%). (l) non-filtered particle because of stuck bit at grayscale level 1. (m) Two particles per image (coincidence). (n) PIP pixel errors. (o) PIP image with low area ratio. (p) Coincidence in the PIP.

not entirely captured within the diode array, as shown in Fig. 4.15(e). For this purpose, images where the first or last element is obscured in the array are classified as "border particles" and subsequently excluded. Additionally, the grayscale level of these border particles can be specified. This approach ensures that images with triggered edge elements at grayscale level 1, when sizing particles considering only levels 2 and 3, do not require filtering out (as exemplified by the particle in Fig. 4.16).

The image properties calculation is performed after applying these two filters (as indicated in Fig. 4.14). The initial filtering process helps eliminate a significant number of images and prevents unnecessary further calculations with them. Most of the calculated properties are comprised in Fig. 4.16. The height and width are computed from either the x or y coordinates of the first and last grayscale pixels in the image, and these values are also stored within the properties. Additionally, the aspect ratio is calculated as the ratio between the width and height. The property "surface" represents the area, defined as the number of pixels above a certain grayscale level, with S_1 , S_2 , and S_3 denoting the number of pixels at grayscale levels 1, 2, and 3.

Each property is given for the three grayscale levels. For example, properties with

suffix "25" take into account all three grayscale level pixels, while properties with suffix "50" consider pixels at the second and third grayscale level, and suffix "75" includes only pixels at the third level. While the grayscale level 1 pixels are not utilized for sizing the particles in our case, having information about the number of pixels at this level can still be valuable for filtering or classification purposes.

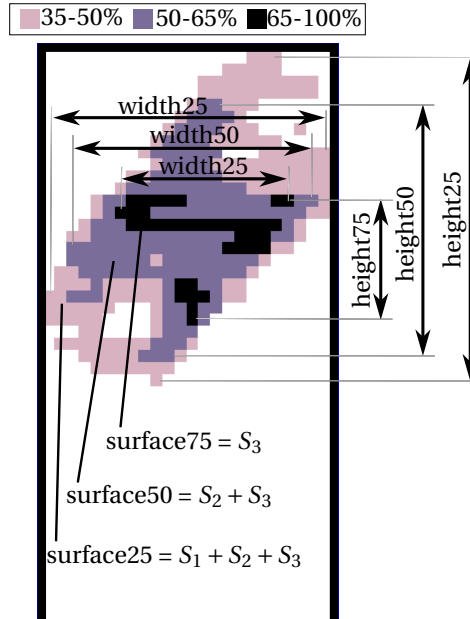


Figure 4.16: Summary of the main grayscale image properties. S_1 , S_2 , and S_3 correspond to the number of pixels at grayscale levels 1, 2, and 3, respectively.

With the help of these properties, additional filters can be calculated and further artifacts can be identified and eliminated: one-pixel, aspect ratio and noise filters.

The one-pixel filter eliminates images containing only one pixel at the sizing grayscale threshold (at grayscale level 2, in this case). The uncertainty of this type of images is considerable, given that one pixel represents the minimum unit of information in the image. It is challenging to determine whether a pixel corresponds to a genuine particle within the size range of 7.5 and 22.5 μm (or between 50 and 150 μm for the PIP), or if it is simply a result of electronic failures triggering an element. While this exclusion results in a loss, the preceding instrument in the size range typically provides better coverage for the excluded size range.

The aspect ratio filter excludes particles whose width is larger than six times the height (width50 for sizing grayscale threshold 2). With this filter, for example, noise such as stuck bit in higher grayscale levels can be filtered out.

The noise filter includes different filters to eliminate further artifacts. These are very instrument specific and even campaign specific, since different ambient conditions and aging of the instrument can lead to different pixel problems (e.g., pixel errors in Fig. 4.15(f)-(h)).

Before proceeding to find the size of the valid images, it is necessary to correct their width. As explained in Section 3.2.1, the appending of the image slices occurs at a rate proportional to the airspeed seen by the probe (probe air speed (PAS)). This airspeed is measured by a pitot tube attached to the instrument, and even though it is warmed by a heater during the flight, it is susceptible of suffering icing. In this case, the PAS readings are not reliable, and the appending of image slices would be troubled, leading to a loss of information. To avoid this, it is preferable to set a fixed PAS, greater than the maximum expected value of PAS. During post-processing, the ratio of real to fixed PAS is determined, and the images can be narrowed accordingly.

As a first step, the PAS and true air speed (TAS) are compared, as shown in Fig. 4.17. The PAS should follow the same profile as the TAS, but with an offset due to the different pressure field under the wings of the aircraft, where the cloud probes are located. In the example of Fig. 4.17, there was a failure in the PAS retrieval. This part was corrected by calculating the ratio of PAS to TAS for the previous flight segments. The green line in the graph indicates the fixed PAS set to 160 ms, always higher than the real PAS. Subsequently, the ratio of real PAS to fixed airspeed can be computed for each particle.

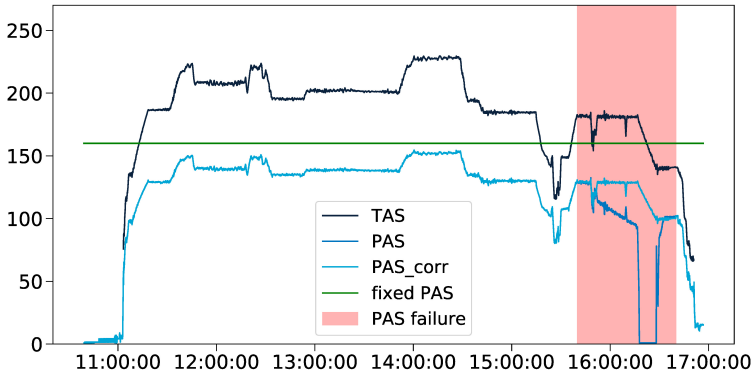


Figure 4.17: Example of airspeed measurements by the aircraft systems (TAS) and the pitot tube in a probe (PAS), with an erroneous PAS reading in the last flight section. Additionally, the corrected and the fixed PAS for the same example flight are included.

The function *image_pas_correction* applies a list of ratios with the same length as the set of images and performs the image transformation. The value of the image background also needs to be specified, since it varies between monoscale (1) and grayscale (3). An example of images before and after the PAS correction is illustrated in Fig. 4.18. After the correction, the image properties are recalculated, since as they undergo changes due to the correction processes. Likewise, the filters defined in the previous step are reapplied.

With the definitive dimensions of the images established, the particles can be sized using the circle fit method described in Section 3.2.2. The key parameters calculated during the circle fit method are the particle's diameter, crucial for the calculation of microphysical properties, and an internal diameter or the diameter of the Poisson spot. Derived from these primary quantities, various parameters such as surfaces, area ratios,

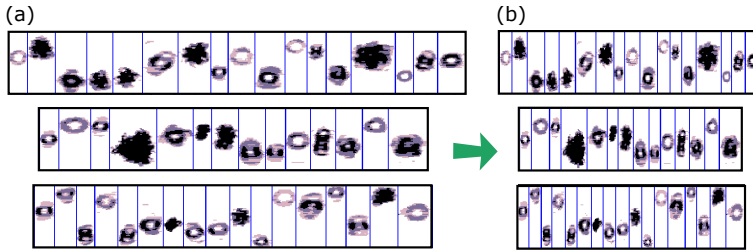


Figure 4.18: Example of artificially elongated particles (a) and corrected images (b) based on the real-to-fixed PAS ratio. Group of particles was selected according to the criteria: ratio < 0.6 and width $_{50} > 15$.

and diameter ratios are computed. These additional metrics play a significant role in further filtering and classifying the images. This collection of particles, each with an assigned size, corresponds to the preprocessed PbP data.

In the final filtering step, images such as those shown in Fig. 4.15(i)-(k) and (m) are excluded, addressing issues that could not be resolved in previous stages due to their specific image properties. Images that are highly blurred and faint, identified by a low circle area ratio (< 0.06), are eliminated. Additionally, excessively large images with diameters surpassing 62 pixels are excluded, considering the size resolution constraint of 62 pixels in the vertical direction. The low area ratio filter also includes images like (k), where the stuck bit is not only at grayscale level 1. In this case, the calculated circle fit, which encloses pixels at 50% shadow intensity, is much larger than the actual size of the particle. Unfortunately, there is currently no method available to correct this issue, necessitating the exclusion of such images. However, Fig. 4.15(l) presents a different scenario where there is a particle with a stuck bit, but it is only at grayscale level 1 and does not distort the circle fit calculation; hence, it is retained. Coincidence events (see Section 3.1.3) can also pose challenges and also apply to OAPs, as shown in Fig. 4.15(m). There is no method available to retain such particles, and therefore, they are filtered as well. However, not all of them are filtered; specifically, those where the circle radius ratio is > 0.6 and the ratio $(\text{surface}_{25} - \text{surface}_{50})/\text{diameter}$ is > 0.3 , are excluded. The rest, which are closer together within the image, are treated as a larger particle with a similar size to their separate contributions.

The last part of the OAP image processing is the microphysical properties calculation using the definitions described in Section 3.3. It should be noted that the calculations are first done particle-by-particle and not per bin. For instance, the sample volume per second is calculated as the sum of each particle's sample volume within a second, or the *IWC* is also calculated summing the specific mass of each particle. As seen in the previous chapter in Section 3.2.1, the sample volume depends on the DoF, which in turn, is dependent on the grayscale threshold and the particle's diameter, and on the L_{eff} , which depends on the selected definition and the particle's diameter. Effectively, the sample volume per second is assumed as the standard or maximum sample volume and later, while computing each property, the computation is weighted applying a ratio of standard sample area to reduced sample area of each particle.

SHATTERING

Shattering refers to the artificially increased number of small particle counts from the breakup of larger particles into many small fragments before crossing the laser beam. This issue was previously mentioned in Sections 3.1.3 and 3.2.3 in relation to the uncertainties associated with the instruments, and a correction must be applied to the definitive set of particles before computing the final microphysical properties.

Field et al. (2003) evaluated the overestimation of small particles in mid-latitude cirrus by factors between 2 or 3 and 5 or 6. They analysed the interarrival time (IAT) of the natural particles and the artificial fragments, finding that shattered parts could be recognized by having a shorter transit time than natural particles. In theory, an ice crystal would impact and break into many smaller pieces. Most of these pieces would travel together in a cluster and reach the sample volume at a higher frequency (higher concentration and shorter interarrival times) than naturally distributed cirrus ice particles would. In these cases, the IAT frequency distribution would show two distinct modes: at around 0.01 and 0.0001 s, depending on the cloud properties and instrument type, as shown in the schema of Fig. 4.19(a).

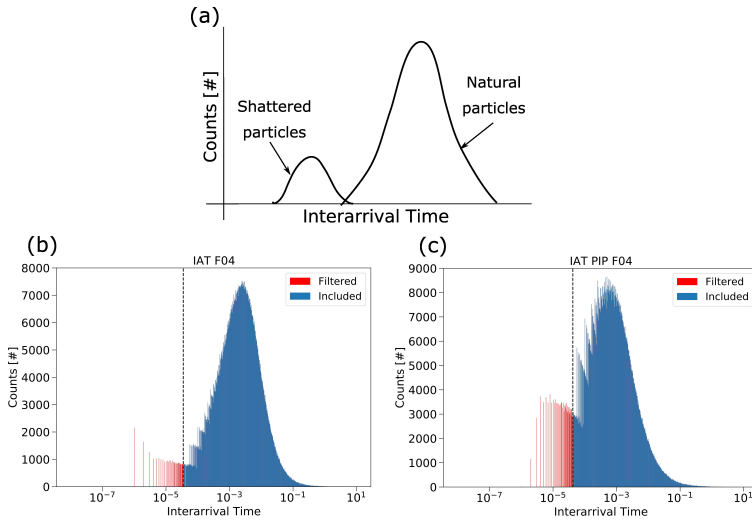


Figure 4.19: Sketch of an interarrival time histogram with an intersection highlighted in red between the modes of natural particles and shattered particles (a). Examples of interarrival time (IAT) histograms from a single flight for the CIPG (b) and the PIP (c).

Shattering events can be identified and filtered based on the IAT. Filtering out particles with shorter IAT than a threshold level can potentially reduce the impact of shattering in the number concentration (Korolev & Isaac, 2005; Field et al., 2006). For the DMT OAPs, the IAT is not directly provided; therefore, I calculate it using the difference between the particle's timestamp.

Fig. 4.19(b) and (c) illustrate the filtered IATs applying a threshold of $3.5 \cdot 10^{-5}$ s and $4.2 \cdot 10^{-5}$ s for the CIPG and PIP, respectively. The shattered particles modes are not fully represented since the last unit of the timestamp is in micrometers. In general, the PIP

is not known to be much affected by shattering, since shattered particles are typically below the pixel resolution of 100 μm . The CIPG is more prone to shattering due to its size range, but the arm tips have the modification of the Korolev tips to physically reduce shattering artifacts (Korolev et al., 2013b).

EXCURSION TO DEAD TIME LOSSES

Significant efforts were dedicated to the investigation of dead-time and particle losses in the OAPs (in collaboration with Manuel Moser). Previous experience with the software System for OAP Data Analysis (SODA; Bansemer (2023)) revealed an anomalous high incidence of "missed" particles, resulting in markedly brief active times and reduced sample volumes, and gaps in the concentration, or the presence of huge and implausible values. This issue motivated to better understand the concept of missed particles and dead time, with a focus on identifying their sources and influential factors.

The period during which the probe acquires and stores data is referred to as the *active time*. However, brief intervals, termed *dead time*, occur when the instrument deals with an exceedingly high data rate that outperforms the capabilities of the electronics (Baumgardner et al., 1985; McFarquhar et al., 2017). During these episodes of overload, the instrument cannot store information simultaneously, resulting in data loss (Gurganus & Lawson, 2018). Calculating the concentration under the assumption that the entire sampling period is all effective time leads to an underestimation. Hence, the sample volume must be adjusted by subtracting the dead time, resulting in a shorter effective time. The 2D-S can directly record when the probe is in overload, enabling precise tracking of dead time, and the sample volume is adjusted accordingly. In contrast, the CIPG lacks this capability, requiring estimation of dead time by accounting for the number of missed particles (McFarquhar et al., 2017; Gurganus & Lawson, 2018).

The concept of missed particles is also introduced in Appendix B. The CIPG features an internal counter, which keeps track of the number of particles sampled. This counter increments each time a particle is detected by the photodetectors, even at the 25% grayscale level, in the case of a grayscale probe. This is crucial because, although one may choose to store only images with at least one pixel at 50% grayscale, the counter still considers particles below this threshold, which are detected but not saved. Calculating missed particles involves comparing the Particle Counter, stored in the particle header, between consecutive particles (see Appendix B). Calculating the difference after filtering particles, however, can lead to erroneous values. In particular, the SODA software had a bug in this calculation. It applied the grayscale filter first, among other filters, and then computed the missed particles. For every particle where the missed particles (between that particle and the previous one) were not zero, its interarrival time was summed up and then subtracted from the active time. In the following, I highlight the inaccuracies of this method and strongly advise against its use.

The example of Table 4.1 consists of seven fictitious particles where the "Maximum GL" column indicates whether the particle has at least one pixel at 75% shadow intensity, 50%, or all pixels at 25%. In this scenario, all three grayscale level particles were saved in the Imagefile. After reading the particles and obtaining the particle counter, it is possible to compute the missed particles. In only one case, there was one missed particle between images 5 and 6, and there is no way to determine at which grayscale level it occurred.

Table 4.1: Academic example of a fictitious set of grayscale image headers for missed particles calculation.

Index	Max. grayscale level	Type	Particle Counter	Missed
0	75%	Particle	25688	0
1	25%	Particle	25689	0
2	25%	Stuck bit	25690	0
3	75%	Particle	25691	0
4	50%	Particle	25692	0
5	25%	Stuck bit	25693	0
6	50%	Particle	25695	1

Now, let's consider a scenario where particles at 25% were not saved by setting the Imaging Threshold at grayscale level 2 (value of 1 in the .ini file), or that the grayscale filtering was applied first before computing the missed particles. This example is illustrated in Table 4.2 using the previous set of images, where only four are left. Since the instrument also detects the images with no pixel below grayscale level 1, the particle counter is incremented. The posterior calculation of missed particles results in a total of four missed particles, while in fact, only one was missed. The calculation of dead time and, consequently, adjustment of the sample volume would be incorrect. Therefore, the conclusion is that missed particles can only be effectively calculated if all particles are saved (Imaging Threshold set to 2 in the .ini file) and no filtering is performed before the missed particles calculation.

Table 4.2: Same example as in Table 4.1 but prefiltered at 50% grayscale threshold.

Index	Max. grayscale level	Type	Particle Counter	Missed
0	75%	Particle	25688	0
1	75%	Particle	25691	2
2	50%	Particle	25692	0
3	50%	Particle	25695	2

However, depending on the instrument, there exist a further problem that hinders the correct calculation of missed particles. In the set of Table 4.1, not all images correspond to real particles, there is also noise in form of stuck bits at grayscale level 1, in this example. The experience with our actual CCP-CIPG is that many images of stuck bits are generated, in both cloud sequences and clear sky. In this situation, it would be hard to say if the missed particle between images 5 and 6 of Table 4.1 is a real particle or stuck bit. Since most of the stuck bit images do not have any pixel above 25% shadow intensity, filtering the first grayscale level and calculating the missed particles would give an extremely and unreal amount of missed particles. It also explains why such a high amount of missed particles was obtained with the SODA software.

The best solution for estimating dead time from the Imagefile would be to store all particles, including the ones below the 50% shadow threshold, to have a real overview of all images missed. In the case of a noisy instrument, it would be necessary to filter stuck bit images and estimate a percentage of incidence in different conditions, since a test in the lab might not be representative. The drawback is the large amount of data that

needs to be stored and processed to be finally filtered out. In favour of the instrument computer performance and processing time, it would be preferred to store only images from 50% shadow intensity. If sufficient estimates are calculated in different conditions, it could be possible to limit the data storage to grayscale threshold 2 and still adjust the sample volume. A further solution is suggested by Gurganus and Lawson (2018), who propose an expression to calculate the dead time using the total particle count provided by the 1D file and the number of images. However, it assumes that the total count in the 1D file comprises also the missed particles and there is no way to identify stuck bits in the 1D file.

For this thesis, no dead time correction has been applied to the data. According to Gurganus and Lawson (2018), the CIPG goes to overload and creates dead time for concentrations higher than 0.35 cm^{-3} . In general, the particle concentration in cirrus is, at most around that value, or below. The percentage of missed particles was checked for two representative flights and found that in most of the cases, it was about 1% of the total particles per second.

4.2.2. CALIBRATION

The size calibration of the OAPs is carried out using a spinning disc provided by DMT LLC, following the instructions described in DMT LLC (DMT, 2017c). This device is positioned between the instrument arms and consists of a glass disc with spherical opaque images. As the disc rotates and is illuminated by the laser beam, it generates a stream of simulated shadow droplet images. Since the diameters of the dots are known, the spinning disc is suitable for calibrating the pixel resolution of the OAPs and verifying if it matches the specifications indicated by the manufacturer. Additionally, it can be used for troubleshooting and monitoring the instruments before and after field campaigns.

The size of the dots on the spinning disc and their opacity vary depending on the instrument for which the disc is designed. Examples of sequences of dots from the CIPG and PIP spinning discs are shown in Fig. 4.20. The CIPG spinning disc features a pattern of six dots repeated twelve times around the disc, with the following sizes: {50, 125, 250, 500, 1000, 2000} [μm]. As depicted in Fig. 4.20(b), the dots exhibit varying opacities, producing shadow images at three grayscale thresholds. In contrast, the PIP spinning disc has opaque dots with sizes of {250, 500, 1000, 3000, 5000} [μm].

Accurate adjustment of the spinning disc is crucial to avoid misrepresentation of dot sizes, preventing erroneous pixel resolution settings. The images must be precisely centered in the laser beam, as in the examples of Fig. 4.20, except for (d), which is an example of an unusable calibration, where the disc is not properly fixed in the mounting and probably oscillates, affecting the quality of the images. In addition, the disc should be centered between the arms to prevent diffraction-induced enlargement of the dots shadow images, as explained in Section 3.2.1. Finally, the applied PAS must be adjusted to ensure that the dot images neither appear shortened (too short PAS) nor elongated (too large PAS).

As explained in Section 3.2.2, for calibration purposes, the particle size is the diameter in the x direction, D_x (or height), as indicated in Fig. 4.20(e). To ensure consistent sizing across all calibration data and flight campaign data for the CIPG, sizing of grayscale dots is carried out using pixels at least at grayscale level 2. Due to imperfect shadow im-

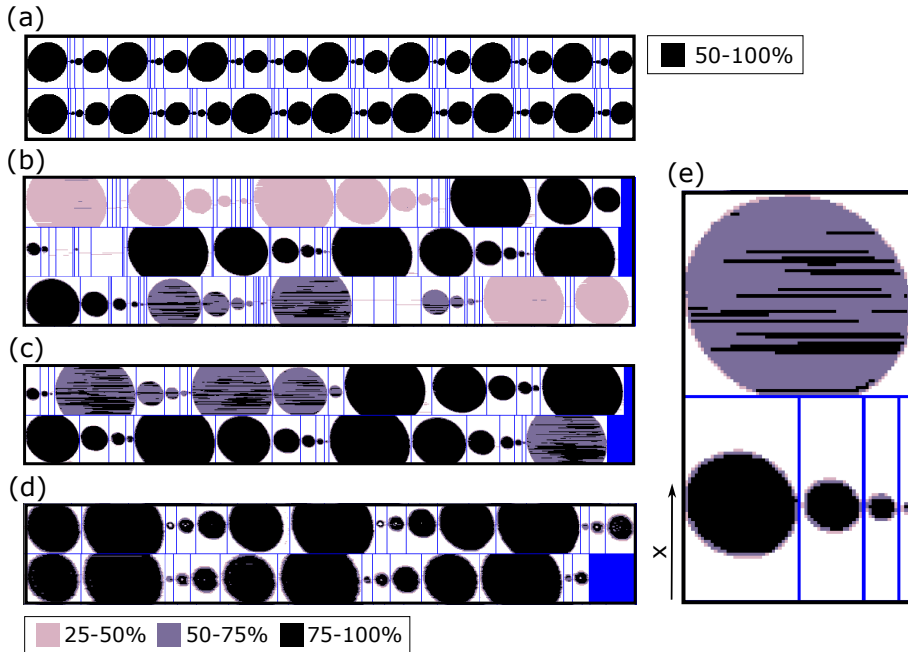


Figure 4.20: Calibration shadow images displaying various patterns, including a repeated arrangement of monoscale dots with theoretical sizes of 250, 500, 1000, 3000, 5000 [μm] employed in (a), and a repeated pattern of dots in grayscale levels 1, 2, and 3 with theoretical sizes 50, 125, 250, 500, 1000, 2000 [μm] employed in (b)-(e). A snapshot of the dots images stored by the CIPG is shown in (b); (c) corresponds to a snapshot of the same calibration but after filtering at grayscale level 3; in (d) a different calibration is shown using grayscale levels 35, 50, and 65%, with a disc misalignment between the arms. Additionally, a zoomed-in view of the shadow images of the grayscale dots is presented in (e).

ages from the grayscale disc dots at 25, 50, and 75%, as evident in Fig. 4.20(b), and the presence of pixels at 50% shadow intensity in dots at grayscale level 1, filtering is necessary. The filtering ensures that sizing at 50% includes only images with at least one pixel at grayscale level 3, guaranteeing correct diameters and avoiding sizing the grayscale level 2 lines contained in the dots at grayscale level 1 (as in Fig. 4.20(b)). A sample of the accepted particles after filtering is depicted in Fig. 4.20(c), where noise is also effectively avoided. The images in Fig. 4.20(d) represent another calibration that was not utilized due to misalignment issues, leading to poorly defined and larger dots. In this case, the grayscale levels were 35, 50, and 65%, as during the flight campaign. It seems that the dots at grayscale level 2 obscure above 65% because there is no difference between the dots at grayscale level 2 and 3 with the altered grayscale level thresholds. It is noteworthy that parts of the dots at grayscale level 2 are obscured above 75%, as dark pixels are visible in the images of Fig. 4.20(b) and (c).

The calibration assessment involves comparing the expected sizes of dots and the measured sizes, assuming nominal pixel resolution of 15 (CIPG) or 100 μm (PIP). While ideally, the dots would exhibit a constant measure of diameter, small deviations result in imperfect centering and a loss of definition in the particle edge, as depicted in the zoom

in of Fig. 4.20(e). Consequently, a distribution of diameters is obtained for each expected size, with broader distributions indicating poorer alignment and larger deviations. The mean and standard deviation of each distribution are calculated and summarized in Table 4.3, alongside the number of samples per size.

Table 4.3: Summary of the calibration of the CIPG on 11 June 2021 from 10:30:05 until 10:30:35 UTC filtering at GL3 and the calibration of the PIP calibration on 30 July 2021 from 06:45:00 until 06:48:12. The number of samples, mean (μ), and standard deviation (σ) of the distribution for each expected size are provided.

Exp. Sizes [μm] CIPG / PIP	CIPG			PIP		
	N samples	μ [μm]	σ [μm]	N samples	μ [μm]	σ [μm]
50/200	3811	49	11	94116	186	34
125/500	6438	125	11	93842	458	49
250/1000	6814	245	9	93282	960	48
500/3000	6613	500	8	88383	2931	46
-/5000	-	-	-	88310	5048	49

The comparison between expected and measured sizes can be visualized by plotting them against each other, and a linear regression fit function of the form $f(x) = mx$ can be calculated, as illustrated in Fig. 4.21. The new probe resolution would be then determined by dividing the nominal resolution by the slope of the regression line. It is worth noting that the two last dots of the CIPG spinning disc have been excluded from the regression since their sizes exceeded the instrument's size range. The nominal pixel resolution of both instruments (15 and 100 μm , respectively) is adopted, as the calibration results indicate minimal deviations in both cases.

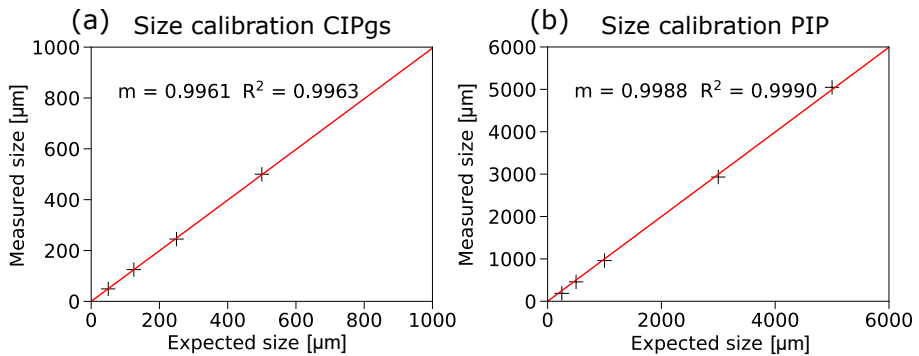


Figure 4.21: Linear fit regressions of the CIPG calibration on 11 June 2021 from 10:30:05 until 10:30:35 UTC at GL3 (a) and of the PIP calibration on 30 July 2021 from 06:45:00 until 06:48:12. The standard deviation of the measured sizes in form of error bars is not shown in the graphs due to the y-scales and the size of the markers. The expected size correspond to the theoretical diameter of the dots in the disc, and the measured size indicates the calculated diameter as D_x from the CIPG images.

The number concentration of calibration dots was calculated with an applied PAS of 12 m/s, along with the amount of missed particles per second. This provides a reference for the order of magnitude of concentrations observed during calibrations, ap-

proximately 1.12 cm^{-3} for the CIPG and 0.12 cm^{-3} for the PIP. A calibration of the PIP on June 11, 2021 was excluded due to a high amount of missed particles (1800 per second compared to 80 in the PIP and 120 in the CIPG accepted calibrations). The applied PAS was set higher at 25 m/s, indicating that the disc was likely powered with 24 instead of 12 V leading to a malfunctioning of the disc.

4.3. COMBINED SIZE DISTRIBUTION

In the preceding sections, I outlined the instruments and methods for processing and analysing their data individually. Nevertheless, the ultimate objective in the data analysis strategy is to integrate these distinct data sets effectively, considering the performance of the instruments within their respective size ranges. It is also important to address the overlaps in the size range and design a unified size distribution. This section will elucidate the analyses performed and the ultimate methodology employed to establish and compute the combined size distributions.

4.3.1. CIPGS-PIP OVERLAP REGION CHARACTERIZATION

The CIPG spans a particle size range between 22.5 and 967.5 μm , whereas the PIP initiates at 150 and extends up to 6450 μm , considering the bin definition and excluding of the first bin in both cases. This situation leads to a significant overlap region between 150 and 967.5 μm . Within this size range, the CIPG provides images with a high resolution of at least 10×10 obscured pixels per particle, while the PIP retrieves images of particles in this size range with the minimum resolution (between 2×2 and 6×6). In Fig. 4.22, a PSD example of the CIPG and PIP is presented, illustrating a notable disparity in the number concentration measured by the CIPG and PIP within the overlap range. This situation was consistently observed across all flights.

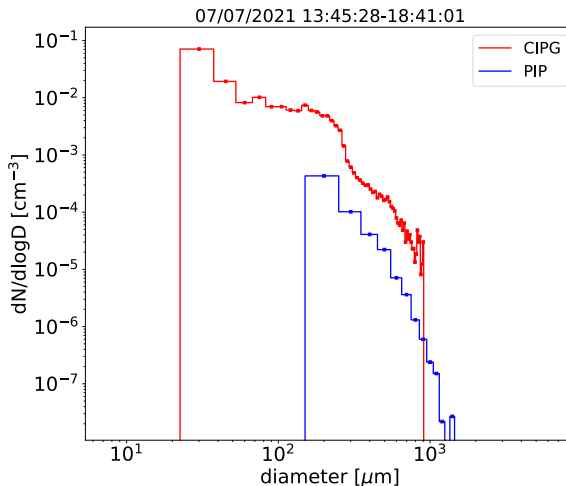


Figure 4.22: CIPG and PIP mean Particle Size Distribution (PSD) for an example flight.

In the following, a simple experiment is described to have a deeper look into the

impact of a large difference in pixel number for resolving particle images. This experiment involved converting ice crystal images, originally captured with $15\ \mu\text{m}$ -pixels in the CIPG, into artificial PIP images, where each PIP pixel is represented by a 7×7 grid of CIPG pixels of $15\ \mu\text{m}$ size. Although the resulting resolution equals 105 instead of the actual $100\ \mu\text{m}$ pixel width of the real PIP, achieving an exact match in resolution was not the primary objective of the test.

Fig. 4.23 displays the original images from the CIPG and their transformation into PIP resolution. The set of particles in Fig. 4.23(a) and (b) corresponds to the size range between $400 - 600\ \mu\text{m}$. After the transformation, the contours and specific shapes of the particles are no longer distinguishable. Even for the particles in panel (c), which come from a size range between $600 - 900\ \mu\text{m}$, the intricate details of the particles cannot be accurately captured in a PIP resolution. In more detail, the impact on sizing of an image with a different resolution is illustrated in Fig. 4.23(e). In this sketch, the less transparent blue pixels represent the image shadow perceived by the artificial PIP with a resolution of $105\ \mu\text{m}$. During the transformation, the image borders and particle tips are lost in the transformation, resulting in a smaller circle fit compared to that of the original image. It is evident that the higher complexity of a particle (or greater the empty space within the particle image), the larger is the difference in the calculated diameter. This implies that aggregates, for example, lose fewer shape details in the transformation, leading to less impact on sizing.

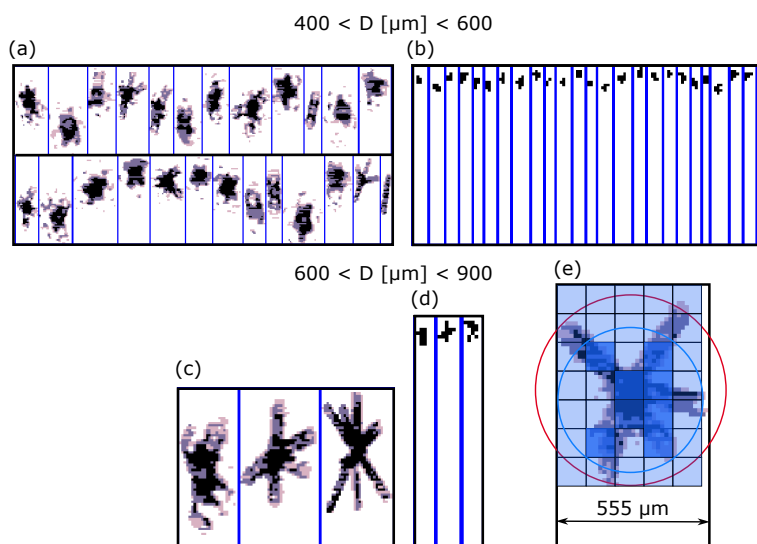


Figure 4.23: Example of a transformation of CIPG images into equivalent images with PIP pixel resolution. (a) and (c) show original CIPG images and, (b) and (d) the transformed images. (e) sketch of the sizing of an original bullet rosette from the CIPG (circle in red) and the transformed image into PIP resolution (circle in blue). Blue shaded grid represent the PIP pixels (7×7 CIPG pixels) and the less transparent pixels indicate the ones that would be triggered for a light intensity lower than 50%.

The analysis of Fig. 4.24 presents the statistics of the transformation performed on an example flight for CIPG images ranging between 200 and $900\ \mu\text{m}$. In panel (a), the

ratio between transformed PIP particle diameters and CIPG diameters is depicted. A significant portion (90669 counts) of the transformed images is no longer visible after the transformation and is not shown in the histogram. Of the remaining transformed PIP images, 85% are sized smaller than their homologous CIPG images.

The analysis of panel (b) shows equivalent PSDs resulting from a division of the set of images in three groups: 200 to 400, 400 to 600, and 600 to 900 μm . Each color shade indicates the portion of the CIPG PSD transformed into the PIP PSD of the same color, highlighting the loss in concentration due to the change of resolution. Larger images experience less loss, but the undersizing contributes to a spreading of the size distribution to lower size ranges.

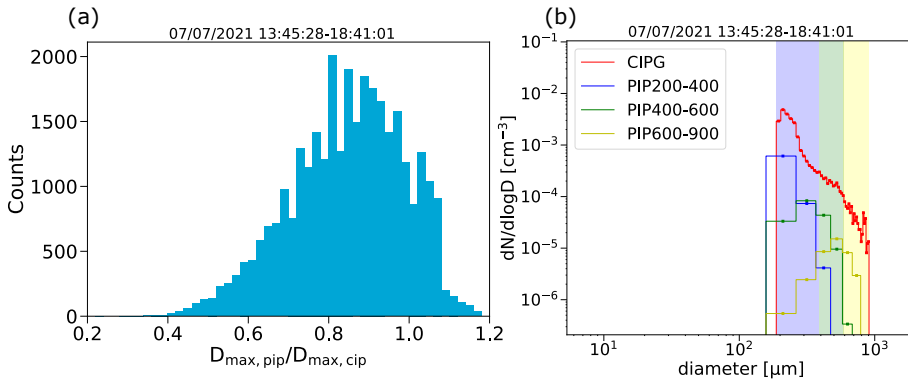


Figure 4.24: (a) Frequency distribution of transformed-PIP diameters to CIPG ratios. (b) PSD of the selected range of the CIPG and the equivalent PSDs of the transformed size ranges to PIP resolution. The color shadings indicate the ranges of the CIPG corresponding to the transformed PIP PSD.

Regarding the CIPG particle size distribution, the concentrations in the larger size bins tend to be overestimated. One contributing factor is the applied all-in method for the effective array width determination. As depicted in Fig. 3.8 of Section 3.2.1, there is a sharp reduction in the SA for particle diameters larger than approximately 500 μm . Larger particles are highly likely to touch the borders of the diode array and be filtered out, resulting in progressively reduced counting statistics with increasing diameter. Another factor is the coincidence of two or more particles in the same image (see Section 4.2.1) and the subsequent circle fit sizing can lead to a misattribution to the image of a large diameter, in most cases. These cases are categorized into the larger size bins, and their impact is amplified when considering the reduced SA for that size range, leading to an overestimation of the concentration in those bins. In conclusion, the concentration in the larger size bins of the CIPG is associated with limited counting statistics and a potential overestimation of the particle concentration.

Considering the problems of both instruments appearing in their overlap region, I decided to calculate an average concentration between the CIPG and PIP, as the optimal solution that takes into account the underestimation of the PIP and the overestimation of the CIPG in the size range between ≈ 200 and 600 μm . The method developed is described in more detail in the following section.

4.3.2. CALCULATION OF THE COMBINED SIZE DISTRIBUTION

The results of the analyses in the previous section led to the calculation of a mean concentration between the CIPG and PIP. Considering that the CIPG tends to overestimate the concentration in the latter part of its size range, and the PIP underestimates in the initial part of its size range, a compromise solution was implemented. The upper limit of the CIPG was set to 247.5 μm and the lower limit of the PIP was set to 637.5 μm , both limits coinciding with CIPG bin edges. A mean concentration for the size range in between was then calculated. Due to the instruments having different bin widths, a direct average of the concentration per bin could not be calculated. Another approach was employed, involving the redefinition of the PIP binning with the same bin edges as the CIPG. The corresponding concentration per bin was calculated using a fitting function of the CIPG PSD. This choice was made to leverage the higher resolution of the CIPG, providing information on the shape of the PSD, instead of assuming a linear distribution within the PIP bins. A new fitting function is computed for each 10-second time interval and subsequently applied to the PIP concentration per bin within the same interval.

To illustrate the method, Fig. 4.25(a) provides a conceptual sketch. For each PIP bin (e.g. 250 – 350 μm), a 5th degree polynomial function is fitted to the corresponding size range of the CIPG distribution. Within the original PIP bins, new sub-bins of 15- μm width are defined (e.g. 250 – 262.5 – 277.5 – 292.5 – 307.5 – 322.5 – 337.5 – 350). This approach guarantees the conservation of the number concentration for each bin ($\int dN'dD' = \int dNdD$, with N' and D' the number concentration and diameter of the new bin PIP bin definition (PIP')). Subsequently, the ratios between the integral of the polynomial fit between the sub-bin's edges and the integral over the entire interval are calculated. Using these ratios, the concentration of the sub-bins (PIP', blue/red squares in Fig. 4.25(a)) is computed. Before averaging the concentration per sub-bin with the CIPG bins, the last sub-bin from each PIP bin is combined with the first sub-bin of the contiguous PIP bin to form 15 μm bins (e.g. 337.5 – 350 – 352.5 \rightarrow 337.5 – 352.5). After this operation, the sub-binning of the PIP matches that of the CIPG for the size range between 247.5 and 637.5 μm , allowing the computation of the mean concentration per bin.

After calculating the averaged concentrations between the CIPG and PIP for the specified size range, a new binning is assigned to facilitate a smooth transition between the 15- μm bin width of the CIPG and the 100- μm bin width of the PIP. The final binning for particle diameters between 247.5 and 637.5 μm starts with two bins of 15 μm followed by two of 30 μm , two of 45 μm , and three more of 60, 75 and 90 μm each. An example of the resulting combined PSD is shown in Fig. 4.25(b).

The final step in combining the particle size distributions is to define the transition between the CDP and the CIPG. Considering its pixel size resolution, the CIPG can detect particles with a diameter as small as 7.5 μm for a grayscale threshold of 50% (if perfectly in-focus). Particles with diameters between 7.5 and 22.5 μm are still represented by one-pixel images and are filtered out (see Section 4.2.1). This means that the CIPG is effective for particles starting from 22.5 μm . On the other hand, the CDP is capable of measuring particles with diameters up to 50 μm .

The larger sample area of the CIPG leading to increased particle counting statistics compared to the CDP, would recommend the use of the CIPG before the CDP. However,

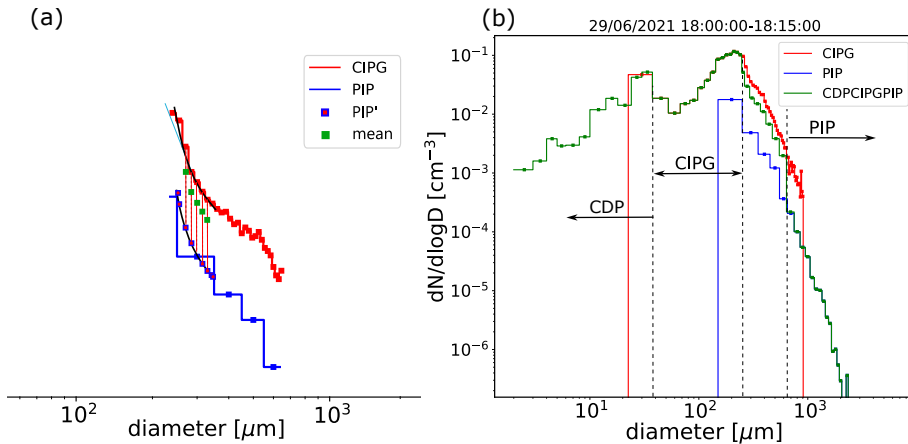


Figure 4.25: (a) Sketch of method for the calculation of the mean concentration between CIPG and PIP bins. The black dashed line represents the fit function (polynomial of degree 5) of the CIPG PSD. PIP' corresponds to the calculated sub-binning according to the CIPG bin edges. (b) Example of the result of a combined PSD from the given CIPG and PIP PSDs, including the CDP.

the limited pixel resolution at the beginning of the CIPG size range entails a certain restriction. To strike a balance between both aspects, the upper size limit of the CDP is set to $37.5 \mu\text{m}$. This allows for a smooth transition between the CDP and the CIPG, starting from the third bin of the CIPG. The last bin used from the CDP is nominally defined between 36 and $38 \mu\text{m}$. For the transition between CDP and the CIPG, the distribution of the particle concentration in this bin is assumed to be linear, and the concentration of the shortened bin at $37.5 \mu\text{m}$ is calculated.

The CDP bins are nominally $1 \mu\text{m}$ wide from 2 to $14 \mu\text{m}$ and $2 \mu\text{m}$ wide from 14 to $50 \mu\text{m}$. As a final step of the combined size distribution, the CDP bins are merged into larger bins with increasing size, leading up to the transition to the $15 - \mu\text{m}$ bins of the CIPG. This merging includes four bins of $1 \mu\text{m}$, two bins of $2 \mu\text{m}$, two bins of $4 \mu\text{m}$, two bins of $6 \mu\text{m}$ and the last bin has $7.5 \mu\text{m}$. This approach serves two purposes: it creates a smoother transition to the next instrument size resolution, and it helps attenuate differences in concentration between adjacent bins.

4.3.3. REMARKS ON UNCERTAINTIES AND IMPLICATIONS

The uncertainties and limitations of the measurement techniques employed in this thesis were detailed in Sections 3.1.3 and 3.2.3 and throughout this chapter. These uncertainties are primarily categorized into counting and sizing uncertainties, which are caused by various factors that scientists have tried to characterize and quantify over the past few decades (e.g., Baumgardner et al. (2017), McFarquhar et al. (2017), and Gurganus and Lawson (2018)). This section provides a summary and discussion of these uncertainties based on available studies in the literature, as well as their implications for the subsequent analysis in Chapter 5. Table 4.4 summarizes the following considerations related to counting and sizing errors for the CDP, CIPG, and PIP, including relevant

references.

Table 4.4: Estimated counting and sizing uncertainties for the CDP, CIPG, and PIP based on the literature and adapted to this thesis, indicating the most relevant associated known limitations.

	CDP		CIPG and PIP	
	Counting	Sizing	Counting	Sizing
Relative error	30%	30%	20%	50%
Limitations	Ice shapes, statistics	Scattering function ambiguities, collection angles, ice shapes	DoF, all-in	out-of-focus, pixel resolution
References	Brennguier et al. (1998), Lance et al. (2010), Baumgardner et al. (2017)		Baumgardner et al. (2017), McFarquhar et al. (2017), Gurganus and Lawson (2018)	

Baumgardner et al. (2017) estimates an uncertainty in counting for forward scattering probes between 10 and 30%. As previously mentioned in Section 3.1.3, coincidence and shattering effects in the CDP are considered negligible for cirrus clouds measurements. The statistical error is identified as the major source of uncertainty for these measurements with the CDP, particularly in thin cirrus, where the particle number concentration measured by the CDP approaches its lower detection limit. In such cases, the error can reach up to 70% (for 2 particles seen in one second). This uncertainty is mitigated when combining the CDP data with the CIPG and PIP, which have larger sample areas and offer better statistics. Ultimately, the upper limit of 30% within the range given by Baumgardner et al. (2017) is assumed here as the overall counting error in the CDP.

For sizing errors, Baumgardner et al. (2017) estimate an uncertainty range of 10 to 50 for scattering probes in general. In the present work, a value of 30% is estimated for the CDP, as coincidence and shattering are not considered to significantly affect sizing. The primary factors contributing to sizing uncertainty include oscillations in the scattering function, slight variations in the collection angles, and variability in the scattering function due to unknown ice crystals shapes (the latter being the most significant) (Lance et al., 2010; Lance, 2012).

The uncertainty range for the OAPs in both counting and sizing is estimated by Baumgardner et al. (2017) to be between 10 and 100%. A more precise estimate is not available, as error estimation for these instruments is complex, with contributing factors often described qualitatively (McFarquhar et al., 2017). Regarding counting, as with the CDP, the shattering and coincidence are neglected for both CIPG and PIP. Although some shattering events were identified in the CIPG and PIP measurements, a correction was applied to mitigate the error introduced by this factor. The most relevant factor affecting CIPG is the variability in the DoF for particles smaller than $\approx 125 \mu\text{m}$ (for the PIP, this applies to particles smaller than approximately $200 \mu\text{m}$, though this range is

not used in this work; see Fig. 3.6). The application of the all-in correction (see Figs. 3.7 and 3.8) would also play a role, but this effect is mitigated through the combination of CIPG and PIP (see Fig. 4.25). In addition, particles do not fall within the larger size range of the PIP for the data used in this work. Considering these factors, an overall counting uncertainty of 20% is estimated.

In the contrary, a larger uncertainty is anticipated for sizing with the OAPs, with an estimated value of 50% being taken as a midpoint of the range suggested by Baumgardner et al. (2017), due to the following considerations. Since there is no correction available for the size of the out-of-focus ice crystal images, which increases with the distance from the object plane, this error must be taken into account (see Fig. 3.6) (Vaillant de Guélis et al., 2019). Although this effect can be particularly relevant for the CIPG, it is mitigated by the averaging method when combining CIPG and PIP size distributions (see Section 4.3). Additionally, the discretization of the size range, limited by the pixel resolution, introduces further uncertainty, though this effect is less important for larger particles (Baumgardner et al., 2017; McFarquhar et al., 2017). Finally, shattering and coincidence effects are, once again, not expected to significantly influence sizing in the OAPs.

The estimation of the combined data from the CDP, CIPG, and PIP is predominantly influenced by the uncertainties associated with the CIPG, as this instrument covers the majority of the cirrus cloud particle size spectrum. This makes the uncertainties associated to the CDP less relevant for this work using combined data. The method used to combine data from these instruments was conceived in such a way, that the individual instruments' uncertainties could be reduced by selecting the size thresholds in the overlap regions accordingly (see Section 4.3).

The number concentration is the cloud property with the smallest uncertainty, as it is only affected linearly by counting errors and, to some extent, by errors in probe air speed readings and sample area determination (Kirschler, 2023) (see also Eq. (3.8)). The error in the effective diameter might be more relevant because it is calculated as the ratio of the third to the second moment of the particle size distribution (see Eq. (3.9)). This calculation is influenced by both counting and sizing errors, which propagate non-linearly. Ice water content is likely the most uncertain of the three properties, as it is derived from the particle volumes (see Eq. (3.11)). However, this thesis primarily focuses on the number concentration and effective diameter. Finally, the extinction coefficient in this thesis is not derived from ice water content and effective diameter, a method that would introduce higher uncertainties as a derived parameter, but is instead calculated directly from particle areas Eq. (3.14).

As a final remark, despite the various uncertainties inherent in these measurements, it is important to recognize that the group of instruments used are the only ones capable of providing such highly resolved microphysical properties of cirrus clouds. This makes in situ measurements extremely valuable, even with their limitations. The analysis in the following Chapter 5 offers comparisons between cirrus groups measured during the same campaign, using a consistent combination of instruments whose performance remained stable throughout the period, and applying the same evaluation methods. This consistency allows for a reasonable assumption that the uncertainties are uniform across measurements. Therefore, while absolute values may vary due to these uncertainties, it

is still possible to highlight differences and accurately characterize the properties of cirrus clouds relative to each other. Furthermore, the strategy employed in the following chapters is predominantly statistical, avoiding direct analysis and characterization of single measurements or sequences. This approach, supported by a high volume of data, ensures robust statistics and that the conclusions drawn are representative.

5

DIFFERENCES IN THE MICROPHYSICAL PROPERTIES OF HIGH AND MID-LATITUDE CIRRUS

This chapter illustrates the main scientific outcome of my work and describes the airborne mission Cirrus in High Latitudes (CIRRUS-HL) to which all of the data used in the thesis belongs. In this chapter, I answer the first two research questions (see Chapter 1): **RQ1.** *Do measurable differences exist in the microphysical properties of cirrus clouds between high latitudes and mid-latitudes? If so, what are they?* **RQ2.** *How do air masses from mid-latitudes influence cirrus at high latitudes? How do their properties change compared to cirrus purely developed at high latitudes?* And investigate the third research question: **RQ3.** *What role do aerosols and atmospheric dynamics play in shaping the properties of high-latitude cirrus in comparison to those at mid-latitudes? How does simulated aerosol concentrations compare to measurement data in air traffic relevant regions?* Details about the campaign execution including the measurement platform used and the installed instrumentation are presented in Section 5.1. While Chapter 4 describes the general methods investigated for particle data processing and evaluation, and represents the fundamental work before further scientific analysis can be performed, Section 5.2 explains the specific methods and further data used for the analysis of this chapter. Further on in Section 5.3, an overview of the variation of the main cirrus microphysical properties with latitude is discussed and thus answering the first research question (RQ). The cirrus microphysics are further investigated from the cloud formation point of view in Section 5.5 and the origin types in Section 5.4, providing answers to the second RQ. To close the study and address the third RQ, aerosol-cloud interac-

Most parts of this chapter have been published in **De La Torre Castro, E.**, Jurkat-Witschas, T., Afchine, A., Grewe, V., Hahn, V., Kirschler, S., Krämer, M., Lucke, J., Spelten, N., Wernli, H., Zöger, M., and Voigt, C.: Differences in microphysical properties of cirrus at high and mid-latitudes, *Atmos. Chem. Phys.*, 23, 13167–13189, <https://doi.org/10.5194/acp-23-13167-2023>, 2023. Some parts appear exactly as published and some have been slightly reformulated to extend the information.

tions are analysed with the help of model in Section 5.6. A discussion of limitations and concluding remarks are briefly exposed in Sections 5.7 and 5.8.

5.1. THE CIRRUS-HL CAMPAIGN

The CIRRUS-HL mission is part of the Priority Programm (Schwerpunktprogramm in german, SPP 1294) "Atmospheric and Earth System Research with HALO" funded by the German Research Foundation (Deutsche Forschungsgemeinschaft, DFG) (HALO-SPP-1294, 2023). The HALO (High Altitude and LONG range) research aircraft is a Gulfstream G-550 business jet modified for carrying scientific equipment. It can reach altitudes up to 15 km (depending on the payload) in a range of 9000 km. This mission was conceived as the succession campaign of the ML-CIRRUS experiment (Cirrus in Mid Latitudes) that took place in 2014 with almost the same instrumentation (Voigt et al., 2017). These campaigns were led by the German Aerospace Center (DLR) and bring together the expertise of several German research institutions and universities.

During the campaign, HALO was equipped with a wide variety of in situ and remote sensing instruments for measuring cloud particles, aerosols, trace gases (H_2O , NO , NO_y , CO , CO_2 , CH_4 and O_3), radiation and basic meteorological parameters (pressure, temperature, position, 3D wind components...). The equipped aircraft is shown in Fig. 5.1. On the upper part of the fuselage of the airplane there are a series of inlets placed for trace gases and aerosol measurements. It also has a nose-boom to perform measurements of the air flow in undisturbed conditions, which is part of the Basic Halo Measurement and Sensor System instrumentation (BAHAMAS). The cloud particle measurements for this study are performed with two of the eight cloud probes located under the aircraft wings, which were extensively described in Chapters 3 and 4. The remaining cloud probes are owned also by DLR and the Karlsruhe Institute for Technology (KIT) and Forschungszentrum Jülich (FZJ). Further details about the other cloud probes and instrumentation installed for this campaign can be found in the [CIRRUS-HL website](#) and in (Voigt et al., 2017).

5



Figure 5.1: High Altitude and LONG range research aircraft (HALO) on the apron of the Oberpfaffenhofen special airport. Photographed by T. Sprünken.

The CIRRUS-HL campaign was performed in June and July 2021. The objective of

the experiment was to investigate cirrus formation and microphysical properties at high latitudes, and aged contrails and contrail cirrus, as well as the radiative impact of cirrus at high latitudes and to contrast those with cirrus at mid-latitudes. In the beginning, the campaign was intended to cover only the Arctic region to complement the mid-latitude cirrus data collected previously during the ML-CIRRUS mission, with data sampled at high latitudes. However, the restrictions during COVID-19 forced to base the mission in Oberpfaffenhofen (Germany) and partially hinder the operations at high latitudes due to the aircraft range limitations. Eventually, it turned out to be very satisfactory and it offered the unique opportunity to compare mid-latitude regions with high latitudes during the same period and weather systems. A total of 24 flights covering regions in the Arctic, North Atlantic and Western Europe were performed. Mainly cirrus clouds in different weather regimes were measured, including warm conveyor belt cirrus, high pressure in situ cirrus, convective cirrus and air traffic induced cirrus were also targeted. The pictures in Fig. 5.2 provide some impressions captured from the aircraft windows on the different situations.

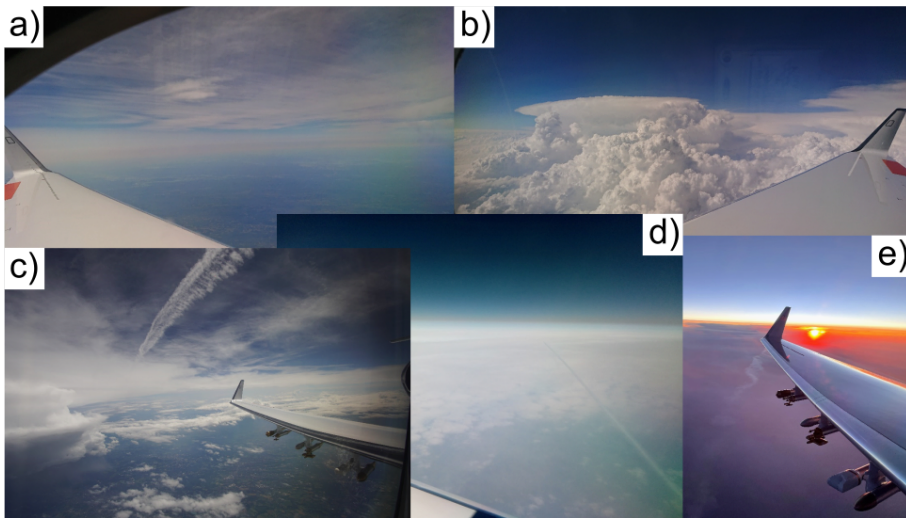


Figure 5.2: Campaign targets in five pictures. (a) Thin cirrus in the Arctic and at mid-latitudes. (b) Convective systems. (c) Contrails and contrail cirrus. (d) Biomass burning layer. (e) Contrail day-night effect. Pictures taken by V. Hahn, L. Tomsche and T. Jurkat-Witschas.

The flight strategy was highly dependent on the weather forecast. Therefore, a dedicated team and a comprehensive set of forecasting tools helped to analyse the synoptic situation and decide on the upcoming flight targets. Cirrus forecast products from European Centre for Medium-Range Weather Forecasts (ECMWF) were provided by the ETH Zurich (Eidgenössische Technische Hochschule Zürich), as well as the Forschungszentrum Jülich (FZJ) provided products from the CLaMS-Ice model (Chemical Lagrangian Model of the Stratosphere with two-moment box model by Spichtinger and Gierens (2009b) for cirrus evolution (Luebke et al., 2016)). An example of various weather maps provided by the forecasting team for different situations during the campaign is shown

in Fig. 5.3. With the help of these products, predictions on in situ or liquid origin cirrus formation over a range of pressure levels were provided, facilitating the targeted flight plan and cruise levels. In addition, the latitudinal origin of the air masses could be predicted by the backwards tracking of the air masses, as well as the updraft speeds at cirrus formation. Supported by this information, the flight planning team designed plans targeting, e.g. thin in situ origin cirrus in the Arctic, or thicker liquid origin cirrus driven by jet stream air masses. However, in-flight modifications of the plan were necessary in order to adapt to the real conditions. These products were complemented by satellite imagery, which was also useful to follow the evolution of convection over Central Europe and contrail outbreaks (as the product for optical thickness prediction in Fig. 5.3(d)). Specific tools for contrail prediction, Saharian dust transport and biomass burning sources were also studied to design an appropriate flight plan to accomplish the campaign objectives. The suggested flight plans were sketched with the MSS tool (Mission Support System, (Rautenhaus et al., 2012; Bauer et al., 2022)) and delivered to the aircraft operations department (DLR).

5

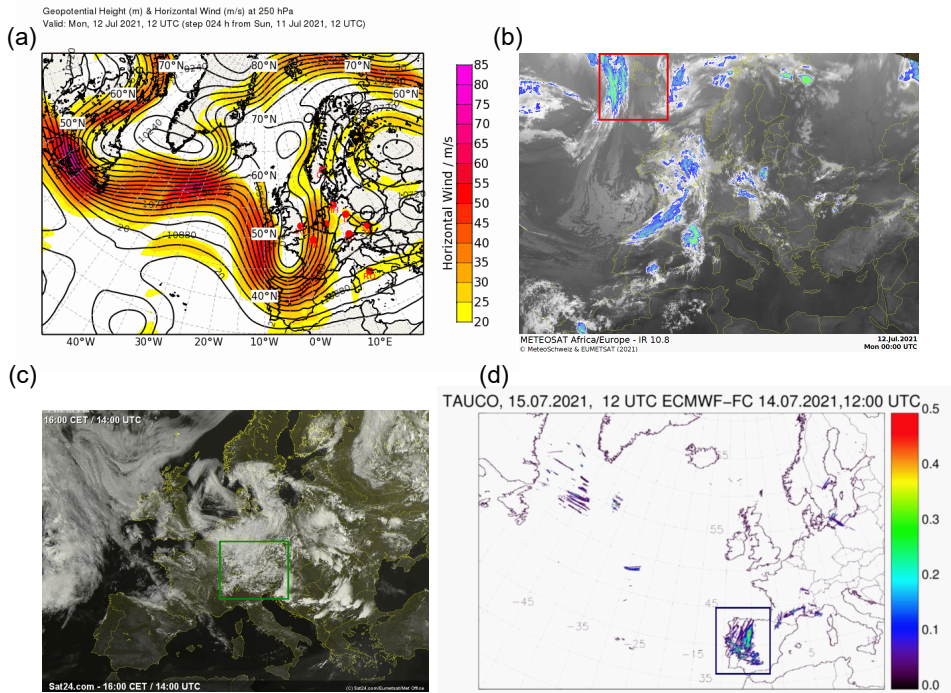


Figure 5.3: (a) ETH forecast product of geopotential height and horizontal wind for the CIRRUS-HL region on July 12, 2021. (b) Enhanced infrared (10.8 μm) brightness temperature (in gray and color scale) for the same day. The target region is marked with a red rectangle. (c) Satellite picture of 1 July 2021 showing shallow convection developing over the afternoon in the Southern part of Germany (green rectangle). (d) Optical thickness prediction of contrails derived from ECMWF showing a contrail outbreak over the Iberian Peninsula (blue rectangle) on July 15, 2021. (Source (a) and (b): weather briefing presentation on July 12, 2021 by A. Dörnbrack (DLR), K. Heitmann (ETH), and J. Mayer (DLR); source (c): flight report on July 1, 2021 by A. Schäfler (DLR); source (d): weather briefing presentation on July 15, 2021 by S. Knobloch (DLR) and H. Binder (ETH).

The general synoptic situation was dominated by the unusually frequent occurrence of upper-level troughs and cutoff lows over Western Europe, which led to statically unstable situations with many thunderstorms and hail over Western and Central Europe. Over the Eastern North Atlantic, several extratropical cyclones with warm conveyor belts occurred, in particular on 7 and 12 July 2021 (according to ECMWF weather forecasts and flight reports), as shown in Fig. 5.3(a) and (b). During some return transfers, outflows of single convective systems were encountered over Germany, such as the example on Fig. 5.3(c).

Table 5.1 provides details on each flight date, measurement time, temperature and altitude ranges and the flight tracks and targets are indicated in the map of Fig. 5.4. A total of 34 h of in situ cloud particle measurements (24.5 h in cirrus) were achieved in different latitudes between 38–76° N at temperatures down to –63 °C and altitudes up to 14.3 km. Note that the information on the table regards only the measurements in cirrus. Flights planned for measuring mid-latitude cirrus are marked in red in the map, blue stands for flights at high latitudes and green for flights in convection (flights on the 8th and 13th of July are not part of the analysis). Collocated flight legs with the Cloud–Aerosol Lidar and Infrared Pathfinder Satellite Observations (CALIPSO) satellite were also performed on the 21st and 28th of July. Cirrus affected by aviation soot particles were also targeted (Urbanek et al., 2018).

Table 5.1: Summary of the specifications of the CIRRUS-HL flights in June and July 2021. Measurement time, altitude and temperature ranges are indicated only for the cirrus regime. (Source: De La Torre Castro et al. (2023))

Flight	Date	t_{meas} [h]	Altitudes [km]	Temperatures [°C]
F02	25.06.21	0.7	[8.5, 9.8]	[–49.5, –38.0]
F03	26.06.21	1.67	[8.8, 11.4]	[–56, –38.0]
F04	28.06.21	2.09	[9.2, 12.2]	[–60.9, –38.0]
F05 / F06	29.06.21	1.9 / 1.35	[9.2, 12.5]	[–62.7, –38.0]
F07	01.07.21	1.02	[8.7, 11.3]	[–55.9, –38.0]
F08 / F09	05.07.21	1 / 1.36	[9.2, 11.6]	[–57, –39.6]
F10 / F11	07.07.21	0.5 / 0.78	[10, 13.8]	[–54.3, –44.2]
F12	08.07.21	1.55	[9, 11.7]	[–53.2, –38.0]
F13 / F14	12.07.21	0.35 / 2.96	[8.8, 11.7]	[–55.1, –38.0]
F15	13.07.21	1.5	[9.5, 12]	[–53.8, –38.0]
F16 / F17	15.07.21	0.36 / 1.17	[8.7, 14.3]	[–61.6, –38.0]
F18 / F19	19.07.21	1.21 / 0.3	[9.1, 11.8]	[–60, –38.0]
F20 / F21	21.07.21	0.66 / 0.35	[9.9, 13.6]	[–56.4, –41.1]
F22	23.07.21	1.06	[9.2, 11.5]	[–57.2, –38.0]
F23	28.07.21	0.69	[7.5, 11.9]	[–52.9, –38.0]

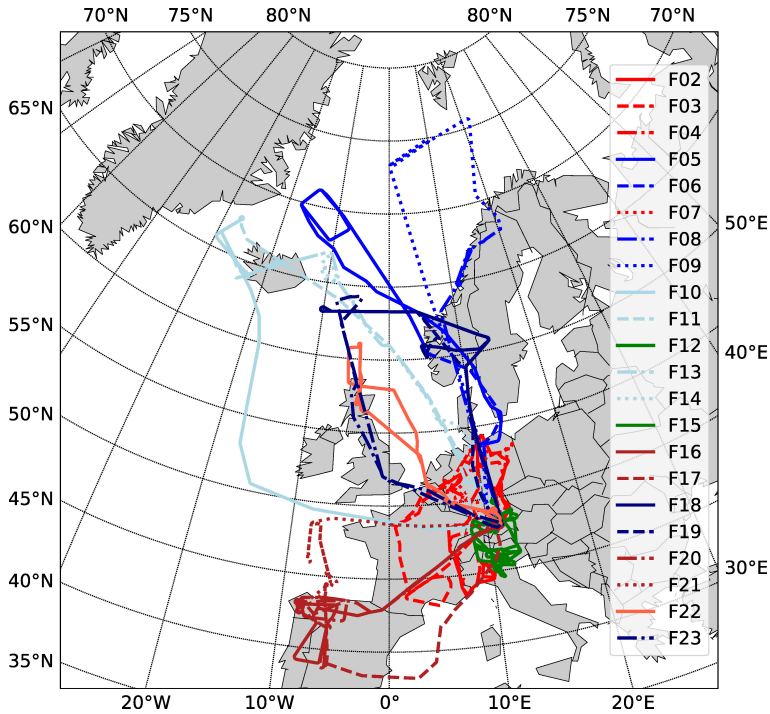


Figure 5.4: Map of the study region in the Arctic, North Atlantic and Western Europe during the CIRRUS-HL mission in 2021. Each line indicates one of the 24 flights performed, marked with reference numbers for each of them (for details see Table 5.1). The blue lines indicate flights directed to high latitudes and the red lines represent those in mid-latitudes. (Source: De La Torre Castro et al. (2023))

5.2. METHODS

In this section, the methods applied for investigating the cirrus microphysical properties during the CIRRUS-HL campaign are briefly described below. Details on the cloud probe data processing and analysis are extensively documented in Chapters 3 and 4. Here, I focus on the additional data included in the analysis and the methods for the evaluation and combination with the cloud particle measurements.

5.2.1. CLOUD PARTICLE, RELATIVE HUMIDITY, AND AIRCRAFT REFERENCE MEASUREMENTS

The cirrus microphysical properties (N , ED and IWC) are derived from the cloud particle measurements applying a combination of the particle size ranges of the three instruments, as explained in Section 4.3. For this study, the microphysical cirrus properties from 20 flights are considered. I exclude two flights dedicated to instrument testing and calibration in temporary reserved areas (TRA) without valuable cloud measurements (F01 and F24) and the two flights targeting convective systems (F12 and F15). Since I am investigating only ice clouds, I consider only measurements below -38°C to ensure completely glaciated clouds, even though ice clouds can exist at higher temperatures.

In general, studies usually use data directly in 1-Hz sample rate. I apply a 2-s mean in order to improve the statistical significance of the low particle concentrations. It means that each data point is separated approximately 400 m, which limits the autocorrelation to a certain extent. A larger averaging interval (e.g. 5 or 10 seconds) corresponds to a large horizontal extension (≈ 2 km for 10-s averages), where local inhomogeneities can be present, and therefore, it excessively attenuates certain features that are of interest, such as contrails, for example.

The pressure, temperature, and wind field measurements were performed by the BAHAMAS system operated by the DLR (German Aerospace Center) Flight Experiments department (Giez et al., 2021). This system also provides the basic aircraft position data of which I use longitude, latitude, and altitude. For the calculation of the RH_i , I use the water vapor mixing ratio measurements from the Sophisticated Hygrometer for Atmospheric ResearCh (SHARC), also developed and operated by DLR Flight Experiments. The measurement range is between 2 – 50000 ppm and the overall relative and absolute uncertainty is 5 % and ± 1 ppm, respectively (Kaufmann et al., 2015; Kaufmann et al., 2018).

5.2.2. AIR MASS TRAJECTORIES¹

Including the history of the measured air masses in the study has been essential to understand the observations and provide a comprehensive analysis. Calculations of 10-day backward trajectories were performed from the flight tracks with the Lagrangian analysis tool LAGRANTO (Wernli & Davies, 1997; Sprenger & Wernli, 2015) provided by the ETH Zurich. Wind, temperature, and cloud fields from the operational European Centre for Medium-Range Weather Forecasts (ECMWF) analyses were used in the model.

Starting from the HALO flight paths, the hourly backward evolution of the IWC and liquid water content (LWC) along the trajectories was evaluated to estimate the time of cloud formation and distinguish between in situ and liquid origin cirrus following the approach described in Wernli et al. (2016). The formation point corresponds to the last time step (at a resolution of one data point per hour) along the trajectory before $IWC = 0$ occurs for the first time (going backward in time). However, if $IWC = 0$ only occurs at one time step, I consider this as "noise", ignore this instance with $IWC = 0$ and repeat the criterion for the next point with $IWC = 0$. Once the formation point is determined, the corresponding in situ measurement is classified as of "liquid origin" if liquid water was present along the trajectory between cloud formation and the measurement ($LWC > 0$). If this was not the case and the air parcel only contained ice water during this time period, it is classified as "in situ origin" cirrus. An example of both scenarios is shown in Fig. 5.5, where the LWC and IWC evolution along each trajectory is indicated. Additionally to the cirrus origin classification, I also analysed the updraft speed along the backward trajectories to better understand the formation process.

¹Data were provided by Heini Wernli but this section was written by the author of the thesis

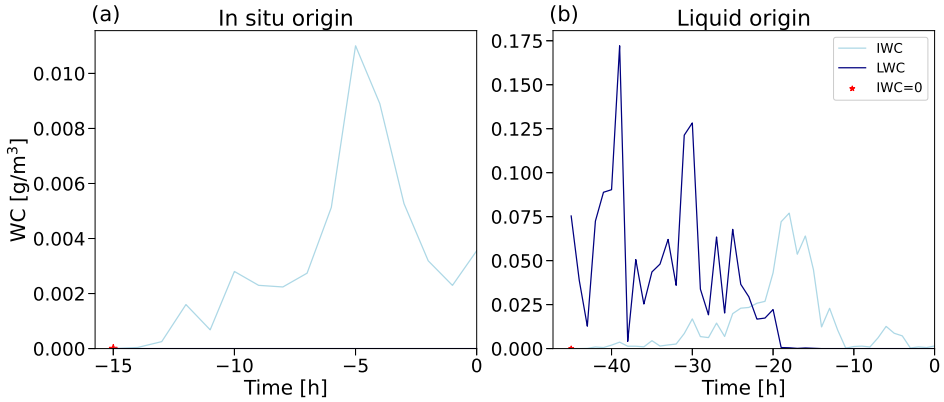


Figure 5.5: Water content (WC) history of the air masses for in situ origin (a) and liquid origin (b). The point calculated as cloud formation is represented with a red star.

5

5.3. OVERVIEW OF THE MICROPHYSICAL PROPERTIES

The cirrus measurements are classified by latitude in order to investigate and compare microphysical properties of cirrus at mid- and high latitudes. For this first classification I consider the latitude at the measurement point. Data obtained at latitudes $< 60^\circ$ N are considered as mid-latitude (ML) cirrus and data collected at $\geq 60^\circ$ N are considered as high-latitude (HL) cirrus. This differentiation is somewhat arbitrary, as there is no universally accepted definition of the three general latitude zones. Perry (1987), for example, defined the mid-latitude in the Northern Hemisphere as the zone between 35° and 56° N but the limits vary according to month and year. However, as I discuss below and in Section 5.5, the variation of the latitude threshold do not modify the conclusions of this work (see also Fig. A.9 in the Appendix A).

Fig. 5.6 shows an overview of the frequency distribution of the measured cirrus microphysical properties with respect to latitude. The normalized frequencies of occurrence allow the comparison between latitudes regardless of the number of observations in each bin. All together, I provide a cirrus data set from 41564 cloud samples in 2-s time resolution, of which 15211 samples are identified as HL cirrus and 26353 samples as ML cirrus. Overall medians of N , ED and IWC (denoted with a tilde) for ML and HL cirrus are indicated in the Fig. 5.6 as well as in Table 5.2. I consider the median instead of the mean, since the mean is more affected by outliers. The overall median N for ML cirrus (0.0086 cm^{-3}) is higher than for HL cirrus (0.001 cm^{-3}) by an order of magnitude. The median ED in ML cirrus is $165 \mu\text{m}$, smaller than that of HL cirrus, $210 \mu\text{m}$ and the median IWC do not differ much between ML and HL cirrus, as it represents a combined effect of N and ED . A similar behavior is observed in the normalized frequency distribution of β_{ext} , which is shown in Fig. A.7 of the Appendix A.

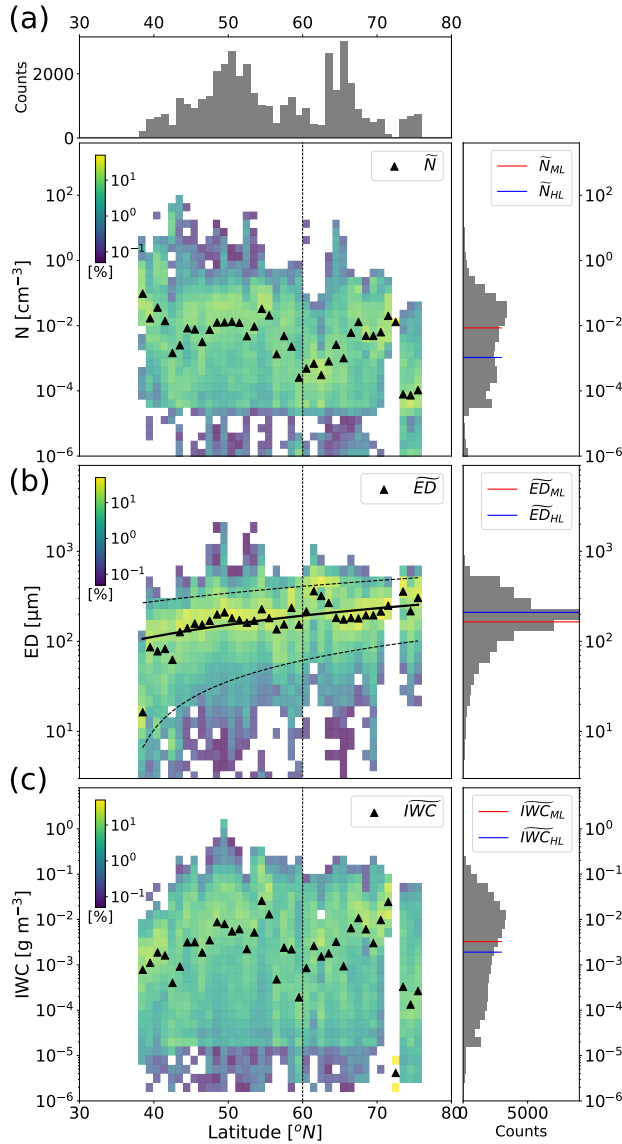


Figure 5.6: Normalized frequency distribution of (a) N , (b) ED and (c) IWC observations as a function of latitude of the measurement during CIRRUS-HL. Latitude bins are 1° wide and vertical bins are logarithmic. The colour code indicates the frequency of occurrence in percent per 1 latitude bin, normalized by the total counts per latitude bin. The vertical dashed line marks the threshold of 60° N for the differentiation of ML and HL cirrus. Triangular markers are medians per latitude bin (\bar{N} , \bar{ED} , \bar{IWC}). The top and right panels are histograms of the corresponding variables. The solid black line in (b) is a linear fit of the ED medians and the dashed lines are the corresponding linear fits of the 5th and 95th percentiles. (Source: De La Torre Castro et al. (2023))

Table 5.2: Median, 25th and 75th percentiles of the microphysical properties N , ED and IWC in mid- and high latitudes during CIRRUS-HL. (Source: De La Torre Castro et al. (2023))

Lat.	N [cm^{-3}]			ED [μm]			IWC [mg m^{-3}]		
	25%	Median	75%	25%	Median	75%	25%	Median	75%
ML	0.0007	0.0086	0.04	98	165	222	0.37	3.3	15
HL	0.00018	0.001	0.0092	146	210	329	0.21	1.9	11

Cirrus measured at mid-latitudes are characterized by higher N (with respect to medians and percentiles of Table 5.2) than those measured at high latitudes. Ice crystal number in HL cirrus are mostly between 0.0001 and 0.01 cm^{-3} . The central range of the ML cirrus measurements is shifted to values that are one order of magnitude larger (0.001 – 0.1 cm^{-3}). In addition, Fig. 5.6(a) also indicates that high particle number concentrations ($N > 1 \text{ cm}^{-3}$) were more frequently observed at mid-latitudes. A linear correlation of the \overline{ED} s is drawn in Fig. 5.6(b) and exhibits a slight and clear positive slope of $\approx 4 \mu\text{m}$ per degree. The correlations of the 5th and 95th percentiles show that the distribution of ED in ML cirrus is broader and smaller ED are more frequently observed with decreasing latitude. In Fig. 5.6, a continuous tendency is observed of increasing ED from mid to high latitudes, which shows that the differences between ML and HL cirrus are continuous and do not depend on the latitude threshold selected. HL cirrus contain a lower IWC , however no significant correlation with latitude is noticed in Fig. 5.6(c). The range of values agree well with the findings by Schiller et al. (2008) for the Arctic and mid-latitudes. Voigt et al. (2017) also reported IWC between 10^{-6} and 0.2 g m^{-3} with a high variability during the ML-CIRRUS campaign at mid-latitudes in spring.

The cirrus properties from these measurements are in line with observations from previous campaigns. Brown and Francis (1995) and Heymsfield et al. (2010), Heymsfield et al. (2013) found in general similar median values of N and IWC (mainly at mid-latitudes and the tropics). However, Brown and Francis (1995), for example, only included data from forward scattering probes. Here I use also the CIPG and PIP, which have higher sample volumes. For this reason, lower IWC than 0.001 g m^{-3} are measured. In general, these results also agree with those reported by Krämer et al. (2016), Luebke et al. (2016), and Krämer et al. (2020) at mid-latitudes, but the larger ED s that result from my analysis are due to the addition of the PIP data and due to different sizing methods applied in the calculation of the diameter from the CIPG images. Here, I consider the maximum dimension of the ice crystals and not the area equivalent diameter. The lower N observed in HL cirrus compared to ML cirrus is consistent with the observations from V. Wolf et al. (2018). Marsing et al. (2023) showed averaged IWC s (0.003 and 0.005 g m^{-3}) of two case studies during the POLSTRACC (Polar Stratosphere in a Changing Climate) campaign in line with the present measurements at high latitudes.

According to the measurements, the combination of higher N and smaller ED ice crystals is characteristic of ML cirrus. The cause of that can be manifold: more anthropogenic activities including aviation at mid-latitudes result in higher aerosol and ice nuclei loads in the upper troposphere. Gayet et al. (2004) also found higher N and lower ED in the more anthropogenically influenced Northern Hemisphere with respect to the more pristine Southern Hemisphere. Aviation-induced cirrus tend to have high number concentrations and lower ED s for several hours after their formation (Voigt et al., 2017;

Schumann & Heymsfield, 2017; Schumann et al., 2017). In general, it is difficult to distinguish aged contrails from thin natural cirrus unaffected by aviation (Li et al., 2022) or embedded contrails in natural cirrus (Unterstrasser et al., 2017a; Unterstrasser et al., 2017b), in particular, as the influence of air traffic over Europe is omnipresent (Voigt et al., 2017; Schumann & Heymsfield, 2017). Even though the thorough analysis on aviation effects is described separately in Chapter 6, it is also necessary to mention in this chapter the influence of contrails in these observations of natural cirrus.

In contrast to the ML cirrus, HL cirrus are often observed with a lower N but larger ED , which could be attributed to the uptake of the ambient water vapor by few INPs and the further growth of less ice crystals that allow larger sizes. The resulting number concentration of the ice crystals depends on the temperature, the updraft and the number of INPs as well as their capability to nucleate ice (Kärcher et al., 2006). V. Wolf et al. (2018) also found lower N at high latitudes and pointed at higher concentrations of INPs at the mid-latitudes compared to the Arctic as a possible explanation. Beer et al. (2022) analysed global model simulations under cirrus formation conditions and showed higher number concentrations of INPs (about 0.1 cm^{-3}) and higher number concentrations of newly-formed ice crystals (about 0.001 cm^{-3}) between $30\text{--}60^\circ \text{ N}$ compared to $60\text{--}90^\circ \text{ N}$. However, a confirmation from airborne measurements of INPs is very challenging, as measurements in the cirrus regime with temperatures lower than -38° C are very scarce. DeMott et al. (2003), DeMott et al. (2010) reported about different measurements of ice particles residuals at temperatures $> -40^\circ \text{ C}$ and show a large variability in INP number concentrations depending on regional and seasonal changes of the aerosol sources. Typically, mineral dust particles are found to have a high nucleation efficiency (DeMott et al., 2003) and black carbon (BC) particles from anthropogenic sources also act as INP. In particular, the importance of aviation soot particles as ice nuclei is not yet well determined. A number of studies investigated the aviation soot impact on cirrus and showed a large range of possible model results, evidencing the uncertainty that exists in this regard (Hendricks et al., 2011; Gettelman et al., 2012; Zhu & Penner, 2020; Righi et al., 2021). In order to verify this hypothesis, I investigate in more detail the interaction between INP concentrations from simulation data and the measured microphysical properties in Section 5.6.

A comparison between ML (red) and HL (blue) cirrus properties (ED and N) over a range of temperatures is presented in Fig. 5.7 sorted in 2.5° C temperature bins. I show temperature along the vertical axis as a representation of altitude. In Fig. 5.7(a) a clear decrease of ED with decreasing temperature is observed for both ML and HL cirrus. Both profiles cover a similar temperature range and correspond to altitudes between 8.5 and 13.5 km, with less measurements at high latitudes. The same decrease of ED is also observed as a function of altitude. This effect has been already observed in previous studies and can be explained by reduced atmospheric water content at lower temperatures (or higher altitude), together with the different altitudes at which in situ and liquid origin cirrus exist (Luebke et al., 2016; Wernli et al., 2016). With increasing altitude (decreasing temperature), cirrus origins change from cirrus dominated by the liquid origin regime with larger ice particles to in situ origin cirrus with smaller particles (consistent with the observations from the study by Voigt et al. (2017)). This is expected due to the low-altitude origin of the liquid origin cirrus (Luebke et al., 2016). Larger particles can also be

found at higher temperatures (lower altitude) resulting from sedimentation processes.

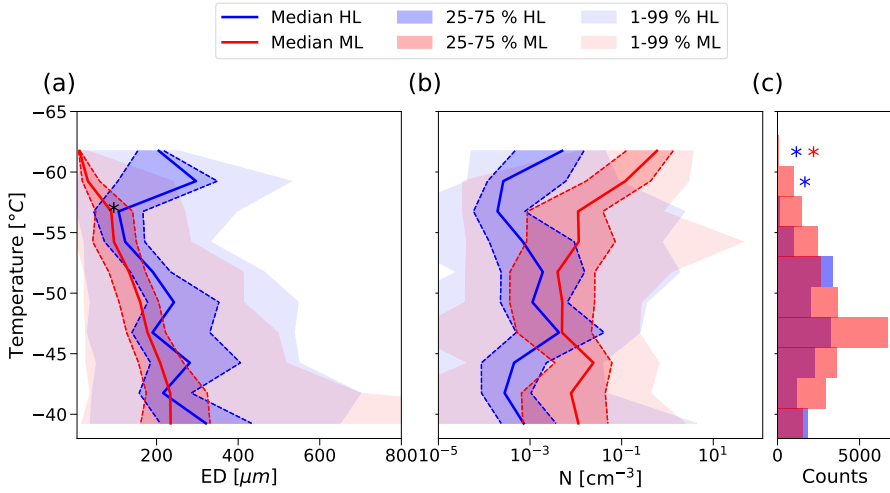


Figure 5.7: Distribution of (a) ED and (b) N observations sorted in temperature bins of $2.5\text{ }^{\circ}\text{C}$ for ML (red) and HL cirrus (blue) and (c) histogram of the total frequency of observations per temperature bin for each group. The thicker solid lines correspond to the median values per temperature bin. The dark shaded areas between the dashed lines comprise the 25th and 75th percentiles of the population. The lighter shaded areas mark the extension between the 1st and 99th percentiles. Black asterisk indicates low statistically significant difference between medians. Blue and red asterisks indicate low statistics in HL and ML data, respectively (see text for further details). (Source: De La Torre Castro et al. (2023))

Between -50 and $-38\text{ }^{\circ}\text{C}$ there is a remarkable difference between the 25th and 75th percentiles in the ED between ML and HL cirrus. This fact probably indicates a more dominant influence of liquid origin cirrus at the high latitudes with enhanced sedimentation as a result of the larger particles at these latitudes. From the cirrus properties variation over temperature I can confirm the larger ED s observed at high latitudes in the general picture of Fig. 5.6(b). Higher ED in HL cirrus compared to ML cirrus are observed in almost all temperature bins. To confirm this finding, I use the U-test according to Wilcoxon, Mann and Whitney (mannwhitneyu function from the Python sub-package scipy.stats) to assess whether there is a statistically significant difference between the ML and HL distributions per temperature bin for ED (and also for N). The null hypothesis that the distributions are equal was rejected for all cases with $p\text{-value} < 10^{-6}$, except for the ED medians between -58 and $-55.5\text{ }^{\circ}\text{C}$ with a $p\text{-value} = 0.028$. Therefore, I conclude that the observed differences are statistically significant. Between -45 and $-38\text{ }^{\circ}\text{C}$ at mid-latitudes, high ED values are observed in the 1st to 99th percentiles. These events are connected to isolated convective systems over Germany with an enhanced growth of the ice particles.

Contrary to the ED , N does not show a clear tendency with decreasing temperature in either case. However, the N in ML and HL cirrus differ at all temperatures by about an order of magnitude, more pronounced at lower temperatures. However, the ML cirrus coldest temperature bin, which mostly contains high N , has reduced statistics with a total of 119 2-s samples measured from four different cloud sequences. Between -62

and -55°C there is an enhancement of N in ML cirrus associated with a steeper decrease in ED , which is probably connected to contrail formation. According to Bräuer et al. (2021b), contrail conditions are particularly favorable between -50 and -60°C , leading to high extinction coefficients. This corresponds to altitudes between 9.5 and 11 km, where short- and medium-range commercial flights are typically located. Contrails are frequently present in ML cirrus above Central Europe. Here, high N and low ED are mostly found around -55 and -60°C in this data set. High N values ($> 1\text{ cm}^{-3}$) in the other temperature ranges are rare and represented by the outliers, which do not impact the medians. Measurements of HL cirrus below -55.5°C are less representative with 210 counts in total. In particular, between -63 and -60.5°C there are 22 2-s consecutive samples from the same cloud sequence. Between -60.5 and -58°C three different cloud sequences were probed with a total of 40 counts. Fluctuations in ED in HL in these temperature ranges in Fig. 5.7(a) can thus be explained by the reduced statistics.

In addition, I examined whether part of the cirrus were measured in the stratosphere, as stratosphere-penetrating extratropical convection is most likely to occur during summer (Dessler, 2009). In addition, the tropopause (TP) height vary strongly between 35 and 50°N and the cirrus measurements of high and mid-latitudes could be differently distributed with respect to the TP height (Dessler, 2009). In order to derive the altitude of the cirrus measurements with respect to the TP, the TP height was extracted from the data set Hoffmann and Spang (2021) and the definition used was the WMO (World Meteorological Organization) 1st TP height from ECMWF's reanalysis ERA5 data (Hoffmann & Spang, 2022). The absolute frequency distribution of the HL and ML cirrus altitudes with respect to the TP is shown in Fig. 5.8 and reveals similar profiles between mid- and high latitudes. From all data points, 2.6% were measurements above the TP, with only 0.2% belonging to HL cirrus and most of the measurements were performed in the upper troposphere at around 1 km below the TP. A substantial influence of stratospheric clouds are not observed, with an even smaller contribution at high latitudes.

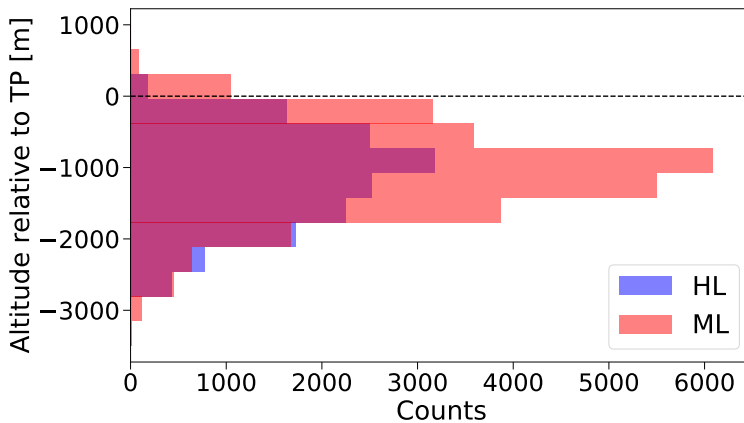


Figure 5.8: Comparison of the frequency distribution of the cirrus altitudes relative to the tropopause (TP) between ML cirrus (red) and HL cirrus (blue) distributed in vertical bins of ≈ 350 m wide. The TP is marked with a black dashed line as reference and separate measurements in the troposphere (below) and in the stratosphere (above). (Source: supplemental material of De La Torre Castro et al. (2023))

5.4. CIRRUS ORIGINS AT MID- AND HIGH LATITUDES

Although differences in the microphysics of the cirrus measured during CIRRUS-HL were observed and discussed in Section 5.3, the argument for these differences could be a greater or lesser presence of in situ or liquid origin cirrus at mid or high latitudes. In order to investigate this, I classify the measurements making use of the information on *LWC* and *IWC* along the backward trajectories after the formation of ice in the cloud, as described in Section 5.2.2. Four groups are obtained with this division: in situ origin HL cirrus, liquid origin HL cirrus, in situ origin ML cirrus and liquid origin ML cirrus.

The frequency of measurements of each group as well as their microphysical properties in terms of *ED* and *N* are presented in Fig. 5.9. Liquid origin cirrus were frequently measured at mid-latitudes and were also the dominant type at high latitudes. Liquid origin HL cirrus were observed almost as frequently as the in situ origin ML cirrus. In situ origin HL cirrus, in turn, were the least measured. However, isolated rare events are not well represented in the diagrams due to the calculation of contours by interpolation.

Larger particles than the total *ED* median value (180 μm) were found in both cirrus types at high latitudes, with larger values for liquid origin cirrus. In situ origin HL cirrus were rather thin, with *N* often under 0.004 cm^{-3} , the median value of all data. The *ED* distribution of both cirrus types at high latitudes exhibits two distinct maxima, which can be understood by two different processes: higher ice crystal growth at high latitudes due to the increased supersaturation leading to the sedimentation of large ice crystals from the upper layers or different nucleation times during their lifetime with an enhanced growth of the larger mode due to fewer INPs and high supersaturation. Large *ED*s representative of liquid origin cirrus are present in mid-latitudes with some outliers of high *ED* and high *N* in convective cells involving also precipitation particles. However, smaller *ED*s than the median, even for the liquid origin cirrus, are more frequent at mid-latitudes.

The observations at high latitudes generally agree well with the measurements in the Arctic from V. Wolf et al. (2018). However, high number concentrations are not found in the present observations of in situ origin HL cirrus in contrast to V. Wolf et al. (2018). The reason is that their measurements of Arctic in situ origin cirrus were dominated by homogeneous nucleation events driven by high updraft motions driven by gravity waves. My analysis of the updraft speed along the backward trajectories and the measured vertical velocities indicate rather low vertical velocities. In particular, Fig. 5.10 illustrates probability distribution functions (PDF) of updraft speeds derived from the aircraft measurements and model data obtained from the backwards trajectories. Since the observations offer only a snapshot of the cloud dynamics, values along the trajectory provide more detailed information. Fig. 5.10(a) displays all values along the trajectory since the formation point, while Fig. 5.10(b) indicates only the maximum value in each trajectory. Consistent with previous studies (Luebke et al., 2016; Krämer et al., 2016; Krämer et al., 2020), higher updraft speeds are observed in the air masses responsible for liquid origin cirrus formation. Updraft velocities from the history of HL cirrus are slightly lower than those at mid-latitudes. The measurements in Fig. 5.10(c) exhibit similar trends but with high higher updraft values, as they represent instantaneous values recorded at a 1Hz rate, contrary to the backward trajectories, which are averaged within the model grid box. The updrafts from the model data fall within the range of synoptic dynamics

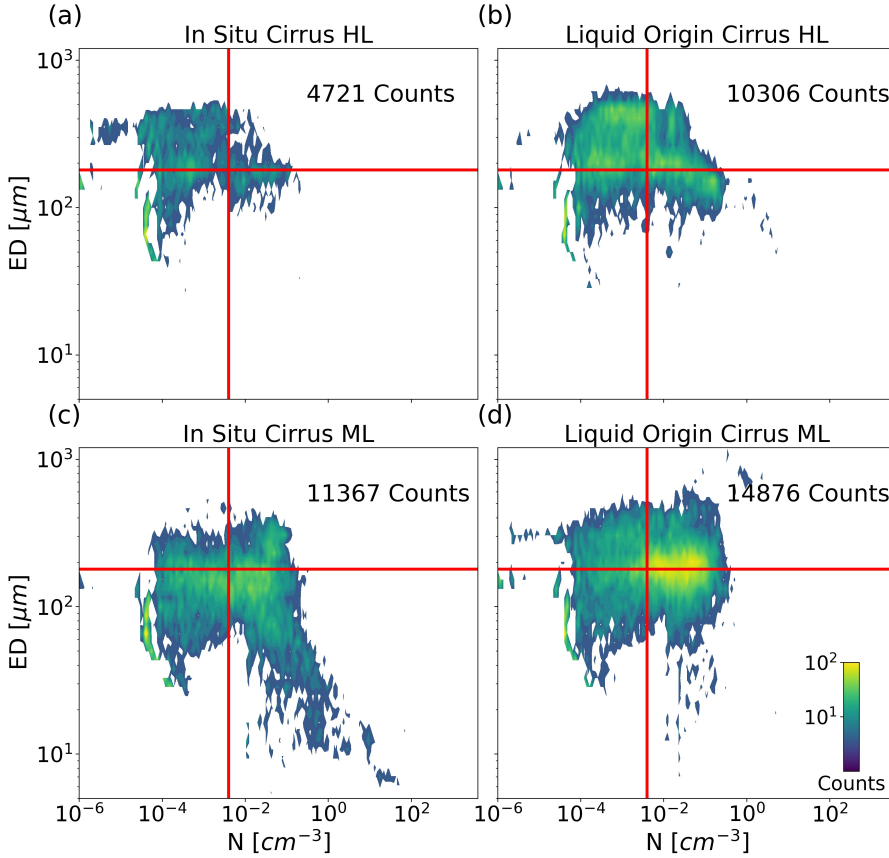


Figure 5.9: Frequency of ED observations in counts as a function of N . The observations are separated in (a) in situ origin HL cirrus, (b) liquid origin HL cirrus, (c) in situ origin ML cirrus, and (d) liquid origin ML cirrus. The method to draw the contours uses a marching squares algorithm. Vertical and horizontal solid red lines indicate overall median values of ED and N , respectively, and are shown to better illustrate differences. The total number of 2-s data points are given on the upper right corner of each panel. (Source: De La Torre Castro et al. (2023))

(< 7 cm s⁻¹), as defined by (Kärcher & Lohmann, 2002b), which also includes gravity waves (7 < updraft[cm s⁻¹] < 100 and convection (> 100 cm s⁻¹).

In any case, orographic cirrus were not a target of the campaign and therefore, mountain wave cirrus with high number concentrations were not expected, justifying the assumption that mainly heterogeneous nucleation defined the cloud formation in this data set. The prevalence of heterogeneous freezing was also shown by Froyd et al. (2022) at mid- and high latitudes in the Northern Hemisphere during spring and summer due to the suppression of homogeneous nucleation by intense dust emissions. Saharian dust emissions were forecasted and reported during the campaign, and the general influence of aerosol on the measured cirrus is further investigated in Section 5.6. However, it is

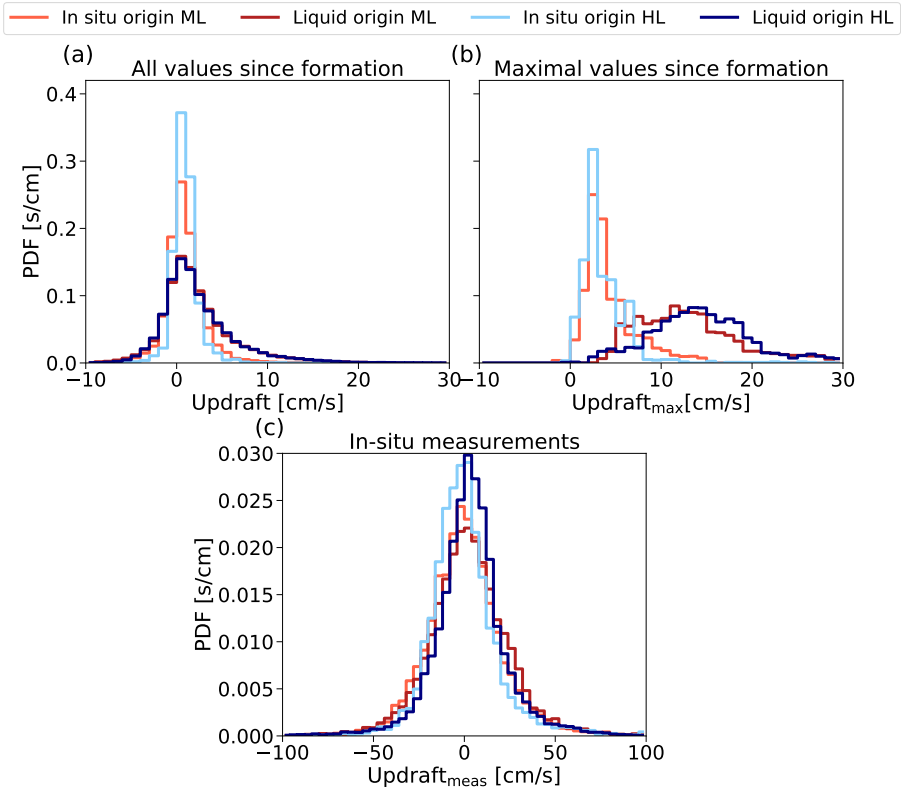


Figure 5.10: Updraft speed probability distribution functions (PDF) for in situ ML cirrus (light red), liquid origin ML cirrus (dark red), in situ HL cirrus (light blue) and liquid origin HL cirrus (dark blue). (a) Distribution of all values along the backward trajectories between formation and measurement. (b) Distribution of maximum values along the backward trajectories between formation and measurement. (c) Distribution of the in situ measured updraft speed from the BAHAMAS system. Lower updrafts in (a) and (b) compared to (c) result from the grid point averages of the backward trajectories calculation. (Source: supplemental material of De La Torre Castro et al. (2023))

essential to note that the temporal resolution of the parameters calculated along the trajectories is one hour; hence, effects on the updrafts from small-scale fluctuations and turbulence are not considered here. Additionally, homogeneous nucleation events are fleeting in the atmosphere, making it extremely challenging to capture such events with aircraft observations (Krämer et al., 2016).

Greater differences are found among the in situ origin cirrus. While in situ origin ML cirrus have higher N with smaller ED s mainly between 70 and 250 μm , in situ origin HL cirrus are mostly composed by low number concentrations of large particles with ED between 150 and 450 μm . As for the ED medians, the values of liquid origin cirrus change from 188 μm at mid-latitudes to 220 at high latitudes, while the in situ origin cirrus does it from 128 at mid-latitudes to 189 μm at high latitudes. I also draw the readers' attention to a feature in the bottom right square of Fig. 5.9(c) of in situ origin ML cirrus,

which differs from the in situ origin HL cirrus observations. Although I did not quantify the contribution, I identified high concentrations of small particles connected to young contrails, aged contrails, contrail cirrus or embedded contrails in natural cirrus. This feature is also weakly present in Fig. 5.9(d) of liquid origin ML cirrus but substantially less pronounced. I discuss in more detail the aviation influence in Chapter 6.

Additional information on the properties of the cirrus groups is given by their particle size distributions (PSDs). Knowing the ice crystal size distribution is vital in order to derive the radiative impact of cirrus. The representation of PSDs of the four groups is not a trivial task in this case. In other publications it is usually found the use of a mean PSD as representative of the considered sequences (e.g., McFarquhar et al. (2007) or Luebke et al. (2016)). However, this campaign deals with a wide variety of situations, including outliers, which were in fact infrequently observed but strongly dominate the mean. These events are, in this case, contrails and convection encounters. This implies that the mean PSD fails to identify the averaged behaviour in the group and the use of medians appears to be a better choice for this case. However, due to the low concentrations in cirrus and the lower sampling efficiency of the CDP compared to the CIPG and PIP, the lower bins are frequently empty in the 2-s sampling rate and do not allow a median value calculation. Therefore, I increase the averaging intervals to 180 s to calculate the median concentration in each size bin. Sensitivity analyses were performed to select the 180 s averaging interval.

The calculated PSD median values are shown for each cirrus group in Fig. 5.11(a) and the means in Fig. 5.11(b) are also included for comparison. The median concentrations in each bin of the liquid origin cirrus are higher than for the in situ origin cirrus for particles $> 20 \mu\text{m}$ at both mid- and high latitudes and the former covers a larger size range than the latter, consistent with previous observations (Krämer et al., 2016; Luebke et al., 2016). The median PSDs of liquid and in situ origin ML cirrus have higher concentrations than HL cirrus. Both ML cirrus profiles have the same behaviour in the smaller bin range (2 – 100 μm) and they differ in the larger sizes. The liquid origin cirrus reveal a second mode, slightly less pronounced than at high latitudes, and the in situ origin ML profile decays fast without a second mode.

As for the mean values, two clear outlying features are detected. Firstly, the size range in liquid origin ML cirrus is larger, which is a consequence of the isolated convective events that were encountered. Secondly, the large number concentrations of small crystals for the in situ origin ML cirrus clearly shows that the microphysics of in situ origin ML cirrus were affected by contrails. The difference in the concentration of the lower bins (from 2 to 10 μm) between the median and the mean is about two orders of magnitude. Then, the mean concentration decays and almost converges with the median at about 40 μm . In general, the median PSDs exhibit lower concentrations than the means, in all bins for the four groups, which is expected due to the right skewness of the lognormal distribution. The mean and median show larger differences the more outliers there are in the distribution. The PSDs of the in situ and liquid origin HL cirrus show a weaker influence of outliers, as the medians profiles do not differ much from the means.

In Fig. 5.11(c) I show another way to represent the radiative impact of cirrus through β_{ext} , which is often used to assess the climate impact of contrails (Bräuer et al., 2021b; Voigt et al., 2021). For a certain *IWC*, the extinction is larger when the ice mass is dis-

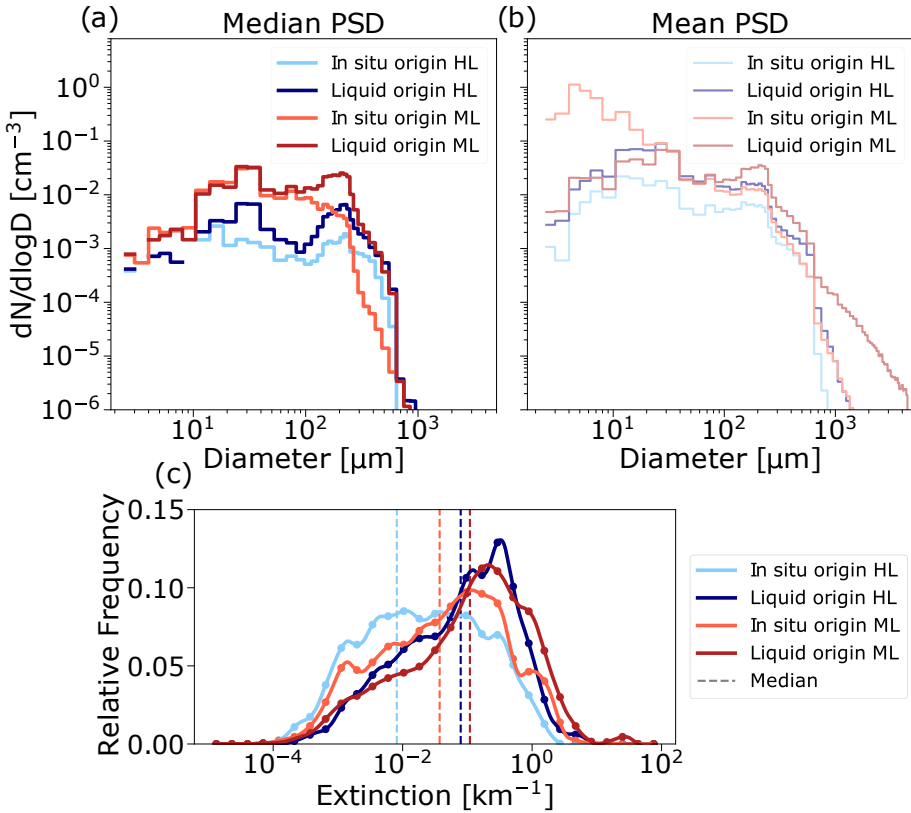


Figure 5.11: (a) Median, (b) mean Particle Size Distribution (PSD), and (c) extinction coefficient (β_{ext}) of the groups: in situ origin HL cirrus (light blue), liquid origin HL cirrus (navy), in situ origin ML cirrus (light red) and liquid origin ML cirrus (dark red). Median PSDs are indicated with thick lines and means with thinner lines. The frequency of occurrence of β_{ext} was calculated in logarithmic bins and fitted with B-Splines. (Source: De La Torre Castro et al. (2023))

tributed in smaller crystals (Unterstrasser & Gierens, 2010). Higher extinction coefficients are observed for the liquid origin cirrus at HL and ML, with slightly higher median for ML, compared to the in situ origin cirrus. This is expected due to the higher *IWC* of the liquid origin cirrus. The lowest extinction corresponds to the in situ origin HL cirrus, since the *N* is lower and the ice particles are larger, which reduces the extinction and the radiative impact. In line with the PSDs, here, a stronger difference between the in situ cirrus at HL and ML is observed, with a shift to larger extinctions at ML. In addition, both frequency distributions of ML cirrus show a small mode at 1 km⁻¹, which is frequently observed in young contrails (Febvre et al., 2009; Voigt et al., 2011; Gayet et al., 2012; Bräuer et al., 2021b).

Even though measurements of contrails do not dominate the campaign observations and therefore are not representative of the general picture, the mean PSD of in situ origin ML cirrus shows how strongly contrail encounters can affect the cirrus microphysics with an enhancement of smaller particles. More importantly, my analyses indicate that

higher number concentration and smaller particles indeed describe the microphysical properties of ML cirrus compared to lower concentrations and larger ice crystals at the more pristine high latitudes.

5.5. INFLUENCE OF CLOUD FORMATION ON CIRRUS PROPERTIES

The main approach of the study is the analysis of cirrus microphysical properties depending on their latitude. So far, I have classified the data in ML and HL cirrus using a latitude threshold at 60° N regarding the measurement point. Now, I investigate the meteorological conditions at the time of cirrus formation and how they affect the observed microphysical properties. Once the formation point of each cirrus sample is determined, as described in Section 5.2.2, cirrus measurements can be classified in four categories: cirrus formed and measured at mid-latitudes (M-M), cirrus formed at mid-latitudes and measured at high latitudes (M-H), cirrus formed at high latitudes and measured at mid-latitudes (H-M), and cirrus formed and measured at high latitudes (H-H). Examples of backward trajectories for each group are shown in Fig. 5.12. The H-M cirrus is excluded from the analysis, as it only contains 36 data points, all of them just at the limits of the boundaries (see Fig. 5.13). In Fig. 5.12, the points with $IWC > 0$ in the trajectory before the purple star indicate a previous formation of ice within the air parcel, which evaporated later.

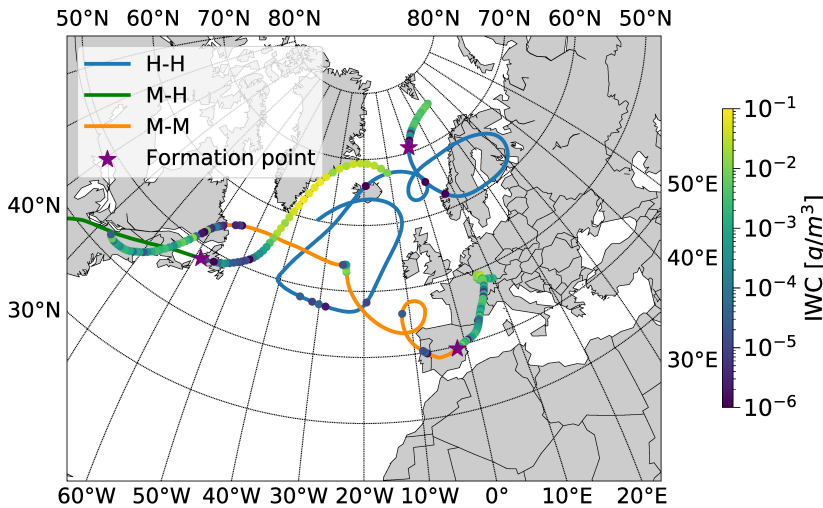


Figure 5.12: IWC (colour coded) along three example trajectories from the cirrus classification: formation and measurement at high latitudes (H-H, blue), formation at mid-latitudes and measurement at high latitudes (M-H, green), and formation and measurement at mid-latitudes (M-M, orange). The formation point is indicated with a purple star. (Source: De La Torre Castro et al. (2023))

Fig. 5.13 shows the distribution of 2-s measurements for the four categories delimited by the 60° N threshold and colour coded according to ED . The three important

categories are M-M in the bottom left, M-H in the bottom right, and H-H in the upper right. Using this categorization, I separate the measurements previously classified as HL cirrus into cirrus formed at high latitudes (H-H) and cirrus formed at mid-latitudes and transported to high latitudes (M-H). The number of data points found in each category (4450 for H-H and 10753 for M-H) indicates that the category M-H contributes more frequently to the Arctic cirrus observed in this measurement campaign.

It turns clear that the distribution of the measured ED is connected with the latitude at the measurement point. Yellow colours represent high ED of up to $1000 \mu\text{m}$ and the dark purple dots represent ED s of about $10 \mu\text{m}$. Higher occurrences of smaller particles are measured in ML cirrus and higher occurrences of larger particle sizes are found in HL cirrus. The differences are smaller when looking at the latitude of formation of cirrus measured in high latitudes. I conclude that the location of the cirrus has a larger influence on the particle size than the formation region.

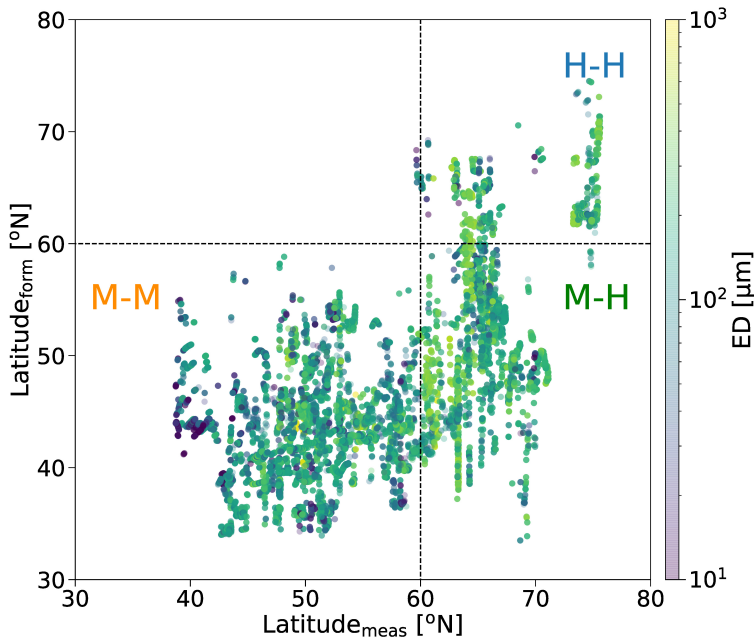


Figure 5.13: Correlation of latitude at the formation and latitude at the measurement for 2-s measurement points. The colour indicates the associated ED . Four regions are delimited with black dashed lines and define the groups: H-H, M-H and M-M (see text for details). (Source: De La Torre Castro et al. (2023))

In order to investigate in more detail how the cirrus properties depend on their source region, Fig. 5.14 illustrates normalized frequency distributions of N , ED and RH_i of the three categories. The maximum of the N distribution of the M-M cirrus lies between 0.01 and 0.1 cm^{-3} . In contrast, the highest probability in the H-H cirrus is shifted to significantly lower values between 0.0001 and 0.001 cm^{-3} . The M-H cirrus distribution exhibits an intermediate behaviour. The medians reflect the same observation, with 0.0086 , 0.0018 and 0.0004 cm^{-3} for the M-M, M-H and H-H cirrus, respectively. The ED

profiles in Fig. 5.14(b) show the opposite trend, as do the medians (164, 206 and 225 μm for M-M, M-H and H-H cirrus, respectively).

In addition, Fig. 5.14(c) shows the measured RH_i for the three categories. In general, the tropopause region in summer 2021 had a high occurrence of supersaturation both at mid- and high latitudes. A clear difference in the RH_i distribution is observed, with lower RH_i with a median of 107 % in M-M cirrus and higher values in the H-H cirrus with a median of 125 %. This can be explained by the lower ice crystal concentrations at high latitudes due to a reduced availability of INPs. The relative humidity is not sufficient to homogeneously nucleate new particles and, instead, the small number of ice crystals available takes up the abundant water vapor increasing their size. On the contrary, water vapor at mid-latitudes is rapidly consumed by the availability of many ice particles present in the upper troposphere, which only leads to a moderate growth.

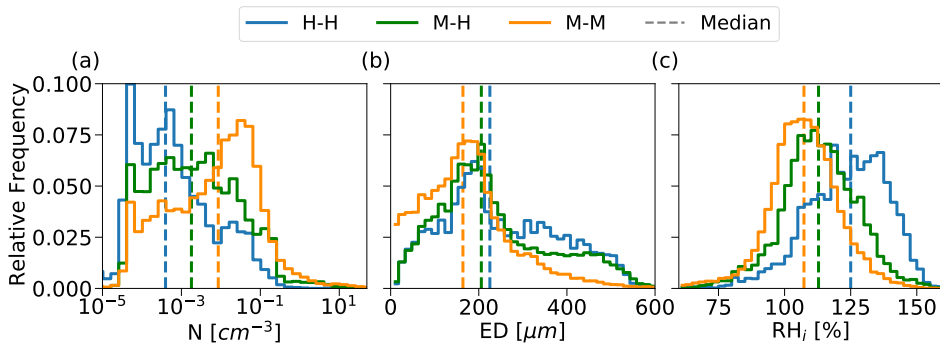


Figure 5.14: Relative frequency distributions of (a) N , (b) ED and (c) RH_i of the cirrus formed and measured at high latitudes (H-H, blue), cirrus formed at mid-latitudes and measured at high latitudes (M-H, green) and cirrus formed and measured at mid-latitudes (M-M, orange). The distribution of N is given in logarithmic bins. Linear bins of 15 μm and 2.5% width have been chosen for ED and RH_i , respectively. The corresponding median values of each variable and category are depicted with dashed lines. (Source: De La Torre Castro et al. (2023))

The M-M cirrus is 57 % of liquid origin and 43 % of in situ origin in the present data set. Regarding HL cirrus, on the one hand I find that 90% of the measurements corresponding to the M-H cirrus have a liquid origin with a larger cloud age. On the other hand, 86% of the H-H cirrus data points are classified as in situ origin cirrus. Therefore, a very likely explanation is that M-H cirrus were formed from the liquid phase in a ML environment rich in nucleating particles (further investigated in the following section Section 5.6). Here many small particles were nucleated in a first stage. Then, the air parcels are advected northwards to high latitudes, bringing the clouds into a highly supersaturated atmosphere allowing the formed ice particles to grow. Cirrus measured at high latitudes can be clearly distinguished from ML cirrus by the bimodality of the ED distribution. The bimodality of the ED distribution of M-H and H-H cirrus can be explained analogously to the 2D frequency distribution from the liquid origin HL cirrus. It can provide a glimpse into sedimentation processes of large ice crystals from upper layers or various nucleation events that occurred at different stages of the lifetime.

These findings together clearly suggest an influence of the ML origin in the develop-

ment of cirrus at high latitudes, conserving the microphysical properties of the ML cirrus while being transported to higher latitudes. In this way, the formation region influences and defines the initial ice crystal properties, which then mix or are modified during their lifetime due to the different atmospheric conditions. Thus, the largest fraction of clouds observed during CIRRUS-HL originate from the mid-latitudes and through long range transport modify the HL cirrus. Opposite influences from high to mid-latitudes have not been observed.

It is concluded that latitudinal differences in microphysical parameters are better understood when looking at both the location of the ice crystals formation and the location of the measurement. The region where the ice crystals are formed influences the initial cirrus properties, in particular the initial N . The latitude at which the cloud particles were measured determines the resulting state of the measured ice crystal properties, strongly influenced by the RH_i throughout the cirrus life-cycle and mainly affects the measured ED . Both processes are largely influenced by the updraft on small and large scales.

5.6. AEROSOL-CLOUD INTERACTIONS²

Up to this point, the lower concentrations and larger effective diameters at high latitudes combined with larger supersaturations were explained by reduced INP concentrations. This is consistent with insights from the global distributions of simulated INPs by Beer et al. (2022). In this section, I investigate in more depth the aerosol-cloud interaction by means of INP modelled data and backward trajectories. The methodology employed for this investigation is described in the following.

5.6.1. AEROSOL MODEL DATA³

To gather insights into the INP concentrations during cloud formation and evolution, a methodology involving the geographical distributions of modelled INPs was employed. Despite the deployment of the high-volume flow aerosol particle filter sampler (HERA) instrument, specifically designed for offline INP analysis, on board the HALO aircraft (Grawe et al., 2023), these measurements could not be utilized for this study due to several reasons. Firstly, like other state-of-the-art INP measurement instruments, it is limited to providing reliable INP measurements only down to approximately $-30\text{ }^\circ\text{C}$ and it does not reach the colder temperatures observed in cirrus. Secondly, an instrument capable of measuring at lower temperatures alone would not suffice; conducting Lagrangian sampling of INPs would be essential to trace the cloud evolution throughout the cloud life-cycle. Therefore, using simulated INP concentrations that are available on the whole globe, for a range of latitudes, longitudes, pressure levels, and times is highly suitable for combining with backward trajectories of the sampled air masses.

The global distributions of INP concentrations were provided from simulations performed with the EMAC model (ECHAM/MESSy Atmospheric Chemistry model; Jöckel et al. (2010)), which incorporates the MADE3 aerosol microphysics submodel (Modal Aerosol Dynamics for Europe, third generation, as detailed in Kaiser et al. (2014) and

²This section corresponds to new analyses not included in De La Torre Castro et al. (2023)

³This section was written by the author of the thesis, while the information on the model setup and simulation data were provided by Christof Beer

Kaiser et al. (2019)) configured as described in Righi et al. (2021) and Beer et al. (2024). The resolution applied in the model is about $2.8^\circ \times 2.8^\circ$ in latitude and longitude, and 41 non-equidistant vertical layers from the surface to 5 hPa. For the comparison with the measurements various options for the temporal resolution of the processed simulation data were explored, including a climatology mean over the campaign months of June and July from 2014 to 2021, as well as resolutions of 11 hours and 1 hour covering the period from June 1st to July 31st, 2021. In particular, the simulations are executed in a nudged mode, where the model meteorological parameters, such as temperature and wind speeds, are relaxed towards fifth generation ECMWF atmospheric reanalysis of the global climate (ERA5; Hersbach et al. (2020)) data for the CIRRUS-HL campaign period.

The EMAC-MADE3 setup applied here is largely based on the settings described in Righi et al. (2021), Righi et al. (2023), Beer et al. (2022), and Beer et al. (2024). A transient emission setup for the respective time period is based on the recent CMIP6 (Coupled Model Intercomparison Project Phase 6) emission inventory for anthropogenic and biomass burning emissions of aerosols and aerosol precursor species (Gidden et al., 2019; Feng et al., 2020). The emission data cover the historical period to the present day (2014) and future projections for years after 2014 based on the Shared Socioeconomic Pathway (SSP2-4.5; O'Neill et al. (2017) and Fricko et al. (2017)). Natural mineral dust emissions are calculated according to the online emission scheme of Tegen et al. (2002), as described and evaluated in Beer et al. (2020).

The aerosol submodel MADE3 simulates the aerosol particle spectrum in a total of nine modes, which are log-normally distributed and represent different size ranges and mixing states. These modes include the Aitken, accumulation, and coarse modes (for a more detailed description of the physical aerosol properties and dynamics see Section 2.3.3). Within each size mode, three sub-modes represent different particle mixing states: particles composed of fully water-soluble components, those composed of insoluble material (eventually coated with thin layers of soluble components), and mixed particles.

This study focuses on aerosols acting as ice nucleating particles (INPs) and the resulting nucleated ice crystals. In this model, the aerosol is coupled to clouds via a two-moment cloud microphysical scheme based on Kuebbeler et al. (2014), which employs the parametrization proposed by Kärcher et al. (2006) for aerosol-driven ice crystal formation in cirrus clouds. The model setup regarding the coupling of aerosols to cirrus clouds, including detailed information on model tuning and evaluation, is described in Righi et al. (2020) and Righi et al. (2021). The cirrus cloud scheme incorporates different cloud processes, including condensational and depositional growth, sublimation, and sedimentation of ice, among others.

This scheme considers both homogeneous and heterogeneous nucleation (see Section 2.2.2), with the number of newly formed ice crystals from each nucleation mode provided at each model grid point and time step. The model represents different heterogeneous freezing modes due to different INPs, as introduced in Section 2.2.2: mineral dust (DU) (from deposition, DUdep, and immersion freezing, DUimm) and soot, or black carbon from surface sources (BC) (Möhler et al., 2006). Similar to the methodology described in Righi et al. (2021), the simulations also allow for the examination of black carbon from aviation (BCav) using a specific feature within the model. This feature

enables the tagging of soot particles originating from distinct sources, such as aviation emissions. The ice nucleation properties of the heterogeneous freezing modes are characterized by two parameters in the model. The active fraction (f_{act}) of INPs, representing the fraction of the INP population capable of nucleating ice, and the critical supersaturation ratio over ice (S_{crit}), at which the freezing process is initiated. The values of these model parameters are summarized in Table 5.3.

Table 5.3: Freezing properties (critical supersaturation S_{crit} and activated fraction f_{act}) of the ice nucleating particles (INPs) similar to Righi et al. (2020) and Beer et al. (2022). S_{crit} is the ambient supersaturation with respect to ice.

Property	DUdep ($T \leq 220\text{K} \mid T > 220\text{K}$)	DUimm	BCav ⁴	BC
S_{crit}	1.1 1.2	1.35	1.2	1.4
f_{act}	$\exp[2(S_i - S_{\text{crit}})] - 1 \mid$ $\exp[0.5(S_i - S_{\text{crit}})] - 1$	0.01	0.001	0.0025

5

The same freezing properties of DUdep and DUimm were used by Beer et al. (2022), based on Möhler et al. (2006) and G. Kulkarni et al. (2014), respectively. This is a more conservative selection of the DUimm properties compared to Righi et al. (2020) (i.e., $S_{\text{crit}} = 1.3$, $f_{\text{act}} = 0.05$). BC and BCav are treated with different freezing properties, following the approach of Righi et al. (2021) and applying the values from experiment S12F01 for BCav. The properties of BC are consistent with the studies by Hendricks et al. (2011), Righi et al. (2020), and Righi et al. (2021), while Beer et al. (2022) assumed the same values of $S_{\text{crit}} = 1.4$ and $f_{\text{act}} = 0.001$ for both BC and BCav.

A new method was applied for this thesis, where the global distributions of INPs were employed in conjunction with air mass trajectories provided by the ETH. As explained in Section 5.2.2, the trajectories are provided on an hourly basis, enabling the tracking of measured air masses over time. By utilizing these trajectories together with the EMAC-MADE3 simulation output, the INP concentration at each point along the cloud's history can be determined. This is achieved by identifying the location in the aerosol model output that is closest to the positions in the trajectories. Subsequently, to characterize the aerosol load experienced throughout the history of the resulting cloud measurement point, the median INP concentration is computed. This median value is derived from all INP concentration values encountered along the trajectory between the cirrus formation (defined in Section 5.2.2) and the subsequent cloud measurement point. Essentially, this approach facilitates the representation of the evolving aerosol conditions experienced by the air mass as it traverses different regions and atmospheric conditions over time.

A similar methodology was employed to calculate the number concentration of newly formed ice crystals along the backward trajectories. Instead of computing a median value along the trajectory for each measurement point, all values along the trajectory (from formation to measurement point) are considered to obtain a histogram of the nucleation events along the trajectory. It should be noted, however, that this method does not account for all nucleation events that might have occurred along the actual cloud trajectory. Instead, it only considers those events included in the model output,

⁴ S_{crit} and f_{act} values for BCav are chosen according to Righi et al. (2021) (experiment S12F01)

whic are determined by the specified time step, with a minimum interval of one hour. Furthermore, sublimation and sedimentation processes are also not considered. Consequently, a direct comparison between this quantity and the ice crystal number obtained from observations at the measurement point is not possible. Instead, the aim is to compare the differences in nucleation mechanisms among the three cirrus groups in order to gain a deeper understanding of the observed differences. This approach is further detailed in Section 5.6 and the limitations are discussed in Section 5.7. Ultimately, the chosen temporal resolution was the 1-hour resolution, because it matches the temporal resolution of the backward trajectories, and the analyses presented in Section 5.6 mainly utilized this hourly model output.

5.6.2. RESULTS

By integrating the model simulations introduced in Section 5.6.1 with the backward trajectories calculated from the measurement locations, a comprehensive analysis of aerosol effects is conducted, focusing on the influence of INPs on cirrus and the formation of ice crystals in the model, via different nucleation mechanisms: heterogeneous nucleation on mineral dust (DU), black carbon from aviation (BCav), and black carbon from surface sources (BC), as well as homogeneous nucleation. Details regarding the model data and methodology applied are elaborated in Section 5.6.1.

Fig. 5.15 illustrates the geographical distribution of the various INP types in the study region and represents visually the method of determining the INP concentration along the backward trajectories for the three cirrus types introduced in Section 5.5. For each measurement point, a median INP concentration of DU, BCav, and BC of all the steps along the trajectory is calculated, indicating the influence of each INP type along the history of each cirrus measurement. Cirrus measurements are grouped following the approach of the previous Section 5.5. It is important to note that the INP concentrations presented in the figures of this section should be interpreted as potential INP concentrations. The actual INP concentrations are determined by applying the respective f_{act} (see Section 5.6.1).

Similarly to Fig. 5.14, the median concentrations of the three types of INP along the trajectories associated to a cloud measurement point are represented in Fig. 5.16 for the three cirrus types (M-M, M-H, and H-H), and the three INP types (DU, BCav, and BC). In addition, the median value of each distribution is shown with dashed lines. The range in the concentration differs between the three INP types since they are present in different concentrations in the atmosphere (Hendricks et al., 2011; Righi et al., 2021; Beer et al., 2022).

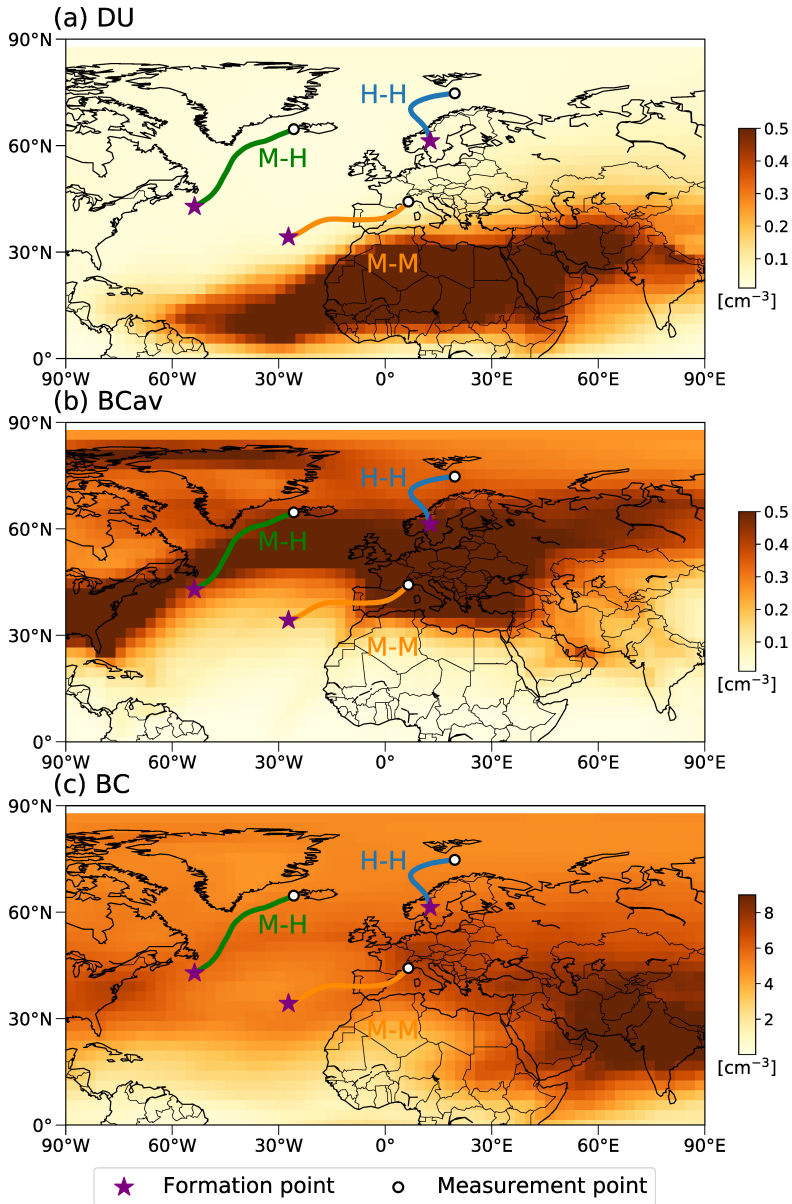


Figure 5.15: Geographical distribution of the number concentration of ice nucleating particles (INPs) from (a) mineral dust (DU), (b) black carbon from aviation (BCav), and (c) black carbon from surface sources (BC) in the study region at 250 hPa. The model output corresponds to a climatological mean from the June-July months over the years 2014-2021. Each panel also includes an example backward trajectory for each cirrus type (cirrus formed and measured at high latitudes (H-H, blue), cirrus formed at mid-latitudes and measured at high latitudes (M-H, green) and cirrus formed and measured at mid-latitudes (M-M, orange), as described in Section 5.5), with a purple star indicating the formation point and a white-black dot representing the measurement location.

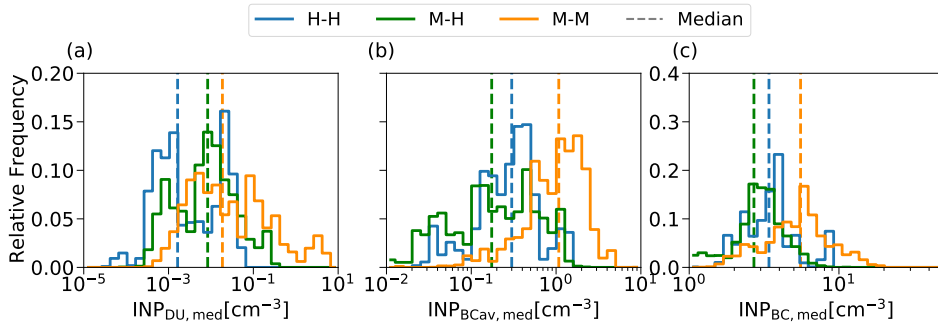


Figure 5.16: Relative frequency distributions of the median number concentration of three types ice nucleating particles (INPs), including mineral dust (DU) (a), black carbon from aviation (BCav) (b), and black carbon from surface sources (BC) (c), along the backward trajectories of cirrus formed and measured at high latitudes (H-H, blue), cirrus formed at mid-latitudes and measured at high latitudes (M-H, green) and cirrus formed and measured at mid-latitudes (M-M, orange). The global distributions of INPs in the model are provided in a temporal resolution of 1 hour.

The distributions of median concentrations of INPs from dust across the three cirrus types exhibit a similar trend to the ice crystal number concentration N shown in Fig. 5.12(a), with higher concentrations in the M-M cirrus compared to H-H cirrus. The higher influence of dust for M-H cirrus compared to H-H cirrus is expected, given that H-H cirrus are predominantly of in situ origin, and the majority of M-H cirrus are of liquid origin. Backward trajectories from liquid origin cirrus cover a broader range of altitudes, including lower altitudes where dust concentrations are higher, in contrast to the altitudes where in situ cirrus typically form (Krämer et al., 2016; Beer et al., 2022). Additionally, as illustrated in Fig. 5.15, mineral dust is more present at lower latitudes and is less frequently transported to higher latitudes, where the H-H cirrus form. This also reinforces the interpretation of the higher concentrations of ice particles in M-H cirrus compared to cirrus purely formed at high latitudes discussed in Section 5.5, which was attributed to the influence of mid-latitude air masses during the initial phases of their formation.

In the case of INPs from BCav and BC, the median concentration distributions of M-H and H-H cirrus display similar profiles, but the overall median values are larger for H-H cirrus (more elaborated below with Fig. 5.19). These distributions and overall medians notably differ from those of the M-M cirrus, which show larger values. Particularly noteworthy are the higher concentrations of BCav observed in the M-M cirrus compared to the other groups. This observation is expected, considering that aviation is more prevalent in the mid-latitudes. Therefore, air masses remaining in these regions have a higher likelihood of accumulating BCav compared to trajectories from air masses that only partially pass through or do not pass through mid-latitudes at all.

The same analyses, but for a climatological mean covering the months of June and July from 2014 to 2021, are included in Fig. A.10 of the Appendix A. Overall, it presents similar results than the 1-hour output for 2021, suggesting that this year is representative and comparable to the climatological average in terms of particle emissions and distribution. The ranges of values for the INP concentrations from DU and BC are reduced in

the climatological average data, while it remains stable for INPs from BCav. This suggests that INP concentrations from BCav over the years might exhibit relatively stable values, whereas the two other sources could be more susceptible to variability, and lower values observed in the hourly output might be smoothed out when averaging over time.

This results suggest a generally higher INP load in the trajectories of cirrus clouds originating and remaining at mid-latitudes compared to either H-H, or even M-H cirrus, which experience less residence time in the mid-latitudes and therefore receive a lower influence of the three INP types. This finding corroborates the hypothesis proposed in previous sections regarding the reduced influence of INP on cirrus formation at high latitudes. However, it is important to note that these results are not a direct indicator of the measured microphysical properties of cirrus and should not be directly compared with the ice crystal N depicted in Fig. 5.14(a), as the relationship between INPs and ice crystals is very non-linear. Only a fraction of the INP concentrations shown in Fig. 5.16 effectively translate into ice crystals. This process in the model depends on the supersaturation levels in the air mass and the freezing properties inherent to each INP type (refer to Section 5.6.1 for further details). In addition, competition for the available water vapor takes place between homogeneous and heterogeneous nucleation between the different INP types (see Section 2.2.2).

To account for all INP-induced nucleation events occurring throughout the age of the cirrus cloud at the measurement location, the newly formed ice crystals at each time step (every hour) along the backward trajectory are computed. However, this method might have a bias introduced by the length of the trajectory; longer trajectories contribute with more values to the overall histogram than shorter ones. The age of the cirrus can be calculated from the backward trajectories as the elapsed time between the formation and measurement point. As illustrated in Fig. 5.17, the cirrus age varies depending on the type of cirrus. Specifically, the age of M-M and H-H cirrus are very similar, averaging 24 and 21 hours, respectively, while M-H cirrus typically have longer ages, averaging 55 hours. The shorter ages of H-H cirrus compared to M-H cirrus can be attributed to their different cirrus origins. H-H cirrus were mostly of in situ origin, while M-H of liquid origin. Liquid origin cirrus originate from lower altitudes and, in general, require more time to reach cirrus altitudes. In contrast, in situ origin cirrus form directly at high altitudes, resulting in shorter ages (Krämer et al., 2016; Luebke et al., 2016; Wernli et al., 2016).

The result is shown in Fig. 5.18 for the three cirrus types and the different types of INP. The upper limit in the distribution is similar for all INP types, indicating a consistent mean maximum ice crystal concentration of about 0.1 cm^{-3} . In contrast, the lower limit of the distribution varies depending on the INP type, with DU displaying a broader spectrum of concentrations of newly formed ice crystals compared to BCav or BC. Interestingly, black carbon appears to be the predominant contributor to higher ice crystal concentrations in cirrus formation, followed by BCav and then DU. This would contrast with previous studies that have highlighted the predominant role of dust in ice nucleation in cirrus (Möhler et al., 2006; Froyd et al., 2022). However, it should be noted that Fig. 5.18 depicts relative frequencies, and thus, it does not directly indicate the fraction of events where heterogeneous nucleation on black carbon occurs. Instead, it highlights that when nucleation on BC happens, it results in the formation of many ice crystals.

The analysis provided in Fig. 5.19 offers another perspective by presenting the ab-

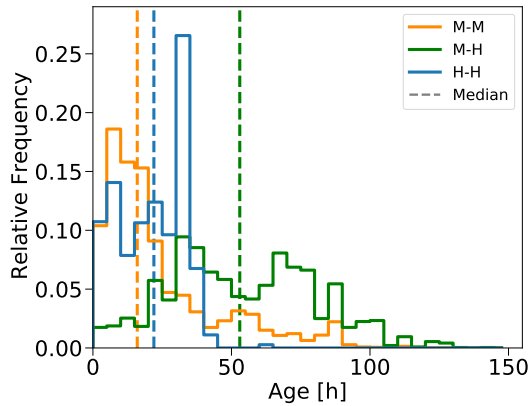


Figure 5.17: Relative frequency distributions of the age at the measurement location of cirrus formed and measured at high latitudes (H-H, blue), cirrus formed at mid-latitudes and measured at high latitudes (M-H, green) and cirrus formed and measured at mid-latitudes (M-M, orange).

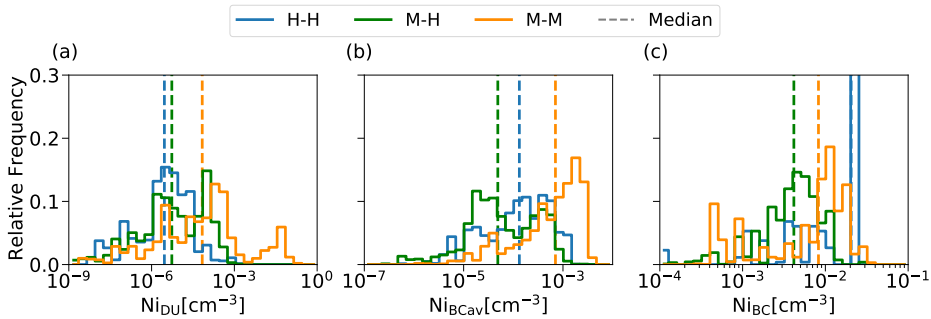


Figure 5.18: Relative frequency distributions of the number concentration of newly formed ice crystals from INPs of mineral dust (DU) (a), black carbon from aviation (BCav) (b), and black carbon from surface sources (BC) (c) of the cirrus formed and measured at high latitudes (H-H, blue), cirrus formed at mid-latitudes and measured at high latitudes (M-H, green) and cirrus formed and measured at mid-latitudes (M-M, orange). The temporal resolution of the concentrations of newly formed ice crystals in the model is 1 hour.

solute frequencies of occurrence for each nucleation mechanism within the same cirrus type. This representation helps to visualize for the same cirrus group, the number of nucleation events of each type. In this case, the absolute frequency distribution of the number concentration of homogeneously nucleated ice crystals is included. At first glance, it becomes apparent that only a small portion of cirrus measurements are influenced by homogeneous nucleation according to the model. Apparently, these events occur very locally for the cirrus trajectories of the CIRRUS-HL campaign. The sensitivity study of Appendix A.5.3 shows similar low absolute frequencies of homogeneous nucleation events for the weather and emission conditions during the same months in 2020 and 2019, confirming that 2021 was not anomalous in this regard.

In general, ice crystals tend to form predominantly on dust particles due to their strong freezing potential, resulting in a broader range of number concentrations. Freez-

ing on DU can begin at lower supersaturations compared to BCav or BC. However, under conditions where more water vapor is available, freezing on BCav and BC can also occur. While in M-H and H-H cirrus exhibit normalized $N_{i,DU}$ concentrations below 0.001 cm^{-3} , the distribution in M-M cirrus displays a small mode at higher concentrations. Maximum concentrations of newly formed ice crystals are observed either through heterogeneous nucleation on black carbon or via homogeneous nucleation. Heterogeneous nucleation on dust for M-M cirrus also produces high concentrations of newly formed ice crystals. These findings should be interpreted with consideration of the assumed freezing properties of the INPs, as described in Section 5.6.1. In particular, this study assumes a relatively high freezing potential for BCav. The impact of these assumptions are discussed in Section 5.7.1.

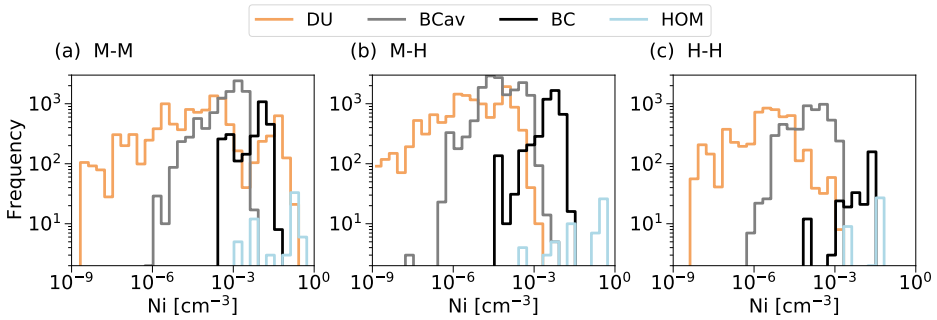


Figure 5.19: Absolute frequency distributions of the number concentration of newly formed ice crystals from different types of INPs. Panels (a), (b), and (c) represent cirrus formed and measured at mid-latitudes (M-M), (b) cirrus formed at mid-latitudes and measured at high latitudes (M-H), and (c) cirrus formed and measured at high latitudes (H-H), respectively. The ice nucleating particle types include mineral dust (DU, orange), black carbon from aviation (BCav, gray), and black carbon (BC, black). Newly formed ice crystals from homogeneous nucleation is also included (HOM, light blue). The temporal resolution of the concentrations of newly formed ice crystals in the model is 1 hour.

The formation of M-H cirrus is characterized by an even contribution from heterogeneous nucleation of the three INP types. In M-M cirrus formation, BC plays a slightly less important role followed by mineral dust and with black carbon from aviation contributing the most in frequency to ice crystal formation. Interestingly, in H-H cirrus, the frequency of events involving heterogeneous nucleation on BC particles is considerably reduced compared to DU or BCav, or to the other two cirrus types. The higher importance of BCav in M-M and H-H cirrus compared to M-H cirrus can be attributed to the higher presence of in situ origin cirrus in these groups (see Section 5.5). These cirrus form at high altitudes and remain within that range throughout their trajectories. While the concentration of black carbon decreases with altitude, black carbon from aviation has another mode of high concentrations at cruise altitudes (Righi et al., 2021; Beer et al., 2022), precisely where the trajectories of in situ cirrus develop. This explains why H-H cirrus tend to accumulate more black carbon from aviation than other sources of black carbon from the ground.

In summary, by utilizing simulated concentrations of INPs from dust, black carbon and black carbon from aviation, along with the corresponding nucleated ice crystals,

valuable insights were gained into the impact of heterogeneous and homogeneous nucleation during the campaign measurements. The analysis revealed a reduced influence of homogeneous nucleation, highlighting the importance of INPs in shaping ice crystal number concentrations across different cirrus types. Specifically, the higher ice crystal number concentrations measured in M-M cirrus are connected with a greater influence of all three INP types and higher concentrations of newly formed ice crystals from the model. Interestingly, H-H cirrus exhibit a significant influence of BCav but a considerable reduction of BC compared to M-M and M-H cirrus.

5.7. DISCUSSION OF LIMITATIONS

In this section, a critical analysis of the limitations is conducted, and several remarks on the representativeness of the study of this chapter are provided. The main influencing parameters are identified in Section 5.7.1, and the outcomes of various sensitivity analyses are discussed there. The latitude threshold is identified as the most crucial parameter, as it defines the classifications established in this study and, consequently, the conclusions drawn. Almost equally important, though much more challenging to assess, is the influence of the different time resolutions of the observations, the backward trajectories tool (LAGRANTO), and the aerosol-chemistry-climate model (EMAC-MADE3). Lastly, relevant aspects influencing the results of Section 5.6.2 include the assumed freezing properties of the INPs and the restriction of INP sources to dust and black carbon (from aviation and from other ground sources), excluding ammonium sulfate (AmmSu) and glassy organics (glPOM) from the model setup (Beer et al., 2022). Section 5.7.2 concludes the discussion with comments on the interpretation of the results from this study, considering the characteristics of the campaign and the resulting data set.

5.7.1. INFLUENCE OF THE METHOD

The selection of the latitude threshold of 60° N is a critical aspect in this study, as it determines the differentiation between mid- and high latitudes and, at the same time, the cirrus classification. I performed a sensitivity study and varied the threshold between 55 – 65° N (see Fig. S4 in the Supplement). Here, I show that the variation of the threshold does not alter the existence of the described differences between the three cirrus groups, even though it influences the absolute values of the medians. In addition, Fig. 5.6(b) shows a continuous tendency of increasing effective diameter from mid- to high latitudes, which shows that the differences between ML and HL cirrus are continuous and do not depend on the threshold.

The classification of cirrus origins of the in situ measurements of this work is susceptible to uncertainties as trajectories were initiated along the flight track every 10 s, which corresponds to ≈ 2 km in horizontal scale. I assume that cirrus measured in this interval have the same origin. In addition, the model parameters calculated along the trajectories are averages of grid points in a $\approx 50 \times 50$ km² domain that does not capture the smallest local variations. I use the vertical motion along trajectories to separate processes connected to the measurements. However, the trajectory approach excludes the analysis of the impact of small-scale temperature and wind fluctuations on cirrus formation. The accuracy of the approach is difficult to assess as the associated uncertainty

is very in-homogeneous, it depends on the location and the meteorological situation. Nevertheless, backward trajectories are a common tool to identify and analyse different influences on cirrus formation and have been employed in other studies (e.g., Voigt et al. (2017) and Urbanek et al. (2018)). Specific studies on the validation and intercomparison of the LAGRANTO tool are available in the literature (Stohl et al., 2001; Cui et al., 2009). The results obtained with this classification method are in line with the findings of previous publications (Krämer et al., 2016; Luebke et al., 2016; Wernli et al., 2016; Krämer et al., 2020).

Similarly, the analysis of the aerosol-cloud interaction is constrained by the horizontal resolution of the EMAC-MADE3 model, which covers approximately $300 \times 300 \text{ km}^2$. This, combined with the different resolution of the LAGRANTO tool for the backward trajectories, introduces a considerable level of uncertainty. Although the concentration of newly formed ice crystals were aggregated along the trajectories to facilitate comparison with the ice crystal number concentrations from in situ measurements, this approach primarily serves to indicate trends rather than allowing for direct comparisons. This is because processes such as sublimation or sedimentation are not considered along the trajectory steps. Further sources of uncertainties of the aerosol-cirrus interactions in the model are extensively described in Beer et al. (2024).

The freezing fraction (f_{act}) of each INP type dictates the number concentration of newly formed ice crystals, while the critical supersaturation (S_{crit}) determines both the number concentration and the absolute frequency of ice nucleation events. Specifically, BCav particles are assumed to act as efficient INPs with $S_{\text{crit}} = 1.2$. However, unlike mineral dust, the freezing properties of BCav and their actual impact on cirrus formation are not yet fully understood (McGraw et al., 2020; Righi et al., 2021). Recently, laboratory study by Testa et al. (2024) shows a poor efficiency of BCav as INP. This might imply that the current assumption for S_{crit} is likely an overestimation. Variations in the ice nucleation ability of BCav not only affect the number concentration of newly formed ice crystals and the frequency of events, but also influence the heterogeneous freezing via DU, BC, and homogeneous nucleation, as they compete for the available water vapor. This could also be affected by including further INP types, which also can compete for the water vapor. A sensitivity study including ammonium sulfate and glassy organics was performed and is included in Appendix A.5.2, showing a negligible impact in the analyses. The decision to assign a high S_{crit} value to the INPs from BCav was made to simplify the interpretation of the results. In addition, given the further focus of this thesis on aviation effects, which will be discussed in Chapter 6, a "worst case scenario" was desired for the freezing potential of BCav as INPs to discuss its impact on cirrus formation.

5.7.2. REPRESENTATIVENESS

This study analyses the differences in the properties of the cirrus that were measured during the CIRRUS-HL campaign according to the latitude. The results are representative of summer 2021, of the regions measured over the Arctic, North Atlantic and Central Europe and of the meteorological situations observed during the campaign. Under this context, these cirrus observations cover a wide range of latitudes between 38 and 76° N and temperatures between -38 and -63° C . The statistical tests I performed indicate a sufficient statistical significance of the differences that I found in these ranges but con-

clusions drawn on the coldest temperatures (between -58 and -63 °C for HL cirrus and -60.5 and -63 °C for ML cirrus) have to be taken cautiously as the number of observations is limited and the samples are mainly from the same cloud sequence. This implies that the observations are correlated to some extent, as they are measured at approximately the same temperature and altitude. However each 2-s sample is horizontally separated by ≈ 400 m and thus the cloud properties are not necessarily connected.

Cirrus classified as formed at mid-latitudes and measured at high latitudes (M-H) were mostly identified as being of liquid origin. This observation may be influenced by the synoptic conditions during the summer months of 2021, which were marked by frequent unstable weather and heavy thunderstorms over Western and Central Europe. In such conditions, strong updrafts and horizontal winds facilitate the formation of liquid origin cirrus at mid-latitudes and their subsequent transport to high latitudes. Future campaigns should investigate the characteristics of the M-H cirrus group in different regions, seasons, and meteorological situations to gain a more comprehensive understanding.

The study indicated a minimal impact of homogeneous nucleation in cirrus formation during the CIRRUS-HL campaign, based on the analysis of newly formed ice crystals from homogeneous nucleation along the trajectories. To verify whether this finding is specific to the year 2021, a sensitivity analysis considering the weather and emissions of 2020 and 2019 was performed and is shown in Appendix A.5.3. The conclusion is that this feature is also observed for those years. However, several remarks should be made in this regard. Firstly, the sampling strategy of these measurements might be biased due to the exclusion of flights in convection and the fact that orographic waves were not part of the campaign objectives. In addition, the hourly resolution of both the backward trajectories and the aerosol model output might miss those events, which occur on a small scale.

Nevertheless, the measurements presented in this thesis can be combined with future observations to build a larger data set and gain a broader perspective. However, it should be noted that directly comparing and integrating this data set with other cirrus measurements performed with different instruments and evaluation methods might not be feasible and could produce misleading results. If only the methods differ, reprocessing and reevaluating the raw data might help to solve conflicts. Comparisons are always possible, provided the differences between data sets are acknowledged and the results are interpreted accordingly.

5.8. SUMMARY AND CONCLUSIONS

This study offers new insights into the microphysical properties of the rarely observed Arctic cirrus and support the analysis by backward trajectories of the cirrus air parcels to investigate cirrus formation and evolution. Even though other campaigns have been previously performed in this region (Schiller et al., 2008; Heymsfield et al., 2013; Krämer et al., 2016; V. Wolf et al., 2018; Marsing et al., 2023), in situ data on the full range of cirrus particle sizes remain limited at high latitudes. Contrary to other campaigns at high latitudes, cirrus at mid-latitudes were measured during the same mission with the same instrumentation, which provided a unique opportunity for comparison. The main findings are stated and discussed in the following:

- High-latitude cirrus measured during summer 2021 are characterized by lower concentrations and higher effective diameters than mid-latitude cirrus. Similar differences in high-latitude cirrus were also observed by V. Wolf et al. (2018) compared to measurements at mid-latitudes (Krämer et al., 2016; Luebke et al., 2016). As V. Wolf et al. (2018), I also suggest the reduced amount of available ice nucleating particles at high latitudes as a possible explanation for these findings. This hypothesis is supported by using simulated ice nucleating particle data from the EMAC-MADE3 model combined with backward trajectories.
- The upper troposphere in the summer 2021 was characterized by high ice supersaturation, especially in high-latitude cirrus ($\overline{RH}_i \sim 125\%$). Contrary to wintertime observations in the Arctic by V. Wolf et al. (2018), which included fast updraft lee wave cirrus, in situ origin high-latitude cirrus were often observed to be formed at lower updrafts. Different from V. Wolf et al. (2018), the analysis of updraft speeds along the backward trajectories and the analysis of newly formed ice crystals from homogeneous nucleation from the EMAC-MADE3 model indicate that heterogeneous freezing dominates cirrus formation during this campaign.
- The Arctic cirrus originate from two processes. First, cirrus formed and existing at high latitudes consisted mainly of heterogeneously formed in situ origin (directly at cirrus altitudes below -38°C) cirrus nucleated in slow updrafts. Few ice nucleating particles and high relative humidity over ice produced low ice number concentrations and larger effective diameters. The high-latitude cirrus that had formed at mid-latitudes were dominated by cirrus originated from liquid or mixed-phase clouds formed at mid-latitudes with higher number concentrations and transported to high latitudes with a subsequent growth of the ice crystals. This category is a mixture of the cirrus properties at mid- and high latitudes and represents how the mid-latitudes influence the properties of cirrus at high latitudes. Both cirrus categories contribute to the larger effective diameter and smaller number concentration measured at high-latitude cirrus compared to mid-latitude cirrus.
- The influence of ice nucleating particles is largest for cirrus formed and measured at mid-latitudes and decreases in the M-H and H-H cirrus. This is particularly true for dust and black carbon from other sources than aviation. Cirrus formed and measured at high latitudes show a significant influence of ice nucleating particles from aviation black carbon and a considerable reduction of particles from black carbon from other sources.
- The selection of the latitude threshold of 60°N and the possible influence on the results is discussed. I found slight variations on the microphysical properties of the investigated cirrus groups but the differences between them remain consistent, regardless of the chosen threshold.
- Although both origin cirrus groups at mid-latitudes exhibit lower effective diameters more frequently than at high latitudes, the differences between in situ origin

cirrus at mid- and high latitudes are more substantial. I point out the contribution of contrail formation within the in situ origin cirrus in flight corridors at mid-latitudes to the differences observed between the in situ origin cirrus in mid- and high latitudes (Voigt et al., 2017). The aviation influence during the CIRRUS-HL campaign is discussed in more detail in Chapter 6.

- An alternative method applying the median for the particle size distribution representation is introduced as a more suitable option in this case, than the commonly used average over the data points. This method helps to obtain particle size distribution that represent the typical values of large sample groups with high variability and strong outliers.

The introduction of the new cirrus classification by taking into account not only the measurement location but also the location at cirrus formation is an important insight for future studies. As the results show, part of the cirrus considered as high-latitude cirrus are actually influenced by mid-latitude air masses that change their properties. In situ measurements of ice nucleating particles in the cirrus regime are much needed to clarify the cause of the different cirrus properties at high latitudes compared to mid-latitudes. Combining in situ observations with modelling studies provided further insights into the underlying processes influencing cirrus formation and cirrus cloud properties. The present study aims to contribute and enhance our knowledge of cirrus formation processes and their microphysical properties in high and mid-latitudes in order to compile a database for studies on their climate impact.

6

CONTRAIL CIRRUS AND NATURAL CIRRUS INTERACTION

This chapter represents a further analysis of the data presented in Chapter 5, but focuses on the effect of contrail cirrus from conventional aircraft operation in the upper troposphere on natural cirrus properties and addresses the fourth research question: **RQ4. How does aviation influence the microphysical properties of natural cirrus?** Building upon the work presented in Chapter 5, which investigated the properties of natural cirrus clouds by using data from the CIRRUS-HL campaign, the aim of this chapter is to provide a comprehensive overview of the observed influence of aviation during this campaign on the properties and lifecycle of natural cirrus. General details of the campaign's instrumentation, objectives, and implementation are described in Section 5.1. The motivation and methodology for identifying contrail cirrus samples are explained in Sections 6.1 and 6.2, respectively. The analysis of these identified events is presented in Section 6.3 and, finally, a summary and final remarks of the results are included in Section 6.4.

6.1. INTRODUCTION

In Chapter 5, I analysed the CIRRUS-HL observations regarding the properties of natural cirrus clouds. A further objective of the research project in the context of the CIRRUS-HL campaign, as mentioned in Chapter 1 and Section 5.1, was to investigate the effects of aviation. Aviation affects natural cloudiness through two primary pathways: the formation of contrail cirrus in the upper troposphere (Voigt et al., 2010; Voigt et al., 2011; Chauvigné et al., 2018), which interact with and impact natural cirrus (Tesche et al., 2016; Marjani et al., 2022; Li et al., 2022; Verma & Burkhardt, 2022), or the emissions of soot (black carbon from aviation, BCav, see Section 5.6) into the atmosphere, which

The figures of this chapter have not been published. Paragraphs discussing aviation effects in De La Torre Castro et al. (2023) have been moved to this chapter in Sections 6.3 and 6.4, and have been slightly adapted to fit within newer parts.

can act as ice nuclei for the formation of natural clouds (Urbanek et al., 2018; Groß et al., 2022). While the latter aspect was briefly addressed in Section 5.6 through the analysis of INP concentrations from BCav among different cirrus types, revealing a higher influence in the M-M cirrus, the focus of this section is on contrail cirrus, which were also measured during the campaign flights¹. These measurements appeared as outliers when considering the overall properties of the observed natural cirrus in Chapter 5, and thus, this chapter aims to characterize them and understand the influence of aviation in the CIRRUS-HL data set. However, it should be noted that the air traffic over Europe in 2021 was still reduced due to the COVID-19 pandemic. According to the International Civil Aviation Organization (ICAO, 2019), the air transport capacity in Europe measured in available seat-kilometers was -46.5% in July 2021 compared to 2019. This means that the observations during the CIRRUS-HL campaign might have a lower influence of aviation compared to the situation before the pandemic.

Generally, aircraft plumes can be identified by enhancements of nitrogen monoxide (NO) and total reactive nitrogen (NO_y) mixing ratios (Schulte et al., 1997). Apart from aircraft engine combustion, nitrogen oxides are emitted into the atmosphere as NO through various combustion processes on the ground (e.g., from industries), by lightning, or from N_2O degradation in the stratosphere and subsequent downward transport. Once released, NO undergoes oxidization to form other reactive nitrogen compounds, such as NO_2 and HNO_3 , collectively represented by NO_y . Specifically, nitrogen oxides (NO_x) in the form of NO and NO_2 are emitted directly at cruise altitudes from aircraft exhaust due to fuel combustion at high temperatures. As the plume mixes with the ambient air, the NO and NO_y mixing ratios decrease due to dilution. Consequently, NO_y can also be used as a tracer, and the NO/ NO_y ratio has been utilized in past studies to estimate the dilution of aircraft emissions and determine the age of the contrail measurements (Schumann et al., 1998; Jeßberger et al., 2013; Harlass et al., 2024).

In the following Section 6.2, the strategy for identifying contrail cirrus samples is described. This task is challenging because the data set does not contain direct measurements of young contrail chase sequences. Some aged contrail encounters were reported in the flight reports by visual observation; however, aged contrails and contrail cirrus can not be clearly visually identified and do not exhibit as clear an enhancement of NO and NO_y compared to young contrail measurements. Therefore, the identification is based on the ice cloud properties N and ED , with measurements of NO and NO_y serving as qualitative indicators.

6.2. METHODOLOGY

The same data set and methods for the analysis of cirrus microphysical properties of Chapter 5 are applied here (see details in Section 5.2). In addition, as mentioned in Section 6.1, in situ measurements of NO and NO_y during the CIRRUS-HL flights are integrated into this analysis. These measurements were provided by Helmut Ziereis (German Aerospace Center) and conducted using the AENEAS (AtmosphERIC Nitrogen ox-

¹The in-depth analysis of the contrail and contrail cirrus measurements from the CIRRUS-HL data set was conducted by Valerian Hahn as part of his PhD thesis using the CAS instrument. All the data presented in this chapter corresponds to my own data set from the CDP-CIPG-PIP combination. Any insights derived from Valerian Hahn's work are explicitly stated in the following sections where applicable.

ides mEAsuring System) instrument, a two-channel chemiluminescence detector. The instrument's overall uncertainty is approximately 8% for volume mixing ratios of 0.5 ppb and about 6.5% for 1 ppb Ziereis et al., 2000; Stratmann et al., 2016; Ziereis et al., 2022.

Similar to Fig. 5.9, Fig. 6.1 shows phase plots of ED as function of N for mid-latitude (a, c) and high-latitude cirrus (b, d). However, in this case, the color coding indicates bin-averaged NO and NO_y mixing ratios. As in Fig. 5.9(c), Fig. 6.1(a) and (c) show a tail-like shape in the lower right corner, which is not present in the high-latitude cirrus. In addition, the NO and NO_y mixing ratios in the central clusters of both cirrus groups are low, while the tail-like feature shows enhancements. However, enhancements are observed not only in the lower right corner but also in the upper right region of the mid-latitude measurements in Fig. 6.1(a) and (c), particularly in the NO mixing ratio in (c). These samples have been identified and correspond to events on June 25 and 29, and July 28. During all these sequences, convective clouds were reported in the flight reports, associated with turbulence and lightning, which is a source of NO . These events can also be clearly distinguished because the ED s tend to be above the overall mean, reaching values of 400 or even 800 μm .

Contrails exhibit a distinct profile characterized by very high ice crystals concentrations in their early stages, often exceeding 100 cm^{-3} , while the ice crystal sizes are just a few micrometers (Petzold et al., 1997; Gayet et al., 2012; Jeßberger et al., 2013; Kleine et al., 2018). As explained in Section 2.4, contrail cirrus form as contrails transition and mix with ambient air, leading to ice crystal growth through water vapor uptake. This process is accompanied by a reduction in concentration due to sublimation from mixing with drier air or sedimentation of the larger ice crystals (Schröder et al., 2000; Unterstrasser & Gierens, 2010; Kübbeler et al., 2011; Voigt et al., 2017; Schumann et al., 2017; Grewe et al., 2017). Here, the tail-like shape connected to the central cluster of Fig. 6.1(a) and (c) represents this transition processes to older ages. As observed, this transition is not abrupt and therefore, potential contrail cirrus measurements might hide within the natural cirrus cluster.

As a consequence of these evidences, the lower most part of the tail is identified as potential contrail and contrail cirrus measurements and these samples are selected by the criterion of $N > 0.1 \text{ cm}^{-3}$ and $ED < 40 \mu\text{m}$. While natural cirrus at high latitudes typically have larger ED s ($> 50 - 60 \mu\text{m}$) and lower concentrations ($< 0.1 \text{ cm}^{-3}$), the chosen criterion is more conservative concerning the sizes. However, a more conservative criterion helps with the analysis and comparison with the rest of the measurements, facilitating the observation of clearer characteristics. These samples are referred to hereafter as "high N and low ED " (HNLED) events. It can already be noted that these events are more frequently observed at mid-latitudes and in situ cirrus (see Fig. 5.9).

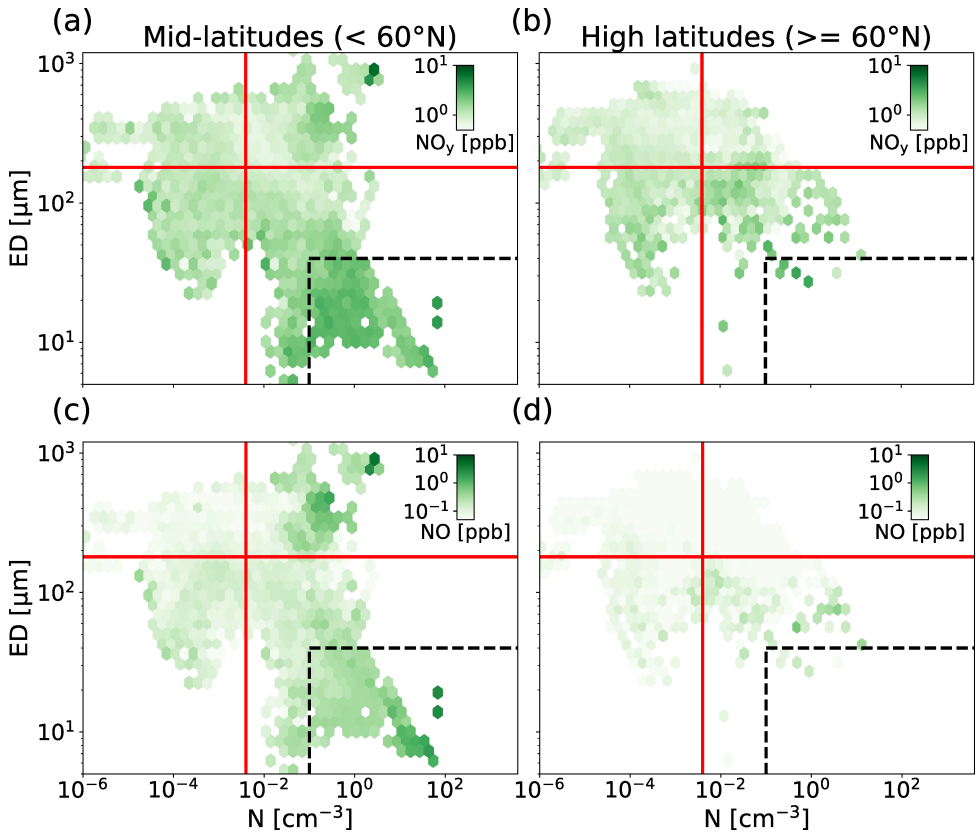


Figure 6.1: Relationship between ED and N in hexagonal bins for (a, c) mid-latitude cirrus and (b, d) high-latitude cirrus. The average of the NO_y (a, b) and NO (c, d) mixing ratios within the hexagonal bins is shown in green color gradient. The overall mean ED and N are shown by red lines, as in Fig. 5.9. The area of the criterion for HNLED events (see text) is marked with black dashed lines.

6.3. INFLUENCE OF CONTRAIL CIRRUS ON NATURAL CIRRUS

In this section, the introduced HNLED are further characterized by their occurrence and by comparing this group of samples with the overall trends. The fraction of HNLED events among all measurements presented in Chapter 5 accounts for 2.4%. Among these HNLED events, only 8% correspond to liquid origin cirrus, while the remaining majority are of in situ origin. Geographically, 96% of these events occurred at mid-latitudes. As discussed in Section 5.3, previous analysis suggested that ML cirrus are more influenced by contrail cirrus. The statistical breakdown of events per day, categorized by liquid and in situ origin, is illustrated in Fig. 6.2. The most significant contribution to the HNLED events stems from F16 and F17 on July 15, 2021, coinciding with a contrail cirrus outbreak over the Iberian Peninsula (see Fig. 5.3(d)). However, other HNLED events are distributed across various days, emphasizing that aviation-induced cloudiness extends beyond forecasted regions of extensive contrail formation to affect natural cloud regions

over Center and Western Europe.

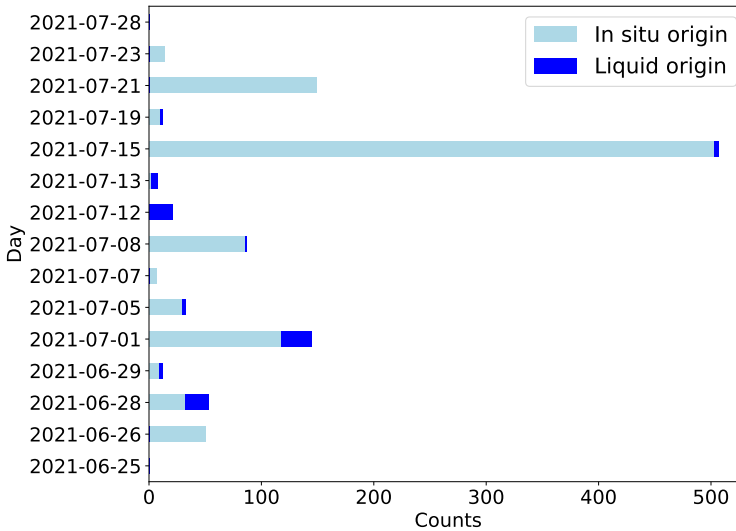


Figure 6.2: Summary of the absolute frequency of 2-second observations of HNLED events for in situ (light blue) and liquid origin cirrus (dark blue) per day during the CIRRUS-HL campaign.

These observations suggest a clearer influence of aviation on in situ origin cirrus events compared to those of liquid origin. Liquid origin clouds typically form at lower altitudes, where both liquid droplets and ice crystals can coexist. As these clouds undergo cooling processes from ascending motions, isobaric mixing or radiative cooling, the relative humidity increases. This sets the state for the Wegener-Bergeron-Findeisen (WBF), where ice crystals grow by water vapor uptake from evaporated liquid droplets, ultimately resulting in complete glaciation of the cloud (Korolev, 2007a; Costa et al., 2017). Consequently, the evolution of liquid origin cirrus allows sufficient time for the available water vapor to be consumed upon reaching the cirrus regime. As noted by Li et al. (2022), liquid origin cirrus often do not meet the Schmidt-Appleman criterion (SAC) for contrail formation due to their higher temperatures. This makes the development of contrails less likely within these clouds.

On the contrary, in situ origin cirrus form directly at high altitudes, where air traffic is also present. Let's imagine a scenario where an in situ origin cirrus cloud begins forming through heterogeneous nucleation by the deposition of water vapor on INPs, and an aircraft exhaust jet is introduced. In this scenario, natural ice particles would be replaced by the freshly formed contrail ice particles, significantly impacting the resulting microphysical properties. The formation of contrails within cirrus can drastically increase the number of ice crystals by several orders of magnitude (Schröder et al., 2000; Voigt et al., 2017; Schumann et al., 2017), particularly when the pre-existing cirrus has high ice water content and low supersaturation levels (Verma & Burkhardt, 2022). Consequently, contrail cirrus formation and evolution are expected to influence the formation process of in situ origin cirrus at cruise altitudes by increasing N and reducing ED . This suggests

a pronounced effect of contrail cirrus-induced changes on the microphysical properties of in situ origin cirrus clouds, as inferred from the mean PSD shown in Fig. 5.11.

In Fig. 6.3, the relative frequency distribution of several atmospheric parameters is presented, including updraft velocity (from the backward trajectories), relative humidity over ice (RH_i), NO/NO_y ratio, and cloud age (based on the formation point in the backward trajectories), for the selected HNLED events. These events are differentiated by the origin of the cirrus, where in situ origin measurements are represented in light blue and liquid origin data points are shown in dark blue. Additionally, the profiles of all data points without selection are depicted in dark gray for reference. Fig. 6.3(a) displays the frequency distribution of all the updrafts observed along the trajectories since cloud formation, with dashed lines indicating the relative frequency of maximum values along each trajectory.

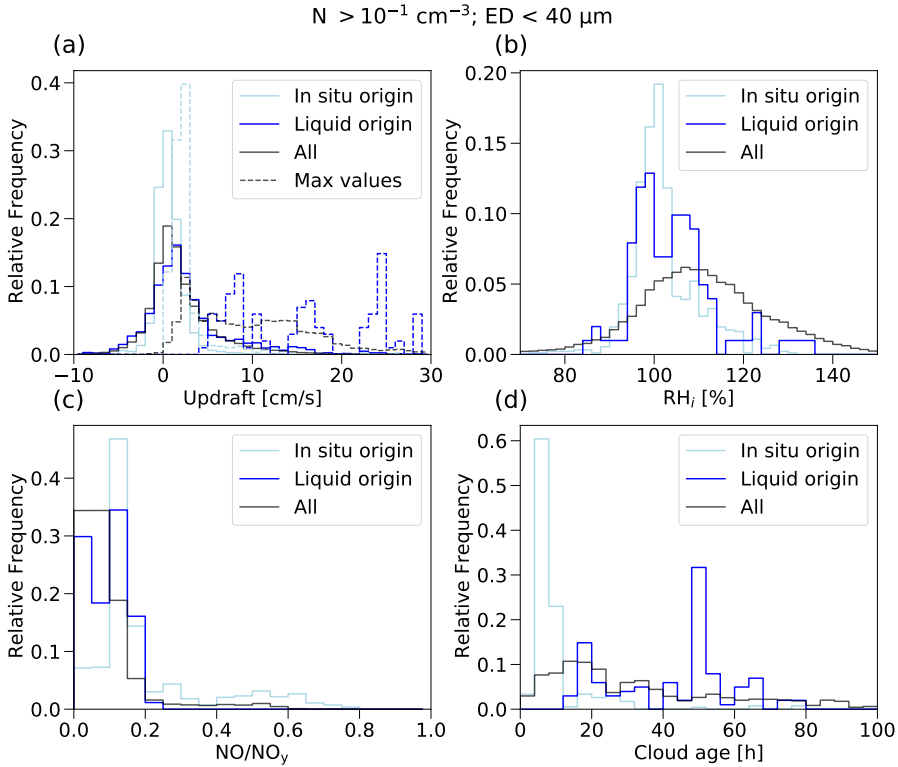


Figure 6.3: Relative frequency of atmospheric parameters during overall CIRRUS-HL measurements and for HNLED events at cruise altitudes ($N > 10^{-1} \text{ cm}^{-3}$, $ED < 40 \text{ } \mu\text{m}$, and altitude $> 8000 \text{ km}$) of (a) updraft velocities along the backward trajectories, (b) relative humidity over ice (RH_i), (c) NO/NO_y ratio and (d) cloud duration. The distribution of the maximum values of vertical velocity along the trajectories is also represented with dashed lines in (a). The selected data (HNLED) are classified in liquid origin (dark blue) and in situ origin (light blue). All data points without selection are represented in dark gray as a reference.

It is noteworthy to examine the updraft speeds as high updrafts, induced by gravity waves or orographic waves, can lead to a high amount of homogeneously nucle-

ated ice crystals. Since these events also produce a high amount of small ice crystals, they would satisfy the criteria for HNLED. However, panel (a) indicates that the measurements identified as HNLED are generally not dominated by strong updrafts along the backward trajectories. Specifically, in situ cirrus of HNLED events exhibit relatively slow updrafts, typically below 10 cm s^{-1} , which are slower than the overall updrafts (in black). Therefore, the explanation of the HNLED events can not be attributed to homogeneously nucleation events, as discussed in Section 5.4. In addition, simulation from the EMAC-MADE3 of newly formed ice crystals from homogeneous nucleation during the campaign period revealed a little influence in the data set (see Section 5.6). Maximum updraft velocities from the history of liquid origin cirrus reveal higher values (between $10 - 30 \text{ cm s}^{-1}$) compared to the in situ cirrus. The majority of data points from both in situ and liquid origin HNLED selection are centered at 100%, although a fraction of the liquid origin data points exhibit higher supersaturation. The higher updrafts and relative humidity found in the liquid origin group could be an indication of wrongly classified as HNLED, corresponding to isolated measurements in convective systems instead of aviation-influenced samples. As mentioned previously, HNLED events seem to be connected to in situ cirrus instead of liquid origin cirrus, which aligns with findings by Li et al. (2022).

In Fig. 6.3(c), the NO/NO_y signature displays enhanced values above 0.1 for the in situ origin HNLED events, while the liquid origin cases generally follow the overall trend observed in all measurements. Jurkat et al. (2011) reported NO/NO_y ratios around 0.8 for young contrail plumes of 60 to 120 s. This ratio decreases notably with older ages.

Fig. 6.4 shows a further analysis of the relative humidity measurements separated in high and mid-latitudes and liquid and in situ origin cirrus, including the fraction of HNLED measurements. Liquid origin HNLED events are barely visible due to the small fraction which they represent. Fig. 5.14(c) showed the frequency distribution of relative humidity for the M-M, M-H, and H-H cirrus classification, observing and increased RH_i in the H-H cirrus. Fig. 6.4 also shows higher supersaturation for both in situ and liquid origin cirrus at high latitudes compared to mid-latitudes. In particular, while in situ cirrus at high latitudes show larger values of RH_i than the liquid origin cirrus, in situ cirrus at mid-latitudes are characterized by smaller values and almost centered at 100%, similar to the HNLED events. Previous studies have indicated a relaxation toward saturation of relative humidity measurements within contrails (Kaufmann et al., 2014).

The relaxation of the relative humidity in cirrus at mid-latitudes is explained by different factors. Firstly, to the direct contribution of the HNLED events, which have been characterized by a direct influence of aviation. Secondly, the HNLED events represents the fraction of aviation-induced cloudiness, which is still detectable and can be disentangled from the whole picture, but older contrail cirrus already overlapping with the natural cirrus microphysical properties would not be included in the HNLED selection but may also show reduced supersaturation. Lastly, the existence of a higher influence from anthropogenic sources at mid-latitudes contribute to higher INP concentrations which can remove the water vapor.

In general, the campaign period was characterized by increased humidity in the upper troposphere, which, in general, contribute to more persistent contrails and a stronger warming effect (Wilhelm et al., 2022; Teoh et al., 2022; Wang et al., 2023). How-

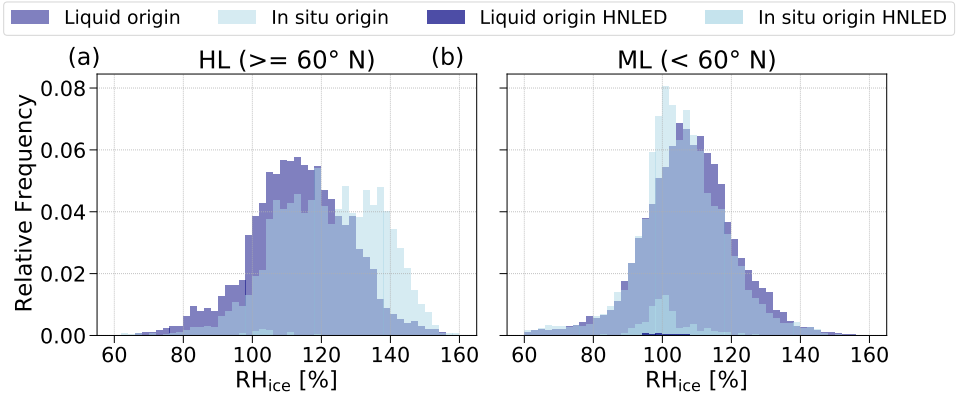


Figure 6.4: Relative frequency of relative humidity with respect to ice measurements (RH_i) of all measurements (light shade) and HNLED events ($N > 10^{-1} \text{ cm}^{-3}$ and $ED < 40 \text{ }\mu\text{m}$, darker shade) for (a) high latitudes and (b) mid-latitudes. The selected data are also classified in liquid origin (dark blue) and in situ origin (light blue). The frequency of occurrence of the HNLED events has been normalized with the total number of all in situ and liquid origin measurements, respectively.

ever, the potential contrail cirrus cover is the lowest during summer over Europe (Dischl et al., 2022). The increase in air temperature in summer hinders the formation and persistence of contrails and their radiative effect is mostly cooling because of the increased sun hours in summer in the North Atlantic corridor (Teoh et al., 2022).

This study does not show a high frequency of direct observations of young contrail encounters, but rather of aged contrails and contrail cirrus. It demonstrates that the influence of aviation, identified conservatively, was almost omnipresent throughout the mission and not limited to days targeted for contrail outbreak measurements. Additionally, it indicates a change in the available supersaturation in regions with high air traffic activity compared to more pristine regions.

6.4. SUMMARY

This chapter provides an overview of a central topic currently under discussion in the scientific community: the impact of contrail formation on natural cirrus clouds and the change in their microphysical properties.

An influence of contrail formation and interaction with natural cirrus could be identified in the data set, even though the conditions for contrail formation are not as favourable in summer compared to winter (Dischl et al., 2022) and even though the air traffic was still reduced in 2021 due to COVID-19 (ICAO, 2022; Schumann et al. (2021) and Voigt et al. (2022)). Measurements with ice number concentrations larger than 0.1 cm^{-3} and effective diameters smaller than $40 \text{ }\mu\text{m}$ (lower right section of Fig. 6.1(a) and (c)) were classified as so-called "high N and low ED" (HNLED) events. This group was analysed regarding specific indicators of aviation influence, such as NO/NO_y ratio or relative humidity over ice, which provided important evidence for identifying the measurements as contrail cirrus. Homogeneous nucleation as the cause of high number

concentrations and small diameters was excluded by analysing modelled and measured updraft speeds during the campaign and was concluded that, in general, high updraft speeds were not present. Additionally, an analysis combining backward trajectories and modelled newly formed ice crystals from homogeneous nucleation and heterogeneous nucleation on diverse ice nucleation particles revealed few homogeneous nucleation events in the clouds history. However, it should be noted that flights targeting and performed in convective systems (F12 and F15) were excluded from the analysis, and orographic waves were not an objective of the mission. Therefore, a potential bias toward more heterogeneous nucleated ice clouds might exist in this data set.

The analysis of events characterized by high number concentration and low effective diameter was supported by flight reports and contrail cirrus predictions and helped to identify enhancement in the NO and NO_y mixing ratios caused by isolated convective clouds. However, the direct association of all HNLED samples with the corresponding emitting aircraft was not performed. This task poses a significant challenge due to the old ages of the contrail cirrus in the measurements included in this analysis, during which atmospheric conditions (e.g., wind speed, wind direction...) can change and complicate backtracking, as well as the busy air traffic over Central Europe.

A stronger influence of aviation was found within in situ origin cirrus compared to liquid origin cirrus. In addition, notably higher supersaturation levels were observed at the high latitudes, while the higher influence of aviation at mid-latitudes likely facilitated the depletion of water vapor in the upper troposphere through contrail formation, thereby relaxing the supersaturation values towards 100%. Importantly, it was shown that the separation between the microphysical properties of contrail cirrus and natural cirrus is diffuse. This is because particles in contrail cirrus grow with contrail age, as well as get reduced in number, and ultimately achieve properties similar to natural cirrus. The contrail cirrus data set contributes to the extension of the limited existing data of contrails with ages exceeding 3000 s.

7

BACKGROUND AEROSOL CONCENTRATIONS FROM OBSERVATIONS AND MODEL

This chapter offers an outlook on the role and relevance of background aerosol in the formation of contrails from low-particle emission propulsion technologies, such as hydrogen-powered aircraft, and it provides further insights into the research question **RQ3**. *What role do aerosols and atmospheric dynamics play in shaping the properties of high-latitude cirrus in comparison to those at mid-latitudes? How does simulated aerosol concentrations compare to measurement data in air traffic relevant regions?*

To provide context and an overview of current knowledge on particle activation in the low-particle-emission regime, a literature review and interpretation of recent findings' implications for future propulsion technology development are included in Section 7.1. The observations of aerosol concentrations during the CIRRUS-HL campaign are shown and compared with model simulations from the EMAC-MADE3 model (see Section 5.6.1) in Section 7.2. This analysis serves two purposes: characterizing the aerosol concentrations during CIRRUS-HL for mid- and high latitudes, and validating the model with a comprehensive background aerosol data set.

A concise overview of the measurement system utilized is provided in Section 7.2.1, along with the method for evaluating data from the simulations from the EMAC-MADE3 model. The analysis and discussion of the results are presented in Section 7.3. This assessment and validation, with data obtained in a representative region for busy air traffic operations, are highly valuable for further studies investigating the role of background aerosol in contrail formation in the low particle emission regime. Finally, a summary is provided in Section 7.4, along with final remarks on further considerations and associated challenges.

The figures of this chapter have not been published.

7.1. INTRODUCTION TO CONTRAIL PARTICLES ACTIVATION IN THE LOW-PARTICLE REGIME AND CONTRAIL FORMATION FROM HYDROGEN AIRCRAFT

A highly relevant and recent area of research of aviation effects focuses on understanding contrail formation and properties in the context of future propulsion technologies. In Section 2.4, the conditions and mechanisms underlying the expansion and mixing of exhaust plumes from conventional aircraft powered by kerosene were explained. The primary precursors of ice particle formation in these contrails are non-volatile particle matter (nvPM), predominantly soot particles typically ranging from 10 to 30 μm , which are residues from fuel combustion (Kärcher, 1999). Additionally, volatile particles (vPM) are present in the exhaust plume, primarily aqueous particles containing sulfuric acid and nitrates nucleated from exhaust gases at an early stage in the plume (Kärcher, 1999). The size of the volatile particles is only several nanometers, often referred to as liquid ultrafine particles. The Kelvin effect, explained in Section 2.2.1, restricts particle activation into droplets based on the particle diameter, requiring high supersaturations for the small vPM to become activated and nucleate homogeneously thereafter (Kärcher & Yu, 2009). Consequently, in the rich-soot regime, ice forms preferentially on soot particles, which are abundant in kerosene combustion exhausts, and vPM can still nucleate on soot particles, serving as coating.

Given the direct relationship between the climate impact of contrails and ice particle number concentrations, which in turn is connected to the number of soot particles, reducing soot emissions can mitigate the climate impact of contrails and contrail cirrus (Bock & Burkhardt, 2019). The adoption of alternative fuels, such as sustainable aviation fuels (SAF), which have reduced fuel aromatic, naphthalene and sulfur contents, facilitates decreased non-volatile and volatile particle emissions and, consequently, reduce ice number concentrations in contrails (Moore et al., 2015; Bräuer et al., 2021b; Voigt et al., 2021; Märkl et al., 2024).

However, the ice number concentration reduction only occurs as long as the soot emissions are within the soot-rich regime (emission index, $EI > 10^{15} \text{ kg-fuel}^{-1}$) (Kärcher & Yu, 2009; Kärcher, 2018). If soot emissions are further reduced ($EI < 10^{13} \text{ kg-fuel}^{-1}$), the ice nucleation in the soot-poor regime is no longer controlled by the soot particles, but by the emitted vPM (or ultrafine particles), or by the entrained background tropospheric aerosol (Kärcher & Yu, 2009). The number of nucleated ice crystals in this regime is determined to a significant extent by the ambient temperature and supersaturation reached in the plume. At colder ambient temperatures, the activation of vPM is enhanced producing a high number of ice crystals, while temperatures closer to the temperature threshold for the SAC might lead to the activation of only background aerosol particles (Kärcher, 2018). This is currently associated to high uncertainties due to the lack of measurements in this regime. Soot emissions of the current aircraft fleet are still in the soot-rich regime, even when using SAF (Bräuer et al., 2021b; Voigt et al., 2021; Märkl et al., 2024).

In the context of contrail formation in the low-soot regime, substituting kerosene with hydrogen as fuel for engine combustion emerges as a promising technology. This shift has a high potential for reducing the aviation climate impact, as combustion of

hydrogen produces primarily water vapor, with no direct CO₂ emissions. Nevertheless, questions remain regarding the non-CO₂ effects. While NO_x emissions are still present as inherent byproducts of the high temperatures reached in the combustion chamber, it would be avoided in a fuel cell application. Moreover, the absence of carbon during combustion means that no soot particles are expected to form, as they typically result from the incomplete combustion of hydrocarbons contained in the conventional fuels.

As described in Section 2.4, the Schmidt-Appleman criterion (SAC) provides the conditions for contrail formation primarily based on the thermodynamics of the plume mixing process (Schumann, 1996), which remains applicable when hydrogen is used as fuel (Schumann, 1996; K. Gierens, 2021). The different fuel and engine parameters for hydrogen compared to kerosene combustion give a different slope of the mixing line (Eq. (2.7)). According to K. Gierens (2021) and Schumann (1996), the slope, G , increases by a factor of 2.6 compared to kerosene under equivalent propulsion efficiency and ambient pressure conditions. Consequently, the SA threshold temperature for hydrogen is estimated to be approximately 10 K warmer than that for kerosene, implying that contrails could form at lower altitudes when hydrogen is the fuel source. However, the ambient temperature still needs to be below the droplet freezing temperature for the contrail ice crystals to form and persist (see Figure 2.10). Moreover, even larger G values are anticipated for fuel cells, allowing for warmer SA threshold temperatures and higher peak supersaturations in the plume, due to cooler exhaust temperatures.

However, despite the theoretically favorable conditions for contrail formation, particles capable of becoming water-activated are necessary to initiate the process, since the supersaturation level might not be high enough to trigger droplet homogeneous nucleation from the gas phase alone. In the absence of soot particles, background aerosols might play a crucial role in facilitating contrail formation from hydrogen propulsion, as illustrated in Fig. 7.1 (Bier et al., 2024). The processes in the exhaust plume are expected to be similar to those from kerosene combustion, with ambient aerosol particles being activated in this case. The lower number of entrained ambient aerosol in the plume, compared to the emitted soot particles from kerosene combustion, would lead to a reduction in the number of nucleated ice crystals but with larger crystal sizes due to the high water vapor content in the plume.

A modelling study by Bier et al. (2024) compares the optical thickness of contrails generated by kerosene combustion to those formed by hydrogen combustion under varying concentrations of background aerosol. The results show a clear reduction in contrail optical thickness when switching to hydrogen due to the higher concentrations of soot typically found in kerosene combustion plumes. However, the variability in contrail optical thickness is expected to be high depending on the available concentration of background aerosol. The size of the particles is only relevant for the contrail particle number for particle radius smaller than 10 nm, which require higher water supersaturations to become activated due to the Kelvin effect, as explained in Section 2.2.1. Aerosol particles larger than 10 nm in radius are all activated.

The conclusive point is that accurate characterization of the aerosol background concentration and size distribution is highly needed for improving predictions of ice number concentrations in the soot-poor regime. However, existing measurements and studies characterizing aerosol number concentrations are mainly in remote areas, which

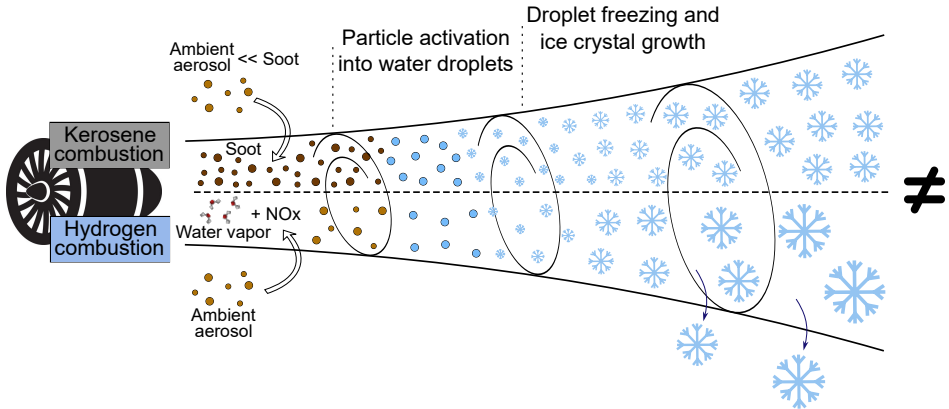


Figure 7.1: Schematic illustration of the hypothesized processes during contrail formation from hydrogen combustion (lower part) compared to kerosene combustion from conventional aircraft (upper part). (Based on Fig. 2 of Kärcher (2018) and Fig. 2.9 of this thesis)

do not directly relate to actual air traffic routes (e.g., Borrmann et al. (2010) and Brock et al. (2021)). Validation of the models assumptions on background aerosol using observational data from busy air traffic regions is key for improving predictions of the climate impact of future technologies.

7.2. COMPARISON OF MEASURED AND MODELLED BACKGROUND AEROSOL CONCENTRATION DURING CIRRUS-HL

The increasing relevance of characterizing background aerosol concentrations in order to address current and future questions on contrail formation in low-particle-emission scenarios has been highlighted in the previous Section 7.1. Motivated by this necessity and taking advantage of the comprehensive data set obtained during CIRRUS-HL, which includes aerosol measurements over key regions such as the North Atlantic and Western and Central Europe, a comparison with the EMAC-MADE3 global aerosol model is conducted and discussed in this section. This comparison focuses on total aerosol number concentrations within the size range of $D \gtrsim 12$ nm and $D \gtrsim 250$. Additionally, the non-volatile particle number concentration of $D \gtrsim 14$ nm from the measurements is also provided. Furthermore, the background aerosol concentrations are separated into mid- and high latitudes, as in the analyses of Chapter 5, to assess the latitudinal differences in aerosol concentrations and relate them to the observed differences in the cirrus micro-physical properties.

7.2.1. OVERVIEW OF MEASUREMENT TECHNIQUES AND MODEL SETUP

The measurement data during the CIRRUS-HL campaign were collected and processed by Daniel Sauer and Jennifer Wolf. As aerosol data evaluation was not a focus of this thesis, a brief overview of the measurement techniques is provided below, along with some words on the model setup applied for this study and the validation approach employed.

The measurements discussed below correspond to two distinct ranges within the aerosol size range spectrum, as outlined in Section 2.3.3: particles with diameters greater than approximately 12 nm, covering the Aitken mode, and particles ranging from $250 < D[\text{nm}] < 3000$, belonging to the accumulation mode and part of the coarse mode. The measurement system utilized by DLR aboard the HALO aircraft is known as the Aerosol Measurement System (AMETYST). Particles exceeding approximately 12 nm are measured using a Condensation Particle Counter (CPC; model Grimm SkyCPC 5.410), while an Optical Particle Counter (OPC; model SkyOPC 1.129) is employed for larger particle sizes (Minikin et al., 2012). Both instruments, manufactured by the company GRIMM Aerosol, were adapted for aircraft applications and operate based on the detection of forward scattered light from a laser beam, similar to the principle of forward scattering cloud probes (see Section 3.1).

Not only does the OPC provide information on the total number of sampled particles, but it also allows for the derivation of particle sizes, with particle counts sorted into various size channels (Walser et al., 2017). However, particles falling within the CPC size range are not directly detectable. Instead, the instrument creates a highly supersaturated environment using the vapor of a working substance, typically butanol, to activate all particles and grow them to sizes detectable by the instrument's optical block (Minikin et al., 2012). A sigmoid function representing the counting efficiency dependent on size enables the determination of the cut-off diameter, which represents the size of particles counted with an efficiency of at least 50%. It mainly depends on the temperature difference between the saturator and condenser, adjustable through laboratory calibrations accordingly (Walser, 2017). However, when using an aircraft as measurement platform, the cut-off diameter is further influenced by losses in the pipelines from the inlet to the instrument.

The AMETYST system comprises three CPCs. CPC0 and CPC3 for total aerosol, with nominal cut-off diameters of ≈ 7 nm and ≈ 18 nm, respectively. However, the real cut-off diameter of the CPC0 increases with decreasing pressure due to inlet losses. Andreae et al. (2018) reported cut-off diameters of 11.2 nm at 500 hPa and 18.5 nm at 150 hPa for the AMETYST system. The inlet system was improved for the CIRRUS-HL campaign, and a smaller cut-off diameter of ≈ 12 nm is assumed for these measurements, based on the PhD thesis by J. Wolf (2023). Additionally, CPC2 is dedicated to measuring non-volatile particles larger than approximately 14 nm. Non-volatile particles can be measured by positioning a thermodenuder upstream of the CPC (Fierz et al., 2007). By adjusting the set temperature to the evaporation temperature of the volatile material, only non-volatile particles are retained. The upper diameter limit of the CPC is governed by the inlet characteristics (specifically, the HASI isokinetic inlet), estimated to fall between 1.5 and 3 μm . However, this upper limit is not particularly relevant as the lower particle size mode dominates, offsetting the contribution of larger particle to the total number concentration. For further details on the measurement techniques employed by both instruments, consult literature sources such as P. Kulkarni et al. (2011).

The model used for the total aerosol concentration comparison is the EMAC-MADE3, which has already been introduced and described in detail in Section 5.6.1. For the simulations performed for this study, the submodel Sampling in 4 Dimensions (S4D; Jöckel et al. (2010)) was used, which is particularly suited for comparisons of observations with

moving platforms, such as aircraft missions (Beer et al., 2020). The output of the model is interpolated across the flight tracks, providing an output every 15 minutes. Given that the altitude of the flight track can change within the 15 minutes and to take into account this variability, the approach used was to consider not only the grid point at the flight track pressure level, but also one pressure level above and below. This approach also increases the statistics of the model, which is limited compared to the measurements due to the corresponding temporal resolution.

7.3. ANALYSIS AND RESULTS

The comparison of the observations during the CIRRUS-HL campaign and the S4D simulations from the EMAC-MADE3 model for the same period, introduced in the previous Section 7.2.1, adopts a statistical approach. Median values, along with the 25th, 75th, 1st, and 99th percentiles are calculated across pressure levels of 40 hPa each, ranging from 900 hPa to 150 hPa.

Firstly, in Fig. 7.2, vertical profiles of measured background aerosol concentrations are depicted for three distinct particle size modes, distinguishing between measurements at mid- and high latitudes and the number of 1-second samples per pressure bin of 40 hPa. The median number concentration of particles in the accumulation mode ($D > 250$ nm) ranges from 4 to 70 cm^{-3} . For total (non-volatile) particles in the Aitken mode ($D > 12$ nm), median values fluctuate between 200 to 3000 cm^{-3} (50 to 1000 cm^{-3}). As discussed previously in Chapter 5, measurements at mid-latitudes were more numerous, and the upper troposphere was sampled with higher frequency.

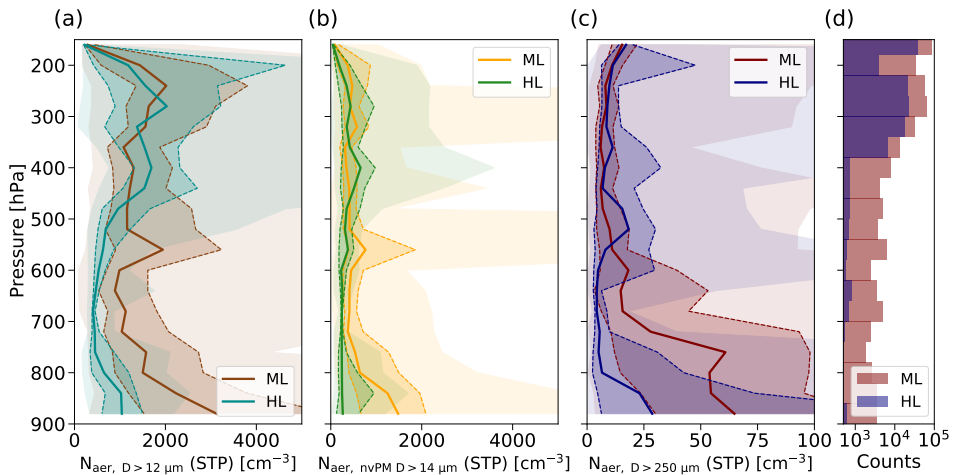


Figure 7.2: Pressure profiles of background aerosol concentrations at high and mid-latitudes during CIRRUS-HL for different size ranges: (a) diameters > 12 nm measured with the CPCs, (b) diameters > 14 nm measured with the CPCs, and (c) diameters > 250 nm measured with the OPCs (see Section 7.2.1). Median profiles are indicated with solid lines, the areas between the 25th and 75th percentiles are indicated within dashed lines. The lightest shadowed areas represent from 1st to 99th percentiles. (d) Number of observations per pressure bin of 40 hPa each. (Data provided by D. Sauer)

In both cases of total and non-volatile particles in the Aitken mode ($D > 12$ nm), as well as for particles in the accumulation mode ($D > 250$ nm), the median values across pressure levels for HL and ML measurements exhibit negligible differences up to approximately 500 hPa. Above this pressure level (at lower altitudes), concentrations at ML are notably higher for the three cases. These differences are, in general, statistically significant. This significance was confirmed through the application of the U-test according to Wilcoxon, Mann and Whitney, as previously employed in Fig. 5.7 within Section 5.3.

Even though differences at lower altitudes are observed between mid- and high latitudes in the three particle size modes, these differences are by factors of 2 to 4, and they do not reach the almost one order of magnitude difference in the ice crystal number concentrations between mid- and high-latitude cirrus observed in Fig. 5.6 in Chapter 5. However, it should be noted that the data here represents total aerosol concentrations and not directly ice nucleating particles. In addition, higher median ice crystal number concentrations at mid-latitudes compared to high latitudes were also attributed to contrail and contrail cirrus formation.

In comparison to previous measurements, Borrmann et al. (2010) report lower concentrations across all altitudes for both the Aitken and accumulation mode compared to these measurements, with the exception of their measurements from the "Test Campaign" in Italy. Furthermore, the background aerosol concentration in the southern hemisphere, as reported by Minikin et al. (2003), also displays lower values. In the northern hemisphere, while the median concentrations from the Aitken mode are slightly lower than the median values shown in Fig. 7.2, the median concentrations of the accumulation mode are higher, particularly in the upper troposphere. Contrasting the concentration of the Aitken mode in the lower troposphere with measurements from Brock et al. (2021) reveals lower concentrations compared to the CIRRUS-HL measurements, which is likely due to a lack of anthropogenic ground emission sources over the targeted remote areas over the oceans. The measurements of Fig. 7.2, therefore provide a valuable addition to the existing data sets on background aerosol concentrations data sets, which are available in the literature. The measurements from CIRRUS-HL might be better suitable for contrail cirrus predictions due to the geographical region covered.

In the following analysis, the observations are compared with data from the EMAC-MADE3 model. Even though the model is validated with data from only one campaign, it is still a relevant insight since the data set includes different meteorological situations and was conducted in a region where air traffic is widely present. This validation is of particular relevance for future studies investigating the properties of contrails formed from background aerosol particles based on model simulations. To this end, Fig. 7.3 offers a comprehensive comparison between the measurements (darker colors) presented in Fig. 7.2 and the model output (lighter colors) for total aerosol number concentrations of particles $D > 12$ nm and $D > 250$ nm. Specifically, the difference between the observations and the model across the pressure levels is shown in Fig. 7.2(d) and (e).

In general, higher variability is found in the observations when comparing the 25th-75th percentiles and 1st-99th percentiles between the model and the observations for both particle size modes. This is expected due to the higher resolution of the measurements and the lower statistics of the model output (one data point every 15 minutes). However, this variability is an important aspect to take into account when consider-

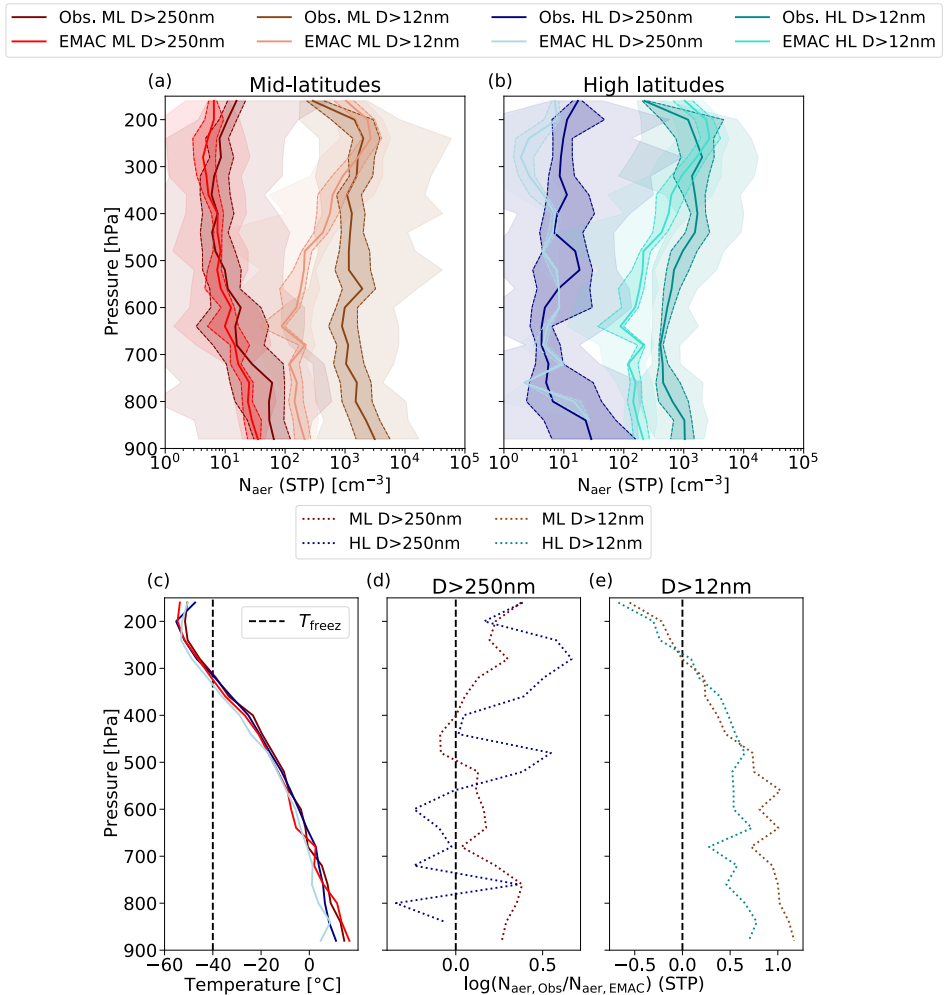


Figure 7.3: Comparison of pressure profiles of background aerosol concentrations in two size ranges between the observations and the EMAC model for (a) mid-latitudes and (b) high latitudes. Median profiles are indicated with solid lines, the areas between the 25th and 75th percentiles are indicated within dashed lines. The lightest shadowed areas represent from 1st to 99th percentiles. (c) Vertical profile of the temperatures from observations and model with the freezing threshold (black dashed line) at -40 °C. Median difference in ratio between observations and model for (d) $D > 250$ nm, and (e) $D > 12$ nm. (Observational data provided by D. Sauer and modelling data by C. Beer)

ing, for example, best- and worst-case scenarios for contrail formation on background aerosol and its climate impact.

A close agreement is observed for the larger particles mode ($D > 250$ nm), particularly at mid-latitudes. Below 300 hPa, the increase in the median concentration from the observation with decreasing pressure is not captured by the model, probably due to local biomass burning events, which were encountered at those altitudes during several

flights. At lower altitudes (> 600 hPa), the difference between observations and model becomes highly variable (ranging from -0.5 to 0.5 in the difference ratio) for high latitudes due to low statistics. In contrast, for mid-latitudes, the difference remains within a range from 0 to 0.4 reaching the maximum difference at 760 hPa. For lower pressure levels (< 400 hPa), the model tends to underestimate the concentration for both mid- and high latitudes, with the largest difference exceeding 0.5 occurring at 280 hPa for high latitudes.

In the Aitken mode ($D > 12$ nm), the sign of the difference between observations and the model changes around 250 hPa. At lower pressure levels, the model tends to overestimate the measurements, possibly due to an overestimation of the upward transport or particle nucleation rate (Kaiser et al., 2019). At lower altitudes (> 300 hPa), the model consistently underestimates the measurements for both mid- and high latitudes. The difference progressively increases from 300 hPa reaching a maximum of 1 for mid-latitudes close to the ground. The model underestimation of the smaller particles in the lower troposphere is known from other studies, such as Kaiser et al. (2019). The comparison of the model data with the INCA and ACCESS-2 campaigns reveals similar discrepancies in the vertical profiles, which are attributed to a possible underrepresentation of natural sources of aerosol in the model.

As discussed previously at the end of Section 7.1, precise data on the concentrations of background aerosols are essential for accurately determining the resulting optical thickness of contrails produced by hydrogen-powered aircraft and, subsequently, its potential impact on the climate. In particular, the background aerosol mixed in the plume acquires even more relevance when the ambient temperature is close to the freezing threshold temperature. In this case, while a contrail from kerosene would not be able to form at such high temperatures, the higher SA threshold temperature for hydrogen propulsion technologies could enable the formation of a contrail, if the conditions for droplet freezing and persistence are also met (Bier et al., 2024). In this context, panel (c) of Fig. 7.3 indicates that ambient temperatures below the freezing threshold are found above approximately 300 hPa during CIRRUS-HL. A generally good agreement from model and observations is observed around 300 hPa, but larger differences appear for lower altitudes (above 400 hPa) at mid-latitudes. The data presented here correspond to the summer period, and lower temperatures are expected during winter, potentially shifting the interesting region downwards. However, these trends might differ for observations and simulation data in winter. Further intercomparisons should be undertaken for verifying these findings across different regions, seasons, and altitudes. This would help to extend the present analysis and improve the statistics and representativity.

7.4. SUMMARY

This chapter primarily offers an outlook on the ongoing process of understanding contrail formation from future technologies designed to mitigate CO_2 emissions. Despite the CO_2 emissions reduction, these technologies still have non- CO_2 effects, mainly from contrail formation, whose implications remain uncertain. This uncertainty is attributed partially to numerous unknowns surrounding the nucleation mechanisms involved and the lack of measurements which validate the theories.

Understanding the mechanisms involved in contrail formation from future propul-

sion technologies is urgently needed due to the unknown potential climate impact. Depending on the characteristics of the nucleation process taking place, various outcomes can arise. Unlike conventional engines emitting high numbers of soot particles, which serve as nuclei for contrail formation, contrail particle formation from hydrogen combustion may initiate from background aerosols in the plume. Depending on the background aerosol concentration, the number of ice particles in the contrail varies, but it is expected to be significantly lower compared to kerosene combustion (Bier et al., 2024). However, very high values of peak supersaturation values might be achieved in the plumes of contrails formed from fuel cells.

In order to investigate the background aerosol concentrations in relevant regions for air traffic, the in situ measurements of aerosol concentrations performed during CIRRUS-HL were analysed and used to evaluate the simulated aerosol concentrations provided by the EMAC-MADE3 global aerosol model along the campaign flight tracks. Differences in the measured aerosol concentrations were found between high and mid-latitudes by a factor of 2 to 4, which is smaller than the difference in ice crystal number concentration described in 5.

The model-observations intercomparison showed, in general, a good agreement, particularly for the accumulation mode at mid-latitudes. Higher discrepancies were found in the median number concentrations of particles in the Aitken mode for pressures above 400 hPa (lower altitudes). This mismatch might affect the prediction of ice crystal number concentrations in contrails from hydrogen-powered aircraft from regional and short-range regimes. Unfortunately, no information on background concentrations in the nucleation mode ($D > 3$ nm) could be provided due to the size limitations of the instrument and sampling line losses, but are expected to be higher than the concentrations in the Aitken mode. Further studies should focus on characterizing this aerosol size mode in air traffic regions to reduce the uncertainties in this regard.

Finally, in addition to background aerosol, vPM might also become relevant in a soot-poor regime. Ultrafine volatile particles can still form from hydrogen combustion from lubrication oils and NO_x emissions inherent to combustion processes at high temperatures. Even fuel cell-powered aircraft might avoid vPM from nitrates but can difficultly avoid lubrication in the moving parts of the propeller. Jet engine lubrication oils have been found to be a significant contribution to the ultrafine particle population near airports due to their high efficiency in new particle formation (Ungeheuer et al., 2021; Ungeheuer et al., 2022). Moreover, Ponsonby et al. (2024) showed that contrail particles from vPM from lubrication oils would follow a similar microphysical path than for soot particles, first by water activation and condensation and then homogeneous freezing. Even though soot particles are more efficient cloud condensation nuclei and would activate earlier (Kärcher & Yu, 2009), vPM from lubrication oil can compete and contribute to ice nucleation in contrails in the soot-poor regime (Ponsonby et al., 2024).

Future investigations should focus on characterizing the emission indices of lubrication oils for different engine concepts. Additionally, efforts on minimizing the nucleation of oil particles in the engine exhaust, by improving the sealing or conceiving an effective oil recovery system, should be done in parallel to the engine technological improvements. Already small fractions of oil contamination in the plume can lead to a number of particles in the same order of magnitude as soot emissions. The future ques-

tion will be on the competition for water vapor between vPM from lubrication oils, nvPM and vPM of background aerosol, or homogeneous droplet nucleation.

8

CONCLUSION

In this chapter, the main conclusions and outcomes of the study are presented, providing a general overview in Section 8.1, along with their scientific and technical implications for society. The chapter concludes with a detailed description in Section 8.2 of how the thesis addresses the research questions formulated at the beginning of this work, explaining the answers in the form of scientific results.

8.1. OVERVIEW

While contrail cirrus and natural cirrus clouds share similarities in terms of their appearance and general properties, they follow distinct microphysical formation pathways (see Chapter 2). In situ measurements of the microphysical properties of natural cirrus clouds and contrail cirrus are essential for enhancing our understanding of atmospheric processes and their climate implications. To investigate differences in microphysical properties between natural cirrus clouds at different latitudes and contrail cirrus, the CIRRUS-HL campaign was conducted and the obtained measurement data were evaluated. This thesis employed a statistical approach to elucidate the extent to which natural and anthropogenic aerosols, and aviation influence cloud formation.

The methodology employed in this research benefited from a variety of methods, allowing an in-depth investigation of the properties and life-cycle of ice clouds. The principal method involved in situ measurements by underwing cloud probes installed on the HALO research aircraft. During the campaign, I operated, calibrated, and maintained these instruments, and participated in flight planning. My main work focused on processing and evaluating this data to answer the research questions. Additionally, measurements from other research groups were used to support the analyses, including wind speed, GPS data, water vapor mixing ratios, nitrogen oxides, and aerosol data. Models such as LAGRANTO (data provided by H. Wernli, ETH) and EMAC-MADE3 (data provided by C. Beer, German Aerospace Center) were also used to obtain more information not covered by the measurements, including backward trajectories of air masses, aerosol loads, and other meteorological parameters computed along the trajectories. The new

ice nucleation origin classification that I introduced has already been adopted by other research groups within the CIRRUS-HL project and is expected to be applied in future publications, highlighting its valuable contribution to the scientific community.

The software developed to process and evaluate the data from the imaging probes for this thesis was an important part of the work and represents a valuable contribution to the research group. It addresses and resolves issues encountered with previously available programs and is already being used by other colleagues. This in-house software provides independence from external tools, which may not be adequately maintained or adapted to new instrumentation and applications. Furthermore, there are plans to share it openly with the scientific community, enhancing its utility and promoting collaborative advancements in the field.

Microphysical properties of cloud samples below -38°C (only ice clouds) were analysed using the data of 22 flights, including approximately 25 hours of in situ measurements in cirrus clouds, within a latitude range between 38°N and 76°N . These data were evaluated based on latitude, temperature, origin type and aerosol influence throughout the cloud's backward trajectories. The main conclusions can be summarized as follows:

- **Data set scope:** The CIRRUS-HL provided an extensive data set of cloud and aerosol microphysical properties for investigating the differences in cirrus microphysical properties across a latitude range between 38°N and 76°N in the Northern Hemisphere over Europe. Due to the large range covered, it proved to be very suitable for model intercomparison.
- **Latitude-based differences:** Cirrus at high latitudes, compared to mid-latitudes, were characterized by lower number concentrations, larger ice crystal sizes, and higher supersaturations in an environment with less aviation influence and fewer anthropogenic sources for ice nucleating particles.
- **Mid-latitude influence on high latitude cirrus properties:** An influence of mid-latitude air masses on the formation of high-latitude cirrus was identified, leading to differences in microphysical properties compared to cirrus formed directly at high latitudes.
- **Aviation effects:** Aviation effects were investigated, revealing more frequent contrail formation at mid-latitudes compared to high latitudes and an impact on natural cloudiness potentially by reducing supersaturation at altitudes where cirrus form.
- **Aerosol influence:** Altitude profiles of aerosol measurements showed smaller differences in median aerosol concentrations between mid- and high latitudes compared to those in ice number concentrations. These measurements were used to validate simulated aerosol data from the EMAC-MADE3 model, showing good agreement.

These findings highlight the importance of comprehensive in situ measurements and advanced modeling to enhance our understanding of the complex interactions between aerosols, cirrus clouds, and aviation-induced cloudiness. The following section

describes in more detail the main findings and how they provide answers to the research questions established at the beginning of this thesis.

8.2. ANSWERS TO RESEARCH QUESTIONS

The four research questions which motivated and guided this study were stated at the beginning of the thesis in Chapter 1. In the following, each question is followed by a description of the related findings and to which extent could be answered.

- **Do measurable differences exist in the microphysical properties of cirrus clouds between high latitudes and mid-latitudes? If so, what are they?**

The first research question was addressed in Sections 5.3 and 5.4, which required a comprehensive data set of cirrus microphysical properties comprising the whole cloud size spectrum across a wide range of latitudes in the Northern Hemisphere. Fig. 5.6 illustrates decreasing number concentration with latitude and increasing effective diameter of ice crystals in cirrus at higher latitudes. The overall median number concentration of mid-latitude cirrus (0.0086 cm^{-3}) is higher than for high-latitude cirrus (0.001 cm^{-3}) by almost an order of magnitude. According to the measurement data, the median effective diameter in mid-latitude cirrus is $165 \mu\text{m}$ compared to $210 \mu\text{m}$ at high latitudes. The vertical profiles of median number concentration and effective diameter for high-latitude cirrus ($\geq 60^\circ \text{ N}$) and mid-latitude cirrus ($< 60^\circ \text{ N}$) over a range of temperatures, as shown in Fig. 5.7, reveal a consistent offset between the two. Both cirrus types exhibit similar temperature ranges. To ensure the comparability of cirrus samples, the altitude of measurements relative to the tropopause was depicted in Fig. 5.8, showing that nearly all measurements were conducted within the troposphere (2.6% in the stratosphere).

Using backward trajectories of the sampled air masses, cirrus samples were classified based on their origin into liquid or in situ origin cirrus. The results presented in Fig. 5.9 indicate that liquid origin cirrus were more frequently observed at both mid- and high latitudes, accounting for approximately 60% of the measurements. Furthermore, while both cirrus origin types exhibited differences in ice number concentration and effective diameter between mid- and high latitudes, these differences were more pronounced for in situ origin cirrus. This finding is also derived from the mean and median particle size distributions of the four groups, as displayed in Fig. 5.11.

The mean particle size distribution was compared between in situ and liquid origin cirrus at high and mid-latitudes. An enhancement by two orders of magnitude for particles smaller than $10 \mu\text{m}$ was observed for in situ cirrus at mid-latitudes. The extinction coefficients of in situ origin cirrus also differed noticeably between mid- and high latitudes, with higher frequencies of extinctions larger than 0.1 km^{-1} at mid-latitudes. These findings indicated the presence of contrail cirrus samples within the measurements and was further investigated in the context of the fourth research question in Chapter 6.

Contributing to the expansion of knowledge on this topic helps to better understand the cloud formation processes in the upper troposphere, which has relevant outcomes for the society. One of the biggest challenges in climate science is the accurate representation of clouds, in particular of cirrus clouds. The remaining unknowns of these

processes also affect the predictability and impact assessment of contrails and contrail cirrus.

- **How do mid-latitude air masses influence cirrus at high latitudes? How do their properties change?**

This topic was investigated in Section 5.5, where a novel approach was applied to classify cirrus measurements based not only on the latitude of the measurement point but also on the latitude at their formation (Figs. 5.12 and 5.13). Cirrus were classified into three types: those formed and measured at mid-latitudes (M-M), those formed at mid-latitudes and later measured at high latitudes (M-H), and those formed and measured at high latitudes (H-H).

Traditionally, all cirrus clouds observed at high latitudes were considered high-latitude cirrus. The use of this new classification, however, reveals the importance of accurately characterizing high-latitude cirrus and shows that mid-latitude air masses significantly influence clouds at high latitudes, as represented by the M-H cirrus category. The data show that 37% of cirrus were measured at high latitudes, with 26% forming at mid-latitudes and only 11% being true high-latitude cirrus (H-H). The rest, 63% of the cirrus samples were measured at mid-latitudes. However, this might be biased by the latitude region covered in this campaign, and the portion of high latitude cirrus formed at mid-latitudes might be smaller when sampling beyond 76° N.

Distinct characteristics were observed between M-M cirrus and H-H cirrus, as depicted in Fig. 5.14. M-M cirrus typically exhibited higher ice crystal number concentrations (0.0086 compared to 0.0004 cm⁻³), smaller diameters (164 compared to 225 μm), and lower relative humidity with respect to ice (107 compared to 125%) compared to H-H cirrus. The M-H cirrus displayed a combination of these characteristics, reflecting their formation at mid-latitudes—where higher concentrations of ice nucleating particles are available—and subsequent growth at high latitudes, where supersaturation levels are higher. This results in more numerous ice crystals than in H-H cirrus but larger than those found in M-M cirrus. Moreover, 90% of M-H cirrus were of liquid origin, forming at lower altitudes and thus encountering higher concentrations of ice nucleating particles. Meanwhile, 86% of the H-H cirrus were of in situ origin. These findings are linked with the following question on the role of aerosols, which was investigated in Section 5.6.

These conclusions need to be further validated through future campaigns covering also a broad range of latitudes (see further discussions in the Outlook in Chapter 9). This extended research will help determine whether the observed patterns are consistent across different regions of the globe. Additionally, it remains to be seen whether M-H cirrus are predominantly of liquid origin or if this observation is specific to the synoptic situation prevailing during the summer months of 2021. A similar question arises for H-H cirrus, which were mainly of in situ origin in this study. Investigating whether a larger contribution of liquid origin cirrus to H-H cirrus could alter their overall properties would be an important aspect to consider for future research.

- **What role do aerosols play in shaping the properties of high-latitude cirrus in comparison to those at mid-latitudes? How does simulated aerosol concentrations compare to measurement data in air traffic relevant regions?**

The effects of aerosols on the microphysical properties of cirrus were primarily examined in Section 5.6, with additional analyses in Section 7.2. Information on the concentrations of ice nucleating particles (INPs) was derived from model simulations (provided by C. Beer, German Aerospace Center) using the EMAC-MADE3 model by means of calculating the INP concentrations and newly formed ice crystals along backward trajectories from the LAGRANTO tool (provided by H. Wernli, ETH), starting from the measurement points.

The results presented in Fig. 5.16 suggest a higher influence of INPs from dust, black carbon from aviation, and black carbon from other anthropogenic sources at mid-latitudes compared to high latitudes. However, this does not necessarily correlate with the number of nucleated ice crystals, which also depend on ambient supersaturation and the fraction of INPs that can be activated. Nevertheless, analyses of newly formed ice crystals along the trajectories in Fig. 5.19 indicated slightly higher number concentrations of INPs for M-M cirrus compared to M-H and H-H cirrus. Interestingly, the absolute frequency of ice crystal nucleation events on INPs from black carbon in H-H cirrus is very limited compared to nucleation events on dust or black carbon from aviation. In contrast, black carbon has a higher relevance in M-M and M-H cirrus than in H-H cirrus, likely due to the in situ origin of H-H cirrus forming at high altitudes where less black carbon is present. Future measurements of ice nucleating particles at the cold temperatures typical of the cirrus regime will help validate the conclusions derived from the model and the approach applied here.

The number of newly formed ice crystals, resulting from either heterogeneous nucleation on INPs or homogeneous nucleation, shown in Fig. 5.19, indicated a limited role of homogeneous nucleation in the cirrus formation processes observed during the CIRRUS-HL campaign. This finding suggests that the number of ice crystals in the sampled cirrus clouds was primarily controlled by the concentration of INPs, together with the ambient supersaturation, and the fraction of the INP population that can be activated. No significant difference in the influence of homogeneous nucleation was found between mid- and high latitudes. However, it should be noted that orographic waves were not an objective of the campaign, and flights targeting convective systems were excluded from this analysis. Consequently, despite encountering some isolated convective events during the return legs, the campaign's sampling strategy might be biased toward a limited number of observations of homogeneous nucleation events.

Regarding total aerosol number concentrations, both observations and model simulations agree on slightly lower concentrations at high latitudes, as shown in Fig. 7.3. This difference is smaller than the one observed for ice crystal numbers. However, it is important to note that total aerosol concentration is not a direct indicator of the cirrus particles precursors, as not all aerosol particles have the ability to nucleate ice. Additionally, a slight discrepancy between the model and observations for altitudes below 400 hPa was identified, which might influence the formation processes of contrails from low-particle-emitting propulsion technologies.

- **How does aviation influence the microphysical properties of natural cirrus?**

Chapter 6 focuses specifically on the effects of aviation, analyzing its influence using the presented data set of natural cirrus. From all measurements presented in Chapter 5,

NO and NO_y mixing ratios were analyzed in Fig. 6.1. An enhancement was found in a group of samples with high number concentrations ($> 0.1 \text{ cm}^{-3}$) and small effective diameters ($< 40 \text{ }\mu\text{m}$), compared to the overall mean values. These samples were identified as aged contrail and contrail cirrus, and various atmospheric parameters were investigated in this group. The values of relative humidity over ice for this group were close to 100%.

These measurements are mostly present in the in situ origin cirrus group at mid-latitudes (as shown in the lower right corner of Fig. 5.9(c)), indicating a higher influence of contrail formation within this group. In contrast, contrails and contrail cirrus are less likely to form and develop within liquid origin cirrus due to the lower altitudes at which these clouds typically form. Contrail cirrus samples were observed not only during targeted flights in predicted contrail outbreaks (as in Fig. 5.3(d)), but also over several days of the campaign period.

Although only 2.4% of all ice cloud measurements were classified as aged contrail encounters, this likely underestimates their actual occurrence. This underestimation arises from two main factors. First, the identification method was conservative, detecting only samples distinctly different from natural cirrus by enhanced NO and NO_y mixing ratios, reduced effective diameter, and increased number concentration. These properties dilute with the surroundings over time, and older samples or already dissipated contrails are not identifiable by this method. Consequently, such undetected contrail cirrus are also part of aviation effects but are not considered here. The second aspect is the non-representativity of the air traffic load in 2021 compared to usual levels, as it was still nearly half of pre-COVID-19 levels. Therefore, fewer contrails were expected during the CIRRUS-HL campaign.

Contrail cirrus impact natural cloudiness by precipitating and sublimating ice crystals at lower altitudes and reducing humidity at upper levels. As shown in Fig. 6.4, supersaturation levels at mid-latitudes are significantly lower than at high latitudes in the CIRRUS-HL region and time period, demonstrating the potential local effect of contrails. Consequently, it could be interpreted that the reduced relative humidity at mid-latitudes, coupled with a relatively high abundance of ice nucleating particles, results in the formation of cirrus clouds with higher number concentrations and smaller ice crystal diameters than those found at high latitudes, which are less affected by anthropogenic emissions, particularly aviation.

9

OUTLOOK

In this chapter, an outlook on the research is provided, critically examining its limitations and open questions, and outlining future lines of investigation. While this study has made valuable contributions to understanding the microphysical properties of cirrus and contrail cirrus, and has advanced methodologies for addressing these questions, several areas might require further exploration. This forward-looking discussion highlights the potential for new insights, as well as technical and methodological improvements, building upon the findings of this work.

9.1. PROSPECTS OF CLOUD MEASUREMENT TECHNIQUES

Various sources of uncertainty are associated with the measurements of the lower size range of the ice particle spectrum conducted with the CDP in this work. The primary issue presented in Chapter 3 was related to the discrepancy between the CDP and CAS particle size distributions under certain cirrus conditions. Despite different analyses, together with the study from McFarquhar et al. (2007), indicating a potential oversampling of shattered particles in the CAS measurements and a higher confidence in the CDP measurements, this issue remains an open problem to be solved, and the analyses provided are indicative, but require further evidence. While McFarquhar et al. (2007) reported similar behavior of the CAS and CDP for aspherical particles, these experiments were conducted in a laboratory setting, leaving open the possibility of the CDP missing ice crystals of particular habits at the aircraft speeds in real atmospheric conditions. Replicating the required conditions of a variety of ice crystal habits passing through the instrument's sample area at speeds of 150 – 200 m/s while obtaining accurate reference values of the particle's concentration poses a significant challenge. However, this clarification would be highly valuable for the scientific community.

Another source of uncertainty relates to the forward scattering technique employed by the CDP and CAS. This technique involves translating the measured scattered light into particle diameters, typically accomplished using Mie theory. However, this theory assumes spherical particles, valid only for liquid clouds. The T-matrix calculations are

an alternative to Mie theory, but are also restricted in their application, since they assume rotationally symmetric particles (Borrmann et al., 2000). This assumption does not accurately represent the complex forms of ice crystals found in cirrus clouds. The dual-wavelength technique commonly used in the radar field (Tetoni et al., 2022), which utilizes two laser sources with different wavelengths, can improve the size and shape retrieval based on Mie theory. It has been employed already for aerosol measurements in the range of 0.1 – 10 μm (Nagy et al., 2007), and could potentially be applied to characterize aspherical ice crystals in cirrus or contrails, especially considering the smaller particle size spectrum of the latter.

A further approach is the discrete dipole approximation (DDA), which offers potential solutions for particles of diverse shapes. This method divides the scatterer object into small volumes (dipoles), solving linear equations defined by the interactions between the dipoles and the incident light, providing a solution for the scattering cross-sections of different forms such as spheres, columns, or ellipsoids, including different orientations (Yurkin & Hoekstra, 2007). A recent study by Jang et al. (2022) utilized an open-source implementation in C called ADDA (Yurkin & Hoekstra, 2011) to evaluate the sizing error of current scattering probes by applying Mie theory. The study compared ADDA calculations for spherical particles and columns with different aspect ratios. This approach could be further explored to assess the variability in the scattering cross-section function for diverse ice particles shapes in cirrus. However, it is important to note that this method also has limitations due to the high computational time required, particularly as particle sizes increase. Moreover, it may not adequately address the inherent challenge of applying a one-to-one correlation of scattering cross-sections to particle size when dealing with cirrus measurements that include a variety of different ice crystal shapes and orientations.

The optical array probes (OAPs) (see Section 3.2 and Section 4.2) have become a reference in measuring larger particles, especially the complex forms of ice crystals, over the past decades. Despite their advantages, such as high sampling rates and large sample areas due to the simplicity of concatenating 1D image slices, which provide robust statistical data, they also suffer from drawbacks such as limited image resolution and sizing errors due to the depth-of-field effect. Neuronal networks (NN) offer a promising solution to enhance data processing from OAPs. Already, NNs have been employed to predict the diameter of spherical particles for the 2D-S (Schollmayer, 2021) and demonstrate good applicability for ice particle shape classification (S. J. O'Shea et al., 2016; Jaffeux et al., 2022). Further research into using NNs for analyzing grayscale images from the CIPG could be beneficial. However, generating a comprehensive training set that considers various ice crystals habits and potential deformations due to depth-of-field effects presents a significant challenge. Nevertheless, taking advantage of NNs in this context could substantially improve ice crystal sizing, since no depth-of-field correction for these measurements is available up until now.

Regarding alternative techniques to the OAPs, the HALOHolo instrument, based on a prior version (Holographic Detector for Clouds, HOLODEC) (Fugal et al., 2004), employs holographic technique, which captures images from the interference pattern of a reference wave and a wave diffracted or scattered by an object (Schlenczek, 2018). Unlike the conventional OAPs, this technique does not provide continuous measurements but

allows for obtaining the 3D coordinates of particles within a snapshot. Additionally, instruments like the Particle Habit Imaging and Polar Scattering (PHIPS) probe, developed and operated by the Karlsruhe Institute of Technology, which has been already operated on board the HALO aircraft during the CIRRUS-HL campaign, offers high-resolution ice particle images. PHIPS combines a Polar Nephelometer (Gayet et al., 1997; Crépel et al., 1997) and a stereo-microscopic imaging system, enabling acquisition of not only 3D images of the particles, but also their scattering properties (Abdelmonem et al., 2016; Schnaiter et al., 2018).

Further interesting developments are being made by companies like Artium with the High-Speed Imager (HSI) and the PI: Ice Crystals. These instruments rely on multi-beam illumination and a digital CMOS camera to capture images at a frame rate of 300 Hz, effectively detecting out-of-focus particles and mitigating depth-of-field effects (Esposito et al., 2019). In addition, compared to the 4 grayscale levels of the CIPG, they retrieve images at 256 grayscale levels, with increased pixel resolution ranging from 1 to 6 μm . This leads to higher quality images, enabling better habit classification. A significant advantage is the robust and high quality software developed for image processing, which does not require a further processing by the user and might help to a higher standardization of processing methods among different users and research groups. However, instruments with high-resolution images have reduced sampling efficiency due to smaller sample areas and lower camera frame rates. Nonetheless, considering the low particle concentrations typical of cirrus clouds, these instruments can complement OAPs effectively. Further research could concentrate on wind tunnel measurements and airborne campaigns utilizing both types of instruments to validate their performance or explore methods to integrate and exploit the strengths of each system.

In situ observations of atmospheric phenomena are crucial to understand the different factors and processes involved, and to enable the design and validation of models simulating those phenomena. However, organizing flight campaigns is complex and costly. Research aircraft flight hours are expensive, and planning the overall mission requires years in advance. Furthermore, there is a limited selection of research aircraft available, each suited for specific types of missions. Schedules are tight, and new ideas for future campaigns often face a waiting period of several years before realization. Additionally, aircraft measurements are limited to sampling one air mass at a time, although this can be expanded to two or three air masses if multiple aircraft are employed for the mission (e.g., the ACTIVATE campaign (Sorooshian et al., 2020) or the HALO-(AC)³ campaign (Wendisch et al., 2024)). This implies a considerable limitation in the number and variety of in situ observations. Unmanned aerial vehicles (UAVs) could be an excellent complement of aircraft research missions, offering maneuvering flexibility, automated operation, and potentially lower costs compared to research aircraft. In addition, swarms of UAVs could extend the horizontal and vertical resolution of in situ measurements improving the understanding of small-scale processes and phenomena. An example of the application of UAVs in atmospheric measurements is demonstrated in the CLOUDLAB experiment, which investigated the seeding of lower stratus clouds. This experiment involved one UAV for cloud seeding and another equipped with a Portable Optical Particle Spectrometer (POPS) for aerosol measurements (Henneberger et al., 2023; Miller et al., 2024). High-Altitude Long Endurance (HALE) UAVs,

such as the NASA Global Hawk, can fly at altitudes higher than 15 km, which makes them very suitable for cirrus measurements (Loegering, 2002). However, limitation on maximum take-off weight can hinder the integration of heavy payloads. More importantly, extreme weather conditions encountered during atmospheric measurements, such as turbulence, thunderstorms, fog or very cloudy conditions, pose significant challenges to ensuring safe and reliable UAV operation. Small and medium-altitude UAVs could still serve as a valuable complement for lower-altitude tasks, such as sampling of air mass origins.

9.2. FURTHER RESEARCH ON CIRRUS AND CONTRAIL CIRRUS

A key aspect in the study enabling direct qualitative comparison between mid- and high latitude cirrus is the simultaneous exploration of both regions during the same period of the year using consistent instrumentation and analysis methodologies across all measurements. However, one might question the representativeness of the conclusions drawn from a single campaign covering a one-and-a-half-month period. Integrating these measurements with data from other campaigns might help to improve the statistics, but is worth noting that involving different instruments or analysis techniques could potentially yield misleading conclusions. Future HALO campaigns, in which DLR's cloud physics group is participating, will employ the same suite of cloud probes (CDP-CIPG-PIP and CAS-DPOL), allowing a direct comparison with the current study.

However, it is crucial to acknowledge that advancements in cloud particle measurement technology are imminent, potentially leading to the replacement of current probes and complicating the integration and comparison with older campaign data. Nonetheless, this transition will require time due to the certification process of the newer instruments on the research aircraft. With this I want to emphasize the importance of the storage of raw instrument data, which is crucial to facilitate reprocessing in light of evolving knowledge about specific methods or corrections over time. While newer instruments hold promise for improving measurement accuracy and reduce sizing and counting uncertainties in future data sets, it is imperative to prioritize consistent upgrades to existing campaign data. This includes addressing biases inherent in older cloud probe suites and incorporating new findings to ensure data quality and reliability.

An open question that has not been addressed in this work is the derivation of the radiative effects of the measured clouds. High-latitude cirrus have larger crystals, which, according to Zhang et al. (1999), would result in a higher net cloud radiative forcing compared to cirrus with smaller particles, such as the mid-latitude cirrus in the data set. However, other parameters, such as the ice water content, cloud thickness, and surface also affect the net radiative effect. Further work could focus on evaluating the different climate impacts exerted by the diverse cirrus groups identified during the CIRRUS-HL campaign, as a follow-up to the study by Marsing et al. (2023). In that study, the lack of direct measurements of effective diameters required parameterization. This limitation could be addressed using the data from this work.

The upcoming HALO South campaign (The interplay of Clouds, Aerosols and Radiation above the Southern Ocean), scheduled for the spring season of the southern hemisphere in 2025 in Wellington, New Zealand, presents an excellent opportunity to extend this study to the Southern Hemisphere (HALO-South, 2024). This campaign will employ

the same set of cloud probes and focus not only on liquid and mixed-phase clouds but also on cirrus clouds, with an emphasis on investigating aerosol-cloud interactions in the pristine Southern Ocean. While various studies have examined mixed phase cloud processes in this region, such as the recent SOCRATES campaign (McFarquhar et al., 2021), existing climatologies based on in situ observations lack information on cirrus clouds in this area (Krämer et al., 2016; Heymsfield et al., 2017a; Krämer et al., 2020). It would be intriguing to ascertain whether the lower anthropogenic influence, including aviation, in the Southern Ocean results in cirrus microphysical properties comparable to those observed at high latitudes in the Northern Hemisphere. Additionally, applying the new cirrus classification introduced in this study to the HALO South campaign measurements could reveal potential influences of air masses from different latitudes.

One of the challenges encountered in this work was assessing the aerosol-cloud interaction of the measured cirrus clouds and linking differences in the ice microphysical properties to the nucleation processes along their lifetime driven by varying aerosol load depending on the cirrus types. This challenge was partially attributed to lack of ice nucleating particle (INP) measurements at cold cirrus temperatures (< -40 °C) due to temperature limitations of the onboard instrument HERA (Grawe et al., 2023). While airborne measurements of INPs are predominantly available for the mixed-phase temperature regime, the upcoming HALO South campaign presents an opportunity to improve this statistical study with the inclusion of a novel instrument, the Portable Ice Nucleation Experiment (PINE) (Möhler et al., 2021). PINE is expected to measure INPs at cirrus cloud temperatures down to -65 °C with a time resolution of 6 minutes, which will significantly improve our understanding in this area.

Moreover, the Earth-CARE (Cloud, Aerosol and Radiation Explorer) satellite promises important advancements in the understanding the role of clouds and aerosol in the climate by incorporating new high-performance instruments. Much work will be dedicated in the coming years to the validation of the satellite data, where in situ measurements will play a key role.

However, the utilization of novel measurements should be complemented by appropriate flight strategies to enhance the insights of this study. This work aimed to correlate measured cirrus microphysical properties with cloud formation and influencing factors throughout their lifecycle. Limited to one-time samples of the targeted clouds and air masses, this approach posed challenges and necessitated the use of modeling data combined with backward trajectories, introducing considerable uncertainty given the different resolution of the in situ measurements and the two different modeling data sets. An interesting approach to gain insights into cloud evolution involves quasi-Lagrangian sampling, as applied during the HALO-(AC)³ campaign in 2022 (Wendisch et al., 2024). This method consists of performing forward instead of backward trajectories to predict the trajectory of an air mass parcel and plan flight routes accordingly to sample the air mass several times. This approach could be performed either within one flight or within consecutive flight days, enabling the sampling of a cloud in its formation region and at a later stage, providing insights into the evolution of cirrus microphysical properties from an in situ perspective.

The Lagrangian sampling strategy could also be an effective approach for capturing the evolution of cirrus properties as contrails develop within a cirrus deck. This method

would allow for cirrus clouds to be sampled both before and after interacting with contrails, potentially providing new insights that, to date, have only been modeled or observed through satellite retrievals. Additionally, while numerous measurements of the initial stages of contrail formation are available in the literature, the aged contrail encounters included in the CIRRUS-HL data set are particularly valuable. Future campaigns should aim to expand this data set to further enhance our understanding of contrail evolution and their impacts.

Finally, the focus of contrail measurements is expected to shift in the coming years with the development and introduction of novel aircraft prototypes and technologies, such as hydrogen combustion, fuel cells, 100% SAF or lean-burn engines. These alternative propulsion technologies aim to reduce the climate impact of aviation. As discussed in Section 7.4, specific questions about the microphysical processes of contrail formation under conditions of reduced or nonexistent soot particles emissions, or higher supersaturations, diverge from our current understanding of contrail formation from conventional propulsion technologies. In order to validate theories and simulations, dedicated measurements are required to understand the conditions under which spontaneous homogeneous nucleation, heterogeneous nucleation on background aerosol, or heterogeneous nucleation on lubricant oil particles might occur.

ACRONYMS

1D	one-dimensional
2D	two-dimensional
2D-S	2D-S (Stereo) Probe
AD	Analog-to-Digital
AIC	aviation-induced clouds
AMETYST	Aerosol Measurement System
BC	black carbon from surface sources
BCav	black carbon from aviation
CAS	Cloud and Aerosol Spectrometer
CAS-DPOL	Cloud and Aerosol Spectrometer with Depolarization
CCN	cloud condensation nuclei
CCP	Cloud Combination Probe
CDP	Cloud Droplet Probe
CGS	Centrimeter-Gram-Second
CIPG	Cloud Imaging Probe Grayscale
CIRRUS-HL	Cirrus in High Latitudes
CPC	Condensation Particle Counter
CPI	cloud particle imager
DDA	discrete dipole approximation
DLR	German Aerospace Center, Deutsches Zentrum für Luft- und Raumfahrt, in german
DMT LLC	Droplet Measurement Technologies
DoF	depth of field
DU	mineral dust
ECMWF	European Centre for Medium-Range Weather Forecasts
ERA5	fifth generation ECMWF atmospheric reanalysis of the global climate
ERF	effective radiative forcing
FSSP	Forward Scattering Spectrometer Probe

H-H	formed and measured at high latitudes
HALO	High Altitude and LOng range
HERA	high-volume flow aerosol particle filter sampler
IAT	interarrival time
INP	ice nucleating particle
IPT	interparticle time
M-H	formed at mid-latitudes and measured at high latitudes
M-M	formed and measured at mid-latitudes
NN	neuronal network
nvPM	non-volatile particle matter
OAP	Optical Array Probe
OPC	Optical Particle Counter
PADS	Particle Analysis and Display System
PAS	probe air speed
PbP	particle-by-particle
PIP	Precipitation Imaging Probe
PSD	Particle Size Distribution
RF	radiative forcing
RQ	research question
SAC	Schmidt-Appleman criterion
SAF	sustainable aviation fuel
SODA	System for OAP Data Analysis
TAS	true air speed
UAV	unmanned aerial vehicle
UTC	Coordinated Universal Time
vPM	volatile particle matter

SYMBOLS

A_p	mean projected area within a size interval
A	density of projected area
c	constant for DoF calculation
C_p	specific heat of air at constant pressure
CO_2	carbon dioxide
D	particle diameter
D_{eq}	area equivalent diameter
D_{max}	maximal diameter
D_x	diameter parallel to the photodiode array direction
D_y	diameter parallel to the flight direction
Δt	sample interval
ED	effective diameter
$EI_{\text{H}_2\text{O}}$	emission index of water vapor
ε	ratio of gas constants of air and water vapor
η	overall propulsion efficiency
IWC	ice water content
λ	wavelength
L_{eff}	effective array width
LWC	liquid water content
$m_{\text{ice},i}$	ice mass per size bin i
N	particle number concentration
n	number of diodes in the diode array of the OAPs
N_i	particle number concentration per size bin i
n_i	number of particles sampled per size bin i
NO_x	nitrogen oxides
p	ambient air pressure
Q	specific heat of combustion

Q_{ext}	extinction efficiency
res	pixel resolution of the OAPs
RH_i	relative humidity with respect to ice
ρ_{ice}	ice density
SA	sample area
SV	sample volume
Z_d	distance from the object plane

BIBLIOGRAPHY

- Abdelmonem, A., Järvinen, E., Duft, D., Hirst, E., Vogt, S., Leisner, T., & Schnaiter, M. PHIPS–HALO: The airborne Particle Habit Imaging and Polar Scattering probe – Part 1: Design and operation. English. *Atmospheric Measurement Techniques*, 9(7), 3131–3144. <https://doi.org/10.5194/amt-9-3131-2016>, (2016).
- Afchine, A., Rolf, C., Costa, A., Spelten, N., Riese, M., Buchholz, B., Ebert, V., Heller, R., Kaufmann, S., Minikin, A., Voigt, C., Zöger, M., Smith, J., Lawson, P., Lykov, A., Khaykin, S., & Krämer, M. Ice particle sampling from aircraft – influence of the probing position on the ice water content. English. *Atmospheric Measurement Techniques*, 11(7). <https://doi.org/10.5194/amt-11-4015-2018>, (2018).
- Andreae, M. O., Afchine, A., Albrecht, R., Holanda, B. A., Artaxo, P., Barbosa, H. M. J., Borrmann, S., Cecchini, M. A., Costa, A., Dollner, M., Fütterer, D., Järvinen, E., Jurkat, T., Klimach, T., Konemann, T., Knote, C., Krämer, M., Krisna, T., Machado, L. A. T., ... Ziereis, H. Aerosol characteristics and particle production in the upper troposphere over the Amazon Basin. English. *Atmospheric Chemistry and Physics*, 18(2), 921–961. <https://doi.org/10.5194/acp-18-921-2018>, (2018).
- Bailey, M., & Hallett, J. Growth Rates and Habits of Ice Crystals between 20° and 70°C. EN. *Journal of the Atmospheric Sciences*, 61(5), 514–544. [https://doi.org/10.1175/1520-0469\(2004\)061<0514:GRAHOI>2.0.CO;2](https://doi.org/10.1175/1520-0469(2004)061<0514:GRAHOI>2.0.CO;2), (2004).
- Baker, B., & Lawson, R. P. Improvement in Determination of Ice Water Content from Two-Dimensional Particle Imagery. Part I: Image-to-Mass Relationships. EN. *Journal of Applied Meteorology and Climatology*, 45(9). <https://doi.org/10.1175/JAM2398.1>, (2006).
- Bansemer, A. (2023). *System for oap data analysis* (Version v2.23.0). Zenodo. <https://doi.org/10.5281/zenodo.7803116>
- Baran, A. J. On the scattering and absorption properties of cirrus cloud. en. *Journal of Quantitative Spectroscopy and Radiative Transfer*, 89(1), 17–36. <https://doi.org/10.1016/j.jqsrt.2004.05.008>, (2004).
- Bauer, R., Grooß, J.-U., Ungermann, J., Bär, M., Geldenhuys, M., & Hoffmann, L. The mission support system (mss v7.0.4) and its use in planning for the southtrac aircraft campaign. *Geoscientific Model Development*, 15(24), 8983–8997. <https://doi.org/10.5194/gmd-15-8983-2022>, (2022).
- Baumgardner, D., Abel, S. J., Axisa, D., Cotton, R., Crosier, J., Field, P., Gurganus, C., Heymsfield, A., Korolev, A., Krämer, M., Lawson, P., McFarquhar, G., Ulanowski, Z., & Um, J. Cloud ice properties: In situ measurement challenges. *Meteorological Monographs*, 58, 9.1–9.23. <https://doi.org/10.1175/AMSMONOGRAPHS-D-16-0011.1>, (2017).
- Baumgardner, D., Brenguier, J. L., Bucholtz, A., Coe, H., DeMott, P., Garrett, T. J., Gayet, J.-F., Hermann, M., Heymsfield, A., Korolev, A., Krämer, M., Petzold, A., Strapp, W., Pilewskie, P., Taylor, J., Twohy, C., Wendisch, M., Bachalo, W., & Chuang,

- P. Airborne instruments to measure atmospheric aerosol particles, clouds and radiation: A cook's tour of mature and emerging technology. *Atmospheric Research*, 102(1), 10–29. <https://doi.org/10.1016/j.atmosres.2011.06.021>, (2011).
- Baumgardner, D., Chepfer, H., Raga, G. B., & Kok, G. L. The shapes of very small cirrus particles derived from in situ measurements. en. *Geophysical Research Letters*, 32(1). <https://doi.org/10.1029/2004GL021300>, (2005).
- Baumgardner, D., French, J., Rodi, A. A., Klitch, D., Detwiler, A., Axisa, D., Hayman, M., & Rosenberg, P. Analysis of measurements from single particle light scattering spectrometers corrections, uncertainties, limitations and intercomparisons (2014).
- Baumgardner, D., Jonsson, H., Dawson, W., O'Connor, D., & Newton, R. The cloud, aerosol and precipitation spectrometer: A new instrument for cloud investigations [13th International Conference on Clouds and Precipitation]. *Atmospheric Research*, 59-60. 13th International Conference on Clouds and Precipitation, 251–264. [https://doi.org/10.1016/S0169-8095\(01\)00119-3](https://doi.org/10.1016/S0169-8095(01)00119-3), (2001).
- Baumgardner, D. (2012). Interactive comment on “particle sizing calibration with refractive index correction for light scattering optical particle counters and impacts upon pcasp and cdp data collected during the fennec campaign” by p. d. rosenberg et al., *atmos. meas. tech. discuss.*, 5, c118–c118, 2012.
- Baumgardner, D., Strapp, W., & Dye, J. E. Evaluation of the Forward Scattering Spectrometer Probe. Part II: Corrections for Coincidence and Dead-Time Losses. EN. *Journal of Atmospheric and Oceanic Technology*, 2(4), 626–632. [https://doi.org/10.1175/1520-0426\(1985\)002<0626:EOTFSS>2.0.CO;2](https://doi.org/10.1175/1520-0426(1985)002<0626:EOTFSS>2.0.CO;2), (1985).
- Beer, C. G., Hendricks, J., & Righi, M. A global climatology of ice-nucleating particles under cirrus conditions derived from model simulations with made3 in emac. *Atmospheric Chemistry and Physics*, 22(24), 15887–15907. <https://doi.org/10.5194/acp-22-15887-2022>, (2022).
- Beer, C. G., Hendricks, J., & Righi, M. Impacts of ice-nucleating particles on cirrus clouds and radiation derived from global model simulations with MADE3 in EMAC. English. *Atmospheric Chemistry and Physics*, 24(5), 3217–3240. <https://doi.org/10.5194/acp-24-3217-2024>, (2024).
- Beer, C. G., Hendricks, J., Righi, M., Heinold, B., Tegen, I., Groß, S., Sauer, D., Walser, A., & Weinzierl, B. Modelling mineral dust emissions and atmospheric dispersion with MADE3 in EMAC v2.54. English. *Geoscientific Model Development*, 13(9), 4287–4303. <https://doi.org/10.5194/gmd-13-4287-2020>, (2020).
- Bellouin, N., Quaas, J., Gryspeerdt, E., Kinne, S., Stier, P., Watson-Parris, D., Boucher, O., Carslaw, K. S., Christensen, M., Daniau, A.-L., Dufresne, J.-L., Feingold, G., Fiedler, S., Forster, P., Gettelman, A., Haywood, J. M., Lohmann, U., Malavelle, F., Mauritsen, T., ... Stevens, B. Bounding Global Aerosol Radiative Forcing of Climate Change. en. *Reviews of Geophysics*, 58(1), e2019RG000660. <https://doi.org/10.1029/2019RG000660>, (2020).
- Bier, A., & Burkhardt, U. Impact of Parametrizing Microphysical Processes in the Jet and Vortex Phase on Contrail Cirrus Properties and Radiative Forcing. en. *Journal of Geophysical Research: Atmospheres*, 127(23). <https://doi.org/10.1029/2022JD036677>, (2022).

- Bier, A., Unterstrasser, S., Zink, J., Hillenbrand, D., Jurkat-Witschas, T., & Lottermoser, A. Contrail formation on ambient aerosol particles for aircraft with hydrogen combustion: A box model trajectory study. English. *Atmospheric Chemistry and Physics*, 24(4), 2319–2344. <https://doi.org/10.5194/acp-24-2319-2024>, (2024).
- Bock, L., & Burkhardt, U. The temporal evolution of a long-lived contrail cirrus cluster: Simulations with a global climate model. en. *Journal of Geophysical Research: Atmospheres*, 121(7), 3548–3565. <https://doi.org/10.1002/2015JD024475>, (2016).
- Bock, L., & Burkhardt, U. Contrail cirrus radiative forcing for future air traffic. English. *Atmospheric Chemistry and Physics*, 19(12), 8163–8174. <https://doi.org/10.5194/acp-19-8163-2019>, (2019).
- Borrmann, S., Kunkel, D., Weigel, R., Minikin, A., Deshler, T., Wilson, J. C., Curtius, J., Volk, C. M., Homan, C. D., Ulanovsky, A., Ravegnani, E., Viciani, S., Shur, G. N., Belyaev, G. V., Law, K. S., & Cairo, F. Aerosols in the tropical and subtropical UT/LS: In-situ measurements of submicron particle abundance and volatility. English. *Atmospheric Chemistry and Physics*, 10(12), 5573–5592. <https://doi.org/10.5194/acp-10-5573-2010>, (2010).
- Borrmann, S., Luo, B., & Mishchenko, M. APPLICATION OF THE T-MATRIX METHOD TO THE MEASUREMENT OF ASPHERICAL (ELLIPSOIDAL) PARTICLES WITH FORWARD SCATTERING OPTICAL PARTICLE COUNTERS. *Journal of Aerosol Science*, 31(7). [https://doi.org/10.1016/S0021-8502\(99\)00563-7](https://doi.org/10.1016/S0021-8502(99)00563-7), (2000).
- Boucher, O., Randall, D., Artaxo, P., Bretherton, C., Feingold, G., Forster, P., Kerminen, V.-M., Kondo, Y., H. Liao, U. L., Rasch, P., Satheesh, S., Sherwood, S., Stevens, B., & Zhang, X. (2013). Clouds and aerosols. In T. Stocker, G.-K. P. D. Qin, M. Tignor, S. Allen, J. Boschung, A. Nauels, Y. Xia, V. Bex, & P. Midgley (Eds.), *Climate change 2013: The physical science basis. contribution of working group i to the fifth assessment report of the intergovernmental panel on climate change*. Cambridge University Press.
- Bräuer, T., Voigt, C., Sauer, D., Kaufmann, S., Hahn, V., Scheibe, M., Schlager, H., Diskin, G. S., Nowak, J. B., DiGangi, J. P., Huber, F., Moore, R. H., & Anderson, B. E. Airborne measurements of contrail ice properties—dependence on temperature and humidity. *Geophysical Research Letters*, 48(8), e2020GL092166. <https://doi.org/10.1029/2020GL092166>, (2021).
- Bräuer, T., Voigt, C., Sauer, D., Kaufmann, S., Hahn, V., Scheibe, M., Schlager, H., Huber, F., Le Clercq, P., Moore, R., & Anderson, B. Reduced ice number concentrations in contrails from low-aromatic biofuel blends. *Atmospheric Chemistry and Physics*, 21, 16817–16826. <https://doi.org/10.5194/acp-21-16817-2021>, (2021).
- Brenguier, J.-L., Bourrienne, T., Coelho, A. A., Isbert, J., Peytavi, R., Trevarin, D., & Weschler, P. Improvements of Droplet Size Distribution Measurements with the Fast-FSSP (Forward Scattering Spectrometer Probe). EN. *Journal of Atmospheric and Oceanic Technology*, 15(5), 1077–1090. [https://doi.org/10.1175/1520-0426\(1998\)015<1077:IODSDM>2.0.CO;2](https://doi.org/10.1175/1520-0426(1998)015<1077:IODSDM>2.0.CO;2), (1998).
- Brock, C. A., Froyd, K. D., Dollner, M., Williamson, C. J., Schill, G., Murphy, D. M., Wagner, N. J., Kupc, A., Jimenez, J. L., Campuzano-Jost, P., Nault, B. A., Schroder, J. C., Day, D. A., Price, D. J., Weinzierl, B., Schwarz, J. P., Katich, J. M., Wang, S., Zeng,

- L., ... Wofsy, S. C. Ambient aerosol properties in the remote atmosphere from global-scale in situ measurements. English. *Atmospheric Chemistry and Physics*, 21(19), 15023–15063. <https://doi.org/10.5194/acp-21-15023-2021>, (2021).
- Brown, P. R. A., & Francis, P. N. Improved measurements of the ice water content in cirrus using a total-water probe. *Journal of Atmospheric and Oceanic Technology*, 12(2), 410–414. [https://doi.org/10.1175/1520-0426\(1995\)012<0410:IMOTIW>2.0.CO;2](https://doi.org/10.1175/1520-0426(1995)012<0410:IMOTIW>2.0.CO;2), (1995).
- Chauvigné, A., Jourdan, O., Schwarzenboeck, A., Gourbeyre, C., Gayet, J.-F., Voigt, C., Schlager, H., Kaufmann, S., Borrmann, S., Molleker, S., Minikin, A., Jurkat, T., & Schumann, U. Statistical analysis of contrail to cirrus evolution during the contrail and cirrus experiment (concert). *Atmospheric Chemistry and Physics*, 18(13), 9803–9822. <https://doi.org/10.5194/acp-18-9803-2018>, (2018).
- Connolly, P. J., Flynn, M. J., Ulanowski, Z., Choulaton, T. W., Gallagher, M. W., & Bower, K. N. Calibration of the Cloud Particle Imager Probes Using Calibration Beads and Ice Crystal Analogs: The Depth of Field. EN. *Journal of Atmospheric and Oceanic Technology*, 24(11), 1860–1879. <https://doi.org/10.1175/JTECH2096.1>, (2007).
- Costa, A., Meyer, J., Afchine, A., Luebke, A., Günther, G., Dorsey, J. R., Gallagher, M. W., Ehrlich, A., Wendisch, M., Baumgardner, D., Wex, H., & Krämer, M. Classification of arctic, midlatitude and tropical clouds in the mixed-phase temperature regime. *Atmospheric Chemistry and Physics*, 17(19), 12219–12238. <https://doi.org/10.5194/acp-17-12219-2017>, (2017).
- Cotton, W. R., Bryan, G., & van den Heever, S. C. (2011). Chapter 10 - the mesoscale structure of extratropical cyclones and middle and high clouds. In W. Cotton, G. Bryan, & S. van den Heever (Eds.), *Storm and cloud dynamics* (pp. 527–672). Academic Press. [https://doi.org/https://doi.org/10.1016/S0074-6142\(10\)09916-X](https://doi.org/https://doi.org/10.1016/S0074-6142(10)09916-X)
- Crépel, O., Gayet, J.-F., Fournol, J.-F., & Oshchepkov, S. A new airborne Polar Nephelometer for the measurement of optical and microphysical cloud properties. Part II: Preliminary tests. English. *Annales Geophysicae*, 15(4), 460–470. <https://doi.org/10.1007/s00585-997-0460-0>, (1997).
- Cui, J., Sprenger, M., Staehelin, J., Siegrist, A., Kunz, M., Henne, S., & Steinbacher, M. Impact of stratospheric intrusions and intercontinental transport on ozone at Jungfraujoch in 2005: Comparison and validation of two Lagrangian approaches. English. *Atmospheric Chemistry and Physics*, 9(10), 3371–3383. <https://doi.org/10.5194/acp-9-3371-2009>, (2009).
- Cziczo, D. J., Froyd, K. D., Hoose, C., Jensen, E. J., Diao, M., Zondlo, M. A., Smith, J. B., Twohy, C. H., & Murphy, D. M. Clarifying the dominant sources and mechanisms of cirrus cloud formation. *Science*, 340(6138), 1320–1324. <https://doi.org/10.1126/science.1234145>, (2013).
- De La Torre Castro, E., Jurkat-Witschas, T., Afchine, A., Grewe, V., Hahn, V., Kirschler, S., Krämer, M., Lucke, J., Spelten, N., Wernli, H., Zöger, M., & Voigt, C. Differences in microphysical properties of cirrus at high and mid-latitudes. *Atmospheric Chemistry and Physics*, 23(20), 13167–13189. <https://doi.org/10.5194/acp-23-13167-2023>, (2023).

- Dekoutsidis, G., Feidas, H., & Bugliaro, L. Contrail detection on SEVIRI images and 1-year study of their physical properties and the atmospheric conditions favoring their formation over Europe. en. *Theoretical and Applied Climatology*, 151(3), 1931–1948. <https://doi.org/10.1007/s00704-023-04357-9>, (2023).
- DeMott, P. J., Cziczo, D. J., Prenni, A. J., Murphy, D. M., Kreidenweis, S. M., Thomson, D. S., Borys, R., & Rogers, D. C. Measurements of the concentration and composition of nuclei for cirrus formation. *Proceedings of the National Academy of Sciences*, 100(25), 14655–14660. <https://doi.org/10.1073/pnas.2532677100>, (2003).
- DeMott, P. J., Prenni, A. J., Liu, X., Kreidenweis, S. M., Petters, M. D., Twohy, C. H., Richardson, M. S., Eidhammer, T., & Rogers, D. C. Predicting global atmospheric ice nuclei distributions and their impacts on climate. *Proceedings of the National Academy of Sciences*, 107(25), 11217–11222. <https://doi.org/10.1073/pnas.0910818107>, (2010).
- Dessler, A. E. Clouds and water vapor in the northern hemisphere summertime stratosphere. *Journal of Geophysical Research: Atmospheres*, 114(D4). <https://doi.org/10.1029/2009JD012075>, (2009).
- Dischl, R., Kaufmann, S., & Voigt, C. Regional and seasonal dependence of the potential contrail cover and the potential contrail cirrus cover over Europe. *Aerospace*, 9(9). <https://doi.org/10.3390/aerospace9090485>, (2022).
- DMT, D. M. T. Form doc-0201 rev b: Image probe data reference manual (2011).
- DMT, D. M. T. Operator manual: Cloud droplet probe (cdp-2) - doc-0343, rev a (2017).
- DMT, D. M. T. Operator manual: Cloud imaging probe (cip) - doc-0028, rev l-5 (2017).
- DMT, D. M. T. Spinning disc calibrator - operator manual - doc-0012 rev d (2017).
- DMT, D. M. T. Operator manual: Cloud aerosol spectrometer depolarization option (cas-dpol) (2018).
- Dye, J. E., & Baumgardner, D. Evaluation of the Forward Scattering Spectrometer Probe. Part I: Electronic and Optical Studies. EN. *Journal of Atmospheric and Oceanic Technology*, 1(4). [https://doi.org/10.1175/1520-0426\(1984\)001<0329:EOTFSS>2.0.CO;2](https://doi.org/10.1175/1520-0426(1984)001<0329:EOTFSS>2.0.CO;2), (1984).
- Esposito, B. M., Bachalo, W. D., Leroy, D., Schwarzenboeck, A., Jurkat, T., Voigt, C., & Bansmer, S. Wind Tunnel Measurements of Simulated Glaciated Cloud Conditions to Evaluate Newly Developed 2D Imaging Probes. en, 2019–01–1981. <https://doi.org/10.4271/2019-01-1981>, (2019).
- Febvre, G., Gayet, J.-F., Shcherbakov, V., Goubeyre, C., & Jourdan, O. Some effects of ice crystals on the FSSP measurements in mixed phase clouds. English. *Atmospheric Chemistry and Physics*, 12(19). <https://doi.org/10.5194/acp-12-8963-2012>, (2012).
- Febvre, G., Gayet, J.-F., Minikin, A., Schlager, H., Shcherbakov, V., Jourdan, O., Busen, R., Fiebig, M., Kärcher, B., & Schumann, U. On optical and microphysical characteristics of contrails and cirrus. *Journal of Geophysical Research: Atmospheres*, 114(D2). <https://doi.org/10.1029/2008JD010184>, (2009).
- Feng, L., Smith, S. J., Braun, C., Crippa, M., Gidden, M. J., Hoesly, R., Klimont, Z., van Marle, M., van den Berg, M., & van der Werf, G. R. The generation of gridded emissions data for CMIP6. English. *Geoscientific Model Development*, 13(2), 461–482. <https://doi.org/10.5194/gmd-13-461-2020>, (2020).

- Field, P. R., Heymsfield, A. J., & Bansemer, A. Shattering and particle interarrival times measured by optical array probes in ice clouds. *Journal of Atmospheric and Oceanic Technology*, 23(10), 1357–1371. <https://doi.org/10.1175/JTECH1922.1>, (2006).
- Field, P. R., Wood, R., Brown, P., Kaye, P., Hirst, E., Greenaway, R., & Smith, J. Ice particle interarrival times measured with a fast fssp. *Journal of Atmospheric and Oceanic Technology*, 20, 249–261. [https://doi.org/10.1175/1520-0426\(2003\)020<0249:ipitmw>2.0.co;2](https://doi.org/10.1175/1520-0426(2003)020<0249:ipitmw>2.0.co;2), (2003).
- Fierz, M., Vernooij, M. G. C., & Burtscher, H. An improved low-flow thermodenuder. *Journal of Aerosol Science*, 38(11), 1163–1168. <https://doi.org/10.1016/j.jaerosci.2007.08.006>, (2007).
- Forster, P., Storelvmo, T., Armour, K., Collins, W., Dufresne, J.-L., Frame, D., Lunt, D., Mauritsen, T., Palmer, M., Watanabe, M., Wild, M., & Zhang, H. (2021). The earth's energy budget, climate feedbacks, and climate sensitivity. In V. Masson-Delmotte, P. Zhai, A. Pirani, S. Connors, C. Péan, S. Berger, N. Caud, Y. Chen, L. Goldfarb, M. Gomis, M. Huang, K. Leitzell, E. Lonnoy, J. Matthews, T. Maycock, T. Waterfield, O. Yelekçi, R. Yu, & B. Zhou (Eds.), *Climate change 2021: The physical science basis. contribution of working group i to the sixth assessment report of the intergovernmental panel on climate change* (pp. 923–1054). Cambridge University Press. <https://doi.org/10.1017/9781009157896.009>
- Fricko, O., Havlik, P., Rogelj, J., Klimont, Z., Gusti, M., Johnson, N., Kolp, P., Strubegger, M., Valin, H., Amann, M., Ermolieva, T., Forsell, N., Herrero, M., Heyes, C., Kindermann, G., Krey, V., McCollum, D. L., Obersteiner, M., Pachauri, S., ... Riahi, K. The marker quantification of the Shared Socioeconomic Pathway 2: A middle-of-the-road scenario for the 21st century. *Global Environmental Change*, 42, 251–267. <https://doi.org/10.1016/j.gloenvcha.2016.06.004>, (2017).
- Froyd, K. D., Yu, P., Schill, G. P., Brock, C. A., Kupc, A., Williamson, C. J., Jensen, E. J., Ray, E., Rosenlof, K. H., Bian, H., Darmenov, A. S., Colarco, P. R., Diskin, G. S., Bui, T., & Murphy, D. M. Dominant role of mineral dust in cirrus cloud formation revealed by global-scale measurements. *Nature Geoscience*, 15(3), 177–183. <https://doi.org/10.1038/s41561-022-00901-w>, (2022).
- Fu, Q., & Liou, K. N. Parameterization of the Radiative Properties of Cirrus Clouds. EN. *Journal of the Atmospheric Sciences*, 50(13). [https://doi.org/10.1175/1520-0469\(1993\)050<2008:POTRPO>2.0.CO;2](https://doi.org/10.1175/1520-0469(1993)050<2008:POTRPO>2.0.CO;2), (1993).
- Fugal, J. P., Shaw, R. A., Saw, E. W., & Sergeev, A. V. Airborne digital holographic system for cloud particle measurements. EN. *Applied Optics*, 43(32), 5987–5995. <https://doi.org/10.1364/AO.43.005987>, (2004).
- Gasparini, B., Meyer, A., Neubauer, D., Münch, S., & Lohmann, U. Cirrus cloud properties as seen by the calipso satellite and echem-ham global climate model. *Journal of Climate*, 31(5), 1983–2003. <https://doi.org/10.1175/JCLI-D-16-0608.1>, (2018).
- Gasparini, B., & Lohmann, U. Why cirrus cloud seeding cannot substantially cool the planet. *Journal of Geophysical Research: Atmospheres*, 121(9), 4877–4893. <https://doi.org/10.1002/2015JD024666>, (2016).
- Gasparini, B., Münch, S., Poncet, L., Feldmann, M., & Lohmann, U. Is increasing ice crystal sedimentation velocity in geoengineering simulations a good proxy for cirrus

- cloud seeding? English. *Atmospheric Chemistry and Physics*, 17(7), 4871–4885. <https://doi.org/10.5194/acp-17-4871-2017>, (2017).
- Gayet, J.-E., Ovarlez, J., Shcherbakov, V., Ström, J., Schumann, U., Minikin, A., Auriol, E., Petzold, A., & Monier, M. Cirrus cloud microphysical and optical properties at southern and northern midlatitudes during the inca experiment. *Journal of Geophysical Research: Atmospheres*, 109(D20). <https://doi.org/10.1029/2004JD004803>, (2004).
- Gayet, J.-E., Crépel, O., Fournol, J. F., & Oshchepkov, S. A new airborne polar Nephelometer for the measurements of optical and microphysical cloud properties. Part I: Theoretical design. English. *Annales Geophysicae*, 15(4), 451–459. <https://doi.org/10.1007/s00585-997-0451-1>, (1997).
- Gayet, J.-E., Shcherbakov, V., Voigt, C., Schumann, U., Schäuble, D., Jessberger, P., Petzold, A., Minikin, A., Schlager, H., Dubovik, O., & Lapyonok, T. The evolution of microphysical and optical properties of an a380 contrail in the vortex phase. *Atmospheric Chemistry and Physics*, 12(14), 6629–6643. <https://doi.org/10.5194/acp-12-6629-2012>, (2012).
- Gettelman, A., Liu, X., Barahona, D., Lohmann, U., & Chen, C. Climate impacts of ice nucleation. *Journal of Geophysical Research: Atmospheres*, 117(D20). <https://doi.org/10.1029/2012JD017950>, (2012).
- Gidden, M. J., Riahi, K., Smith, S. J., Fujimori, S., Luderer, G., Kriegler, E., van Vuuren, D. P., van den Berg, M., Feng, L., Klein, D., Calvin, K., Doelman, J. C., Frank, S., Fricko, O., Harmsen, M., Hasegawa, T., Havlik, P., Hilaire, J., Hoesly, R., ... Takahashi, K. Global emissions pathways under different socioeconomic scenarios for use in CMIP6: A dataset of harmonized emissions trajectories through the end of the century. English. *Geoscientific Model Development*, 12(4), 1443–1475. <https://doi.org/10.5194/gmd-12-1443-2019>, (2019).
- Gierens, K. Selected topics on the interaction between cirrus clouds and embedded contrails. *Atmospheric Chemistry and Physics*, 12(24), 11943–11949. <https://doi.org/10.5194/acp-12-11943-2012>, (2012).
- Gierens, K. Theory of Contrail Formation for Fuel Cells. en. *Aerospace*, 8(6), 164. <https://doi.org/10.3390/aerospace8060164>, (2021).
- Giez, A., Mallaun, C., Nenakhov, V., & Zöger, M. (2021). *Calibration of a nose boom mounted airflow sensor on an atmospheric research aircraft by inflight maneuvers* (tech. rep.).
- Grawe, S., Jentsch, C., Schaefer, J., Wex, H., Mertes, S., & Stratmann, F. Next-generation ice-nucleating particle sampling on board aircraft: Characterization of the High-volume flow aERosol particle filter sAmplifier (HERA). English. *Atmospheric Measurement Techniques*, 16(19), 4551–4570. <https://doi.org/10.5194/amt-16-4551-2023>, (2023).
- Grewe, V., Dahlmann, K., Flink, J., Frömming, C., Ghosh, R., Gierens, K., Heller, R., Hendricks, J., Jöckel, P., Kaufmann, S., Kölker, K., Linke, F., Luchkova, T., Lührs, B., Van Manen, J., Matthes, S., Minikin, A., Niklaß, M., Plohr, M., ... Ziereis, H. Mitigating the climate impact from aviation: Achievements and results of the dlr wecare project. *Aerospace*, 4(3). <https://doi.org/10.3390/aerospace4030034>, (2017).

- Groß, S., Jurkat-Witschas, T., Li, Q., Wirth, M., Urbanek, B., Krämer, M., Weigel, R., & Voigt, C. Investigating an indirect aviation effect on mid-latitude cirrus clouds – linking lidar derived optical properties to in-situ measurements. *Atmospheric Chemistry and Physics Discussions*, 2022, 1–21. <https://doi.org/10.5194/acp-2022-721>, (2022).
- Gryspeerd, E., Sourdeval, O., Quaas, J., Delanoë, J., Krämer, M., & Kühne, P. Ice crystal number concentration estimates from lidar–radar satellite remote sensing – Part 2: Controls on the ice crystal number concentration. English. *Atmospheric Chemistry and Physics*, 18(19), 14351–14370. <https://doi.org/10.5194/acp-18-14351-2018>, (2018).
- Gurganus, C., & Lawson, P. Laboratory and Flight Tests of 2D Imaging Probes: Toward a Better Understanding of Instrument Performance and the Impact on Archived Data. EN. *Journal of Atmospheric and Oceanic Technology*, 35(7), 1533–1553. <https://doi.org/10.1175/JTECH-D-17-0202.1>, (2018).
- HALO-South. (2024). Halo-south - the interplay of clouds, aerosols and radiation above the southern ocean [<https://halo-research.de/science/future-missions/halo-south/>, accessed 2024-02-27].
- HALO-SPP-1294. (2023). Atmospheric and earth system research with halo [<http://www.halo-spp.de/Home/>, accessed 2023-08-07].
- Harlass, T., Dischl, R., Kaufmann, S., Märkl, R., Sauer, D., Scheibe, M., Stock, P., Bräuer, T., Dörnbrack, A., Roiger, A., Schlager, H., Schumann, U., Schripp, T., Grein, T., Bondorf, L., Renard, C., Gauthier, M., Johnson, M., Luff, D., ... Voigt, C. (2024). Measurement report: In-flight and ground-based measurements of nitrogen oxide emissions from latest generation jet engines and 100% sustainable aviation fuel. <https://doi.org/10.5194/egusphere-2024-454>
- Hartmann, D. L., Ockert-Bell, M. E., & Michelsen, M. L. The Effect of Cloud Type on Earth's Energy Balance: Global Analysis. EN. *Journal of Climate*, 5(11), 1281–1304. [https://doi.org/10.1175/1520-0442\(1992\)005<1281:TEOCTO>2.0.CO;2](https://doi.org/10.1175/1520-0442(1992)005<1281:TEOCTO>2.0.CO;2), (1992).
- Hendricks, J., Kärcher, B., & Lohmann, U. Effects of ice nuclei on cirrus clouds in a global climate model. *Journal of Geophysical Research: Atmospheres*, 116(D18). <https://doi.org/10.1029/2010JD015302>, (2011).
- Henneberger, J., Ramelli, F., Spirig, R., Omanovic, N., Miller, A. J., Fuchs, C., Zhang, H., Bühl, J., Hervo, M., Kanji, Z. A., Ohneiser, K., Radenz, M., Rösch, M., Seifert, P., & Lohmann, U. Seeding of Supercooled Low Stratus Clouds with a UAV to Study Microphysical Ice Processes: An Introduction to the CLOUDLAB Project. EN. *Bulletin of the American Meteorological Society*, 104(11), E1962–E1979. <https://doi.org/10.1175/BAMS-D-22-0178.1>, (2023).
- Hersbach, H., Bell, B., Berrisford, P., Hirahara, S., Horányi, A., Muñoz-Sabater, J., Nicolas, J., Peubey, C., Radu, R., Schepers, D., Simmons, A., Soci, C., Abdalla, S., Abellan, X., Balsamo, G., Bechtold, P., Biavati, G., Bidlot, J., Bonavita, M., ... Thépaut, J.-N. The ERA5 global reanalysis. en. *Quarterly Journal of the Royal Meteorological Society*, 146(730), 1999–2049. <https://doi.org/10.1002/qj.3803>, (2020).
- Heymsfield, A. J. On measurements of small ice particles in clouds. *Geophysical Research Letters*, 34(23). <https://doi.org/10.1029/2007GL030951>, (2007).

- Heymsfield, A. J., Krämer, M., Luebke, A., Brown, P., Cziczo, D. J., Franklin, C., Lawson, P., Lohmann, U., McFarquhar, G., Ulanowski, Z., & Tricht, K. V. Cirrus Clouds. *Meteorological Monographs*, 58(1), 2.1–2.26. <https://doi.org/10.1175/AMSMONOGRAPHS-D-16-0010.1>, (2017).
- Heymsfield, A. J., Krämer, M., Wood, N. B., Gettelman, A., Field, P. R., & Liu, G. Dependence of the ice water content and snowfall rate on temperature, globally: Comparison of in situ observations, satellite active remote sensing retrievals, and global climate model simulations. *Journal of Applied Meteorology and Climatology*, 56(1), 189–215. <https://doi.org/10.1175/JAMC-D-16-0230.1>, (2017).
- Heymsfield, A. J., & Parrish, J. L. A computational technique for increasing the effective sampling volume of the pms two-dimensional particle size spectrometer. *Journal of Applied Meteorology and Climatology*, 17(10), 1566–1572. [https://doi.org/10.1175/1520-0450\(1978\)017<1566:ACTFIT>2.0.CO;2](https://doi.org/10.1175/1520-0450(1978)017<1566:ACTFIT>2.0.CO;2), (1978).
- Heymsfield, A. J., Schmitt, C., & Bansemer, A. Ice cloud particle size distributions and pressure-dependent terminal velocities from in situ observations at temperatures from 0° to 86°C. *Journal of the Atmospheric Sciences*, 70(12), 4123–4154. <https://doi.org/10.1175/JAS-D-12-0124.1>, (2013).
- Heymsfield, A. J., Schmitt, C., Bansemer, A., & Twohy, C. H. Improved representation of ice particle masses based on observations in natural clouds. *Journal of the Atmospheric Sciences*, 67(10), 3303–3318. <https://doi.org/10.1175/2010JAS3507.1>, (2010).
- Hoffmann, L., & Spang, R. An assessment of tropopause characteristics of the era5 and era-interim meteorological reanalyses. *Atmospheric Chemistry and Physics*, 22(6), 4019–4046. <https://doi.org/10.5194/acp-22-4019-2022>, (2022).
- Hoffmann, L., & Spang, R. (2021). Reanalysis Tropopause Data Repository. <https://doi.org/10.26165/JUELICH-DATA/UBNGI2>
- Hoose, C., & Möhler, O. Heterogeneous ice nucleation on atmospheric aerosols: A review of results from laboratory experiments. English. *Atmospheric Chemistry and Physics*, 12(20), 9817–9854. <https://doi.org/10.5194/acp-12-9817-2012>, (2012).
- ICAO. (2019). Air transport monitor [<https://www.icao.int/sustainability/pages/air-traffic-monitor.aspx>, accessed 2022-10-20].
- IPCC. (2013). Summary for policymakers. In T. Stocker, D. Qin, G.-K. Plattner, M. Tignor, S. Allen, J. Boschung, A. Nauels, Y. Xia, V. Bex, & P. Midgley (Eds.), *Climate change 2013: The physical science basis. contribution of working group i to the fifth assessment report of the intergovernmental panel on climate change* (pp. 1–30). Cambridge University Press. <https://doi.org/10.1017/CBO9781107415324.004>
- Jaffeux, L., Schwarzenböck, A., Coutris, P., & Duroure, C. Ice crystal images from optical array probes: Classification with convolutional neural networks [Publisher: Copernicus GmbH]. English. *Atmospheric Measurement Techniques*, 15(17). Publisher: Copernicus GmbH, 5141–5157. <https://doi.org/10.5194/amt-15-5141-2022>, (2022).
- Jang, S., Kim, J., McFarquhar, G. M., Park, S., Lee, S. S., Jung, C. H., Park, S. S., Cha, J. W., Lee, K., & Um, J. Theoretical Calculations of Directional Scattering Intensities

- of Small Nonspherical Ice Crystals: Implications for Forward Scattering Probes. en. *Remote Sensing*, 14(12), 2795. <https://doi.org/10.3390/rs14122795>, (2022).
- Järvinen, E., Wernli, H., & Schnaiter, M. Investigations of mesoscopic complexity of small ice crystals in midlatitude cirrus. *Geophysical Research Letters*, 45(20), 11, 465–11, 472. <https://doi.org/10.1029/2018GL079079>, (2018).
- Jensen, E. J., Lawson, P., Baker, B., Pilson, B., Mo, Q., Heymsfield, A. J., Bansemer, A., Bui, T. P., McGill, M., Hlavka, D., Heymsfield, G., Platnick, S., Arnold, G. T., & Tanelli, S. On the importance of small ice crystals in tropical anvil cirrus. *Atmospheric Chemistry and Physics*, 9(15), 5519–5537. <https://doi.org/10.5194/acp-9-5519-2009>, (2009).
- Jensen, E. J., Lawson, R. P., Bergman, J. W., Pfister, L., Bui, T. P., & Schmitt, C. G. Physical processes controlling ice concentrations in synoptically forced, midlatitude cirrus. *Journal of Geophysical Research: Atmospheres*, 118(11), 5348–5360. <https://doi.org/10.1002/jgrd.50421>, (2013).
- Jensen, E. J., Toon, O. B., Tabazadeh, A., Sachse, G. W., Anderson, B. E., Chan, K. R., Twohy, C. W., Gandrud, B., Aulenbach, S. M., Heymsfield, A., Hallett, J., & Gary, B. Ice nucleation processes in upper tropospheric wave-clouds observed during SUCCESS. en. *Geophysical Research Letters*, 25(9), 1363–1366. <https://doi.org/10.1029/98GL00299>, (1998).
- Jeßberger, P., Voigt, C., Schumann, U., Sölch, I., Schlager, H., Kaufmann, S., Petzold, A., Schäuble, D., & Gayet, J.-F. Aircraft type influence on contrail properties. *Atmospheric Chemistry and Physics*, 13(23), 11965–11984. <https://doi.org/10.5194/acp-13-11965-2013>, (2013).
- Jöckel, P., Kerkweg, A., Pozzer, A., Sander, R., Tost, H., Riede, H., Baumgaertner, A., Gromov, S., & Kern, B. Development cycle 2 of the Modular Earth Submodel System (MESSy2). English. *Geoscientific Model Development*, 3(2), 717–752. <https://doi.org/10.5194/gmd-3-717-2010>, (2010).
- Jurkat, T., Voigt, C., Arnold, F., Schlager, H., Kleffmann, J., Aufmhoff, H., Schäuble, D., Schaefer, M., & Schumann, U. Measurements of HONO, NO, NO_y and SO₂ in aircraft exhaust plumes at cruise: EXHAUST PLUME MEASUREMENTS OF HONO AND SO₂. en. *Geophysical Research Letters*, 38(10), n/a–n/a. <https://doi.org/10.1029/2011GL046884>, (2011).
- Kaiser, J. C., Hendricks, J., Righi, M., Riemer, N., Zaveri, R. A., Metzger, S., & Aquila, V. The MESSy aerosol submodel MADE3 (v2.0b): Description and a box model test. English. *Geoscientific Model Development*, 7(3), 1137–1157. <https://doi.org/10.5194/gmd-7-1137-2014>, (2014).
- Kaiser, J. C., Hendricks, J., Righi, M., Jöckel, P., Tost, H., Kandler, K., Weinzierl, B., Sauer, D., Heimerl, K., Schwarz, J. P., Perring, A. E., & Popp, T. Global aerosol modeling with MADE3 (v3.0) in EMAC (based on v2.53): Model description and evaluation. English. *Geoscientific Model Development*, 12(1), 541–579. <https://doi.org/10.5194/gmd-12-541-2019>, (2019).
- Kanji, Z. A., Ladino, L. A., Wex, H., Boose, Y., Burkert-Kohn, M., Cziczko, D. J., & Krämer, M. Overview of ice nucleating particles. *Meteorological Monographs*, 58, 1.1–1.33. <https://doi.org/10.1175/AMSMONOGRAPHS-D-16-0006.1>, (2017).

- Kärcher, B. Aviation-Produced Aerosols and Contrails. en. *Surveys in Geophysics*, 20(2), 113–167. <https://doi.org/10.1023/A:1006600107117>, (1999).
- Kärcher, B., Burkhardt, U., Bier, A., Bock, L., & Ford, I. J. The microphysical pathway to contrail formation. en. *Journal of Geophysical Research: Atmospheres*, 120(15), 7893–7927. <https://doi.org/10.1002/2015JD023491>, (2015).
- Kärcher, B., DeMott, P. J., Jensen, E. J., & Harrington, J. Y. Studies on the Competition Between Homogeneous and Heterogeneous Ice Nucleation in Cirrus Formation. en. *Journal of Geophysical Research: Atmospheres*, 127(3). <https://doi.org/10.1029/2021JD035805>, (2022).
- Kärcher, B., Hendricks, J., & Lohmann, U. Physically based parameterization of cirrus cloud formation for use in global atmospheric models. *Journal of Geophysical Research: Atmospheres*, 111(D1). <https://doi.org/10.1029/2005JD006219>, (2006).
- Kärcher, B., Kleine, J., Sauer, D., & Voigt, C. Contrail Formation: Analysis of Sublimation Mechanisms. en. *Geophysical Research Letters*, 45(24), 13, 547–13, 552. <https://doi.org/10.1029/2018GL079391>, (2018).
- Kärcher, B., & Lohmann, U. A Parameterization of cirrus cloud formation: Homogeneous freezing including effects of aerosol size. en. *Journal of Geophysical Research: Atmospheres*, 107(D23). <https://doi.org/10.1029/2001JD001429>, (2002).
- Kärcher, B., & Lohmann, U. A parameterization of cirrus cloud formation: Homogeneous freezing of supercooled aerosols. *Journal of Geophysical Research: Atmospheres*, 107(D2), AAC 4-1-AAC 4–10. <https://doi.org/10.1029/2001JD000470>, (2002).
- Kärcher, B., & Lohmann, U. A parameterization of cirrus cloud formation: Heterogeneous freezing. *Journal of Geophysical Research: Atmospheres*, 108(D14). <https://doi.org/10.1029/2002JD003220>, (2003).
- Kärcher, B., & Yu, F. Role of aircraft soot emissions in contrail formation. en. *Geophysical Research Letters*, 36(1). <https://doi.org/10.1029/2008GL036649>, (2009).
- Kärcher, B. Formation and radiative forcing of contrail cirrus. en. *Nat Commun*, 9(1), 1824. <https://doi.org/10.1038/s41467-018-04068-0>, (2018).
- Kaufmann, S., Voigt, C., Heller, R., Jurkat-Witschas, T., Krämer, M., Rolf, C., Zoeger, M., Giez, A., Buchholz, B., Ebert, V., Thornberry, T., & Schumann, U. Intercomparison of midlatitude tropospheric and lower-stratospheric water vapor measurements and comparison to ecmwf humidity data. *Atmospheric Chemistry and Physics*, 18, 16729–16745. <https://doi.org/10.5194/acp-18-16729-2018>, (2018).
- Kaufmann, S., Voigt, C., Jeßberger, P., Jurkat, T., Schlager, H., Schwarzenboeck, A., Klingebiel, M., & Thornberry, T. In situ measurements of ice saturation in young contrails. en. *Geophysical Research Letters*, 41(2), 702–709. <https://doi.org/10.1002/2013GL058276>, (2014).
- Kaufmann, S., Voigt, C., Jurkat, T., Thornberry, T., Fahey, D., Gao, R.-S., Schlage, R., Schaeuble, D., & Zoeger, M. The airborne mass spectrometer aims – part 1: Aims-h2o for utls water vapor measurements. *Atmospheric Measurement Techniques Discussions*, 8, 13525–13565. <https://doi.org/10.5194/amtd-8-13525-2015>, (2015).
- Kirschler, S. (2023). *Effekte von aerosol und dynamik auf die eigenschaften ozeanischer wolken im nordwestatlantik* (Doctoral dissertation). Mainz, Johannes

- Gutenberg-Universität Mainz. <https://doi.org/http://doi.org/10.25358/openscience-9749>
- Kirschler, S., Voigt, C., Anderson, B. E., Chen, G., Crosbie, E. C., Ferrare, R. A., Hahn, V., Hair, J. W., Kaufmann, S., Moore, R. H., Painemal, D., Robinson, C. E., Sanchez, K. J., Scarino, A. J., Shingler, T. J., Shook, M. A., Thornhill, K. L., Winstead, E. L., Ziemba, L. D., & Sorooshian, A. Overview and statistical analysis of boundary layer clouds and precipitation over the western North Atlantic Ocean. English. *Atmospheric Chemistry and Physics*, 23(18), 10731–10750. <https://doi.org/10.5194/acp-23-10731-2023>, (2023).
- Kleine, J., Voigt, C., Sauer, D., Schlager, H., Scheibe, M., Jurkat, T., Kaufmann, S., Kärcher, B., & Anderson, B. In situ observations of ice particle losses in a young persistent contrail. *Geophysical Research Letters*, 45. <https://doi.org/10.1029/2018GL079390>, (2018).
- Kleine, J. (2019). *Flugzeuggetragene messungen von eis- und rußpartikeln in kondensstreifen bei verwendung konventioneller und synthetischer treibstoffe* (Doctoral dissertation).
- Klingebiel, M., de Lozar, A., Molleker, S., Weigel, R., Roth, A., Schmidt, L., Meyer, J., Ehrlich, A., Neuber, R., Wendisch, M., & Borrmann, S. Arctic low-level boundary layer clouds: In situ measurements and simulations of mono- and bimodal supercooled droplet size distributions at the top layer of liquid phase clouds. *Atmospheric Chemistry and Physics*, 15(2), 617–631. <https://doi.org/10.5194/acp-15-617-2015>, (2015).
- Knollenberg, R. G. The optical array: An alternative to scattering or extinction for airborne particle size determination. *Journal of Applied Meteorology and Climatology*, 9(1), 86–103. [https://doi.org/10.1175/1520-0450\(1970\)009<0086:TOAAAT>2.0.CO;2](https://doi.org/10.1175/1520-0450(1970)009<0086:TOAAAT>2.0.CO;2), (1970).
- Koop, T., Luo, B. P., Tsias, A., & Peter, T. Water activity as the determinant for homogeneous ice nucleation in aqueous solutions. *Nature*, 406, 611–614 (2000).
- Korolev, A., Emery, E., Strapp, J., Cober, S., & Isaac, G. Quantification of the effects of shattering on airborne ice particle measurements. *Journal of Atmospheric and Oceanic Technology*, 30, 2527–2553. <https://doi.org/10.1175/JTECH-D-13-00115.1>, (2013).
- Korolev, A., Emery, E. F., Strapp, J. W., Cober, S. G., Isaac, G. A., Wasey, M., & Marcotte, D. Small ice particles in tropospheric clouds: Fact or artifact? airborne icing instrumentation evaluation experiment. *Bulletin of the American Meteorological Society*, 92(8), 967–973. <https://doi.org/10.1175/2010BAMS3141.1>, (2011).
- Korolev, A., Kuznetsov, S. V., Makarov, Y. E., & Novikov, V. S. Evaluation of Measurements of Particle Size and Sample Area from Optical Array Probes. EN. *Journal of Atmospheric and Oceanic Technology*, 8(4), 514–522. [https://doi.org/10.1175/1520-0426\(1991\)008<0514:EOMOPS>2.0.CO;2](https://doi.org/10.1175/1520-0426(1991)008<0514:EOMOPS>2.0.CO;2), (1991).
- Korolev, A., Strapp, J. W., & Isaac, G. A. Evaluation of the Accuracy of PMS Optical Array Probes. EN. *Journal of Atmospheric and Oceanic Technology*, 15(3), 708–720. [https://doi.org/10.1175/1520-0426\(1998\)015<0708:EOTAOP>2.0.CO;2](https://doi.org/10.1175/1520-0426(1998)015<0708:EOTAOP>2.0.CO;2), (1998).

- Korolev, A. Limitations of the Wegener–Bergeron–Findeisen mechanism in the evolution of mixed-phase clouds. *Journal of the Atmospheric Sciences*, 64(9), 3372–3375. <https://doi.org/10.1175/JAS4035.1>, (2007).
- Korolev, A. Reconstruction of the Sizes of Spherical Particles from Their Shadow Images. Part I: Theoretical Considerations. EN. *Journal of Atmospheric and Oceanic Technology*, 24(3), 376–389. <https://doi.org/10.1175/JTECH1980.1>, (2007).
- Korolev, A. Rates of phase transformations in mixed-phase clouds. en. *Quarterly Journal of the Royal Meteorological Society*, 134(632), 595–608. <https://doi.org/10.1002/qj.230>, (2008).
- Korolev, A., Emery, E., & Creelman, K. Modification and tests of particle probe tips to mitigate effects of ice shattering. *Journal of Atmospheric and Oceanic Technology*, 30(4), 690–708. <https://doi.org/10.1175/JTECH-D-12-00142.1>, (2013).
- Korolev, A., & Isaac, G. A. Shattering during Sampling by OAPs and HVPS. Part I: Snow Particles. *Journal of Atmospheric and Oceanic Technology*, 22(5), 528–542. <https://doi.org/10.1175/JTECH1720.1>, (2005).
- Korolev, A., & Mazin, I. P. Supersaturation of Water Vapor in Clouds [Publisher: American Meteorological Society Section: Journal of the Atmospheric Sciences]. EN. *Journal of the Atmospheric Sciences*, 60(24). Publisher: American Meteorological Society Section: Journal of the Atmospheric Sciences, 2957–2974. [https://doi.org/10.1175/1520-0469\(2003\)060<2957:SOWVIC>2.0.CO;2](https://doi.org/10.1175/1520-0469(2003)060<2957:SOWVIC>2.0.CO;2), (2003).
- Krämer, M., Rolf, C., Luebke, A., Afchine, A., Spelten, N., Costa, A., Meyer, J., Zöger, M., Smith, J., Herman, R. L., Buchholz, B., Ebert, V., Baumgardner, D., Borrmann, S., Klingebiel, M., & Avallone, L. A microphysics guide to cirrus clouds – part 1: Cirrus types. *Atmospheric Chemistry and Physics*, 16(5), 3463–3483. <https://doi.org/10.5194/acp-16-3463-2016>, (2016).
- Krämer, M., Rolf, C., Spelten, N., Afchine, A., Fahey, D., Jensen, E., Khaykin, S., Kuhn, T., Lawson, P., Lykov, A., Pan, L. L., Riese, M., Rollins, A., Stroh, F., Thornberry, T., Wolf, V., Woods, S., Spichtinger, P., Quaas, J., & Sourdeval, O. A microphysics guide to cirrus – part 2: Climatologies of clouds and humidity from observations. *Atmospheric Chemistry and Physics*, 20(21), 12569–12608. <https://doi.org/10.5194/acp-20-12569-2020>, (2020).
- Kristensson, A., Gayet, J.-F., Ström, J., & Auriol, F. In situ observations of a reduction in effective crystal diameter in cirrus clouds near flight corridors. *Geophysical Research Letters*, 27(5), 681–684. <https://doi.org/10.1029/1999GL010934>, (2000).
- Kübbeler, M., Hildebrandt, M., Meyer, J., Schiller, C., Hamburger, T., Jurkat, T., Minikin, A., Petzold, A., Rautenhaus, M., Schlager, H., Schumann, U., Voigt, C., Spichtinger, P., Gayet, J.-F., Gourbeyre, C., & Krämer, M. Thin and subvisible cirrus and contrails in a subsaturated environment. *Atmospheric Chemistry and Physics*, 11(12), 5853–5865. <https://doi.org/10.5194/acp-11-5853-2011>, (2011).
- Kuebbeler, M., Lohmann, U., Hendricks, J., & Kärcher, B. Dust ice nuclei effects on cirrus clouds. English. *Atmospheric Chemistry and Physics*, 14(6), 3027–3046. <https://doi.org/10.5194/acp-14-3027-2014>, (2014).
- Kulkarni, G., Sanders, C., Zhang, K., Liu, X., & Zhao, C. Ice nucleation of bare and sulfuric acid-coated mineral dust particles and implication for cloud properties.

- en. *Journal of Geophysical Research: Atmospheres*, 119(16), 9993–10011. <https://doi.org/10.1002/2014JD021567>, (2014).
- Kulkarni, P., Baron, P. A., & Willeke, K. (2011). *Aerosol measurement: Principles, techniques, and applications*. John Wiley & Sons.
- Lance, S., Brock, C. A., Rogers, D., & Gordon, J. A. Water droplet calibration of the Cloud Droplet Probe (CDP) and in-flight performance in liquid, ice and mixed-phase clouds during ARCPAC. English. *Atmospheric Measurement Techniques*, 3(6), 1683–1706. <https://doi.org/10.5194/amt-3-1683-2010>, (2010).
- Lance, S. Coincidence Errors in a Cloud Droplet Probe (CDP) and a Cloud and Aerosol Spectrometer (CAS), and the Improved Performance of a Modified CDP. EN. *Journal of Atmospheric and Oceanic Technology*, 29(10), 1532–1541. <https://doi.org/10.1175/JTECH-D-11-00208.1>, (2012).
- Lawson, R. P., Baker, B., Pilson, B., & Mo, Q. In Situ Observations of the Microphysical Properties of Wave, Cirrus, and Anvil Clouds. Part II: Cirrus Clouds. EN. *Journal of the Atmospheric Sciences*, 63(12), 3186–3203. <https://doi.org/10.1175/JAS3803.1>, (2006).
- Lawson, R. P., Baker, B. A., Schmitt, C. G., & Jensen, T. L. An overview of microphysical properties of Arctic clouds observed in May and July 1998 during FIRE ACE. en. *Journal of Geophysical Research: Atmospheres*, 106(D14), 14989–15014. <https://doi.org/10.1029/2000JD900789>, (2001).
- Lee, D. S., Fahey, D. W., Skowron, A., Allen, M. R., Burkhardt, U., Chen, Q., Doherty, S. J., Freeman, S., Forster, P. M., Fuglestedt, J., Gettelman, A., De León, R. R., Lim, L. L., Lund, M. T., Millar, R. J., Owen, B., Penner, J. E., Pitari, G., Prather, M. J., ... Wilcox, L. J. The contribution of global aviation to anthropogenic climate forcing for 2000 to 2018. eng. *Atmos Environ (1994)*, 244, 117834. <https://doi.org/10.1016/j.atmosenv.2020.117834>, (2021).
- Leroy, D., Fontaine, E., Schwarzenboeck, A., & Strapp, J. W. Ice Crystal Sizes in High Ice Water Content Clouds. Part I: On the Computation of Median Mass Diameter from In Situ Measurements [Publisher: American Meteorological Society Section: Journal of Atmospheric and Oceanic Technology]. EN. *Journal of Atmospheric and Oceanic Technology*, 33(11). Publisher: American Meteorological Society Section: Journal of Atmospheric and Oceanic Technology, 2461–2476. <https://doi.org/10.1175/JTECH-D-15-0151.1>, (2016).
- Li, Y., Mahnke, C., Rohs, S., Bundke, U., Spelten, N., Dekoutsidis, G., Groß, S., Voigt, C., Schumann, U., Petzold, A., & Krämer, M. Upper tropospheric slightly ice-subsaturated regions: Frequency of occurrence and statistical evidence for the appearance of contrail cirrus. *Atmospheric Chemistry and Physics Discussions*, 2022, 1–32. <https://doi.org/10.5194/acp-2022-632>, (2022).
- Lin, H., Noone, K. J., Ström, J., & Heymsfield, A. J. Small Ice Crystals in Cirrus Clouds: A Model Study and Comparison with In Situ Observations [Publisher: American Meteorological Society Section: Journal of the Atmospheric Sciences]. EN. *Journal of the Atmospheric Sciences*, 55(11). Publisher: American Meteorological Society Section: Journal of the Atmospheric Sciences, 1928–1939. [https://doi.org/10.1175/1520-0469\(1998\)055<1928:SICICC>2.0.CO;2](https://doi.org/10.1175/1520-0469(1998)055<1928:SICICC>2.0.CO;2), (1998).

- Liou, K.-N. Influence of Cirrus Clouds on Weather and Climate Processes: A Global Perspective. EN. *Monthly Weather Review*, 114(6), 1167–1199. [https://doi.org/10.1175/1520-0493\(1986\)114<1167:IOCCOW>2.0.CO;2](https://doi.org/10.1175/1520-0493(1986)114<1167:IOCCOW>2.0.CO;2), (1986).
- Loefering, G. Global Hawk - A New Tool for Airborne Atmospheric Sensing. en. *1st UAV Conference*. <https://doi.org/10.2514/6.2002-3458>, (2002).
- Luebke, A. E., Afchine, A., Costa, A., Grooß, J.-U., Meyer, J., Rolf, C., Spelten, N., Avallone, L. M., Baumgardner, D., & Krämer, M. The origin of midlatitude ice clouds and the resulting influence on their microphysical properties. *Atmospheric Chemistry and Physics*, 16(9), 5793–5809. <https://doi.org/10.5194/acp-16-5793-2016>, (2016).
- Luebke, A. E., Avallone, L. M., Schiller, C., Meyer, J., Rolf, C., & Krämer, M. Ice water content of arctic, midlatitude, and tropical cirrus – part 2: Extension of the database and new statistical analysis. *Atmospheric Chemistry and Physics*, 13(13), 6447–6459. <https://doi.org/10.5194/acp-13-6447-2013>, (2013).
- Maciel, F. V., Diao, M., & Patnaude, R. Examination of aerosol indirect effects during cirrus cloud evolution. *Atmospheric Chemistry and Physics Discussions*, 2022, 1–34. <https://doi.org/10.5194/acp-2022-519>, (2022).
- Marjani, S., Tesche, M., Bräuer, P., Sourdeval, O., & Quaas, J. Satellite observations of the impact of individual aircraft on ice crystal number in thin cirrus clouds. *Geophysical Research Letters*, 49(5). <https://doi.org/10.1029/2021GL096173>, (2022).
- Märkl, R. S., Voigt, C., Sauer, D., Dischl, R. K., Kaufmann, S., Harlaß, T., Hahn, V., Roiger, A., Weiß-Rehm, C., Burkhardt, U., Schumann, U., Marsing, A., Scheibe, M., Dörnbrack, A., Renard, C., Gauthier, M., Swann, P., Madden, P., Luff, D., ... Le Clercq, P. Powering aircraft with 100% sustainable aviation fuel reduces ice crystals in contrails. English. *Atmospheric Chemistry and Physics*, 24(6), 3813–3837. <https://doi.org/10.5194/acp-24-3813-2024>, (2024).
- Marsing, A., Meerkötter, R., Heller, R., Kaufmann, S., Jurkat-Witschas, T., Krämer, M., Rolf, C., & Voigt, C. Investigating the radiative effect of arctic cirrus measured in situ during the winter 2015–2016. *Atmospheric Chemistry and Physics*, 23(1), 587–609. <https://doi.org/10.5194/acp-23-587-2023>, (2023).
- McFarquhar, G. M., Baumgardner, D., Bansemer, A., Abel, S. J., Crosier, J., French, J., Rosenberg, P., Korolev, A., Schwarzenboeck, A., Leroy, D., Um, J., Wu, W., Heymsfield, A. J., Twohy, C., Detwiler, A., Field, P., Neumann, A., Cotton, R., Axisa, D., & Dong, J. Processing of Ice Cloud In Situ Data Collected by Bulk Water, Scattering, and Imaging Probes: Fundamentals, Uncertainties, and Efforts toward Consistency. EN. *Meteorological Monographs*, 58(1), 11.1–11.33. <https://doi.org/10.1175/AMSMONOGRAPHS-D-16-0007.1>, (2017).
- McFarquhar, G. M., Bretherton, C. S., Marchand, R., Protat, A., DeMott, P. J., Alexander, S. P., Roberts, G. C., Twohy, C. H., Toohey, D., Siems, S., Huang, Y., Wood, R., Rauber, R. M., Lasher-Trapp, S., Jensen, J., Stith, J. L., Mace, J., Um, J., Järvinen, E., ... McDonald, A. Observations of clouds, aerosols, precipitation, and surface radiation over the southern ocean: An overview of capricorn, marcus, mire, and socrates. *Bulletin of the American Meteorological Society*, 102(4), E894–E928. <https://doi.org/10.1175/BAMS-D-20-0132.1>, (2021).

- McFarquhar, G. M., & Heymsfield, A. J. The Definition and Significance of an Effective Radius for Ice Clouds. EN. *Journal of the Atmospheric Sciences*, 55(11). [https://doi.org/10.1175/1520-0469\(1998\)055<2039:TDASOA>2.0.CO;2](https://doi.org/10.1175/1520-0469(1998)055<2039:TDASOA>2.0.CO;2), (1998).
- McFarquhar, G. M., Hsieh, T.-L., Freer, M., Mascio, J., & Jewett, B. F. The characterization of ice hydrometeor gamma size distributions as volumes in n_0 — phase space: Implications for microphysical process modeling. *Journal of the Atmospheric Sciences*, 72(2), 892–909. <https://doi.org/10.1175/JAS-D-14-0011.1>, (2015).
- McFarquhar, G. M., Um, J., Freer, M., Baumgardner, D., Kok, G. L., & Mace, G. Importance of small ice crystals to cirrus properties: Observations from the tropical warm pool international cloud experiment (twp-ice). *Geophysical Research Letters*, 34(13). <https://doi.org/10.1029/2007GL029865>, (2007).
- McGraw, Z., Storelvmo, T., Samset, B. H., & Stjern, C. W. Global Radiative Impacts of Black Carbon Acting as Ice Nucleating Particles. en. *Geophysical Research Letters*, 47(20), e2020GL089056. <https://doi.org/10.1029/2020GL089056>, (2020).
- Mie, G. Beiträge zur optik trüber medien, speziell kolloidaler metallösungen. *Annalen der Physik*, 330(3), 377–445. <https://doi.org/10.1002/andp.19083300302>, (1908).
- Miller, A. J., Ramelli, F., Fuchs, C., Omanovic, N., Spirig, R., Zhang, H., Lohmann, U., Kanji, Z. A., & Henneberger, J. Two new multirotor uncrewed aerial vehicles (UAVs) for glaciogenic cloud seeding and aerosol measurements within the CLOUDLAB project. English. *Atmospheric Measurement Techniques*, 17(2), 601–625. <https://doi.org/10.5194/amt-17-601-2024>, (2024).
- Minikin, A., Petzold, A., Ström, J., Krejci, R., Seifert, M., van Velthoven, P., Schlager, H., & Schumann, U. Aircraft observations of the upper tropospheric fine particle aerosol in the Northern and Southern Hemispheres at midlatitudes. en. *Geophysical Research Letters*, 30(10). <https://doi.org/10.1029/2002GL016458>, (2003).
- Minikin, A., Petzold, A., Weinzierl, B., & Gayet, J.-F. (2012). In Situ Measurement Methods for Atmospheric Aerosol Particles and Cloud Elements. In U. Schumann (Ed.), *Atmospheric Physics: Background – Methods – Trends* (pp. 297–315). Springer Berlin Heidelberg. https://doi.org/10.1007/978-3-642-30183-4_18
- Mitchell, D. L., Lawson, R. P., & Baker, B. Understanding effective diameter and its application to terrestrial radiation in ice clouds [Publisher: Copernicus GmbH]. English. *Atmospheric Chemistry and Physics*, 11(7). Publisher: Copernicus GmbH, 3417–3429. <https://doi.org/10.5194/acp-11-3417-2011>, (2011).
- Mitchell, D. L., Rasch, P., Ivanova, D., McFarquhar, G., & Nousiainen, T. Impact of small ice crystal assumptions on ice sedimentation rates in cirrus clouds and GCM simulations. en. *Geophysical Research Letters*, 35(9). <https://doi.org/10.1029/2008GL033552>, (2008).
- Möhler, O., Field, P. R., Connolly, P., Benz, S., Saathoff, H., Schnaiter, M., Wagner, R., Cotton, R., Krämer, M., Mangold, A., & Heymsfield, A. J. Efficiency of the deposition mode ice nucleation on mineral dust particles. English. *Atmospheric Chemistry and Physics*, 6(10), 3007–3021. <https://doi.org/10.5194/acp-6-3007-2006>, (2006).
- Möhler, O., Stetzer, O., Schaefers, S., Linke, C., Schnaiter, M., Tiede, R., Saathoff, H., Krämer, M., Mangold, A., Budz, P., Zink, P., Schreiner, J., Mauersberger, K., Haag,

- W., Kärcher, B., & Schurath, U. Experimental investigation of homogeneous freezing of sulphuric acid particles in the aerosol chamber AIDA. English. *Atmospheric Chemistry and Physics*, 3(1), 211–223. <https://doi.org/10.5194/acp-3-211-2003>, (2003).
- Möhler, O., Adams, M., Lacher, L., Vogel, E., Nadolny, J., Ullrich, R., Boffo, C., Pfeuffer, T., Hobl, A., Weiß, M., Vepuri, H. S. K., Hiranuma, N., & Murray, B. J. The Portable Ice Nucleation Experiment (PINE): A new online instrument for laboratory studies and automated long-term field observations of ice-nucleating particles. English. *Atmospheric Measurement Techniques*, 14(2), 1143–1166. <https://doi.org/10.5194/amt-14-1143-2021>, (2021).
- Moore, R. H., Shook, M., Beyersdorf, A., Corr, C., Herndon, S., Knighton, W. B., Miakelyle, R., Thornhill, K. L., Winstead, E. L., Yu, Z., Ziemba, L. D., & Anderson, B. E. Influence of Jet Fuel Composition on Aircraft Engine Emissions: A Synthesis of Aerosol Emissions Data from the NASA APEX, AAFEX, and ACCESS Missions. *Energy & Fuels*, 29(4), 2591–2600. <https://doi.org/10.1021/ef502618w>, (2015).
- Muhlbauer, A., Ackerman, T. P., Comstock, J. M., Diskin, G. S., Evans, S. M., Lawson, R. P., & Marchand, R. T. Impact of large-scale dynamics on the microphysical properties of midlatitude cirrus. en. *Journal of Geophysical Research: Atmospheres*, 119(7), 3976–3996. <https://doi.org/10.1002/2013JD020035>, (2014).
- Muri, H., Kristjánsson, J. E., Storelmo, T., & Pfeffer, M. A. The climatic effects of modifying cirrus clouds in a climate engineering framework. *Journal of Geophysical Research: Atmospheres*, 119(7), 4174–4191. <https://doi.org/10.1002/2013JD021063>, (2014).
- Murphy, D. M., & Koop, T. Review of the vapour pressures of ice and supercooled water for atmospheric applications. *Quarterly Journal of the Royal Meteorological Society*, 131 (2005).
- Nagel, D., Maixner, U., Strapp, W., & Wasey, M. Advancements in Techniques for Calibration and Characterization of In Situ Optical Particle Measuring Probes, and Applications to the FSSP-100 Probe. EN. *Journal of Atmospheric and Oceanic Technology*, 24(5). <https://doi.org/10.1175/JTECH2006.1>, (2007).
- Nagy, A., Szymanski, W. W., Gál, P., Golczewski, A., & Czitrovsky, A. Numerical and experimental study of the performance of the dual wavelength optical particle spectrometer (DWOPS). *Journal of Aerosol Science*, 38(4), 467–478. <https://doi.org/10.1016/j.jaerosci.2007.02.005>, (2007).
- O'Neill, B. C., Krieglger, E., Ebi, K. L., Kemp-Benedict, E., Riahi, K., Rothman, D. S., van Ruijven, B. J., van Vuuren, D. P., Birkmann, J., Kok, K., Levy, M., & Solecki, W. The roads ahead: Narratives for shared socioeconomic pathways describing world futures in the 21st century. *Global Environmental Change*, 42, 169–180. <https://doi.org/10.1016/j.gloenvcha.2015.01.004>, (2017).
- O'Shea, S., Crosier, J., Dorsey, J., Gallagher, L., Schledewitz, W., Bower, K., Schlenzcek, O., Borrmann, S., Cotton, R., Westbrook, C., & Ulanowski, Z. Characterising optical array particle imaging probes: Implications for small-ice-crystal observations. *Atmospheric Measurement Techniques*, 14(3), 1917–1939. <https://doi.org/10.5194/amt-14-1917-2021>, (2021).

- O'Shea, S., Crosier, J., Dorsey, J., Schledewitz, W., Crawford, I., Borrmann, S., Cotton, R., & Bansenmer, A. Revisiting particle sizing using greyscale optical array probes: Evaluation using laboratory experiments and synthetic data. *Atmospheric Measurement Techniques*, 12(6), 3067–3079. <https://doi.org/10.5194/amt-12-3067-2019>, (2019).
- O'Shea, S. J., Choulaton, T. W., Lloyd, G., Crosier, J., Bower, K. N., Gallagher, M., Abel, S. J., Cotton, R. J., Brown, P. R. A., Fugal, J. P., Schlenzcek, O., Borrmann, S., & Pickering, J. C. Airborne observations of the microphysical structure of two contrasting cirrus clouds. en. *Journal of Geophysical Research: Atmospheres*, 121(22), 13, 510–13, 536. <https://doi.org/10.1002/2016JD025278>, (2016).
- Parol, F., Buriez, J., Brogniez, G., & Fouquart, Y. Information content of avhrr channels 4 and 5 with respect to the effective radius of cirrus cloud particles. *Journal of Applied Meteorology*, 30, 973–984. <https://doi.org/10.1175/1520-0450-30.7.973>, (1991).
- Patnaude, R., & Diao, M. Aerosol indirect effects on cirrus clouds based on global aircraft observations [e2019GL086550 2019GL086550]. *Geophysical Research Letters*, 47(10). e2019GL086550 2019GL086550, e2019GL086550. <https://doi.org/10.1029/2019GL086550>, (2020).
- Perry, A. (1987). Middle latitude climates. In *Climatology* (pp. 581–583). Springer US. https://doi.org/10.1007/0-387-30749-4_116
- Petzold, A., Busen, R., Schröder, F. P., Baumann, R., Kuhn, M., Ström, J., Hagen, D. E., Whitefield, P. D., Baumgardner, D., Arnold, F., Borrmann, S., & Schumann, U. Near-field measurements on contrail properties from fuels with different sulfur content. *Journal of Geophysical Research: Atmospheres*, 102(D25), 29867–29880. <https://doi.org/10.1029/97JD02209>, (1997).
- Pinnick, R. G., Garvey, D. M., & Duncan, L. D. Calibration of Knollenberg FSSP Light-Scattering Counters for Measurement of Cloud Droplets. EN. *Journal of Applied Meteorology and Climatology*, 20(9). [https://doi.org/10.1175/1520-0450\(1981\)020<1049:COKFLS>2.0.CO;2](https://doi.org/10.1175/1520-0450(1981)020<1049:COKFLS>2.0.CO;2), (1981).
- Ponsonby, J., King, L., Murray, B. J., & Stettler, M. E. J. Jet aircraft lubrication oil droplets as contrail ice-forming particles. English. *Atmospheric Chemistry and Physics*, 24(3), 2045–2058. <https://doi.org/10.5194/acp-24-2045-2024>, (2024).
- Pruppacher, H., & Klett, J. (2010). *Microphysics of Clouds and Precipitation* (L. A. Mysak & K. Hamilton, Eds.; Vol. 18). Springer Netherlands. <https://doi.org/10.1007/978-0-306-48100-0>
- Rautenhaus, M., Bauer, G., & Dörnbrack, A. A web service based tool to plan atmospheric research flights. *Geoscientific Model Development*, 5(1), 55–71. <https://doi.org/10.5194/gmd-5-55-2012>, (2012).
- Righi, M., Hendricks, J., & Beer, C. G. Exploring the uncertainties in the aviation soot-cirrus effect. *Atmospheric Chemistry and Physics*, 21(23), 17267–17289. <https://doi.org/10.5194/acp-21-17267-2021>, (2021).
- Righi, M., Hendricks, J., & Brinkop, S. The global impact of the transport sectors on the atmospheric aerosol and the resulting climate effects under the Shared Socioeconomic Pathways (SSPs). English. *Earth System Dynamics*, 14(4), 835–859. <https://doi.org/10.5194/esd-14-835-2023>, (2023).

- Righi, M., Hendricks, J., Lohmann, U., Beer, C. G., Hahn, V., Heinold, B., Heller, R., Krämer, M., Ponater, M., Rolf, C., Tegen, I., & Voigt, C. Coupling aerosols to (cirrus) clouds in the global EMAC-MADE3 aerosol–climate model. English. *Geoscientific Model Development*, 13(3), 1635–1661. <https://doi.org/10.5194/gmd-13-1635-2020>, (2020).
- Rosenberg, P. D., Dean, A. R., Williams, P. I., Dorsey, J. R., Minikin, A., Pickering, M. A., & Petzold, A. Particle sizing calibration with refractive index correction for light scattering optical particle counters and impacts upon PCASP and CDP data collected during the Fennec campaign. English. *Atmospheric Measurement Techniques*, 5(5). <https://doi.org/10.5194/amt-5-1147-2012>, (2012).
- Sassen, K., & Campbell, J. R. A midlatitude cirrus cloud climatology from the facility for atmospheric remote sensing. part i: Macrophysical and synoptic properties. *Journal of the Atmospheric Sciences*, 58(5), 481–496. [https://doi.org/10.1175/1520-0469\(2001\)058<0481:AMCCCF>2.0.CO;2](https://doi.org/10.1175/1520-0469(2001)058<0481:AMCCCF>2.0.CO;2), (2001).
- Schiller, C., Krämer, M., Afchine, A., Spelten, N., & Sitnikov, N. Ice water content of arctic, midlatitude, and tropical cirrus. *Journal of Geophysical Research: Atmospheres*, 113(D24). <https://doi.org/10.1029/2008JD010342>, (2008).
- Schlenczek, O. (2018). *Airborne and ground-based holographic measurement of hydrometeors in liquid-phase, mixed-phase and ice clouds* (Doctoral dissertation). <https://doi.org/10.25358/OPENSOURCE-4124>
- Schmale, J., Zieger, P., & Ekman, A. M. L. Aerosols in current and future Arctic climate. en. *Nature Climate Change*, 11(2), 95–105. <https://doi.org/10.1038/s41558-020-00969-5>, (2021).
- Schnaiter, M., Järvinen, E., Abdelmonem, A., & Leisner, T. PHIPS-HALO: The airborne particle habit imaging and polar scattering probe – Part 2: Characterization and first results. English. *Atmospheric Measurement Techniques*, 11(1), 341–357. <https://doi.org/10.5194/amt-11-341-2018>, (2018).
- Schollmayer, D. (2021). *A neural network for particle size retrieval in optical array probe image data analysis* (Master's thesis). Johannes Gutenberg-Universität Mainz.
- Schröder, F., Kärcher, B., Durore, C., Ström, J., Petzold, A., Gayet, J.-E., Strauss, B., Wendling, P., & Borrmann, S. On the transition of contrails into cirrus clouds. *Journal of the Atmospheric Sciences*, 57(4), 464–480. [https://doi.org/10.1175/1520-0469\(2000\)057<0464:OTTOCI>2.0.CO;2](https://doi.org/10.1175/1520-0469(2000)057<0464:OTTOCI>2.0.CO;2), (2000).
- Schulte, P., Schlager, H., Ziereis, H., Schumann, U., Baughcum, S. L., & Deidewig, F. NO_x emission indices of subsonic long-range jet aircraft at cruise altitude: In situ measurements and predictions. en. *Journal of Geophysical Research: Atmospheres*, 102(D17), 21431–21442. <https://doi.org/10.1029/97JD01526>, (1997).
- Schumann, U., Baumann, R., Baumgardner, D., Bedka, S. T., Duda, D. P., Freudenthaler, V., Gayet, J.-E., Heymsfield, A. J., Minnis, P., Quante, M., Raschke, E., Schlager, H., Vázquez-Navarro, M., Voigt, C., & Wang, Z. Properties of individual contrails: A compilation of observations and some comparisons. *Atmospheric Chemistry and Physics*, 17(1), 403–438. <https://doi.org/10.5194/acp-17-403-2017>, (2017).
- Schumann, U., Mayer, B., Gierens, K., Unterstrasser, S., Jessberger, P., Petzold, A., Voigt, C., & Gayet, J.-E. Effective radius of ice particles in cirrus and contrails. *Journal of*

- the Atmospheric Sciences*, 68(2), 300–321. <https://doi.org/10.1175/2010JAS3562.1>, (2011).
- Schumann, U., Penner, J. E., Chen, Y., Zhou, C., & Graf, K. Dehydration effects from contrails in a coupled contrail–climate model. *Atmospheric Chemistry and Physics*, 15(19), 11179–11199. <https://doi.org/10.5194/acp-15-11179-2015>, (2015).
- Schumann, U., Schlager, H., Arnold, F., Baumann, R., Haschberger, P., & Klemm, O. Dilution of aircraft exhaust plumes at cruise altitudes. *Atmospheric Environment*, 32(18), 3097–3103. [https://doi.org/10.1016/S1352-2310\(97\)00455-X](https://doi.org/10.1016/S1352-2310(97)00455-X), (1998).
- Schumann, U. On conditions for contrail formation from aircraft exhausts. *Meteorologische Zeitschrift*, 5(1), 4–23. <https://doi.org/10.1127/metz/5/1996/4>, (1996).
- Schumann, U., & Heymsfield, A. J. On the life cycle of individual contrails and contrail cirrus. *Meteorological Monographs*, 58, 3.1–3.24. <https://doi.org/10.1175/AMSMONOGRAPHS-D-16-0005.1>, (2017).
- Schumann, U., Poll, I., Teoh, R., Koelle, R., Spinielli, E., Molloy, J., Koudis, G. S., Baumann, R., Bugliaro, L., Stettler, M., & Voigt, C. Air traffic and contrail changes over Europe during covid-19: A model study. *Atmospheric Chemistry and Physics*, 21, 7429–7450 (2021).
- Seinfeld, J. H., & Pandis, S. N. (1998). *Atmospheric chemistry and physics: From air pollution to climate change* (I. John Wiley Sons, Ed.). Wiley-Interscience.
- Serreze, M. C., & Barry, R. G. Processes and impacts of arctic amplification: A research synthesis. *Global and Planetary Change*, 77(1), 85–96. <https://doi.org/https://doi.org/10.1016/j.gloplacha.2011.03.004>, (2011).
- Shupe, M. D., Rex, M., Blomquist, B., Persson, P. O. G., Schmale, J., Uttal, T., Althausen, D., Angot, H., Archer, S., Bariteau, L., Beck, I., Bilberry, J., Bucci, S., Buck, C., Boyer, M., Brasseur, Z., Brooks, I. M., Calmer, R., Cassano, J., ... Yue, F. Overview of the MOSAiC expedition: Atmosphere [00060]. *Elementa: Science of the Anthropocene*, 10(1). 00060. <https://doi.org/10.1525/elementa.2021.00060>, (2022).
- Sorooshian, A., Corral, A. F., Braun, R. A., Cairns, B., Crosbie, E., Ferrare, R., Hair, J., Kleb, M. M., Hossein Mardi, A., Maring, H., McComiskey, A., Moore, R., Paine-mal, D., Scarino, A. J., Schlosser, J., Shingler, T., Shook, M., Wang, H., Zeng, X., ... Zuidema, P. Atmospheric Research Over the Western North Atlantic Ocean Region and North American East Coast: A Review of Past Work and Challenges Ahead. en. *Journal of Geophysical Research: Atmospheres*, 125(6), e2019JD031626. <https://doi.org/10.1029/2019JD031626>, (2020).
- Sourdeval, O., Gryspeerdt, E., Krämer, M., Goren, T., Delanoë, J., Afchine, A., Hemmer, E., & Quaas, J. Ice crystal number concentration estimates from lidar–radar satellite remote sensing – part I: Method and evaluation. *Atmospheric Chemistry and Physics*, 18(19), 14327–14350. <https://doi.org/10.5194/acp-18-14327-2018>, (2018).
- Spang, R., Müller, R., & Rap, A. (2023). *Radiative impact of thin cirrus clouds in the lowermost stratosphere and tropopause region* (preprint). Clouds, Precipitation/Remote Sensing/Stratosphere/Physics (physical properties, and processes). <https://doi.org/10.5194/egusphere-2023-1234>

- Spichtinger, P., & Cziczo, D. J. Impact of heterogeneous ice nuclei on homogeneous freezing events in cirrus clouds. *Journal of Geophysical Research: Atmospheres*, 115(D14). <https://doi.org/10.1029/2009JD012168>, (2010).
- Spichtinger, P., & Gierens, K. M. Modelling of cirrus clouds – part 1b: Structuring cirrus clouds by dynamics. *Atmospheric Chemistry and Physics*, 9(2), 707–719. <https://doi.org/10.5194/acp-9-707-2009>, (2009).
- Spichtinger, P., & Gierens, K. M. Modelling of cirrus clouds – Part 1a: Model description and validation. *Atmospheric Chemistry and Physics*, 9(2), 685–706. <https://doi.org/10.5194/acp-9-685-2009>, (2009).
- Sprenger, M., & Wernli, H. The lagranto lagrangian analysis tool – version 2.0. *Geoscientific Model Development*, 8(8), 2569–2586. <https://doi.org/10.5194/gmd-8-2569-2015>, (2015).
- Stephens, G. L. Cloud Feedbacks in the Climate System: A Critical Review. EN. *Journal of Climate*, 18(2), 237–273. <https://doi.org/10.1175/JCLI-3243.1>, (2005).
- Stohl, A., Haimberger, L., Scheele, M. P., & Wernli, H. An intercomparison of results from three trajectory models. en. *Meteorological Applications*, 8(2), 127–135. <https://doi.org/10.1017/S1350482701002018>, (2001).
- Storelvmo, T. Aerosol effects on climate via mixed-phase and ice clouds. *Annual Review of Earth and Planetary Sciences*, 45(1), 199–222. <https://doi.org/10.1146/annurev-earth-060115-012240>, (2017).
- Storelvmo, T., Boos, W., & Herger, N. Cirrus cloud seeding: A climate engineering mechanism with reduced side effects? *Philosophical transactions. Series A, Mathematical, physical, and engineering sciences*, 372. <https://doi.org/10.1098/rsta.2014.0116>, (2014).
- Stratmann, G., Ziereis, H., Stock, P., Brenninkmeijer, C., Zahn, A., Rauthe-Schöch, A., Velthoven, P., Schlager, H., & Volz-Thomas, A. No and noy in the upper troposphere: Nine years of caribic measurements onboard a passenger aircraft. *Atmospheric Environment*, 133, 93–111. <https://doi.org/10.1016/j.atmosenv.2016.02.035>, (2016).
- Tegen, I., Harrison, S. P., Kohfeld, K., Prentice, I. C., Coe, M., & Heimann, M. Impact of vegetation and preferential source areas on global dust aerosol: Results from a model study. en. *Journal of Geophysical Research: Atmospheres*, 107(D21), AAC 14–1–AAC 14–27. <https://doi.org/10.1029/2001JD000963>, (2002).
- Teoh, R., Schumann, U., Gryspeerd, E., Shapiro, M., Molloy, J., Koudis, G., Voigt, C., & Stettler, M. E. J. Aviation contrail climate effects in the north atlantic from 2016 to 2021. *Atmospheric Chemistry and Physics*, 22(16), 10919–10935. <https://doi.org/10.5194/acp-22-10919-2022>, (2022).
- Teoh, R., Engberg, Z., Schumann, U., Voigt, C., Shapiro, M., Rohs, S., & Stettler, M. E. J. Global aviation contrail climate effects from 2019 to 2021 [Publisher: Copernicus GmbH]. English. *Atmospheric Chemistry and Physics*, 24(10). Publisher: Copernicus GmbH, 6071–6093. <https://doi.org/10.5194/acp-24-6071-2024>, (2024).
- Tesche, M., Achtert, P., Glantz, P., & Noone, K. J. Aviation effects on already-existing cirrus clouds. *Nature Communications*, 7. <https://doi.org/10.1038/ncomms12016>, (2016).

- Testa, B., Durdina, L., Alpert, P. A., Mahrt, F., Dreimol, C. H., Edebeli, J., Spirig, C., Decker, Z. C. J., Anet, J., & Kanji, Z. A. Soot aerosols from commercial aviation engines are poor ice-nucleating particles at cirrus cloud temperatures. English. *Atmospheric Chemistry and Physics*, 24(7), 4537–4567. <https://doi.org/10.5194/acp-24-4537-2024>, (2024).
- Tetoni, E., Ewald, F., Hagen, M., Köcher, G., Zinner, T., & Groß, S. Retrievals of ice microphysical properties using dual-wavelength polarimetric radar observations during stratiform precipitation events. English. *Atmospheric Measurement Techniques*, 15(13), 3969–3999. <https://doi.org/10.5194/amt-15-3969-2022>, (2022).
- Thornberry, T. D., Rollins, A. W., Avery, M. A., Woods, S., Lawson, R. P., Bui, T. V., & Gao, R.-S. Ice water content-extinction relationships and effective diameter for TTL cirrus derived from in situ measurements during ATTREX 2014. en. *Journal of Geophysical Research: Atmospheres*, 122(8), 4494–4507. <https://doi.org/10.1002/2016JD025948>, (2017).
- Twomey, S. Pollution and the planetary albedo. *Atmospheric Environment* (1967), 8(12), 1251–1256. [https://doi.org/10.1016/0004-6981\(74\)90004-3](https://doi.org/10.1016/0004-6981(74)90004-3), (1974).
- Ungeheuer, F., Caudillo, L., Ditas, F., Simon, M., van Pinxteren, D., Kılıç, D., Rose, D., Jacobi, S., Kürten, A., Curtius, J., & Vogel, A. L. Nucleation of jet engine oil vapours is a large source of aviation-related ultrafine particles. en. *Communications Earth & Environment*, 3(1), 1–8. <https://doi.org/10.1038/s43247-022-00653-w>, (2022).
- Ungeheuer, F., van Pinxteren, D., & Vogel, A. L. Identification and source attribution of organic compounds in ultrafine particles near Frankfurt International Airport. English. *Atmospheric Chemistry and Physics*, 21(5), 3763–3775. <https://doi.org/10.5194/acp-21-3763-2021>, (2021).
- Unterstrasser, S., & Gierens, K. Numerical simulations of contrail-to-cirrus transition – Part 2: Impact of initial ice crystal number, radiation, stratification, secondary nucleation and layer depth [Publisher: Copernicus GmbH]. English. *Atmospheric Chemistry and Physics*, 10(4). Publisher: Copernicus GmbH, 2037–2051. <https://doi.org/10.5194/acp-10-2037-2010>, (2010).
- Unterstrasser, S., Gierens, K., Sölch, I., & Lainer, M. Numerical simulations of homogeneously nucleated natural cirrus and contrail-cirrus. part 1: How different are they? *Meteorologische Zeitschrift*, 26(6), 621–642. <https://doi.org/10.1127/metz/2016/0777>, (2017).
- Unterstrasser, S., Gierens, K., Sölch, I., & Wirth, M. Numerical simulations of homogeneously nucleated natural cirrus and contrail-cirrus. part 2: Interaction on local scale. *Meteorologische Zeitschrift*, 26(6), 643–661. <https://doi.org/10.1127/metz/2016/0780>, (2017).
- Urbanek, B., Groß, S., Wirth, M., Rolf, C., Krämer, M., & Voigt, C. High depolarization ratios of naturally occurring cirrus clouds near air traffic regions over europe. *Geophysical Research Letters*, 45(23), 13, 166–13, 172. <https://doi.org/10.1029/2018GL079345>, (2018).

- Vaillant de Guélis, T., Schwarzenböck, A., Shcherbakov, V., Gourbeyre, C., Laurent, B., Dupuy, R., Coutris, P., & Duroure, C. Study of the diffraction pattern of cloud particles and the respective responses of optical array probes. English. *Atmospheric Measurement Techniques*, 12(4), 2513–2529. <https://doi.org/10.5194/amt-12-2513-2019>, (2019).
- Vali, G., DeMott, P. J., Möhler, O., & Whale, T. F. Technical Note: A proposal for ice nucleation terminology [Publisher: Copernicus GmbH]. *Atmospheric Chemistry and Physics*, 15(18). Publisher: Copernicus GmbH, 10263–10270. <https://doi.org/10.5194/acp-15-10263-2015>, (2015).
- Verma, P., & Burkhardt, U. Contrail formation within cirrus: Icon-lem simulations of the impact of cirrus cloud properties on contrail formation. *Atmospheric Chemistry and Physics*, 22(13), 8819–8842. <https://doi.org/10.5194/acp-22-8819-2022>, (2022).
- Vidaurre, G., & Hallett, J. Particle Impact and Breakup in Aircraft Measurement. EN. *Journal of Atmospheric and Oceanic Technology*, 26(5), 972–983. <https://doi.org/10.1175/2008JTECHA1147.1>, (2009).
- Voigt, C., Schumann, U., Jurkat, T., Schäuble, D., Schlager, H., Petzold, A., Gayet, J.-E., Krämer, M., Schneider, J., Borrmann, S., Schmale, J., Jessberger, P., Hamburger, T., Lichtenstern, M., Scheibe, M., Gourbeyre, C., Meyer, J., Kübbeler, M., Frey, W., ... Dörnbrack, A. In-situ observations of young contrails – overview and selected results from the concert campaign. *Atmospheric Chemistry and Physics*, 10(18), 9039–9056. <https://doi.org/10.5194/acp-10-9039-2010>, (2010).
- Voigt, C., Kleine, J., Sauer, D., Moore, R. H., Bräuer, T., Le Clercq, P., Kaufmann, S., Scheibe, M., Jurkat-Witschas, T., Aigner, M., Bauder, U., Boose, Y., Borrmann, S., Crosbie, E., Diskin, G. S., DiGangi, J., Hahn, V., Heckl, C., Huber, F., ... Anderson, B. E. Cleaner burning aviation fuels can reduce contrail cloudiness [Number: 1 Publisher: Nature Publishing Group]. en. *Commun Earth Environ*, 2(1). Number: 1 Publisher: Nature Publishing Group, 1–10. <https://doi.org/10.1038/s43247-021-00174-y>, (2021).
- Voigt, C., Lelieveld, J., Schlager, H., Schneider, J., Curtius, J., Meerkötter, R., Sauer, D., Bugliaro, L., Bohn, B., Crowley, J., Erbertseder, T., Gro, S., Hahn, V., Li, Q., Mertens, M., Pöhlker, M., Pozzer, A., Schumann, U., Tomsche, L., & Rapp, M. Cleaner skies during the covid-19 lockdown. *Bulletin of the American Meteorological Society*, 103. <https://doi.org/10.1175/BAMS-D-21-0012.1>, (2022).
- Voigt, C., Schumann, U., Jessberger, P., Jurkat, T., Petzold, A., Gayet, J.-E., Krämer, M., Thornberry, T., & Fahey, D. Extinction and optical depth of contrails. *Geophysical Research Letters*, 38, 1–5. <https://doi.org/10.1029/2011GL047189>, (2011).
- Voigt, C., Schumann, U., Minikin, A., Abdelmonem, A., Afchine, A., Borrmann, S., Boettcher, M., Buchholz, B., Bugliaro, L., Costa, A., Curtius, J., Dollner, M., Dörnbrack, A., Dreiling, V., Ebert, V., Ehrlich, A., Fix, A., Forster, L., Frank, E., & Zoeger, M. Ml-cirrus: The airborne experiment on natural cirrus and contrail cirrus with the high-altitude long-range research aircraft halo. *Bulletin of the American Meteorological Society*, 98, 271–288. <https://doi.org/10.1175/BAMS-D-15-00213.1>, (2017).

- Walser, A. (2017). *On the saharan air layer aerosol and its role as a reservoir of cloud condensation nuclei*. Ludwig-Maximilians-Universität München.
- Walser, A., Sauer, D., Spanu, A., Gasteiger, J., & Weinzierl, B. On the parametrization of optical particle counter response including instrument-induced broadening of size spectra and a self-consistent evaluation of calibration measurements. English. *Atmospheric Measurement Techniques*, 10(11), 4341–4361. <https://doi.org/10.5194/amt-10-4341-2017>, (2017).
- Wang, Z., Bugliaro, L., Jurkat-Witschas, T., Heller, R., Burkhardt, U., Ziereis, H., Dekoutsidis, G., Wirth, M., Groß, S., Kirschler, S., Kaufmann, S., & Voigt, C. Observations of microphysical properties and radiative effects of a contrail cirrus outbreak over the North Atlantic. *Atmospheric Chemistry and Physics*, 23(3), 1941–1961. <https://doi.org/10.5194/acp-23-1941-2023>, (2023).
- Wendisch, M., Brückner, M., Crewell, S., Ehrlich, A., Notholt, J., Lüpkes, C., Macke, A., Burrows, J. P., Rinke, A., Quaas, J., Maturilli, M., Schemann, V., Shupe, M. D., Akansu, E. F., Barrientos-Velasco, C., Bärfuss, K., Blechschmidt, A.-M., Block, K., Bougoudis, I., ... Zeppenfeld, S. Atmospheric and surface processes, and feedback mechanisms determining arctic amplification: A review of first results and prospects of the (ac)3 project. *Bulletin of the American Meteorological Society*, 104(1), E208–E242. <https://doi.org/10.1175/BAMS-D-21-0218.1>, (2023).
- Wendisch, M., Brückner, M., Burrows, J., Crewell, S., Dethloff, K., Ebell, K., Lüpkes, C., Macke, A., Notholt, J., Quaas, J., Rinke, A., & Tegen, I. Understanding causes and effects of rapid warming in the arctic. *Eos*, 98. <https://doi.org/10.1029/2017EO064803>, (2017).
- Wendisch, M., Crewell, S., Ehrlich, A., Herber, A., Kirbus, B., Lüpkes, C., Mech, M., Abel, S. J., Akansu, E. F., Ament, F., Aubry, C., Becker, S., Borrmann, S., Bozem, H., Brückner, M., Clemen, H.-C., Dahlke, S., Dekoutsidis, G., Delanoë, J., ... Zinner, T. Overview: Quasi-Lagrangian observations of Arctic air mass transformations – introduction and initial results of the HALO–(ac)³ aircraft campaign [Publisher: Copernicus GmbH]. English. *Atmospheric Chemistry and Physics*, 24(15). Publisher: Copernicus GmbH, 8865–8892. <https://doi.org/10.5194/acp-24-8865-2024>, (2024).
- Wendisch, M., Pilewskie, P., Pommier, J., Howard, S., Yang, P., Heymsfield, A. J., Schmitt, C. G., Baumgardner, D., & Mayer, B. Impact of cirrus crystal shape on solar spectral irradiance: A case study for subtropical cirrus. *Journal of Geophysical Research: Atmospheres*, 110(D3). <https://doi.org/10.1029/2004JD005294>, (2005).
- Wendisch, M., Yang, P., & Pilewskie, P. Effects of ice crystal habit on thermal infrared radiative properties and forcing of cirrus. *Journal of Geophysical Research: Atmospheres*, 112(D8). <https://doi.org/10.1029/2006JD007899>, (2007).
- Wernli, H., Boettcher, M., Joos, H., Miltenberger, A. K., & Spichtinger, P. A trajectory-based classification of era-interim ice clouds in the region of the north atlantic storm track. *Geophysical Research Letters*, 43(12), 6657–6664. <https://doi.org/10.1002/2016GL068922>, (2016).
- Wernli, H., & Davies, H. A lagrangian-based analysis of extratropical cyclones. i: The method and some applications. *Quarterly Journal of the Royal Meteorological Society*, 123, 467–489. <https://doi.org/10.1002/qj.49712353811>, (1997).

- Wilhelm, L., Gierens, K., & Rohs, S. Meteorological conditions that promote persistent contrails. *Applied Sciences*, 12, 4450. <https://doi.org/10.3390/app12094450>, (2022).
- Wolf, J. (2023). *Charakterisierung von Verschmutzungs-aerosolen bezüglich der mikro-physikalischen Eigenschaften in Europa und Asien während der EMeRGe - Kampagne* (PhDThesis). Ludwig-Maximilians-Universität München.
- Wolf, V., Kuhn, T., Milz, M., Voelger, P., Krämer, M., & Rolf, C. Arctic ice clouds over northern sweden: Microphysical properties studied with the balloon-borne ice cloud particle imager b-ici. *Atmospheric Chemistry and Physics*, 18(23), 17371–17386. <https://doi.org/10.5194/acp-18-17371-2018>, (2018).
- Wu, W., & McFarquhar, G. M. On the Impacts of Different Definitions of Maximum Dimension for Nonspherical Particles Recorded by 2D Imaging Probes. EN. *Journal of Atmospheric and Oceanic Technology*, 33(5), 1057–1072. <https://doi.org/10.1175/JTECH-D-15-0177.1>, (2016).
- Yang, P., Liou, K.-N., Bi, L., Liu, C., Yi, B., & Baum, B. A. On the radiative properties of ice clouds: Light scattering, remote sensing, and radiation parameterization. en. *Advances in Atmospheric Sciences*, 32(1), 32–63. <https://doi.org/10.1007/s00376-014-0011-z>, (2015).
- Yang, P., Wei, H., Huang, H.-L., Baum, B. A., Hu, Y. X., Kattawar, G. W., Mishchenko, M. I., & Fu, Q. Scattering and absorption property database for nonspherical ice particles in the near- through far-infrared spectral region. EN. *Applied Optics*, 44(26), 5512–5523. <https://doi.org/10.1364/AO.44.005512>, (2005).
- Yurkin, M. A., & Hoekstra, A. G. The discrete dipole approximation: An overview and recent developments. *Journal of Quantitative Spectroscopy and Radiative Transfer*, 106(1), 558–589. <https://doi.org/10.1016/j.jqsrt.2007.01.034>, (2007).
- Yurkin, M. A., & Hoekstra, A. G. The discrete-dipole-approximation code ADDA: Capabilities and known limitations. *Journal of Quantitative Spectroscopy and Radiative Transfer*, 112(13), 2234–2247. <https://doi.org/10.1016/j.jqsrt.2011.01.031>, (2011).
- Zhang, Y., Macke, A., & Albers, F. Effect of crystal size spectrum and crystal shape on stratiform cirrus radiative forcing. *Atmospheric Research*, 52(1), 59–75. [https://doi.org/https://doi.org/10.1016/S0169-8095\(99\)00026-5](https://doi.org/https://doi.org/10.1016/S0169-8095(99)00026-5), (1999).
- Zhu, J., & Penner, J. E. Radiative forcing of anthropogenic aerosols on cirrus clouds using a hybrid ice nucleation scheme. *Atmospheric Chemistry and Physics*, 20(13), 7801–7827. <https://doi.org/10.5194/acp-20-7801-2020>, (2020).
- Ziereis, H., Hoor, P., Groß, J.-U., Zahn, A., Stratmann, G., Stock, P., Lichtenstern, M., Krause, J., Bense, V., Afchine, A., Rolf, C., Woiwode, W., Braun, M., Ungermann, J., Marsing, A., Voigt, C., Engel, A., Sinnhuber, B.-M., & Oelhaf, H. Redistribution of total reactive nitrogen in the lowermost arctic stratosphere during the cold winter 2015/2016. *Atmospheric Chemistry and Physics*, 22(5), 3631–3654. <https://doi.org/10.5194/acp-22-3631-2022>, (2022).
- Ziereis, H., Schlager, H., Fischer, H., Feigl, C., Hoor, P., Marquardt, R., & Wagner, V. Aircraft measurements of tracer correlations in the arctic subvortex region during the polar stratospheric aerosol experiment (polstar). *Journal of Geophys-*

cal Research: Atmospheres, 105(D19), 24305–24313. <https://doi.org/10.1029/2000JD900288>, (2000).

A

APPENDIX: ADDITIONAL FIGURES

A.1. CDP AND CAS-DPOL INTERCOMPARISON

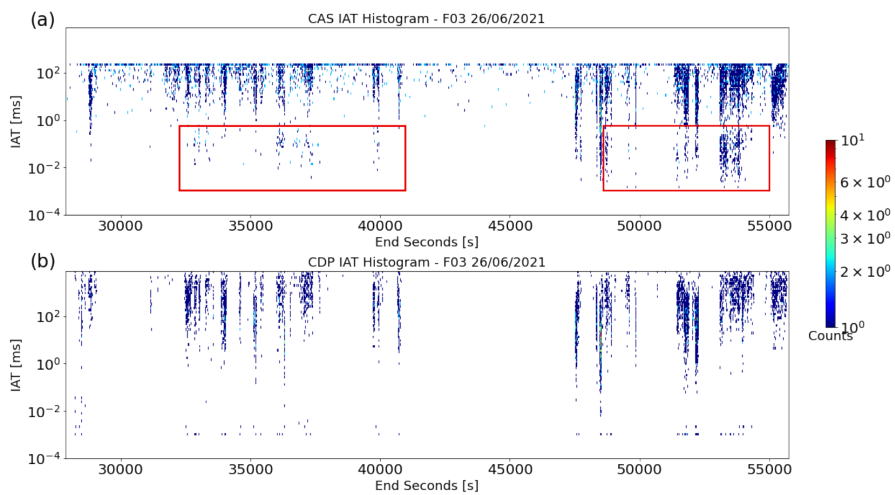


Figure A.1: Interarrival time (IAT) histograms showing the interarrival times for the CAS (upper panel) and CDP (lower panel) during flight F03. The color code indicates the frequency of occurrence. The red rectangles highlight the sequences where a second mode in the CAS IAT histogram appears, which contrast with the CDP.

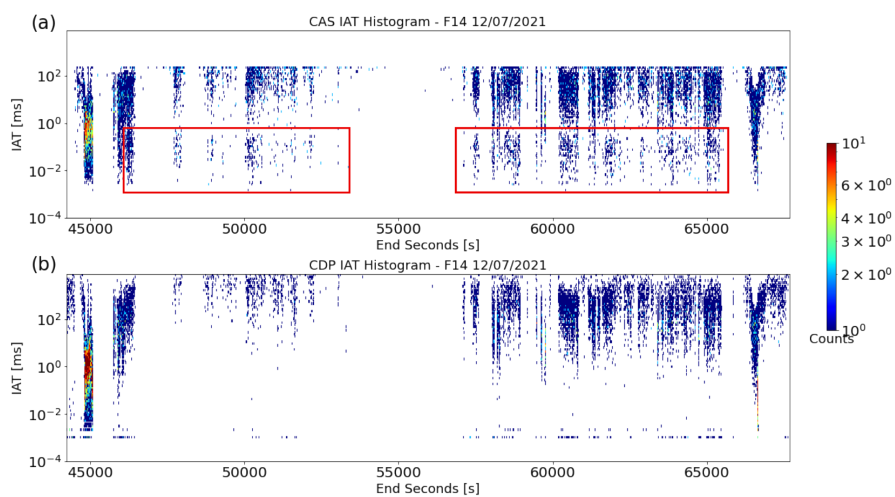


Figure A.2: Same as Fig. A.1 but for flight F14.

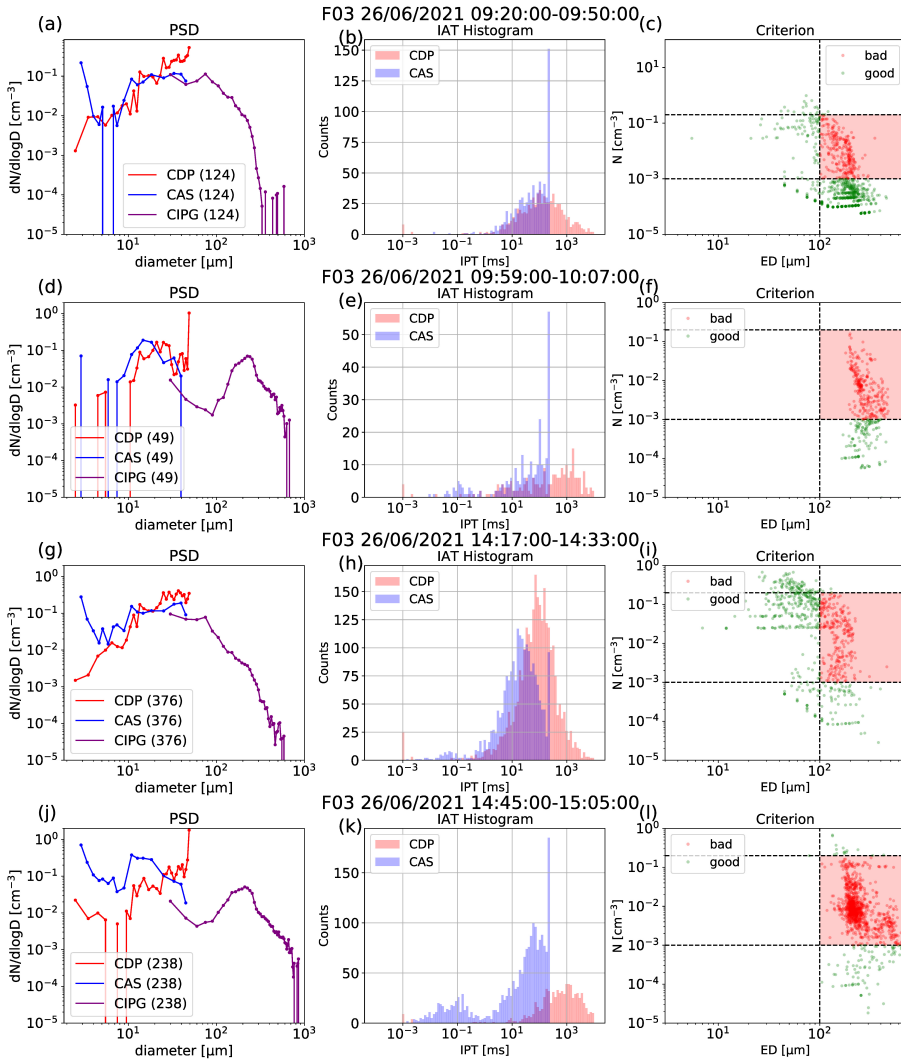


Figure A.3: Analysis of example cirrus sequences from the flight F03, where the upper row represents a case of bad agreement and the lower row a better agreement. Particle Size Distribution (PSD) of the CDP (red), CAS (blue) and CIPG (purple) with the number of samples in parenthesis (a, d). Interarrival time (IAT) histograms of the CDP (red) and CAS (blue) from the particle-by-particle information (b, e). Phase plots of N as a function of ED of the combined size spectrum (CDP-CIPGs-PIP) (c, f). Dashed lines indicate the limits of the criterion definition, and the critical area is shaded in red. Green dots indicate points outside the critical area (good agreement), and red dots indicate points inside (bad agreement).

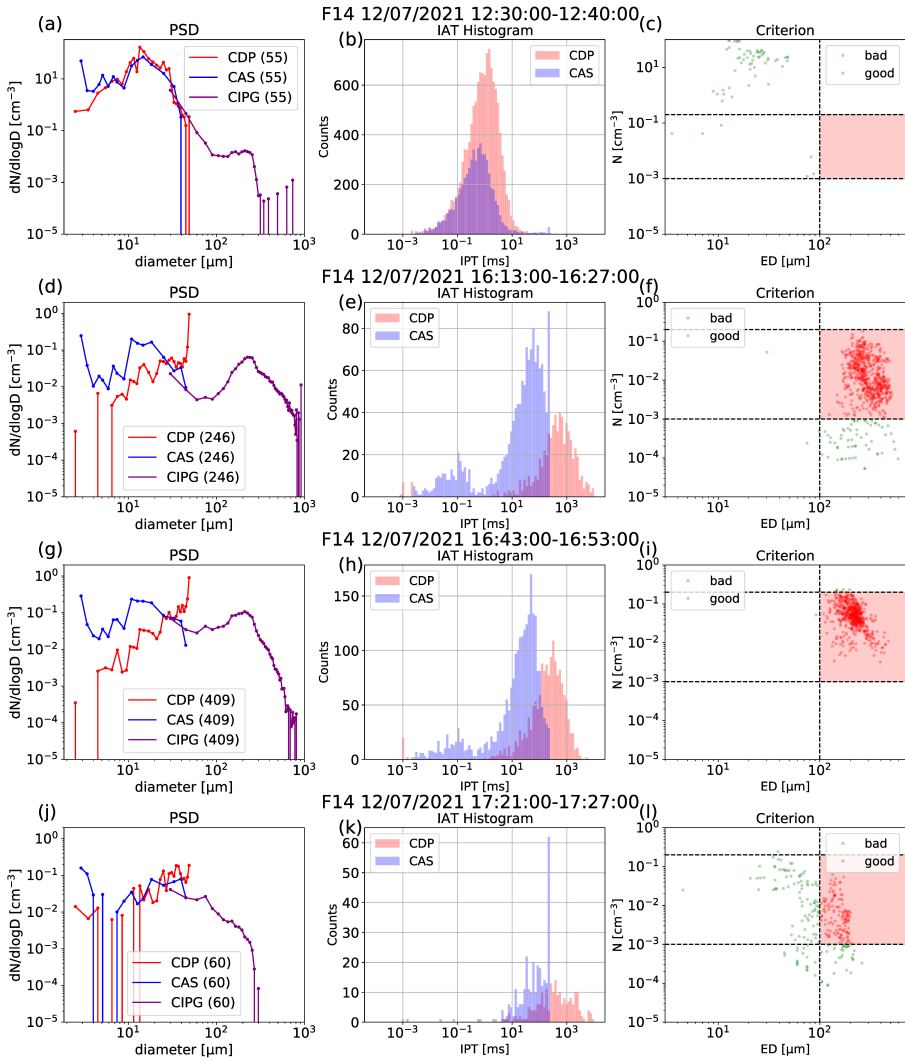


Figure A.4: Same as Fig. A.3 but for flight F14.

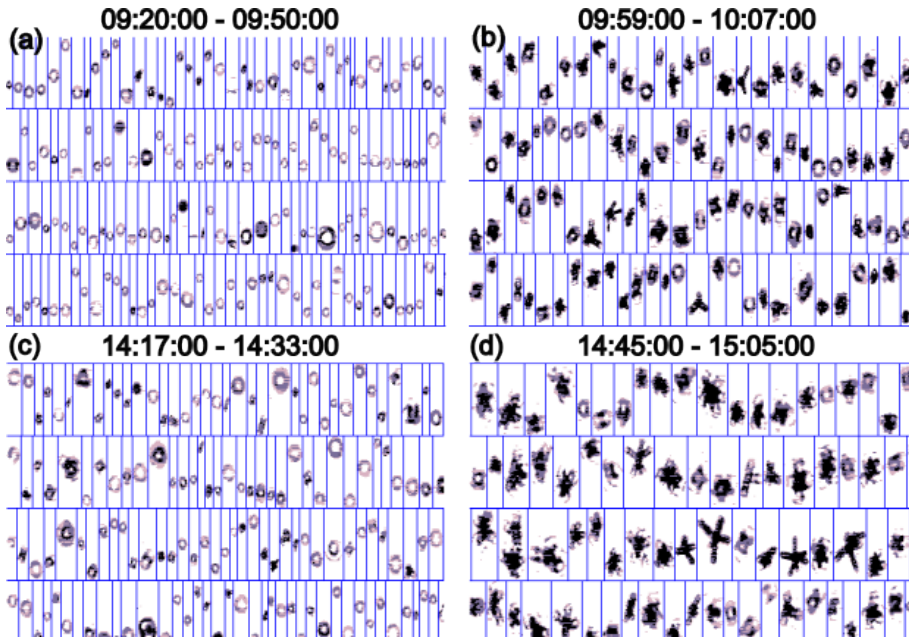


Figure A.5: Extracts of the set of particle images from the CIPG corresponding to the sequences shown in Fig. A.3.

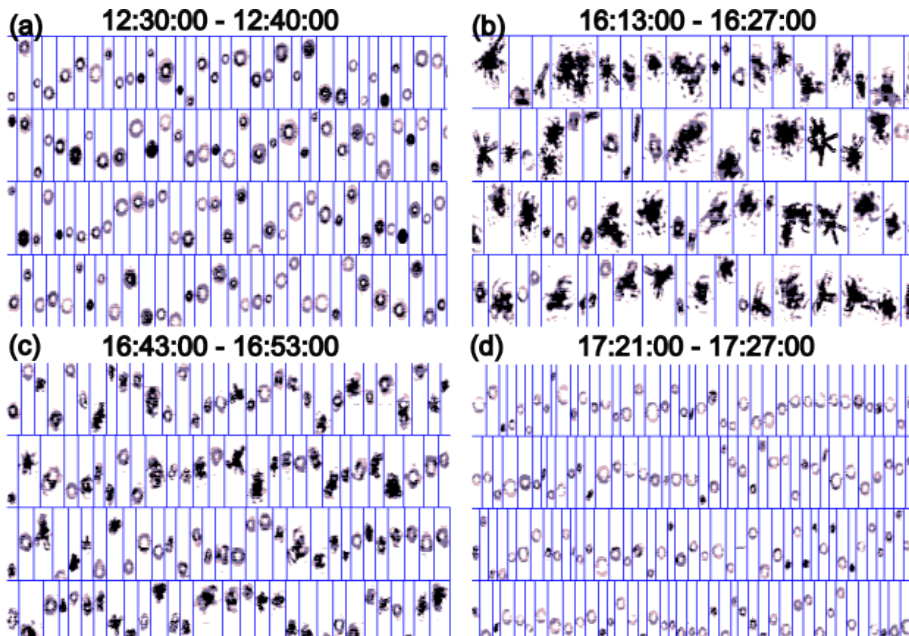


Figure A.6: Same as Fig. A.5 but for sequences in Fig. A.4 of flight F14.

A.2. EXTINCTION COEFFICIENT OF HIGH AND MID-LATITUDE CIRRUS

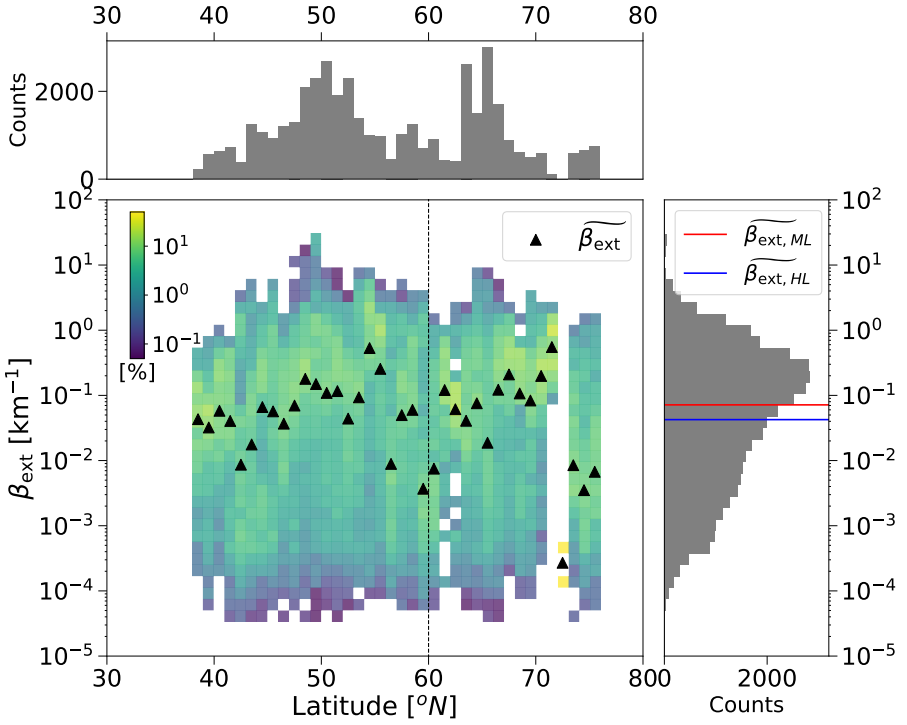


Figure A.7: Normalized frequency distribution of the extinction coefficient (β_{ext}) from the observations as a function of latitude of the measurement during CIRRUS-HL. Latitude bins are 1° wide and vertical bins are logarithmic. The colour code indicates the frequency of occurrence in percent per 1 degree latitude bins, normalized by the total counts per latitude bin. The vertical dashed line marks the threshold of 60° N for the differentiation of ML and HL cirrus. Triangular markers are medians per latitude bin ($\widehat{\beta}_{\text{ext}}$). The top and right panels are histograms of the corresponding variables. See a similar representation for N, ED and IWC in the main text.

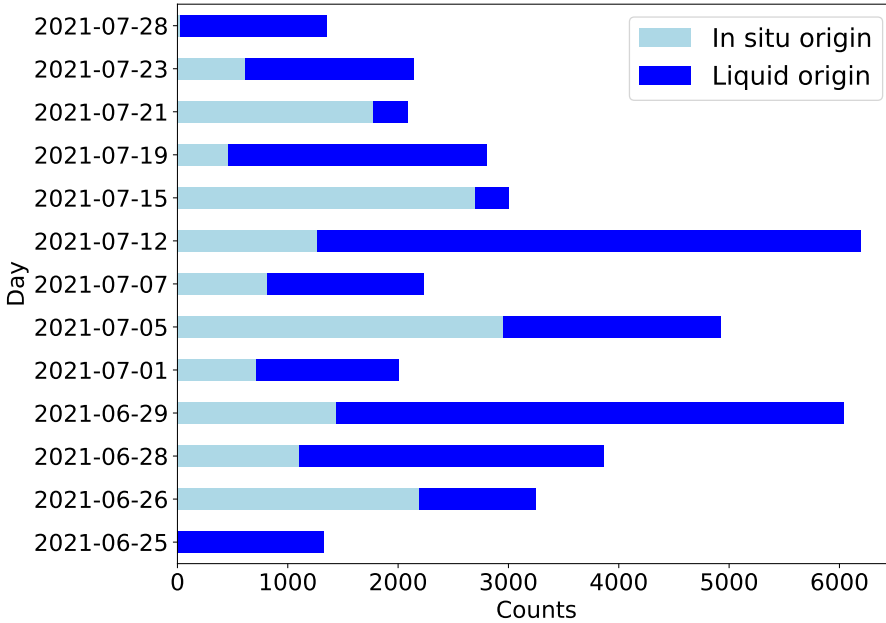
A.3. IN SITU AND LIQUID ORIGIN MEASUREMENTS PER DAY

Figure A.8: Summary of the 2-s observations frequency of cirrus origin (in situ, light blue and liquid origin, darker blue) per day during the CIRRUS-HL flights. The frequency is represented by the total number of counts.

A.4. SENSITIVITY STUDY OF LATITUDE THRESHOLD 60°N

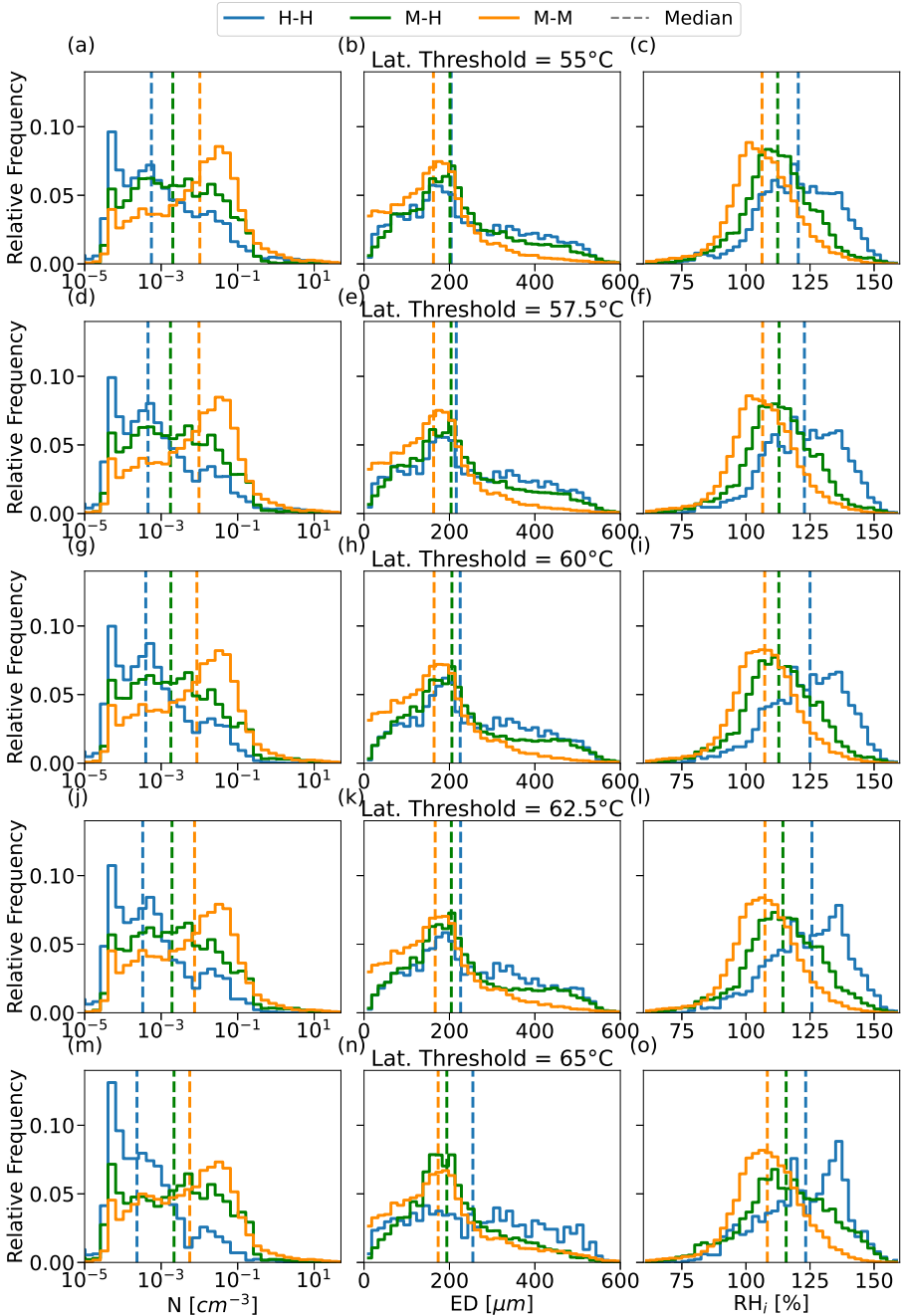


Figure A.9: Sensitivity study of the latitude threshold selection. The relative frequency of the variables N (left-hand side), ED (center) and RH_i (right-hand side) are represented for the H-H cirrus (blue), M-H cirrus (green) and M-M cirrus (orange) depending on the specified latitude threshold: 55, 57.5, 60, 62.5 and 65 °N. See Fig. 6 in the main text for further details on the relative frequency distributions.

A.5. ADDITIONAL ANALYSES FOR AEROSOL-CLOUD INTERACTION

A.5.1. EXTRA ANALYSES WITH CLIMATOLOGICAL DATA

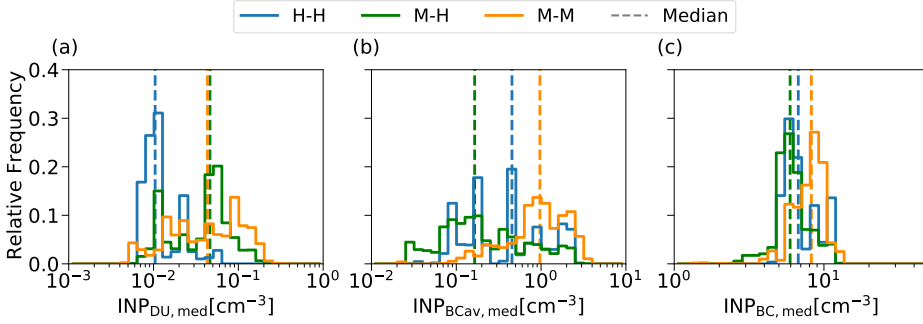


Figure A.10: Same analysis as Fig. 5.16 but for a climatological mean of the June-July months between 2014 and 2021.

A.5.2. SENSITIVITY STUDY OF SIMULATIONS INCLUDING AMMONIUM SULFATE AND GLASSY ORGANICS

The simulations used in Section 5.6 were repeated to include ammonium sulfate (AmSu) and glassy organic particles (glPOM) with the freezing properties detailed in Table A.1 from Beer et al. (2022). The objective of this sensitivity study was to determine whether the inclusion of these additional INP types would affect the conclusions drawn in Section 5.6 for mineral dust, black carbon from aviation, and black carbon from other ground sources. The same graphs presented in Figs. 5.16, 5.18 and 5.19 are shown here in Figs. A.11 to A.13 for the new case and reveal negligible changes in the relative frequency distributions of the studied parameters.

Table A.1: Freezing properties (critical supersaturation S_{crit} and activated fraction f_{act}) of the additional ice nucleating particles (INPs) as in Beer et al. (2022).

Property	AmSu	glPOM
S_{crit}	1.25	1.3
f_{act}	0.001	0.001

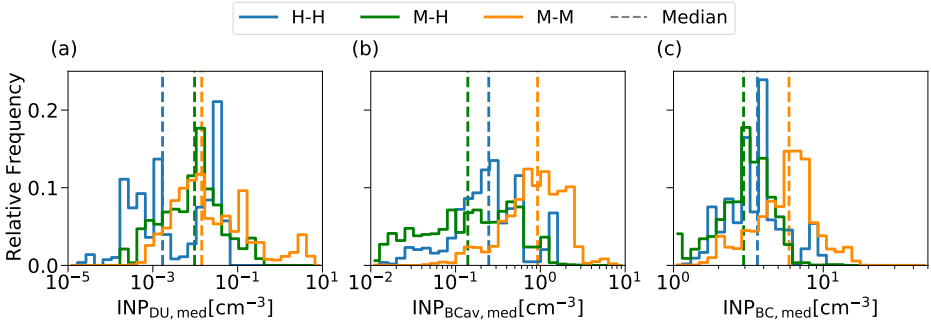


Figure A.11: Same analysis as Fig. 5.16 but with simulations including ammonium sulfate and glassy organic particles as INPs.

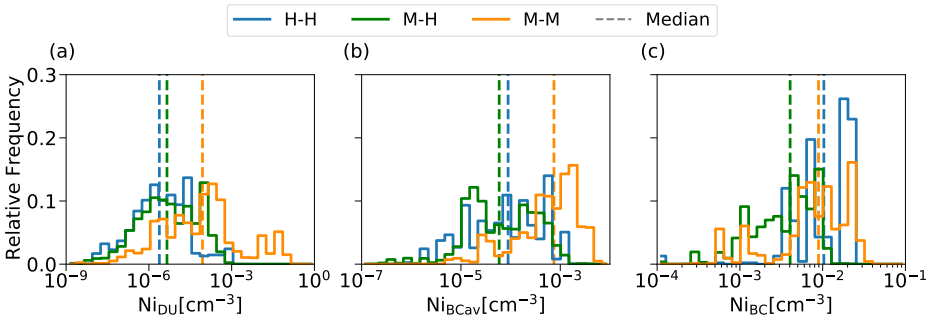


Figure A.12: Same analysis as Fig. 5.18 but with simulations including ammonium sulfate and glassy organic particles as INPs.

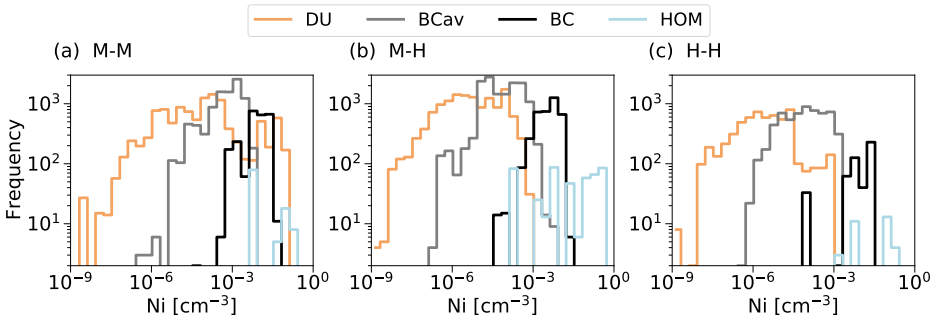


Figure A.13: Same analysis as Fig. 5.19 but with simulations including ammonium sulfate and glassy organic particles as INPs.

A.5.3. SENSITIVITY STUDY FOR YEARS 2020 AND 2019

In this study, further simulations were conducted using emissions data for the years 2020 and 2021 (see details on the model setup in Section 5.6.1). It is important to note that the emissions data are based on predicted scenarios from the year 2015 and therefore

do not account for the emission reduction effects observed in 2020 due to the COVID-19 pandemic (Voigt et al., 2021). The main insight from this sensitivity test is that the few cases of homogeneous nucleation observed for the real campaign period of 2021, are not a particularity of that year, but it is also observed for the same period in 2019 and 2020.

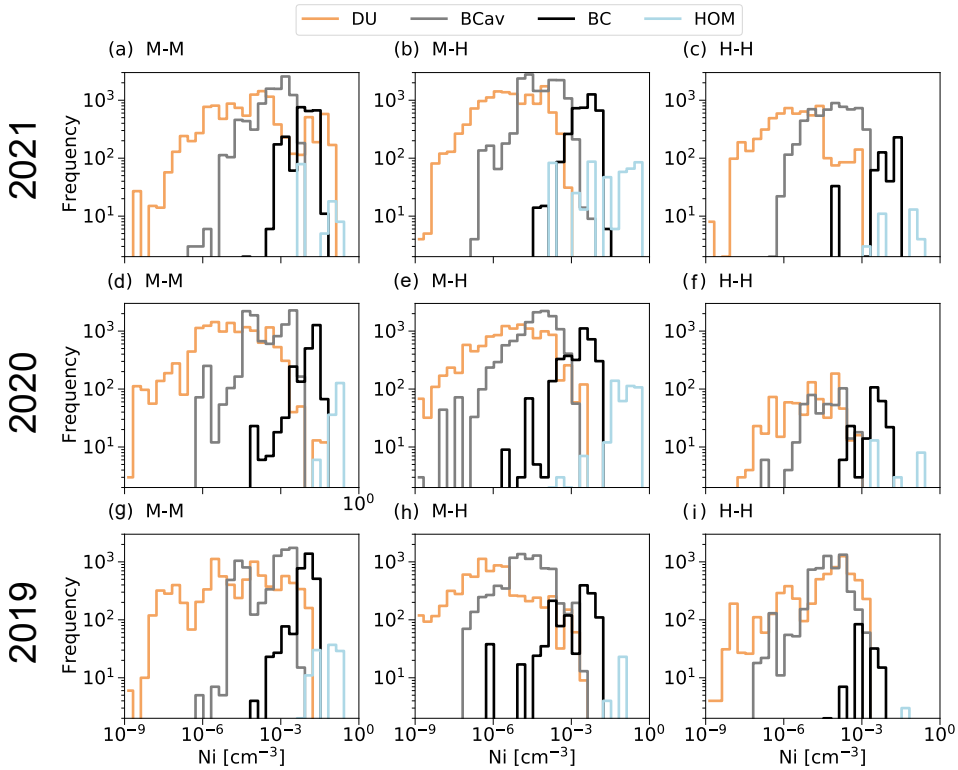


Figure A.14: Same analysis as Fig. 5.19 but with additional simulations of the years 2020 and 2019 as comparison for 2021.

B

APPENDIX: IMAGE DATA DECOMPRESSION

This appendix offers a detailed description of reading and interpreting the binary data format used by DMT LLC for both monoscale and grayscale OAPs. It covers details about the data structure, compression algorithms, and provides specific information of the image pre-processing implementation in Python.

As commented at the end of Section 3.2.1, two types of files are generated, one containing 1D sizing data in 1-s time resolution, and a second one with compressed 2D image data. While the 1D sizing data provides counts per second and classifies them into size bins, these retrievals can only be used to monitor the measurement during flight and obtain a rough idea of the statistics. The 2D image data is essential for operating directly with the images, detecting possible pixel errors and artifacts, filtering them, and performing an accurate sizing by considering the two dimensions of the images. However, before the image data can be processed, it needs to undergo decompression. The algorithm's development was guided by the instructions on image data storage and compression provided by DMT LLC (DMT, 2011), and it was based on the available decompression algorithms in my group for the monoscale 2D-S imaging probe (Kirschler, 2023; Schollmayer, 2021).

The 64-diode array state is stored at high frequency and the shadow intensity of a diode is translated into a digital signal with a 1-bit number for monoscale probes: "1" if illuminated, or "0" if shadowed; and 2-bit number for grayscale probes: "11" if illuminated, "10" if at least 25% shadowed, "01" if at least 50% obscured, and "00" if at least 75% shadowed. This concept is sketched in Fig. B.1 and represents the conversion of an ice crystal shadow slice into electronic data. Since the array is composed by 64 diodes, an image slice of a monoscale probe is translated into 64 bits, while an image slice of a grayscale probe needs 128 bits. This is the first and main difference between the data structure of both instruments.

An image consists of a series of slices stored one after the other. Once the current particle has moved out of the laser, the data recording of that particle stops and the next

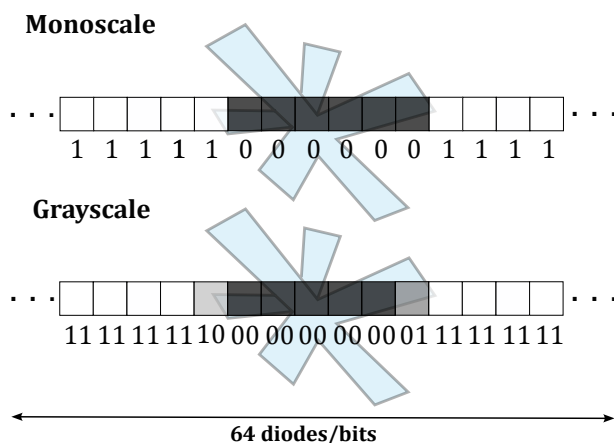


Figure B.1: Schematic of an example of an ice crystal shadow state of the diode array in monoscale and grayscale modus.

particle recording starts. Accompanying the image slices, there is further information about each particle, which makes it identifiable among the whole images in the stream. This information is comprised in a so-called *particle header*. In addition, there is a row of bytes with a certain format (1010's in monoscale and 1's in grayscale) to indicate the ending of a particle and the beginning of the next one. Bytes of image data and particle headers are recorded successively forming a stream of bytes. Since many of these bytes are usually repeated (e.g. particle background of all ones), the data is compressed following different patterns of run-length encoding for monoscale and grayscale probes, which will be explained later.

4096 bytes of compressed image data defines a *buffer* and each buffer has its corresponding *buffer header*, what makes it a total of 4112 bytes per buffer. Buffers are written in an Imagefile until it reaches the size of ≈ 80 MB (20000 buffers) and then a new Imagefile is started. Important to note is that every file starts with a buffer header followed by 4096 bytes of compressed image data. The structure of the image data described here is summarized in the diagram of Fig. B.2. Note that the buffers in monoscale probes are organized in sets of 8 bytes (64 bits) while the grayscale probes are composed by 128-bit slices.

I developed two distinct Python scripts for processing image data from monoscale and grayscale DMT probes. The *bitstring* module from Python made the manipulation of binary data quite easy and mainly the *BitArray* and *ConstBitStream* classes were used. The program has been strongly optimized using the *cProfile* module for Python and *SnakeViz* (browser-based graphical viewer of the output). The amount of data being processed is large (specially for our CIPGs) and thus, a good program performance with reduced computation time is key. Computation in a cluster is recommended for processing flights with several Imagefiles. It takes about 15 minutes to read a complete PIP Imagefile with parallel computing with 8 cores (2 minutes in a cluster with 128 processors). The time increases for an Imagefile of the CIPG up to 45 minutes (6 minutes in a cluster with 128 processors).

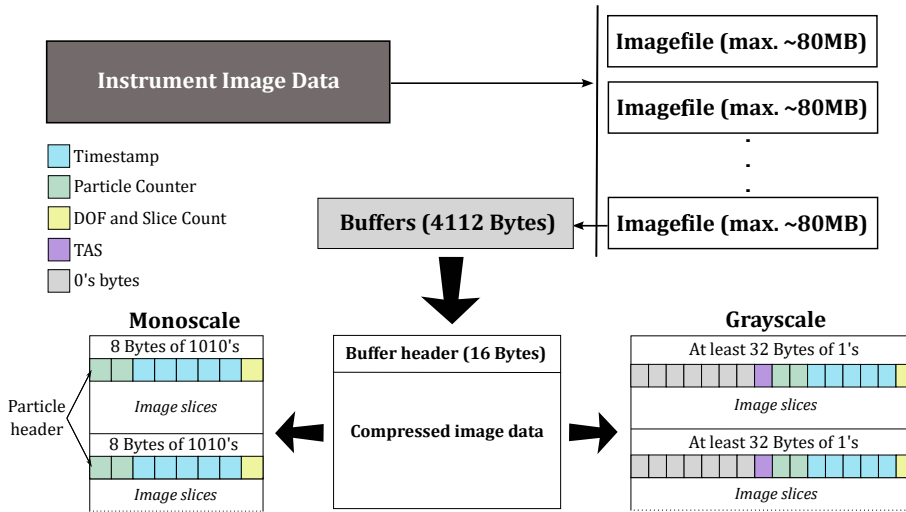


Figure B.2: Diagram of the data structure of the image data from a DMT imaging probe. Colored squares indicate the type of information included in the particle headers and the buffers structure is indicated for monoscale (left side) and grayscale (right side) option.

The flow chart depicted in Fig. B.3 shows the main working principle of the algorithm. It is important to differentiate between the original stream, directly read from the Imagefile, and the decompressed stream resulting from the original stream's decompression. The *switch* function verifies the position in the whole stream and remits to the functions *read_buffer*, if it is the beginning of a buffer, or to *read_image*, if the position is inside the buffer. The *read_buffer* function reads first the buffer header, then decompress the buffer (following 4096 bytes) and finally finds the particle boundaries within the decompressed stream. Besides that, the *read_image* is called as many times as particles are in the decompressed stream. It reads the particle header (*read_parthead*) and as many slices of image data as the particle has (*get_image_slices*). The particle header together with the reconstruction of the image itself is the information that is saved and written in a file for particle analyses and post-processing. When the end of the decompressed stream is reached, the position in the original stream shifts to the beginning of the next buffer (next 4112 bytes) and the same process is repeated until the end of the original stream is met. The following is a more detailed explanation of the steps presented here.

BUFFER HEADER

Each buffer is preceded by a header of 16 uncompressed bytes, which contains a timestamp, as depicted in Fig. B.2. Every 2 bytes correspond to a unit of the timestamp beginning with the year and following the month, day, hour, minute, second, millisecond and weekday. Each pair of 2 bytes in the byte stream is written in reversed order. Therefore, it should be read as a byte-wise little-endian unsigned integer. For example, if the two bytes for year are "E707" in hexadecimal format, one needs to swap the bytes as "07E7" to obtain the number 2023.

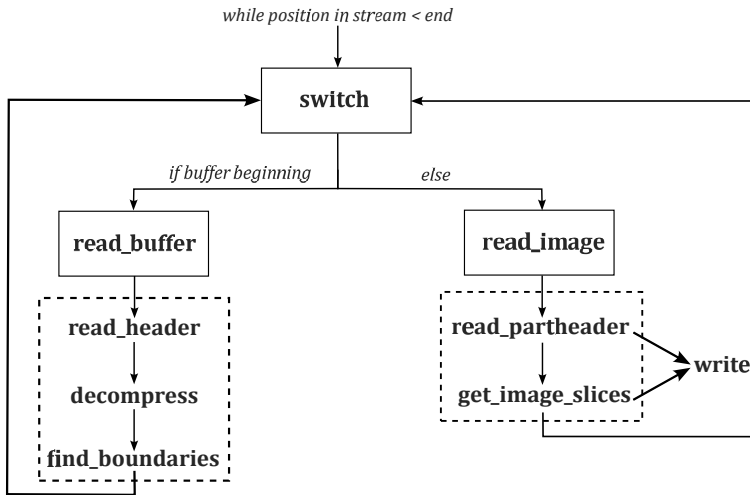


Figure B.3: Flow chart of the Imagefile data processing algorithm structure and main functions. The structure is the same for monoscale and grayscale probes, the functions itself are internally different.

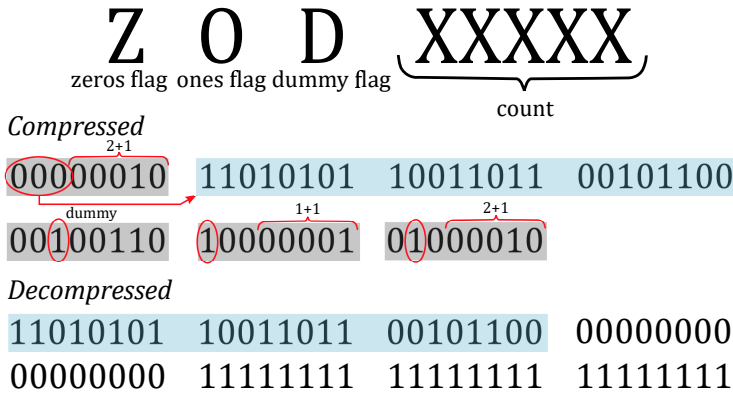
The structure and format of the buffer header are the same for both monoscale and grayscale probes. Following the buffer header, there are 4096 compressed bytes that require decompression using different schemas for monoscale and grayscale probes, which are explained below.

COMPRESSION ALGORITHM MONOSCALE

Monoscale data is compressed following a schema controlled by run-length encoding header bytes (RLEHB). These bytes serve as indicators of the format and repetitions of the next bytes and follow the structure indicated in Fig. B.4. In this structure, each byte is separated into bits, where the relevant bits are Z , O , and D . The remaining 5 bits, which should be interpreted as an unsigned integer, provide the count. This count indicates the number of bytes +1 of a certain type that follows. If Z is 1, the subsequent bytes (count +1) are all zero bytes; if O is 1, the next bytes (count +1) are all bytes of ones. If D is 1, the current RLEHB is a dummy byte that should be ignored, and the next byte should be read, which will be a new RLEHB. If all three flags are 0, the next (count +1) bytes are data bytes and should be added to the decompressed byte stream as they are. An example of bytes decompression is shown in Fig. B.4.

The decompression of a buffer (consisting of 4096 subsequent bytes) begins after reading the buffer header. The algorithm starts by examining the first byte in the buffer, which is always a RLEHB since every buffer starts with one. It reads the first 3 bits of the RLEHB separately and the next 5 bits together as an unsigned integer. Depending on the flags, it appends either count +1 zero bytes or bytes of ones to the decompressed stream. If all three flags are zero, it reads the subsequent count +1 bytes from the stream and adds them to the decompressed stream. If $D = 1$, it proceeds to interpret the next byte as another RLEHB.

The algorithm continues to read bytes from the original stream as long as the byte



B

Figure B.4: Format of a run-length encoding header byte (RLEHB) for monoscale data and an example of decompressed data. The RLEHBs are shaded in gray and the data bytes in blue.

position is 4112 times the number of buffers read + 1.

COMPRESSION ALGORITHM GRAYSCALE

The best way to understand the grayscale data is to keep in mind that the pixel state is translated into a 2-bit quantity, so the compression schema processes the data in a stream of 2-bits. Analog to monoscale data decompression, the grayscale decompression algorithm starts reading bytes after processing the buffer header. Bytes in the compressed stream can take different formats: either as data bytes or count bytes:

- Data byte (6 bits): 01xxxxxx → The 6-bit data following the "01" pair is directly added to the decompressed stream.
- Data byte (4 bits): 0001xxxx → The 4-bit data following the "0001" group is directly added to the decompressed stream.
- Data byte (2 bits): 000001xx → The 2-bit data following the "000001" group is directly added to the decompressed stream.
- Count byte: 1xxxxxxx → The 7 bits following the "1" indicate the number of times to repeat the last 2-bit data added to the decompressed stream.

In processing each byte of the available 4096 in the buffer, the algorithm checks whether the most significant bit of the byte is a 1. If it is not, the algorithm checks for the other three formats, adds the corresponding data pairs, and saves the last pair for the next round in case a count byte comes, and the last 2 bits have to be repeated and added to the decompressed stream.

PARTICLE BOUNDARIES

I employ the same approach to identify particles in the decompressed stream of monoscale and grayscale data, despite the differently coded indicators for particle boundaries. The

key is to leverage the useful *findall()* function of the *ConstBitStream* class, which generates a list of positions in the stream, where the specified group of bytes (or bits) is found.

For monoscale data, the algorithm searches for a byte-aligned sequence of 8 consecutive bytes of "10101010" (or "aa" in hexadecimal). As the function provides the starting position for that group of bytes, the beginnings of particles are shifted by 8 bytes from the obtained positions. These shifted positions are saved in a list and are utilized by the *read_image* function to determine where to start reading an image each time, regardless of the previous image. Since the image data in a buffer may not necessarily start at a particle header and more frequently begins in the middle of a particle, it is crucial to consistently use particle boundaries to navigate the stream.

For grayscale data, 16 consecutive non-byte-aligned bytes of all ones indicate the particle boundary. A similar procedure is applied as for monoscale data.

PARTICLE HEADERS

After a particle boundary, the image data starts with the particle header, which contains crucial information about the particle (see Fig. B.2). The most important information stored in the particle header include the particle counter and the timestamp. The timestamp signifies the time (in 125 ns resolution) at which the particle ends, and the particle counter is a number ranging from 1 and 65535 generated by a counter that increments each time the probe hardware detects a particle. Although the counter theoretically progresses continuously without jumps, in practise, electronics limitations can result in missed recordings when the particle rate exceeds the system's capabilities. If the difference between the counter of one particle and the previous one exceeds one, there are particle lost in between, and the number of them is designated as *missed particles*. The method for interpreting the information in the particle header, differentiating between monoscale and grayscale versions, is detailed below.

For monoscale data, once aligned at the beginning of a particle header, reading the first two bytes in reversed order (with the most significant byte written after the least significant byte) as an unsigned integer provides the particle counter. The next 5 bytes correspond to the timestamp and are also reversed. After reversal, they are treated as a row of bits, read in specific groups as unsigned integers. The first 5 bits denote the hour, the next 6 signify the minutes, the seconds are obtained from the subsequent 6 bits, milliseconds from the next 10, and the last 13 bits represent the unit of minimum resolution. This unit must be multiplied by $125 \cdot 10^3$ to obtain the microseconds. The next 7 bits in the decompressed stream provide the slice count, indicating the number of image slices +1 forming the particle image. The final bit is the depth-of-field flag, set to 1 if at least one pixel of the image is shadowed by 2/3, meaning that the particle is more centered in the depth of field, reducing the overestimation of the particle size.

The documentation of DMT LLC (DMT, 2011) lacks reliability and is quite confusing regarding grayscale decompressed data. Extensive testing was conducted to ascertain the actual format. After positioning at the beginning of the particle header, the entire particle header (128 bits) must be read in 2-bits pairs, and the order of pairs reversed (e.g., 11 – 01 – 00 – 10 → 10 – 00 – 01 – 11). Subsequently, the following information can be extracted from the slice by reading the specified number of bits as unsigned integers

in the given order: slice count (first 8 bits), hour (5 bits), minute (6), second (6), millisecond (10), microsecond (10) added to the minimum resolution (3) multiplied by $125 \cdot 10^3$, particle counter (16) and TAS (8). The last 56 bits are all zeros.

The information of the particle header is crucial, without the correct timestamp, particles can not be correctly ordered, and any attempt to calculate particle concentration will yield inaccurate results. If the particle header is incorrectly read, for instance, the particle counter is negative or the timestamp is implausible (e.g. hour greater than 24), there is a misalignment in the decompressed stream, leading to incorrect interpretation of image data. It is highly recommended to verify the particle header to ensure accurate data reading. For this reason, the information in the particle header is saved together with the image data itself.

IMAGE SLICES

After assuring the alignment at the particle boundary was successful and the particle header was correctly interpreted, the remaining bytes until the next particle boundary are image data bytes. In the monoscale version, each 64-bit slice should be read byte-wise and the order of the bytes reversed ($B_0 B_1 B_2 B_3 B_4 B_5 B_6 B_7 \rightarrow B_7 B_6 B_5 B_4 B_3 B_2 B_1 B_0$). The slices are added one after the other in a row and saved in binary format for writing out the data together with the particle header. If one wants to visualize the image, it is enough to rearrange the slices in a matrix of $n_{\text{slices}} \times 64$.

In the grayscale variant, the 128-bit slices are read in pairs of 2-bits instead of byte-wise. To allow for a conversion into a $n_{\text{slices}} \times 64$ matrix representing the actual particle shape, the 2-bit quantities defining the state of the diodes are converted into integer from 0 to 3: 3 for "11" (background), 2 for "10" (at least 25% obscured, first shadow level), 1 for "01" (at least 50% obscured, second shadow level), and 0 for "00" (at least 75% obscured, third shadow level). After the conversion, the 64 elements of the slice are reversed and the image data is stored analogously to monoscale data.

ACKNOWLEDGEMENTS

I want to give my deepest thanks to everyone who has been part of this exciting journey...

I would like to begin by acknowledging my promotors Prof. Dr. Christiane Voigt, Prof. Dr. Volker Grewe and my supervisor Dr. Tina Jurkat-Witschas for their support and the time they have dedicated over the years, which has helped me become a better scientist. Thank you, Christiane, for giving me the opportunity to work and conduct my research at the Cloud Physics Department at the German Aerospace Center (DLR). Your warm welcome during the unusual times of winter 2020, in the middle of the Covid-19 pandemic, and your efforts in building and maintaining such a great group are truly appreciated. Volker, I am very grateful for the opportunity to pursue my PhD at the Technical University of Delft and for your meticulous and rigorous review of my work, especially during the final stages. A special thank you to Tina, who has guided me wisely throughout this journey. Thank you for all the discussions and the trust you always had on me. Your enthusiasm and passion are inspiring, making our work together a great pleasure!

I would also like to acknowledge the positive cooperation with the aerosol modelling colleagues at DLR: Dr. Christof Beer, Dr. Johannes Hendricks, and Dr. Mattia Righi. A particular thanks to Christof for the many discussions and for reviewing parts of my work. I cannot forget to mention Dr. Daniel Sauer, for his support with the aerosol measurement data.

I want to thank all my colleagues from the Cloud Physics Department at DLR for all the moments we shared over the years at the institute, in the lab, and during measurement campaigns. In particular, Simon Kirschler, for your wise input and advice, countless conversations, and your priceless help in software development. Johannes Lucke, thank you for your open and generous assistance on numerous occasions. Valerian Hahn, I appreciate your support during the CIRRUS-HL campaign, and more recently during the Nephel campaign, sharing moments of frustration and your endless knowledge with the CAPS. Manuel Moser and Johanna Mayer, thank you for the great time and teamwork during the (AC)³ campaign in Svalbard.

I am also grateful to Natalie Keur, Ilona Hennig and Christine Renz for their administrative support, patience, and kindness answering my questions. Additionally, to Björn Brötz and Winfried Beer for the IT support. My sincere thanks go to the aircraft engineers and pilots from DLR, Alfred-Wegener-Institute (AWI), and AV Experts LCC., for enabling our measurements and bringing us home safely. Further, a big thank you to all the colleagues from other groups and institutions I had the pleasure to work with during my three aircraft measurement campaigns.

I am very grateful to my parents, María José and Juan, and my brother, Pablo, for their unconditional support and motivation at every step of my education. I would not have come this far without you! I must also mention my aunt Virtudes, for her motivational speeches. Last, but certainly not least, I am eternally grateful to Santiago, my partner and daily support, for being there for me through the highs and lows. You are my grounding.

CURRICULUM VITÆ

Elena De La Torre Castro

30-07-1995 Born in Madrid, Spain.

EDUCATION

1998–2007 Colegio Público Miguel de Cervantes, Collado Villalba, Spain

2007–2013 Instituto de Educación Secundaria María Guerrero, Collado Villalba, Spain

2013–2017 Bachelor of Science in Aerospace Engineering
Universidad Politécnica de Madrid (UPM), Madrid, Spain

2014–present Bachelor in Law
Universidad Nacional de Educación a Distancia (UNED), Madrid, Spain

2017–2020 Master of Science in Aerospace Engineering
Technische Universität München (TUM), Germany

2021–2024 PhD Candidate at Delft University of Technology
Thesis: Microphysical properties and interplay of natural cirrus, contrail cirrus and aerosol at different latitudes
Promotors: Prof. dr. V. Grewe and Prof. dr. C. Voigt

AWARDS

2013 Excellence Scholarship for the Spanish University Admission Tests, Madrid

2014 Excellence Scholarship for the first university year, Madrid

2023 Best HALO Publication 2023 by a PhD Early Career Scientist

LIST OF PUBLICATIONS

1. **E. De La Torre Castro**, T. Jurkat-Witschas, A. Afchine, V. Grewe, V. Hahn, S. Kirschler, M. Krämer, J. Lucke, N. Spelten, H. Wernli, M. Zöger, and C. Voigt, *Differences in microphysical properties of cirrus at high and mid-latitudes*, [Atmos. Chem. Phys.](#), **23**, 13167–13189, 2023.
2. J. Lucke, T. Jurkat-Witschas, D. Baumgardner, F. Kalinka, M. Moser, **E. De La Torre Castro**, and C. Voigt, *Characterization of Atmospheric Icing Conditions during the HALO-(AC)³ Campaign with the Nevzorov Probe and the Backscatter Cloud Probe with Polarization Detection*, [SAE International](#), 2023.
3. F. Kalinka, M. Butter, T. Jurkat-Witschas, **E. De La Torre Castro**, and C. Voigt, *A Simple Prototype to Forecast High Ice Water Content Using TAT Anomalies as Training Data*, [SAE International](#), 2023.
4. M. Wendisch, S. Crewell, A. Ehrlich, A. Herber, B. Kirbus, C. Lüpkes, M. Mech, ..., **E. De La Torre Castro**, ..., *Overview: Quasi-Lagrangian observations of Arctic air mass transformations – Introduction and initial results of the HALO-(AC)³ aircraft campaign*, [Atmospheric Chemistry and Physics](#), 2024.
5. A. Ehrlich, S. Crewell, A. Herber, M. Klingebiel, C. Lüpkes, M. Mech, ..., **E. De La Torre Castro**, ..., and M. Wendisch, *A comprehensive in-situ and remote sensing data set collected during the HALO-(AC)³ aircraft campaign*, [Earth Syst. Sci. Data Discuss.](#) [preprint], in review, 2024.
6. T. Jurkat-Witschas, ..., **E. De La Torre Castro**, ..., *CIRRUS-HL - Picturing the high- and mid-latitude summer cirrus with airborne measurements from the High Altitude- and Long-range research aircraft HALO*, [Bulletin of American Meteorology Society](#), in review, 2024.
7. G. Neumann, A. Marsing, T. Harlass, D. Sauer, C. Heckl, P. Stock, **E. De La Torre Castro**, V. Hahn, A. Roiger, C. Voigt, S. Unterstraßer, J. Cammas, C. Renard, R. Vansenden, A. Vansenden, and T. Jurkat-Witschas, *First in-flight aircraft emission measurements of a turboprop engine using a novel contrail and emission measurement payload*, [Atmospheric Measurement Techniques](#), to be submitted, 2024.